FAILURE OF LASER WELDS AND FORMABILITY OF BIMATERIAL THIN STEEL SHEETS

by

Kamran Asim

A dissertation submitted in partial fulfillment
of the requirements for the degree of
Doctor of Philosophy
(Mechanical Engineering)
in The University of Michigan
2011

Doctoral Committee:

Professor Jwo Pan, Chair
Professor William F. Hosford, Jr.
Professor Jyotirmoy Mazumder
Associate Professor Wei Lu

Dedicated to my father, mother and family
for their continuous support and love.

ACKNOWLEDGMENTS

I would like to express my sincere gratitude and thanks to my advisor, Professor Jwo Pan, for his continuous guidance and encouragement throughout my research work. His intellectual support helped me organize my random research endeavors into a Ph.D. thesis that is makes sence and is technically correct. I also wish to extend my gratitude to my doctoral committee, Professor William F. Hosford, Jr., Professor Jyotirmoy Mazumder and Professor Wei Lu for their guidance and valuable suggestions.

I am also thankful to Professor Jwo Pan's research group, especially, Kulthida Sripicahi and Jaewon Lee. Their assistance with the computational part of my thesis is instrumental in shaping up my thesis. I also acknowledge the advice and support that I received from Dr. Van-Xuan Tran, on both the academic and personal levels. I am also grateful to Teresa Franklin for her support in preparing for my defense. I express my thanks and well wishes to Catherine Amodeo, Md Yusuf Ali, Katherine Avery and Seung Hoon Hong. I will always appreciate the efforts of Won Ho Jo, Paul Smith and Amit Ranjan in helping me with my experimental work. I am also thankful to Dr. Thomas Bress for helping me with the equipment at the Auto Lab undergraduate laboritories. My special thanks to all the staff members at the Auto Lab graduduate workshop for their support and guidance in using the CNC and other machines at the workshop.

I also acknowledge the support of Dr. Scott Weil and Dr. Sung-Tae Hong in the Nb-clad stainless steel research. Dr. Sung-Yu Pan provided great help in the polymer-

coated research part. I also express my gratitude and thanks to Mr Steve Stoetzer of Acheson Colloids, MI for preparing the epoxy sheet for tensile tests. I am very grateful to Dr. Mike Li of TWB, Monroe, who provided the laser welded sheets and was always available to answer my queries. The stress-life fatigue test data for SAE 950X was provided by Dr. Peter Friedman, for which I am very grateful to him. Finally, I would like to thank the Ministry of Science and Technology, Government of Pakistan for their financial support during my academic and research work.

TABLE OF CONTENTS

DEDICATIONS ii

ACKNOWLEDGMENTS iii

LIST OF FIGURES viii

LIST OF TABLES xvi

CHAPTER

I INTRODUCTION 1

1.1. Part I : Failure of laser welds in lap-shear specimens 1
1.2. Part II : Formability of biomaterial thin steel sheets 5
References 8

II FAILURE MODE OF LASER WELDS IN LAP-SHEAR SPECIMENS OF HIGH STRENGTH LOW ALLOY (HSLA) STEEL SHEETS 9

2.1. Introduction 9
2.2. Experiments 11
2.2.1. Lap-shear specimen 11
2.2.2. Weld microstructure 13
2.2.3. Micro-hardness test of welded joint 14
2.2.4. Tensile test of base metal 14
2.2.5. Quasi-static test of lap-shear specimen 15
2.3. Failure mechanism of welded joint 17
2.4. *J* integral solutions for non-homogenous 3-zone material model 22
2.5. Discussion on the effects of sheet thickness on failure mode 26
2.5.1. *J* integral solutions for specimens with different thicknesses 27
2.5.2. Scalability of the *J* integral solutions 29
2.6. Conclusions 31
References 57

III FATIGUE BEHAVIOR OF LASER WELDS IN LAP-SHEAR SPECIMENS OF HIGH STRENGTH LOW ALLOY STEEL SHEETS 59

3.1. Introduction 59
3.2. Experiments 61
3.2.1. Quasi-static test of lap-shear specimen 63
3.2.2. Fatigue test of lap-shear specimen 64
3.3. Failure modes of laser welds under quasi-static and cyclic loading conditions 65
3.3.1. Failure mode under quasi-static (QC) loading conditions 66
3.3.2. Failure mode under low-cycle (LC) loading conditions 68
3.3.3. Failure mode under high-cycle loading conditions with high load ranges (HCHL) 70
3.3.4. Failure mode under high cycle loading conditions with low load ranges (HCLL) 72
3.4. Global and local stress intensity factor solutions 75
3.5. A Structural stress model 80
3.6. Fatigue life estimations 81
3.7. Discussions 85
3.8. Conclusions 86
References 109

IV EFFECT OF SHEET THICKNESS AND GAP BETWEEN THE SHEETS ON STRESS INTENSITY FACTOR SOLUTIONS FOR LASER WELDS IN LAP-SHEAR SPECIMENS 111

4.1. Introduction 111
4.2. Stress intensity factor solutions for sheets with different thicknesses 113
4.2.1. Analytical stress intensity factor solutions for specimens with different sheet thicknesses 113
4.2.2. Computational stress intensity factor solutions for specimens with different sheet thicknesses 118
4.3. Effect of gap on fatigue behavior of laser welds 122
4.3.1. Experimental observations 122
4.3.2. Analytical local stress intensity factor solutions for kinked cracks 124
4.3.3. Stress intensity factor solutions for cracks from notch tips 125
4.4. A structural stress model for welds with gap and fatigue life estimations 128
4.5. Conclusions 130
References 146

V MECHANICAL BEHAVIOR AND FAILURE MECHANISMS OF Nb-CLAD STAINLESS STEEL SHEETS 148

5.1. Introduction 148

5.2. Clad assembly preparation 149
5.3. Experiments 150
5.3.1. Tensile test 150
5.3.2. Bend and flattening test 150
5.3.3. Nano-indentation 151
5.4. Results and discussion 151
5.4.1. Microstructural analysis 151
5.4.2. Tensile test 153
5.4.2.1. Mechanical properties 153
5.4.2.2. Canoeing phenomenon 153
5.4.2.3. Nb layer delamination 154
5.4.3. Bend and flattening test 155
5.4.4. Nano-indentation 156
5.5. Conclusions 159
References 181

VI FAILURE MECHANISMS OF POLYMER-GRAPHITE COATED STAINLESS STEEL SHEETS 183

6.1. Introduction 183
6.2. Coated assembly preparation 184
6.3. Experiments 186
6.3.1. Tensile test of polymer coated stainless steel sheets 186
6.3.2. Tensile test of EB-815 polymer epoxy sheets 187
6.3.3. Semi-guided bend test 188
6.3.4. Flattening test 189
6.3.5. Micrographic examination of the cross-sections of the bent and flattened specimens 190
6.3.6. ball punch deformation test 190
6.4. Discussion 192
6.5. Conclusions 193
References 212

VII CONCLUSIONS 214

LIST OF FIGURES

Figure 2.1 (a) A top view and (b) a bottom view of a laser-welded lap-shear specimen, and (c) a schematic of a lap-shear specimen with the loading direction shown as the bold arrows. 36

Figure 2.2 An optical micrograph of the etched cross section of a laser welded joint (3% Nital used as the etchant), and close-up views of (b) the base metal (BM), (c) the heat affected zone (HAZ) and (d) the fusion zone (FZ) as marked in (a) 37

Figure 2.3 (a) An optical micrograph of the cross section of a laser weld with the micro-indentations, and (b) the distributions of the hardness values across the weld 39

Figure 2.4 The engineering stress-strain curves for the base metal from three representative sheet specimens. 41

Figure 2.5 The load-displacement curves from quasi-static tests of three lap-shear specimens 42

Figure 2.6 Side views of specimens at the applied displacements of (a) 0.2 mm (b) 1.0 mm (c) 1.9 mm and (d) about 2.1 mm with the left sheet separated from the weld 43

Figure 2.7 Optical micrographs of the cross sections of the weld for (a) a nearly failed and (b) a failed weld 44

Figure 2.8 (a) An optical micrograph of the etched cross section of a failed weld, and close-up views of (b) the lower left sheet near the failure surface and (c) the upper right sheet near the pre-existing crack tip (3% Nital solution used as the etchant) 45

Figure 2.9 (a) A scanning electron micrograph of the failure surface on the separated sheet side, (b) a close-up view of region I in (a), and close-up views of portions of (c) region A, (d) the transition region between regions A and B, and (e) the transition region between regions B and C 46

Figure 2.10 (a) An optical micrograph of the etched cross section of a weld in a lap-shear specimen at the applied displacement of 1.95 mm prior to the final failure, and the deformed mesh near a weld in a lap-shear specimen at the applied displacement of 2.4 mm from the finite element analysis based on (b) the 3-zone model and (c) the 6-zone model. 47

Figure 2.11 A schematic of a crack and an arbitrary contour Γ surrounding the crack tip..... 48

Figure 2.12 (a) A schematic of a two-dimensional finite element model of a lap-shear specimen and the boundary conditions, (b) the finite element mesh near the weld, and (c) a close-up view of the finite element mesh near the right pre-existing crack tip..... 49

Figure 2.13 The tensile stresses as functions of the plastic strain for the base metal, heat affected and fusion zones used in the 3-zone finite element analysis 51

Figure 2.14 The J integral solutions for contours 4 to 8 for the right pre-existing crack tip as functions of the normalized load from the finite element analysis 52

Figure 2.15 The J integral solution for contour 8 for the right pre-existing crack tip as a function of the normalized load from the finite element analysis 53

Figure 2.16 The J integral solutions for contour 8 for the right pre-existing crack tip as functions of the normalized load from the finite element analyses of the specimens with the sheet thicknesses of t, $2t$, $3t$, $4t$ and $5t$ 54

Figure 2.17 The values of the normalized $\bar{J}(= J/t)$ for contour 8 for the right pre-existing crack tips as functions of the normalized load from the finite element analyses of the specimens with the sheet thicknesses of t, $3t$ and $5t$ 55

Figure 2.18 The values of the failure load P_f as functions of the sheet thickness t for different values of J_c 56

Figure 3.1 (a) A top view and (b) a bottom view of a laser welded lap-shear specimen 90

Figure 3.2 A schematic of a lap-shear specimen with the loading directions shown as the bold arrows..... 90

Figure 3.3 (a) An optical micrograph of the etched cross section of a laser weld in lap-shear specimen perpendicular to the welding direction, and close-up views of (b) the base metal, (c) the left and (d) the right pre-existing crack tips 91

Figure 3.4 The experimental results of the fatigue tests of laser welds in lap-shear specimens under cyclic loading conditions 93

Figure 3.5 Optical micrographs of the etched cross sections of (a) a partially failed weld and (b) a failed weld under quasi-static (QS) loading conditions 94

Figure 3.6 (a) A scanning electron micrograph of the failure surface of the lower left sheet of a failed specimen under quasi-static (QS) loading conditions, and close-up views of portions of (b) region A, (c) the transition region between regions A and B and (d) region C of the failure surface 95

Figure 3.7 Optical micrographs of the etched cross sections of (a) a partially failed weld at the fatigue life of 6.47×10^{3} cycles and (b) a failed weld at the fatigue life of 8.6×10^{3} cycles under a load range of 1.99 kN (low-cycle (LC) loading conditions) 96

Figure 3.8 (a) A scanning electron micrograph of the failure surface of the lower left sheet of a failed specimen at the fatigue life of 5.44×10^{3} cycles under a load range of 2.11 kN (low-cycle (LC) loading conditions), and close-up views of portions of (b) region A, (c) region B and (d) region C of the failure surface 97

Figure 3.9 Optical micrographs of the etched cross sections of (a) a partially failed weld at the fatigue life of 1.02×10^{4} cycles and (b) a failed weld at the fatigue life of 1.45×10^{4} cycles under a load range of 1.64 kN (high-cycle loading conditions with a high load range (HCHL)) 98

Figure 3.10 (a) A scanning electron micrograph of the failure surface of the upper right sheet of a failed specimen at the fatigue life of 1.08×10^{4} cycles under a load range of 1.64 kN (high-cycle loading conditions with a high load range (HCHL)), and close-up views of portions of (b) region A and (c) the transition region between regions B and C of the failure surface 99

Figure 3.11 Optical micrographs of the etched cross sections of (a) a partially failed weld at the fatigue life of 1.09×10^{5} cycles and (b) a failed weld at the fatigue life of 1.65×10^{5} cycles under a load range of

0.82 kN (high-cycle loading conditions with a low load range (HCLL)) 100

Figure 3.12 (a) A scanning electron micrograph of the failure surface of the upper right sheet of a failed specimen at the fatigue life of 1.65×10^5 cycles under a load range of 0.82 kN (high-cycle loading conditions with a low load range (HCLL)), close-up views of portions of (b) region A, (c) region A, (d) the transition region between regions A and B, and (e) the transition region between regions B and C of the failure surface 101

Figure 3.13 A schematic of a main crack and a kinked crack with the kink length a and the kink angle α 102

Figure 3.14 (a) A schematic of a two-dimensional finite element model of a lap-shear specimen with the boundary and loading conditions, and (b) a close-up view of the finite element mesh near the weld with $w/t =$ 0.86 103

Figure 3.15 (a) A schematic of a two-dimensional finite element model of a lap-shear specimen with two kinked cracks and the boundary and loading conditions, and (b) a close-up view of the finite element mesh near the right kinked crack tip for $a/t = 0.2$ 104

Figure 3.16 The values of $k_{\mathrm{I}}/(k_{\mathrm{I}})_0$ for the kinked cracks emanating from the right and left per-existing crack tips as functions of the normalized kink length a/t for $w/t = 0.86$ and $\alpha = 90°$. The results of Sripichai et al. [14] for an idealized weld with $w/t = 1$ and $\alpha = 90°$ are also shown 105

Figure 3.17 The values of $k_{II}/(k_I)_0$ for the kinked cracks emanating from the right and left per-existing crack tips as functions of the normalized kink length a/t for $w/t = 0.86$ and $\alpha = 90°$. The results of Sripichai et al. [14] for an idealized weld with $w/t = 1$ and $\alpha = 90°$ are also shown 106

Figure 3.18 (a) A schematic of a two-beam model under lap-shear loading conditions. The idealized weld is shown as the shaded region and (b) a schematic of the two-beam model under an equivalent loading of (a) 107

Figure 3.19 Experimental results and the fatigue life estimates based on the kinked fatigue crack growth models and structural stress model 108

Figure 4.1 A schematic of a lap-shear specimen with sheets of equal thicknesses. The loading directions are shown as the bold arrows 132

Figure 4.2 (a) A schematic of the cross section near an idealized weld as a two-strip model under lap-shear loading conditions with the weld shown as the shaded region and (b) a schematic of the two-strip model under an equivalent loading of (a) 133

Figure 4.3 Schematics of (a) the left part of the two-strip model and (b) the two-strip model of different thicknesses with connection 134

Figure 4.4 (a) A schematic of a two-dimensional finite element model of a lap-shear specimen and the boundary and loading conditions, and (b) a close-up view of the finite element mesh near the pre-existing crack tips for $w/t_u = 4$ 135

Figure 4.5 The analytical and computational normalized K_I and K_{II} solutions for (a) the right crack and (b) the left crack as functions of w/t_u for $\delta = 0.5$ 136

Figure 4.6 (a) The normalized K_I and (b) the normalized K_{II} solutions for the right and left pre-existing crack tips based on the analytical model of strips with different thicknesses 138

Figure 4.7 Optical micrograph of the etched cross section of a partially failed weld with a gap under quasi-static loading conditions. 140

Figure 4.8 A schematic of a main crack and a kinked crack with the kink length a and the kink angle α 140

Figure 4.9 (a) A schematic of a two-dimensional finite element model of a lap-shear specimen with gap and two cracks. The boundary and loading conditions are also shown in the schematic. (b) A close-up view of the finite element mesh near the weld for the normalized gap $g/t = 0.1$ and the normalized crack length $a/t = 0.1$ 141

Figure 4.10 (a) The value of $k_{\mathrm{I}}/(k_{\mathrm{I}})_0$ and (b) the value of $|k_{\mathrm{II}}|/(k_{\mathrm{I}})_0$ as functions of the normalized crack length a/t for $\alpha = 90°$ and different values of the normalized gap g/t 142

Figure 4.11 (a) A schematic of a lap-shear specimen with gap under the applied load per unit width F/b marked as the bold arrow, (b) a schematic of the applied loading condition near the right edge surface of the

specimen and (c) the resultant forces F_1/b and F_2/b and the resultant moment M_1 acting on the cross section of the upper right sheet at the weld 144

Figure 4.12 Fatigue life estimates based on the structural stress model for different values of the normalized gap g/t 145

Figure 5.1 Optical micrographs of the cross-sections of (a) as-rolled and (b) annealed 1050/60 specimens 164

Figure 5.2 A scanning electron micrograph of the cross-section of the annealed (a) 850/15 and (b) 950/15 specimens 165

Figure 5.3 The engineering stress-strain curves for the as-rolled specimen and the specimens with different annealing conditions 166

Figure 5.4 "Canoeing" effect in annealed (a) 850/60 and (b) 1050/60 specimens 167

Figure 5.5 Radius of curvature after failure under uniaxial loading conditions for specimens with different annealing conditions 168

Figure 5.6 Radius of curvature for the annealed 1050/60 specimens as a function of uniaxial strain 169

Figure 5.7 Delamination of the Nb layer form the stainless steel sheet in an annealed 1050/60 specimen after uniaxial strain of about 47% 170

Figure 5.8 A schematic of a guided-bend test apparatus 171

Figure 5.9 Springback angles for specimens with different annealing conditions 172

Figure 5.10 A schematic of a flattening test apparatus 173

Figure 5.11 Surface examination of (a) an as-rolled specimen flattened by a load per width of 15 kN/m, annealed (b) 1050/15 (c) 950/60 and (d) 1050/60 specimens flattened by a load per width of 60 kN/m 174

Figure 5.12 Optical micrographs of the cross sections of (a) an as-rolled and (b) an annealed 1050/60 specimens after flattening tests 175

Figure 5.13 An optical micrograph of the cross section of an annealed 1050/60 specimen showing the nano-indents 176

Figure 5.14 Plots of the values of (a) hardness and (b) elastic modulus of individual layers in the as-rolled and 1050/60 specimens 177

Figure 5.15 Load-displacement curves from the nano-indentations tests for (a) the Nb and (b) the stainless steel layers of the as-rolled and 950/60, 1050/15 and 1050/60 specimens 179

Figure 5.16 Load-displacement curves from the nano-indentation tests for different layers of an annealed 1050/60 specimen 180

Figure 6.1 Scanning electron micrographs of the cross sections of EB-815 coating at a magnification of (a) 1000x and (b) 1500x. Selective measured values of the (c) EB-815 coating thickness and (d) graphite particle sizes at a magnification of 1500x 194

Figure 6.2 Scanning electron micrographs of the surface of EB-815 coating at the center of the coated sheet at a magnification level of (a) 100x, (b) 250x and (c) 500x 195

Figure 6.3 Scanning electron micrographs of the surface of EB-815 coating at the edge of the coated sheet at a magnification level of (a) 100x, (b) 250x and (c) 500x 196

Figure 6.4 The engineering stress-strain curves for representative stainless steel and polymer-coated stainless steel sheets 197

Figure 6.5 Optical micrographs of the surface texture for tensile specimens subjected to a uniaxial strain of (a) 8%, (b) 10% , (c) 11%, (d) 12%, (e) 13.5%, (f) 14.5%, (g) 16% and (h) 17% 198

Figure 6.6 Plot of R_a values for different uniaxial strains 200

Figure 6.7 The engineering stress-strain curves EB-815 epoxy sheets from four test specimens 201

Figure 6.8 A schematic of the semi-guided bend test apparatus 202

Figure 6.9 Optical micrographs of the outer surfaces of the coating in the bend tip after the 180^o bend tests with a bend radius of (a) 0.8 mm, (b) 1.0 mm, (c) 2.4 mm and (d) 3.2 mm. The bend axis is along the longitudinal direction 203

Figure 6.10 Optical micrographs of the outer surfaces of the coating in the bend tip after the 180^o bend tests with a bend radius of (a) 0.8 mm, (b) 1.0 mm, (c) 2.4 mm and (d) 3.2 mm. The bend axis is perpendicular to the longitudinal direction 204

Figure 6.11 Optical micrographs of the outer coated surfaces on the bend tip after flattening test with a bend radius of (a) 0.8 mm, (b) 1.0 mm, (c) 2.4 mm and (d) 3.2 mm. The bend axis is along the longitudinal direction 205

Figure 6.12 Optical micrographs of the outer coated surfaces on the bend tip after flattening test with a bend radius of (a) 0.8 mm, (b) 1.0 mm, (c) 2.4 mm and (d) 3.2 mm. The bend axis is perpendicular to the longitudinal direction 206

Figure 6.13 Optical micrographs of the cross sections of two-sided coated stainless steel sheets flattened to a separation distance of 0.6 mm. The bend radius is (a) 0.8 mm (b) 1.0 mm 207

Figure 6.14 Optical micrographs of the cross sections of the one-sided coated stainless steel sheets, flattened to a separation distance of 0.5 mm with a bend radius of (a) 0.8 mm, (b) 1.0 mm, (c) 2.4 mm and (d) 3.2 mm. The bend axis is along the longitudinal direction 208

Figure 6.15 Optical micrographs of the cross sections of the one-sided coated stainless steel sheets, flattened to a separation distance of 0.5 mm with a bend radius of (a) 0.8 mm, (b) 1.0 mm, (c) 2.4 mm, and (d) 3.2 mm. The bend axis is perpendicular to the longitudinal direction 209

Figure 6.16 A schematic of the ball punch deformation test apparatus 210

Figure 6.17 Optical micrographs of the outer coated surfaces of the specimens after ball punch deformation tests with a penetrator displacement of (a) 3.5 mm, (b) 3.6 mm, (c) 4.0 mm and (d) 4.85 mm 211

LIST OF TABLES

Table 2.1 Dimensions of the lap-shear specimen 34

Table 2.2 Material parameters from tensile tests of the base metal..... 34

Table 2.3 The hardness values from indentation tests and the scaled initial yield stresses for the base metal, heat affected and fusion zones for the 3-zone model 35

Table 2.4 The hardness values from indentation tests and the scaled initial yield stresses for the base metal, heat affected and fusion zones for the 6-zone model 35

Table 3.1 Laser beam parameters 88

Table 3.2 The normalized computational global stress intensity factor $\overline{K}_{\mathrm{I}}$ and $\overline{K}_{\mathrm{II}}$ solutions for the right and left pre-existing crack tips..... 89

Table 3.3 The normalized local stress intensity factor $k_I/(k_I)_0$ solutions for $w/t = 0.86$ and $\alpha = 90°$ 89

Table 3.4 The normalized local stress intensity factor $k_{II}/(k_I)_0$ solutions for $w/t = 0.86$ and $\alpha = 90°$ 89

Table 5.1 Measured thicknesses of intermetallic layer for various annealed specimens 161

Table 5.2 Mechanical properties of the Nb-clad stainless steel sheets from tensile tests 162

Table 5.3 The ratio of the maximum indentation depth to the residual indentation depth h_r/h_m of different layers for specimens annealed at different annealing condition 163

CHAPTER I

INTRODUCTION

This thesis is written in two parts. The first part is related to the study of the failure mechanisms of laser welds under quasi-static and cyclic loading conditions. The effects of different sheet thicknesses and gap between the welded sheets on the stress intensity factor solutions are also investigated. Chapters II, III and IV constitute the first part of the thesis. The second part of the thesis is related to the experimental study of the formability of Niobium cladded and polymer-graphite coated stainless steel sheets. Chapters V and VI detail the results of the study for the Nb-clad and Polymer-graphite coated stainless steel sheets, respectively. Note that all these chapters were prepared as independent papers. Therefore, some parts of the thesis may be found repeated in these chapters.

1.1. Part I: Failure of laser welds in lap-shear specimens

Laser welding has been in the industry for over three decades now. It offers many advantages over the conventional welding processes. These advantages include narrow heat affected zone, high penetration, small weld width and high welding speeds. Laser welding usually does not require a filler material which produces welds with little or no contamination. Laser welding is also attractive for manufacturing and industrial applications due to its inherent flexibility and ease of automation. Other benefits include

aesthetically appealing welds due to non contact single sided welding process. Laser welding can also be carried out for some materials that are difficult to weld for example Titanium and quartz. Laser welding is widely used in the medical devices manufacturing. Laser welds are also employed in the automotive industry [1-3]. Tailor welded blanks are available in the market using laser welding technology [4]. Automotive manufacturers have also realized the potential of laser welding for the production of body-in-white assembly parts. Laser welded joints have been investigated by many researchers in the past two decades. However, there is limited research on the strength of laser welds in lap-shear specimens and is mostly experimental in nature. Fatigue behavior of laser welded joints has been investigated more extensively. However, the effects of weld geometry and sheet thickness on the failure mechanisms are not explored in detail. The main objective of the research is to investigate the failure mode and failure mechanisms in laser welded lap-shear joints under quasi-static and cyclic loading conditions. The effects of weld geometry, sheet thickness and gap between the welded sheets on the failure mechanisms are also investigated.

In Chapter II, the failure mode of laser welds in lap-shear specimens of non-galvanized SAE J2340 300Y high strength low alloy (HSLA) steel sheets under quasi-static loading conditions is examined based on experimental observations and finite element analyses. Micrographs of the cross sections of laser welded lap joints were obtained before and after quasi-static tests. Micro-hardness tests were conducted to provide an assessment of the mechanical properties near the weld which has a varying material microstructure due to the welding process. Scanning electron micrographs of failed specimens were also obtained to understand the failure mechanism. The results of

the finite element analyses of Lee et al. [5] were summarized here and compared with the experimental observations for completeness. Finite element analyses based on the non-homogenous 3-zone material model of Lee et al. [5] were then conducted to obtain the J integral solutions for the pre-existing cracks. The J integral solutions obtained from the finite element analyses based on the 3-zone material model can be used to explain the observed necking/shear failure mode of lap-shear specimens in the experiments. The effects of the sheet thickness on the failure mode of laser welds in lap-shear specimens were investigated for laser welds with a fixed ratio of the weld width to the thickness based on the non-homogeneous 3-zone finite element models. The J integral solutions from the finite element analyses are used to explain the failure modes of laser welds in lap-shear specimens of different thicknesses. Finally, the failure load is expressed as a function of the sheet thickness to demonstrate the use of the failure curves to determine the failure load and the failure mode of the welds.

In Chapter III, the fatigue behavior of laser welds in lap-shear specimens of non-galvanized SAE J2340 300Y high strength low alloy (HSLA) steel sheets is investigated based on experimental observations and two fatigue life estimation models. Optical micrographs of the welds before and after failure under quasi-static and cyclic loading conditions are examined to investigate the microstructure and failure mechanisms of the welds. Scanning electron micrographs of the failure surfaces are also used to explain the failure modes of laser welds in lap-shear specimens under quasi-static and cyclic loading conditions. Finite element analyses of the laser welded lap-shear specimens with consideration of the weld bead protrusion were carried out to obtain the global and local stress intensity factor solutions for the main cracks and kinked cracks, respectively. The

stress intensity factor solutions are used to explain the kinked fatigue crack growth patterns under high-cycle loading conditions. A kinked fatigue crack growth model based on the global and local stress intensity factor solutions for finite kinked cracks obtained from the finite element analyses and a structural stress model based on the closed-form structural stress solutions of the beam bending theory are adopted to estimate the fatigue lives of the laser welds. Finally, the estimated fatigue lives based on the kinked fatigue crack growth model and the structural stress model are compared with the experimental results.

In Chapter IV, the effects of the sheet thickness and the gap between the sheets on the stress intensity factor solutions of laser welds in lap-shear specimens are investigated. The analytical stress intensity factor solutions of Zhang [6] for spot welds with similar material and different sheet thicknesses in terms of the structural stresses are adopted to calculate the stress intensity factor solutions for laser welds in lap-shear specimens with different sheet thicknesses. The structural stresses for the stress intensity factor solutions are obtained from the beam bending theory for a two-beam model with connection under plain strain conditions. Two-dimensional finite element analyses are carried out to compare the computational results with the analytical stress intensity factor solutions. As the stress intensity factor solutions are higher for the right pre-existing crack tip as compared to those for the left pre-existing crack tip when the lower sheet is thicker than the upper sheet, the stress intensity factor solutions are proposed for the right pre-existing crack tip that can cover a wide range of the normalized weld width. Finite element analyses are also carried out to study the effect of the gap between the sheets on the stress intensity factor solutions for the cracks emanating from the pre-existing notches formed

by the gap. A closed-form structural stress solution is developed for laser welded lap-shear specimens with a gap between the sheets. This closed-form structural stress model is also used to investigate the effect of the gap between the sheets on the fatigue lives of the welds.

1.2. Part II: Formability of bimaterial thin steel sheets

Fuel cells are emerging as an attractive alternative for fossil fuels. Fuel cells directly convert the chemical energy into electrical energy without having an intermediate combustion process. This makes them very efficient and environment friendly. Polymer electrolyte membrane (PEM) fuel cells have the potential for use in automotive propulsion system because of their low operating temperatures ($< 80\,^{\circ}C$) which gives them quick start-up time. They have higher power density as compared to other fuel cells. They also respond swiftly to varying loads and can sustain large load cycles. The main challenge facing the commercialization of fuel cells is their cost and reliability. One of the important components of PEM fuel cells is the bipolar plate (BP) which makes up about 80% of the total stack weight and 45% of its cost [7]. Many materials have been considered for use as BPs, including machined graphite, coated/non-coated metals and composite polymers. Each one has its own merits and disadvantages. However stainless steel appears to be a promising candidate for future use as BP that can meet the Department of Energy (DOE) targets set for BPs due to their relatively high strength, high chemical stability, low gas permeability, wide range of alloy choice, and applicability to mass production and low cost [8].

Candidate stainless steel sheets have been tested and used as BPs. However, its main drawback is the corrosive products produced in a low pH environment of a fuel cell and the contact resistance of the surface passivation film. To overcome this problem coated metal sheets are under investigation. Two types of coatings, carbon-based and metal-based, have been investigated for this purpose [8, 9]. Noble metals, metal nitrides and metal carbides are some of the metal-based coatings. Different types of BP coatings for stainless steels were also investigated [10, 11]. However, there is no commercial product available yet due to the issues of corrosion resistance and electrical contact resistance. Further the coefficient of thermal expansion of the base metal and the coating should be as close as possible to eliminate the formation of micro-pores and micro-cracks in coatings due to unequal expansion [12]. The main objective of the research is to study the formability of biomaterial metallic sheets for application as bipolar plates in automotive fuel cells. Nb cladding and polymer-graphite coating on stainless steel thin sheets will be considered as model material systems.

In Chapter V, the results of an experimental investigation of Nb-clad 304L stainless steel sheets are presented to study the effects of annealing conditions on the ductility and formability of these sheets. As-rolled and annealed specimens were tested in tension, bending and flattening tests to understand the mechanical behavior and failure mechanisms of these sheets for different annealing temperatures and times. The annealed specimens showed warping along the longitudinal axis during the tensile tests forming a canoe-like shape. Nb layer delamination was observed above a uniaxial strain of about 27%. Micrographic analyses of bent and flattened specimens showed that the as-rolled specimens have limited ductility and that the annealed specimens developed an

intermetallic layer of thickness of a few microns. The annealed specimens failed due to the breakage of intermetallic layer causing localized necking and the subsequent failure of Nb layer. The springback angles of the as-rolled and annealed specimens were also obtained from the guided-bend tests. Nano-indentation tests indicated that the intermetallic layer exhibits much higher values of hardness and elastic modulus as compared to those of the stainless steel and Nb sheets.

In Chapter VI, the results of an experimental investigation of polymer-graphite coated 316L stainless steel sheets are presented. The formability and ductility of polymer-graphite coated stainless steel sheets and the failure mechanisms of the protective polymer-graphite layer are investigated. A polymer-graphite coating EB-815 was selected in this investigation. Uniaxial tensile, bend and flattening and spherical metallic punch deformation tests were carried out to determine the mechanical behavior and failure mechanisms of these sheets under different straining conditions. Failure of EB-815 coating was observed at about 17% tensile strain in the uniaxial tensile tests. A micrographic analysis of the bent and flattened specimens showed that these specimens can sustain a strain of about 15% without surface damage. Failure of the polymer-graphite coating in the bent and flattened specimens depends on the bend radius and the extent of flattening. The polymer-graphite coating can also survive the metallic punch displacement of about 3.5 mm during the spherical punch deformation test without any visible surface damage.

It is anticipated that the results presented in Chapters V and VI will provide a better understanding of the mechanical behavior of cladded and coated thin metallic sheets for use as bipolar plates in PEM fuel cells. The experimental results obtained from

these tests will be helpful in future application of these sheets as bipolar plates in PEM fuel cells and will help realize the cost effective and reliable production of PEM fuel cells. It will also help the commercialization of stainless steel based bipolar plates while meeting the DOE requirements for fuel cell performance.

References

[1] Shiner W. Lasers improve auto manufacturing productivity. Automotive Engineering 1986; 94: 62-68.

[2] Bourges Ph, Berniolles J. Laser beam welding of high hardness steels : Application to armoured vehicles. ICALO 1992; 574-583.

[3] Hanicke L, Strandberg Ö. Roof laser welding in series production. SAE Technical Paper No. 930028. Society of Automotive Engineers, Warrendale, PA: 1993.

[4] Prange W, Wonneberger I. Laser – A tool for light weight steel solutions for the automotive industry. Proceedings of SPIE 2003; 4831: 363-368.

[5] Lee J, Asim K, Pan J. Modeling of failure mode of laser welds in lap-shear specimens of HSLA steel sheets. Eng Fract Mech 2011; 78: 374-396.

[6] Zhang S. Stress intensities derived from stresses around a spot weld. International Journal of Fracture 1999; 99: 239-257.

[7] Hermann A, Chaudhuri T, Spagnol P. Bipolar plates for PEM fuel cells: A review. International Journal of Hydrogen Energy 2005; 30: 1297-1302.

[8] Borup RL, Vanderborgh NE. Design and testing criteria for bipolar plate materials for PEM fuel cell applications. Proceedings of Materials Research Society Symposium 1995; 393: 151-155.

[9] Mehta V, Cooper JS. Review and analysis of PEM fuel cell design and manufacturing. Journal of Power Sources 2003; 114: 32-53.

[10] Zafar I, Guiheen J, Dave N, Timothy R. World Patent No. WO 00,128,019, 2001.

[11] Li Y, Meng W, Swathirajan S, Harris S, Doll G. US patent No. 5,624,769, 1997.

[12] Woodman AS, Anderson EB, Jayne KD, Kimble MC. Development of Corrosion-Resistant Coatings for Fuel Cell Bipolar Plates. Proceedings of AESF SUR/FIN 1999; 6: 21.

CHAPTER II

FAILURE MODE OF LASER WELDS IN LAP-SHEAR SPECIMENS OF HIGH STRENGTH LOW ALLOY (HSLA) STEEL SHEETS

2.1. Introduction

Laser welding has been used in the automotive and other industries. Advantages of laser welding include narrow heat affected zone, high penetration due to increased power density, low distortion, relatively high welding speed, potential for automation, and inherent flexibility of the process. Laser welded joints have been a topic of extensive research and investigation in the past two decades. A lap joint is a common weld joint. The geometry of a lap joint provides pre-existing crack or notch tips at the edges of the weld bead. Therefore, fatigue cracks were usually observed to be initiated from the pre-existing crack or notch tips. Structures with laser welded lap joints are often subjected to cyclic loading conditions. Therefore, many research investigations [1-9] were conducted on the fatigue lives of laser welded lap joints. However, limited research investigations were conducted on the strength of laser welded lap joints under quasi-static loading conditions. Quasi-static tests were mostly carried out in conjunction with the fatigue testing of laser welded lap-joints.

Ono et al. [10] investigated the static and fatigue strengths of laser welded lap joints in thin steel sheets and correlated the static strength of laser welded lap joints with the tensile strength of the base metal and the hardness values of the weld. Kaitanov et al. [6] conducted experiments to determine the static and fatigue strengths of laser welded

lap joints of steel sheets with different weld widths and penetration depths. They found that the weld width and pattern have significant effects on the static strength of the weld joints. Chien et al. [11] examined the shear failure of laser welded aluminum blanks under uniaxial and biaxial straining conditions. Taban et al. [12] experimentally investigated the static and fatigue strengths of laser welded butt joints of 12% Cr stainless steel plates. Casavola et al. [13] examined the static strength of laser welded butt joints of titanium sheets as well as their fatigue strength. They conducted a two dimensional plane strain elastic finite element analysis to understand the stress concentration near the weld.

Recently, Lee et al. [14] conducted finite element analyses to investigate the failure mode of laser welded lap-shear specimens of high strength low alloy steel sheets based on the experimental results reported in this chapter. Lee et al. [14] developed finite element models with consideration of different material sections for the weld and the weld bead geometry based on the micrograph of the cross section near the weld reported in this investigation. The tensile stress-plastic strain relation of the base metal obtained from uniaxial tensile tests was used to scale the stress-plastic strain curves of the material sections in the heat affected and fusion zones in the finite element models based on the results of the micro-hardness tests reported here. The results of the finite element analyses of Lee et al. [14] were compared very well with the results of the experimental observations.

In this investigation, micrographs of the cross sections of laser welded lap joints were obtained before and after quasi-static tests. Micro-hardness tests were conducted to provide an assessment of the mechanical properties near the weld which has a varying

material microstructure due to the welding process. Scanning electron micrographs of failed specimens were also obtained to understand the failure mechanism. The results of the finite element analyses of Lee et al. [14] were summarized here and compared with the experimental observations for completeness. Finite element analyses based on the non-homogenous 3-zone material model of Lee et al. [14] were then conducted to obtain the J integral solutions for the pre-existing cracks. The J integral solutions obtained from the finite element analyses based on the 3-zone material model can be used to explain the observed necking/shear failure mode of lap-shear specimens in the experiments. The effects of the sheet thickness on the failure mode of laser welds in lap-shear specimens were investigated for laser welds with a fixed ratio of the weld width to the thickness based on the non-homogeneous 3-zone finite element models. The J integral solutions from the finite element analyses are used to explain the failure modes of laser welds in lap-shear specimens of different thicknesses. Finally, the failure load is expressed as a function of the sheet thickness to demonstrate the use of the failure curves to determine the failure load and the failure mode of the welds.

2.2. Experiments

2.2.1. Lap-shear specimen

HSLA steel sheets with a thickness of 0.93 mm were welded together using a 6 kW CO_2 laser at a welding speed of 8 m/min. Helium was used as the shielding gas with a discharge rate of 20 ℓ/min. No heat treatment was carried out after the welding process. The welded sheets were sheared into 275 mm by 27 mm strips that were used to make

lap-shear specimens for the present study. These lap-shear specimens were then machined into a dog-bone shaped profile using a CNC milling machine. The specimen geometry in general follows the guidelines of the ANSI/AWS B4.0:2007 standard for the mechanical testing of welds. The objective of the reduced width for the central portion of the specimen is to investigate the failure mechanism in the vicinity of the laser welds and to avoid the failure of the specimen due to the necking of the specimen sheets far away from the laser welds. Figures 2.1(a) and 2.1(b) show top and bottom views of a laser welded lap-shear specimen, respectively. As shown in these figures, the laser weld width is very narrow. The average weld width was measured to be about 1 mm. The width and length of the uniform straight part in the reduced width section were measured at 8 mm and 13.5 mm, respectively. Specimens with similar shapes were adopted by a number of researchers for the study of laser welded joints, for example, see Anand et al. [15] and Sripichai et al. [16].

Figure 2.1(c) shows a schematic of a lap-shear specimen. As shown in the figure, the specimen has a width W, sheet thickness t, and overall length L for the upper and lower sheets. The specimen has a width b and a length c for the central portion of the specimen, an overlap length V, and a width w for the weld zone which is indicated as the shaded area in the figure. Two doublers were used for aligning the fixtures to avoid the initial realignment of the specimen. The doubler has a length s and a width W as shown in the figure. The detailed dimensions of the lap-shear specimens are listed in Table 1. The loading direction is indicated by two bold arrows on the right and left sides of the specimen. These bold arrows are also used to indicate the loading directions in the subsequent figures. After machining, the specimen edges were manually smoothed by

using 1200 grit coarse polishing papers. This was done to remove notches or irregularities along the edges which may produce stress concentration sites.

2.2.2. Weld microstructure

The laser welded joints of the lap-shear specimens were sectioned using a low speed diamond saw perpendicular to the welding direction. The specimens were then ground through a series of grinding steps and polished by diamond polishing compounds. The cross sections were then chemically etched to examine the microstructure of the welded area. 3% Nital solution was used as the etchant. Samples were etched by immersion in the etchant solution for about 20 to 30 seconds. Figure 2.2(a) shows an optical micrograph of the etched cross section of a laser welded joint. Three different regions can be identified from the micrograph based on their distinct grain structures, namely, the base metal (BM), the heat affected zone (HAZ) and the fusion zone (FZ). Close-up views of the BM, HAZ and FZ are provided in Figures 2.2(b), 2.2(c) and 2.2(d), respectively. The base metal has fine and randomly oriented grains [15]. The HAZ between the fusion zone and the base metal has a mixture of fine and coarse grains. The coarse grain indicates grain growth in this region due to the welding process. The span of this narrow HAZ varies from 0.05 to 0.17 mm on both sides of the fusion zone along the thickness direction. The width of the fusion zone is about 0.80 mm along the middle surface of the weld. A similar micro-structural composition of the three weld zones was also reported for laser welded high strength galvanized steel sheets in Mei et al. [17]. The micrograph in Figure 2.2(a) also shows that the weld is free of porosities and other welding defects such as cracks and voids.

2.2.3. Micro-hardness test of welded joint

Micro-hardness tests were carried out using an automated CM-400AT Sun-Tech Inc. Clark micro-hardness tester. All the indentations were made with a 500 grams load and a dwell time of 15 seconds. The tests were done using a pyramidal tip to record the Vickers hardness number. The indentations were carried out at a regular interval of about 150 μm in the transverse direction across the weld zone from the base metal to the fusion zone and to the base metal on the other side. Figure 2.3(a) shows an optical micrograph of the cross section of a laser weld with micro-indentations. The hardness values from these tests are plotted in Figure 2.3(b) for both the upper and lower sheets as well as the middle surface of the fusion zone between the pre-existing crack tips. Figure 2.3(b) shows that the hardness variations remain fairly consistent along the thickness direction. The base metal has a hardness value of less than 150 HV500. The hardness value increases sharply in the heat affected zone from 150 HV500 and reaches the highest value of about 230 HV500 in the fusion zone near the weld center. The hardness values obtained from these tests were used to estimate the stress-plastic strain curves of the heat affected and fusion zones based on the stress-plastic strain curve of the base metal for the finite element analyses in Lee et al. [14] and the finite element analyses discussed later.

2.2.4. Tensile test of base metal

Tensile tests were conducted for the base metal sheets according to the ASTM E8-04 standard for tension testing of metallic materials. The HSLA sheets were cut into 200 mm rectangular specimens with a gauge length of 50 mm. The dog bone profile was

made by a water-jet cutting machine. The specimen edges were manually coarse polished using 1200 grit grinding papers. The tests were carried out using an automated MTS tensile testing machine with a 10 kN load cell. An extensometer with a two inch gauge length was used to automatically record the extension in the uniform gauge section. The cross-head speed was maintained at 2.54 mm/min throughout the tests. The engineering stress-strain curves are shown in Figure 2.4 for the base metal from three representative sheet specimens. A total of six specimens were tested. The material parameters obtained from these tests are listed in Table 2. The stress-plastic strain curves for the heat affected and fusion zones were estimated by scaling the stress-plastic strain curve of the base metal according to the hardness values of the heat affected and fusion zones [14]. These stress-plastic strain curves were used as the input parameters for the finite element analyses in Lee et al. [14] and the finite element analyses discussed later.

2.2.5. Quasi-static test of lap-shear specimen

Quasi-static tests of lap-shear specimens were carried out under displacement controlled conditions. These tests were conducted using an automated MTS testing machine at a constant cross-head speed of 1 mm/min. Figure 2.5 shows the load-displacement curves obtained from quasi-static tests of three lap-shear specimens. The average failure or maximum load and the maximum displacement obtained from these tests were about 3.1 kN and 2.16 mm, respectively. The results of these tests were used as the reference load and displacement by Sripichai et al. [16] for fatigue testing of laser welded lap-shear specimens of HSLA steel sheets.

It was also observed during these tests that the weld bead rotated as the applied displacement increased. Figure 2.6 shows the side views of four specimens that had been subjected to different displacements during the quasi-static tests. Figures 2.6(a), 2.6(b) and 2.6(c) show the side views of the specimens from the tests that were interrupted at the displacement of 0.2 mm, 1.0 mm and 1.9 mm, respectively, while Figure 2.6(d) shows the side view of a failed specimen at the final displacement of about 2.1 mm. The angle of rotation continued to increase throughout the tests and the final angles between $45°$ and $50°$ with respect to the load line were observed for completely failed specimens. A similar weld rotation was reported by researchers, for example, in Radaj et al. [18] for resistance spot welds. Ono et al. [10] also observed the weld rotation in laser welded lap-shear specimens and experimentally determined a maximum rotation angle of less than $25°$ for their specimens. The weld rotation is caused by the non-uniform plastic deformation through the thickness in the two load carrying sheets of the lap-shear specimen and by the relative rigidity of the weld bead as compared to the base metal [14]. The weld rotation is also dependent on the weld width [14]. The necking of the sheet metal near the weld zone is also somewhat visible from Figure 2.6(d) for the separated lower left sheet after the complete failure of the laser weld. For a total of eight tests, the failure of all the specimens occurred in the lower left load carrying sheets near the weld beads.

To further study the failure mechanism in detail, the tested specimens were sectioned perpendicular to the weld direction using a low speed diamond saw and prepared for a micrographic analysis. The sectioned specimens were ground with grinding papers of different grit size in a series of steps to remove any cold work effects

which might have been left at the sheet edges due to the machining. The specimens were then polished using diamond suspension compounds. A detailed analysis of these micrographs is presented in the following sections.

2.3. Failure mechanism of welded joint

A micrographic analysis of nearly failed and failed laser welds under quasi-static loading conditions is presented here. Figure 2.7(a) shows an optical micrograph of the cross section near the weld in a specimen just prior to its complete separation. The bold arrows in the figure indicate the loading direction. The upper right and lower left sheets were the two load carrying sheets in these tests. The necking of the upper right and lower left sheets can be observed. A crack formation at a distance from the pre-existing crack tip on the inner surface of the lower left sheet can also be observed and is marked in Figure 2.7(a). A close-up view of the region near the crack formation is provided as an insert in Figure 2.7(a). The weld rotation with respect to the loading direction is also visible from the figure. From the micrograph, it appears that this rotation causes the relatively rigid weld bead to compress the outer surface of the lower left sheet to create a notch. The notch further promotes the shear/necking instability and the final rupture of the lower left sheet.

Figure 2.7(b) shows a micrograph of the cross section of a completely failed weld. The thickness of the upper right sheet near the failure surfaces was noticeably reduced due to the necking. It is noted that the necking took place at a distance from the pre-existing crack tips. Although the opening of the pre-existing crack tips is observed from the micrographs in Figures 2.7(a) and 2.7(b), the final failure was not initiated directly

from these crack tips. The lower left sheet finally failed by ductile shear fracture as shown in Figure 2.7(b). This may seem to be a departure from the existing understanding of the fatigue failure of laser welds in which the failure is directly initiated from the pre-existing crack tip due to the stress and strain singularities based on the fracture mechanics approach [9, 10, 16, 19]. Therefore, the failure mechanism of the necking/shear for laser welded lap joints of thin sheets under quasi-static loading conditions in the present study seems to be different from that under cyclic loading conditions.

Figure 2.8(a) shows an optical micrograph of the etched cross section of another completely failed weld. The opening of the pre-existing cracks and the sheet necking are visible in the micrograph. As shown in the figure, the non-load carrying sheets were cut for convenience of mounting the failed weld. As shown in the figure, the failure location is near the boundary of the base metal and the HAZ of the lower left load carrying sheet. The grains in this region are significantly stretched as seen in close-up views of the lower left sheet near the failure surface and the upper right sheet near the pre-existing crack tip in Figures 2.8(b) and 2.8(c), respectively.

In order to study the failure modes in the failed sheets, the failure surfaces of the separated sheets were examined under a scanning electron microscope. Figure 2.9(a) shows a scanning electron micrograph that gives an overview of the failure surface on the separated sheet side as indicated in Figure 2.7(b). The upper portion of the failure surface in Figure 2.9(a) shows the stretch marks corresponding to the stretched inner surface of the lower sheet. The stretch marks suggest that this part of the sheet was subjected to tensile deformation and experienced significant plastic deformation. Note that the ratio of the width to the thickness is 8.6 for the specimens. The large ratio

suggests that the majority of the weld was possibly subjected to plane strain loading conditions. Only a limited amount of necking in the transverse direction on both sides of the failure surface is shown in the figure. A close-up view of region I in Figure 2.9(a) is shown in Figure 2.9(b). Three distinct regions A, B and C are identified from the scanning electron micrograph of the failure surface. Region A exhibits a fracture surface of large and small dimples. A close-up view of a portion of this region is shown in Figure 2.9(c). This portion of the failure surface corresponds to the crack initiation and growth. Region B exhibits a fracture surface with small elongated dimples. Region B of the failure surface indicates a shear dominant failure mode. A close-up view of a portion of the transition region between regions A and B is shown in Figure 2.9(d). Region C of the failure surface in Figure 2.9(a) shows a flat and cleavage fracture surface. The cleavage fracture surface corresponds to the final stage of the separation of the weld joint due to the loss of the load carrying capacity. A close-up view of a portion of the transition region between regions B and C is shown in Figure 2.9(e).

In a separate study [16], it was observed that the fatigue failure in laser welded lap-shear specimens of HSLA steel sheets occurred due to the kinked crack growth from the pre-existing crack tip. The experimental observations in the present study indicate that the failure of laser welded lap-shear specimens under quasi-static loading conditions is driven by two distinct mechanisms that occur concurrently. One of the mechanisms involves the sheet necking/thinning due to the combined axial and bending nature of the loading condition. The other mechanism is related to the weld rotation producing a notch in the HAZ of the lower left sheet adjacent to the weld bead protrusion due to the material inhomogeneity of the welded region and the geometry of the weld bead

protrusion. The net area of the load carrying sheet to support the load is further reduced by the crack formation on the inner surface of the lower left sheet. The lower left sheet finally fails due to the loss of the load carrying capacity. The scanning electron micrographs of the failure surface shown in Figures 2.9(d) and 2.9(e) indicate the presence of both small elongated dimples and cleavage surface corresponding to the final stage of the failure due to the loss of the load carrying capability of the sheet.

The results of the finite element analyses of Lee et al. [14] are briefly reviewed here for completeness. Lee et al. [14] conducted finite element analyses with and without consideration of void nucleation and growth to investigate the failure mode of the laser welds in lap-shear specimens based on the experimental results reported here. They used non-homogenous 3-zone and 6-zone material models to more realistically represent the material behavior in the base metal, heat affected and fusion zones. The stress-plastic strain curves for the material sections in the heat affected and fusion zones were estimated by scaling the stress-plastic strain curve of the base metal according to the hardness values of the different material sections of the heat affected and fusion zones. The assumed hardness values and the yield stresses of the material sections in the 3-zone and 6-zone models are listed in Tables 3 and 4, respectively. The detailed information on the 3-zone and 6-zone material model can be found in Lee st al. [14].

Figure 2.10(a) shows an optical micrograph of the etched cross section of the weld in a lap-shear specimen shown in Figure 2.7(a). The weld in Figure 2.10(a) was subjected to the applied displacement of 1.95 mm prior to the final failure. Figures 2.10(b) and 2.10(c) show the deformed meshes near a weld in a lap-shear specimen at the applied displacement of 2.4 mm from the finite element analyses of Lee et al. [14] based

on the 3-zone and 6-zone models, respectively. The necking of the two load carrying sheets is apparent in Figures 2.10(b) and 2.10(c). Figures 2.10(b) and 2.10(c) show that the plastic deformation concentrates in the base metal near the boundary of the base metal and the heat affected zone for both load carrying sheets. When Figures 2.10(b) and 2.10(c) are compared, the deformed mesh of the 6-zone model near the crack tips is smoother than that of the 3-zone model. The details of the finite element analyses and the selection of the material parameters can be found in Lee et al. [14] and are not reported here. It should be noted that in these finite element analyses, no failure criteria were adopted. Therefore, the finite element analyses can continue until a numerical instability takes place.

The Gurson's yield function was also adopted in the finite element analyses to identify the fracture initiation site near the weld in lap-shear specimens under quasi-static loading conditions. The location of the highest void volume fraction of the material elements from the finite element analysis based on the Gurson's yield function is indicated on the deformed mesh in Figure 2.10(c). This location corresponds to region a shown in the micrograph in Figure 2.10(a). The fracture surface with large dimples in Figure 2.9(c) corresponds to region a in Figure 2.10(a). The creation of the artificial notch due to the buckling of the outer surface of the lower left sheet is shown in the deformed meshes in Figures 2.10(b) and 2.10(c). The creation of the notch from the finite element analyses agree well with the experimental observation of a notch marked as b in the micrograph in Figure 2.10(a). In general, the deformed meshes based on the 3-zone and 6-zone models resemble the experimental observations shown in Figure 2.10(a). Although Figures 2.10(a) and 2.10(c) correspond to different displacements, the

general trend of the necking and the outer surface buckling of the lower left sheet can still be qualitatively correlated.

2.4. J integral solutions for non-homogenous 3-zone material model

In this section the J integral solutions obtained from the finite element analyses based on the 3-zone material model are used to explain the ductile failure mode observed in the experiment. Figure 2.11 shows a schematic of a crack and an arbitrary contour Γ surrounding the crack tip. As shown in the figure, a Cartesian coordinate system is centered at the crack tip. The J integral is defined as [20]

$$\int_{\Gamma}\left(Wn_x - T_i\frac{\partial u_i}{\partial x}\right)ds,\ (i=x,y,z) \tag{1}$$

where Γ represents a counterclockwise contour from the lower crack face to the upper crack face, ds represents the differential arc length of the contour Γ, n_x represents the x component of the unit outward normal $\mathbf{n}$ to the differential arc length ds, T_i $\left(=\sigma_{ij}n_j\right)$ represent the components of the traction vector $\mathbf{T}$ on the differential arc length ds, and u_i represent the components of the displacement vector $\mathbf{u}$. In the above equation, the strain energy density W is defined as

$$W=\int_0^{\varepsilon_{ij}}\sigma_{ij}d\varepsilon_{ij},\ (i,j=x,y,z) \tag{2}$$

The J integral is path independent for a crack in a homogenous non-linear elastic material. For elastic-plastic power-law strain hardening materials under proportional loading conditions, the J integral can be used to represent the singularity amplitude of the crack-tip stress and strain fields. Figure 2.12(a) shows a schematic of a two-

dimensional finite element model of a lap-shear specimen and the boundary conditions. The Cartesian $x-y$ coordinate system is also shown in the figure. The middle surface of the left edge is fixed while displacement in the $+x$ direction is applied at the middle surface of the right edge. The specimen has the length L, the overlap length V, and the weld width w. Both the upper and lower sheets have the same thickness t. The two-dimensional plane-strain finite element model has the sheet thickness $t = 0.93$ mm, length $L = 95$ mm, overlap length $V = 30$ mm, and weld width $w =$ 0.86 mm between the two pre-existing crack tips. The width b of the central reduced width portion of the specimen is taken as 8 mm to calculate the applied force. First-order, plane strain, quadrilateral, reduced integration (CPE4R) elements are used in this model.

Figure 2.12(b) shows the finite element mesh near the weld based on the 3-zone material model of Lee et al. [14] for the ratio of the weld width to the sheet thickness, $w/t = 0.86$. As shown in the figure, there are three types of material zones: base metal, heat affected and fusion zones. A finer mesh is used near the pre-existing crack tips with the element size of about 4.75 μm. Figure 2.12(c) shows a close-up view of the mesh near the right pre-existing crack tip. A total of eight contours were assigned in the HAZ of the finite element model to obtain the J integral solutions. These contours are shown as thick lines surrounding the right pre-existing crack tip in Figure 2.12(c). Since all eight contours are in the HAZ which is homogenous, the J integral should be path independent and represents a fracture parameter of the crack tip under nearly proportional loading conditions. Note that near the crack tips in the HAZs, the grain size varies from several μm to about 30 μm as shown in Asim et al. [9]. The J integral, instead of a local crack tip parameter such as the crack tip opening displacement (CTOD) or crack tip

opening angle (CTOA), is selected here for the fracture parameter because the J integral is a macroscopic continuum path independent fracture parameter whereas the local CTOD or CTOA is mesh dependent from finite element analyses.

The elastic modulus and the Poisson's ratio are taken as 206 GPa and 0.3, respectively, for the elastic material properties for the base metal, heat affected and fusion zones in the finite element analyses. The three different stress-plastic strain curves for the base metal, heat affected and fusion zones, scaled by the hardness values [14], are adopted here. The hardness values and the scaled initial yield stresses for the base metal, heat affected and fusion zones are listed in Table 3. The scaled stress-plastic curves for the base metal, heat affected and fusion zones are shown in Figure 2.13. The Mises yield function is adopted to describe the elastic-plastic behavior of the material with the tensile stress-plastic strain curve used as the effective stress-plastic strain curve. The yield surface evolution is assumed to follow the isotropic hardening rule. It should also be noted that the residual stresses near the weld are not considered in this study due to the lack of quantitative information. Computations were performed using the commercial finite element code ABAQUS [21].

The J integral contours are numbered 1 to 8 where contour 1 is closest to the tip and contour 8 is farthest away from the tip. The J integral solutions from the finite element analysis for contours 4 to 8 for the right pre-existing crack tip are plotted as functions of the normalized applied load in Figure 2.14. The reference load $P_o \ \left(=\sigma_o bt\right)$ was used to normalize the applied load where σ_o is the yield stress of the base metal. It should be noted that the J integral solutions from the finite element analysis are higher for the right pre-existing crack tip as compared to those for the left pre-existing crack tip

due to the presence of the weld bead protrusion on the lower surface of the weld. Therefore, the J integral solution for the right pre-existing crack tip is considered in this study since the fracture will be initiated from the right pre-existing crack tip when the J integral reaches a critical value. It should also be noted that the J integral is path independent for a crack in a homogenous nonlinear elastic material [20]. The maximum variation of the J integral solutions for contours 4 to 8 is less than 15% for a given load. However, the general trends of the solutions are quite consistent.

Figure 2.15 shows the J integral solution for contour 8 as a function of the normalized load from the finite element analysis. Figure 2.15 also shows the failure curves that can be used to predict the failure mode of the laser welds in lap-shear specimens. The vertical dashed line in Figure 2.15 represents the failure load due to the plastic collapse or necking/shear as observed in the experiments. The normalized failure load $\overline{P}_f$ can be defined as

$$\overline{P}_f = \frac{P_f}{P_o} \tag{3}$$

where P_f is the failure load and P_o is a reference load. The failure load P_f can be estimated as

$$P_f = \sigma_u bt \tag{4}$$

where σ_u is the tensile strength, b is the reduced specimen width and t is the sheet thickness. The reference load P_o is again defined as

$$P_o = \sigma_o bt \tag{5}$$

Therefore,

$$\overline{P}_f = \frac{\sigma_u}{\sigma_o} \tag{6}$$

For the given HSLA steel, $\overline{P}_f$ is 1.31 from the results of the tensile tests. This is in good agreement with the experimental results of the failure or maximum loads of the laser welds in lap-shear specimens. The horizontal dashed line in Figure 2.15 represents the critical J_c of the heat affected zone in which the fracture initiation takes place at the pre-existing crack-tip. Due to the unavailability of the actual critical J_c for the HAZ of the HSLA steel sheet under investigation, an average value of 40 kN/m for the fracture toughness of low carbon steels is selected as the critical J_c for the heat affected zone to demonstrate the use of the failure curves in the present study. Figure 2.15 shows that for the specimen with a sheet thickness of t = 0.93 mm, the weld is likely to fail in the plastic collapse or necking/shear failure mode as the applied load reaches the failure load P_f before reaching the critical J_c.

2.5. Discussion on the effects of sheet thickness on failure mode

Ono et al. [10] reported failures of laser welds in the base metal of lap-shear specimens of thin steel sheets and correlated the weld strength to the tensile strength of the base metal. They also reported failures of laser welds in the weld and correlated the weld strength to the hardness of the weld. The failure mechanism of thin HSLA steel sheets under quasi-static loading conditions in the present study is observed to be the necking/shear in the base metal near the HAZ and the buckling of the lower left sheet, but a different failure mode dominated by fracture initiation from the pre-existing crack tip may be observed in welds of thicker sheets. In order to study the failure mode based on

fracture initiation from the pre-existing crack tip and to evaluate the effect of sheet thickness on the failure mode, the J integral approach is adopted and discussed below.

2.5.1. J integral solutions for specimens with different thicknesses

In this study, the sheet thickness t in the finite element model is varied in order to investigate the effect of the sheet thickness on the J integral solutions and, in turn, on the failure mode of the laser welds in lap-shear specimens. It should be noted that the weld width, weld geometry and the material variation in the weld area can affect the failure mode of the weld as investigated by Lee et al. [14]. Due to the unavailability of the actual welded specimens of different sheet thicknesses, all the dimensions of the weld and the specimen are scaled up proportionally by the sheet thickness in the finite element models in the present study. Therefore, the ratio of the weld width to the sheet thickness, $w/t = 0.86$, is kept the same for all finite element models with different thicknesses. The finite element models were scaled up by factors of 2, 3, 4 and 5 to represent the specimens with larger thicknesses. Therefore, five different thicknesses of t, $2t$, $3t$, $4t$ and $5t$, were used in the finite element models. Here, t represents the sheet thickness of the original lap-shear specimen and is equal to 0.93 mm.

Figure 2.16 shows the J integral solutions for contour 8 for the right pre-existing crack tips from the finite element analyses of the specimens with the sheet thicknesses of t, $2t$, $3t$, $4t$ and $5t$. The J integral solutions are plotted as functions of the normalized applied load for the specimens with the different thicknesses. Figure 2.16 shows that the J integral solutions for a given normalized applied load increase as the sheet thickness increases. The failure curves in Figure 2.16 can be used to predict the

failure mode of the laser welds in these lap-shear specimens. The vertical dashed line in Figure 2.16 represents the normalized failure load due to plastic collapse or necking/shear. The horizontal dashed line in Figure 2.16 represents the critical J_c which is taken as 40 kN/m for the weld in the present study. For the specimens with the sheet thicknesses of t and $2t$, the plastic collapse or the necking/shear failure loads are reached before the critical J_c is reached. For the specimens with the sheet thicknesses of $3t$, $4t$ and $5t$, the critical J_c is met before the plastic collapse failure loads are reached. A critical thickness $t_c = 2.22$ mm can be determined for the given critical J_c of 40 kN/m and normalized failure load $\overline{P}_f$ of 1.31 for the transition of the failure mode from the plastic collapse to the fracture initiation from the right pre-existing crack tip. This critical thickness depends on the critical J_c of the heat affected zone and the tensile strength of the base metal. If the welding process causes a reduction of the critical J_c of the heat affected zone, then a failure by fracture initiation from the right pre-existing crack tip is more likely to occur for thinner sheets. Conversely, a lower tensile strength of the base metal can cause a failure by plastic collapse or necking/shear for thicker sheets. It should be noted that the effect of the weld width is not investigated in this study. Laser welds normally have a very small weld width. However, a larger ratio of the weld width to the sheet thickness is needed to prevent any interfacial fracture through the weld.

It should be noted that Ono et al. [10] reported that for the lap-shear specimens of thin steel sheets used in their investigation with sheet thicknesses above 1.2 mm, the fracture occurred in the weld metal instead of the base metal as observed in the specimens with thinner sheets. This observation of the change of failure location of the

welds based on sheet thickness motivates the present study and can be explained based on the use of the failure curves in Figures 2.15 and 2.16. However, a more detailed experimental investigation for welds with different sheet thicknesses and for other types of metals can be conducted to verify the concept of the failure curves presented here.

2.5.2. Scalability of the J integral solutions

As shown in Figure 2.16, for a given normalized load, the J integrals are larger for specimens with larger thicknesses. When the thickness t and the weld width w are the most important length parameters for the homogenous material model of the lap-shear specimen with a weld [14], the J integral should be scaled to the thickness for both linear elastic and pure power-law hardening material for a fixed ratio of w/t. In order to determine if the scalability of the J integral by the sheet thickness is possible for the nonhomogenous 3-zone model, the J integral solutions normalized by the sheet thickness t are plotted as functions of the normalized load in Figure 2.17. Figure 2.17 shows the values of the normalized J integral, $\bar{J}(= J/t)$, for contour 8 for the right pre-existing crack tips from the finite element analyses of the specimens with the sheet thicknesses of t, $3t$ and $5t$. Figure 2.17 shows that the normalized J integral solutions collapse into a single curve. This indicates the scalability of the J integral by the sheet thickness t for the specimens with different thicknesses for the given ratio of $w/t = 0.86$.

For pure power-law hardening homogeneous materials, the J integral should be scaled by the only significant length dimension of the geometry of interest [22]. For the laser welds in lap-shear specimens, when the weld width is significantly larger than the thickness, the thickness becomes the only significant length dimension according to the

beam bending theory. For the given ratio $w/t = 0.86$, the stress intensity factor solutions derived from the beam bending theory are reasonably close to the actual stress intensity factor solutions obtained from the finite element analysis for linear elastic homogeneous materials [8]. This suggests that the beam bending theory may be approximately applicable to laser welds in lap-shear specimens for the given ratio $w/t = 0.86$ under elastic-plastic deformation. For pure power-law hardening homogeneous materials, it can be shown that the J integral should be scaled by the thickness for the two-strip model of Sripichai et al. [8]. For the 3-zone finite element model, the J integral for the crack tip in the HAZ should depend on the sheet thickness, the width of the HAZ, the width of the fusion zone, the remaining ligament between the crack tip and the fusion zone, and the material variation in the weld zone. When the weld geometry is scaled up proportionally with respect to the sheet thickness while the material variation is kept to be the same, the J integrals is apparently scaled by the sheet thickness as indicated in Figure 2.17.

The failure curve and the scaled J integral curves for a sheet of unit thickness can be used to conveniently determine the critical sheet thickness for the transition of the failure mode. As a demonstration, the value $\bar{J}_c = J_c/t$ obtained from the normalized J integral curve in Figure 2.17 for the normalized failure load $\bar{P}_f$ of 1.31 is about 18 MPa as shown in the figure. Dividing the selected fracture toughness of 40 kN/m by this value of $\bar{J}_c$ gives a value of 2.22 mm for the critical sheet thickness t_c as mentioned earlier.

Based on the earlier discussion, the failure load P_f can be expressed as

$$P_f = \sigma_u bt \qquad t \le t_c \tag{7}$$

$$P_f = \sigma_o bt\bar{P}\left(\bar{J}_c\right) \qquad t > t_c \tag{8}$$

where $\bar{P}(\bar{J}_c)$ represents the normalized load $\bar{P}$ as a function of $\bar{J}_c$. Figure 2.18 shows the plots of the failure load P_f as a function of the sheet thickness t based on Equations (7) and (8) for specimens with different thicknesses. Different J_c values of 30, 40 and 50 kN/m are used to plot three different curves representing Equation (8). Figure 2.18 shows that for sheet thicknesses smaller than the critical sheet thickness t_{c1} for J_c = 30 kN/m, t_{c2} for J_c = 40 kN/m, and t_{c3} for J_c = 50 kN/m, the failure load based on the plastic collapse failure mode is lower than the failure load required to initiate fracture from the pre-existing crack tips. For sheet thicknesses larger than the critical sheet thickness t_{c1} for J_c = 30 kN/m, t_{c2} for J_c = 40 kN/m, and t_{c3} for J_c = 50 kN/m, the failure load to cause fracture initiation is smaller than the failure load based on the plastic collapse failure mode, and the failure is likely to occur by fracture initiation from the pre-existing crack tips. It should be noted that the critical sheet thickness t_c decreases as the critical J_c decreases. This indicates that for a weld with a lower critical J_c, the failure by fracture initiation can occur at a smaller thickness. In summary, the failure criteria of welds based on the plastic collapse failure mode should be used cautiously for welds of thicker sheets due to possible lower failure loads due to the fracture initiation from the pre-existing crack tips.

2.6. Conclusions

In this paper, the failure mode of laser welds in lap-shear specimens of non-galvanized SAE J2340 300Y high strength low alloy (HSLA) steel sheets under quasi-static loading conditions is examined based on experimental observations and finite

element analyses. Laser welded lap-shear specimens with reduced cross sections were made. Optical micrographs of the cross sections of the welds in the specimens before and after tests are examined to understand the microstructure and failure mode of the welds. Micro-hardness tests were also conducted to provide an assessment of the mechanical properties in the base metal, heat affected and fusion zones. The micrographs indicate that the weld failure appears to be initiated from the base metal near the boundary of the base metal and the heat affected zone at a distance from the pre-existing crack tip, and the specimens fail due to the necking/shear of the lower left load carrying sheets. Finite element analyses based on non-homogenous multi-zone material models were conducted to model the ductile necking/shear failure and to obtain the J integral solutions for the pre-existing cracks. The results of the finite element analyses are used to explain the ductile failure initiation sites and the necking/shear of the lower left load carrying sheets. The J integral solutions obtained from the finite element analyses based on the 3-zone finite element model indicate that the J integral for the pre-existing cracks at the failure loads are low compared to the fracture toughness and the specimens should fail in a plastic collapse or necking/shear mode. The effects of the sheet thickness on the failure mode were then investigated for laser welds with a fixed ratio of the weld width to the thickness. For the given non-homogenous material model, the J integral solutions appear to be scaled by the sheet thickness. With consideration of the plastic collapse failure mode and fracture initiation failure mode, a critical thickness can be obtained for the transition of the plastic collapse or necking/shear failure mode to the fracture initiation failure mode. Finally, the failure load is expressed as a function of the sheet thickness according to the governing equations based on the two failure modes. The

results demonstrate that the failure mode of welds of thin sheets depends on the sheet thickness, ductility of the base metal, and fracture toughness of the heat affected zone. Therefore, failure criteria based on either the plastic collapse failure mode or the fracture initiation failure mode should be used cautiously for welds of thin sheets.

Acknowledgements

Partial support of this work by the National Science Foundation under grant No. DMI-0456755 is greatly appreciated. The support of Dr. M. Li of TWB (Monroe, MI) to provide the laser welded specimens used in this investigation is also greatly appreciated.

Table 2.1. Dimensions of the lap-shear specimen.

Width of the grip section (W)	27.0 mm
Width of the central portion (b)	8.0 mm
Fillet radius (R)	9.5 mm
Length of the central portion (c)	13.5 mm
Length of the doubler (s)	50.0 mm
Weld width (w)	1.0 mm
Length of each leg (L)	95.0 mm
Overlap length (V)	30.0 mm

Table 2.2. Material parameters from tensile tests of the base metal.

Elastic Modulus (GPa)	Yield Strength (MPa)	Tensile Strength (MPa)	Hardening Exponent n	Strength Coefficient K (MPa)
206	315	415	0.15	633

Table 2.3. The hardness values from indentation tests and the scaled initial yield stresses for the base metal, heat affected and fusion zones for the 3-zone model.

	Base metal	Heat-affected zone	Fusion zone
Vickers hardness	150	190	230
Yield stress σ_0 (MPa)	315	400	484

Table 2.4. The hardness values from indentation tests and the scaled initial yield stresses for the base metal, heat affected and fusion zones for the 6-zone model.

	Base metal	HAZ 1	HAZ 2	Fusion zone 1	Fusion zone 2	Fusion zone 3
Vickers hardness	150	166	182	198	214	230
Yield stress σ_0 (MPa)	315	349	382	416	450	484

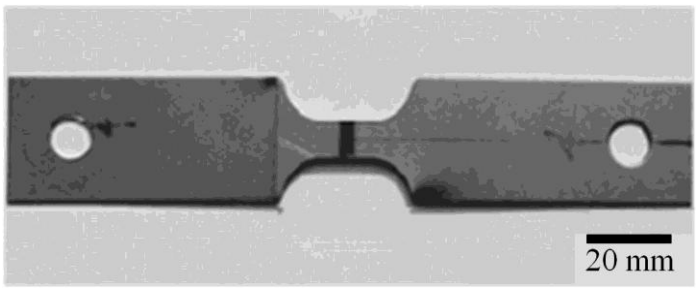

(a)

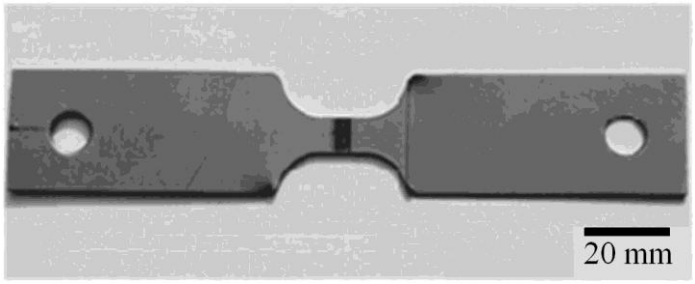

(b)

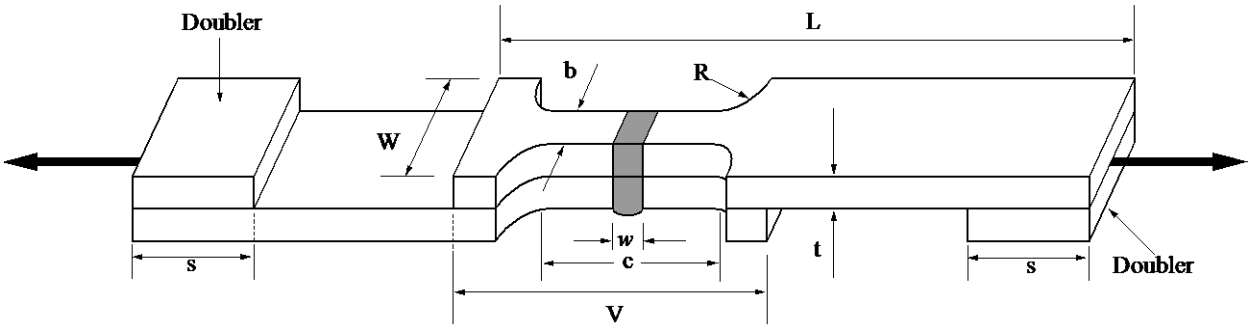

(c)

Figure 2.1. (a) A top view and (b) a bottom view of a laser-welded lap-shear specimen, and (c) a schematic of a lap-shear specimen with the loading direction shown as the bold arrows.

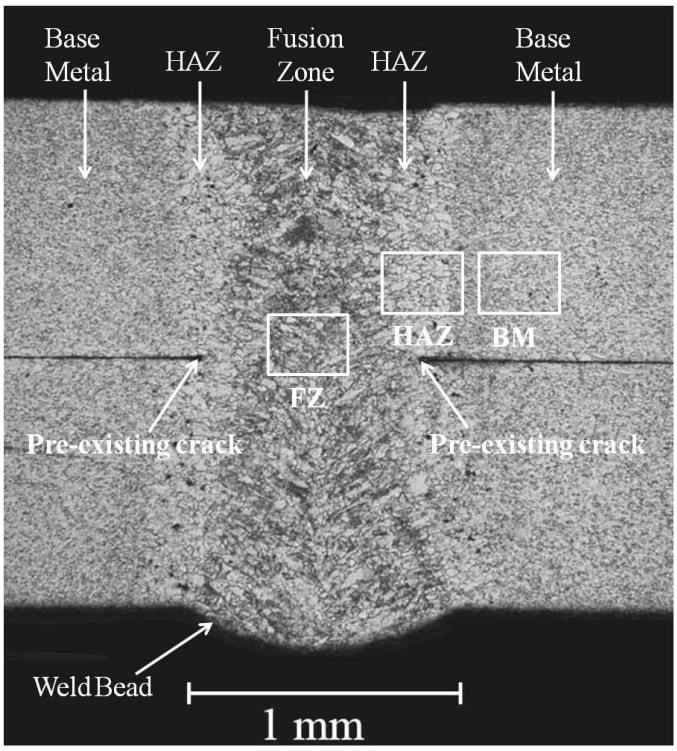
Base Metal
HAZ
Fusion Zone
HAZ
Base Metal
HAZ
BM
FZ
Pre-existing crack
Pre-existing crack
Weld Bead
1 mm

(a)

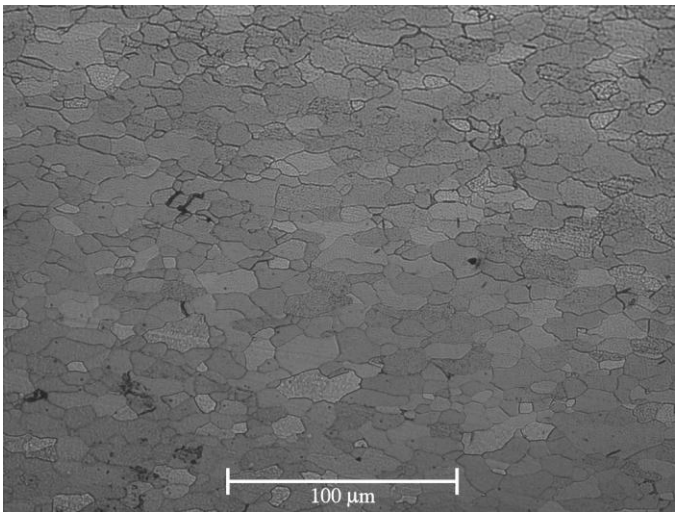
100 µm

(b)

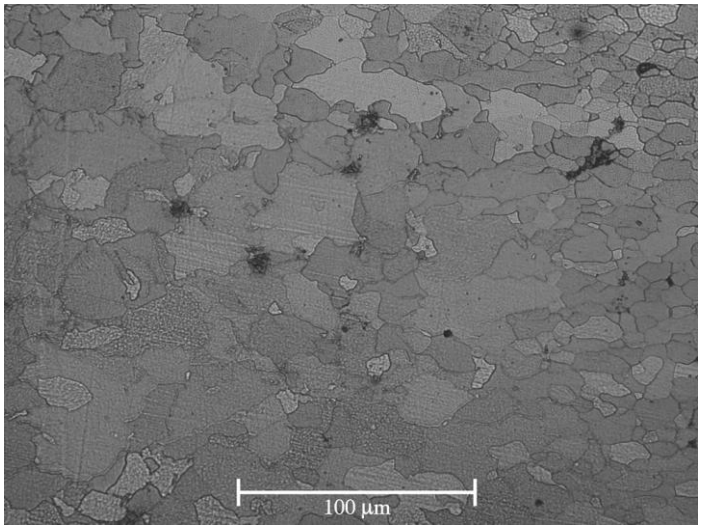

(c)

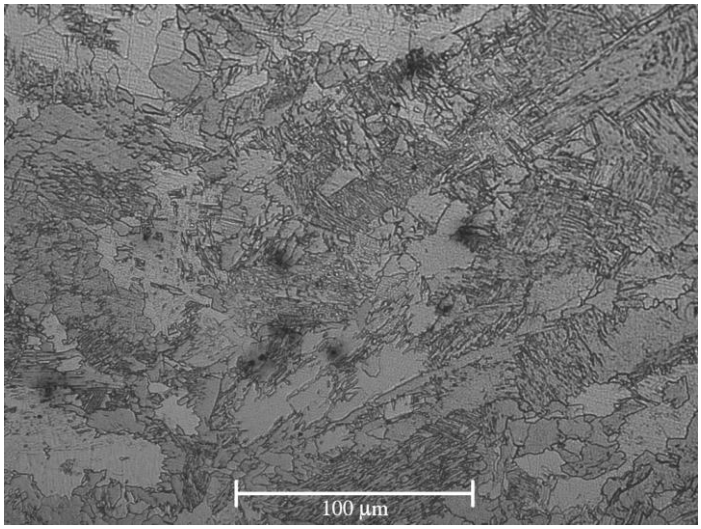

(d)

Figure 2.2 (a) An optical micrograph of the etched cross section of a laser welded joint (3% Nital used as the etchant), and the close-up views of the optical micrographs of (b) the base metal (BM), (c) the heat affected zone (HAZ) and (d) the fusion zone (FZ) as marked in (a).

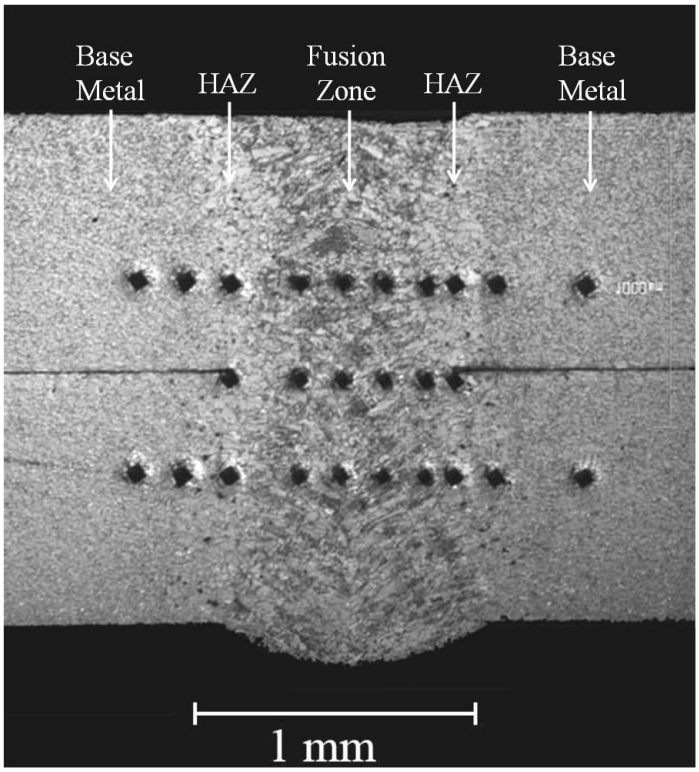

(a)

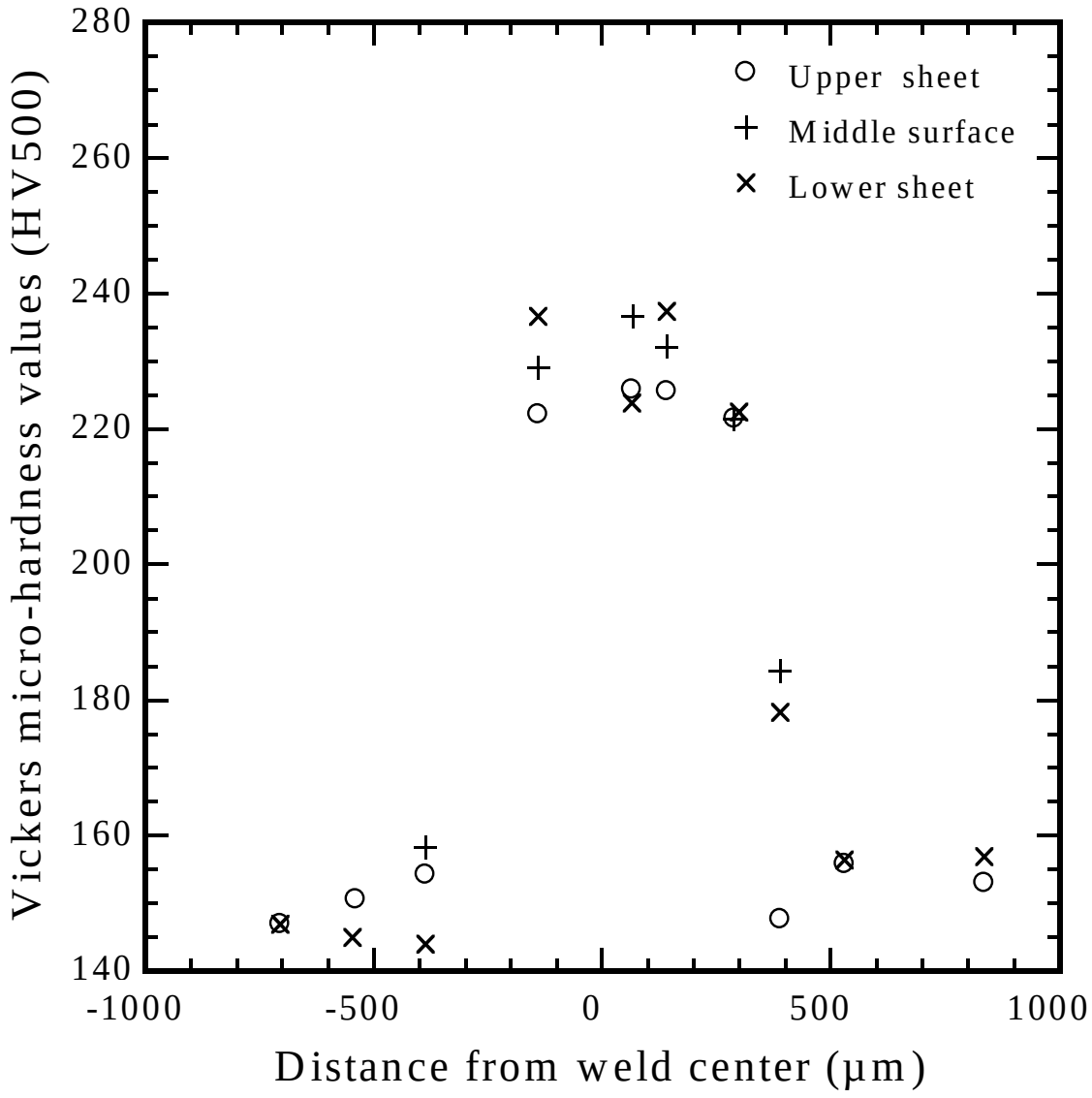

(b)

Figure 2.3. (a) An optical micrograph of the cross section of a laser weld with the micro-indentations, and (b) the distributions of the hardness values across the weld.

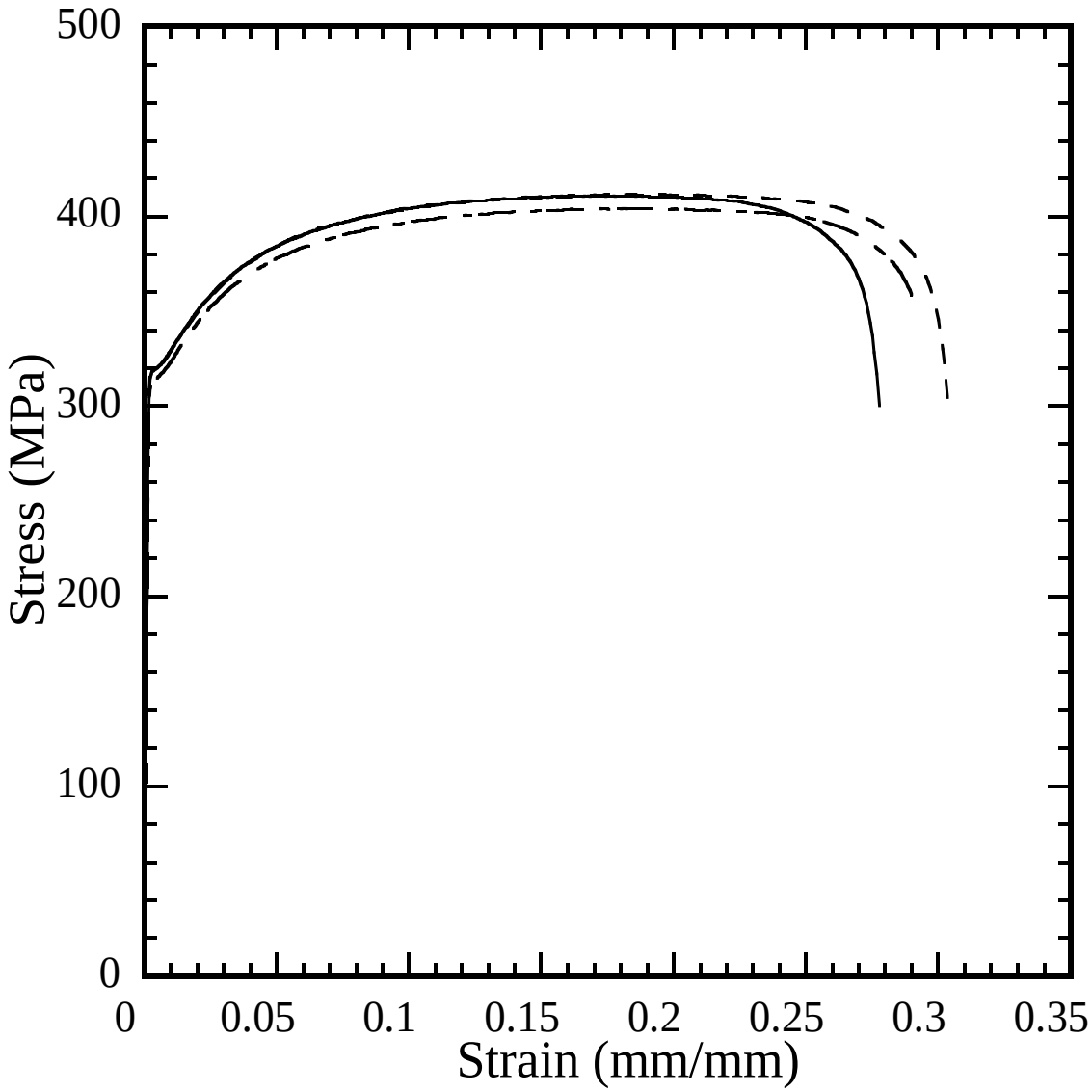

Figure 2.4. The engineering stress-strain curves for the base metal from three representative sheet specimens.

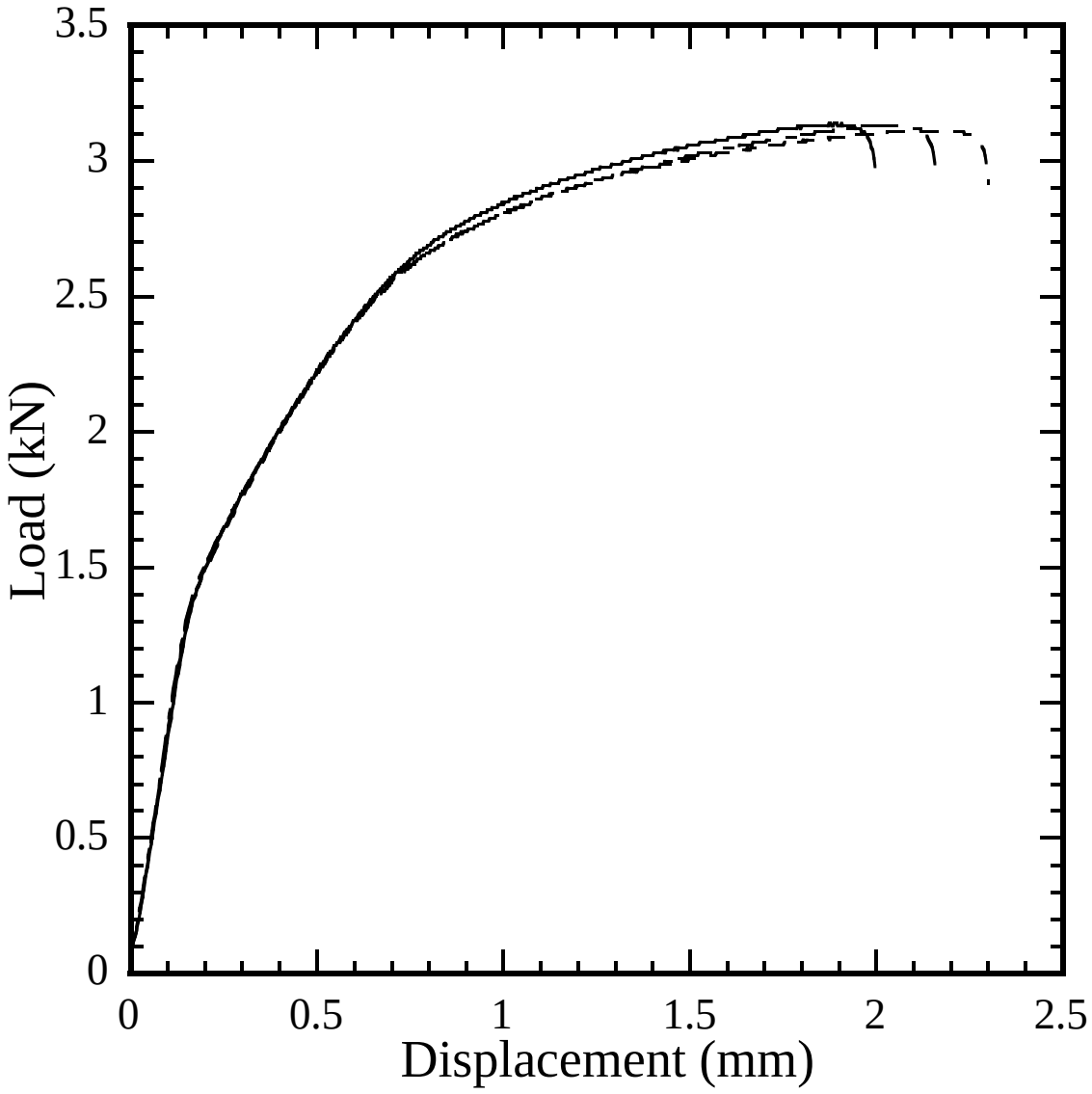

Figure 2.5. The load-displacement curves from quasi-static tests of three lap-shear specimens.

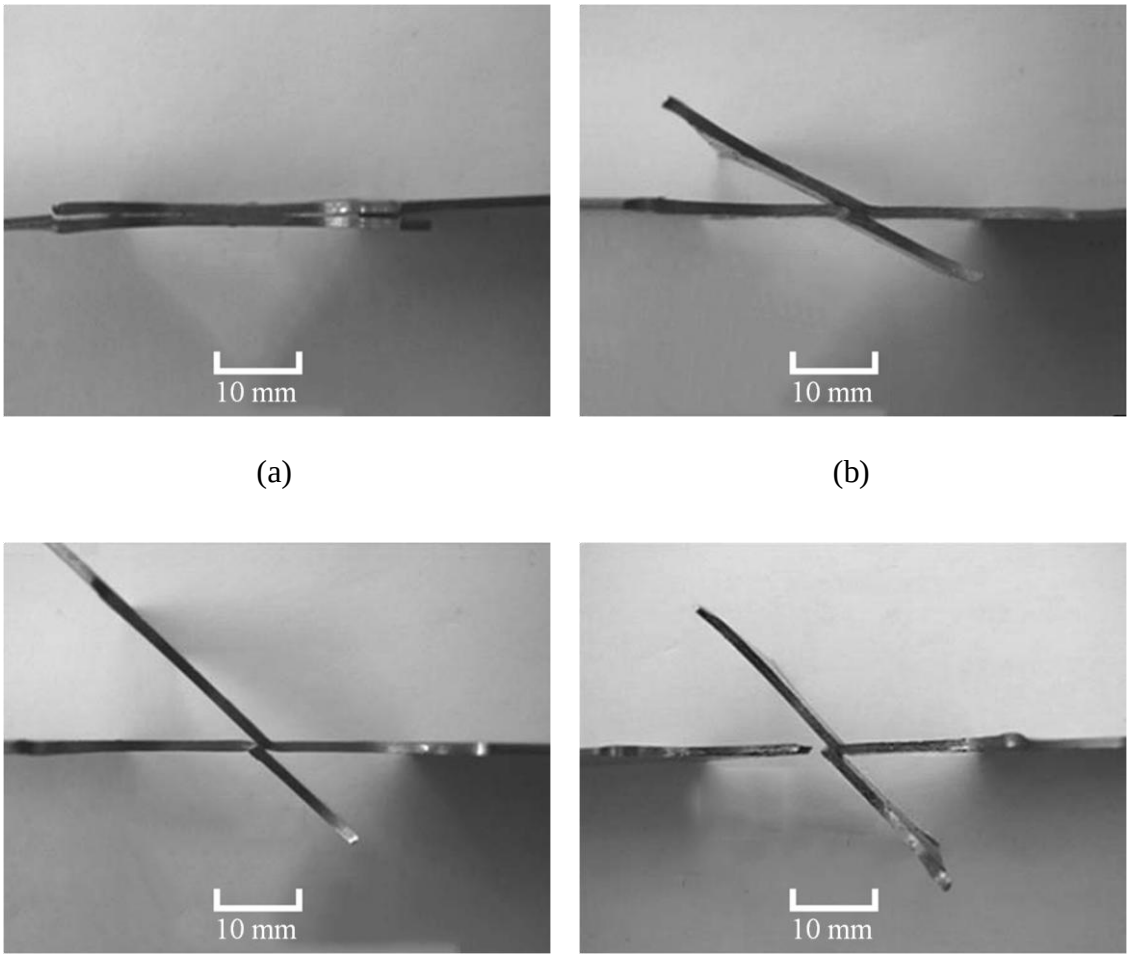

Figure 2.6. Side views of specimens at the applied displacements of (a) 0.2 mm (b) 1.0 mm (c) 1.9 mm and (d) about 2.1 mm with the left sheet separated from the weld.

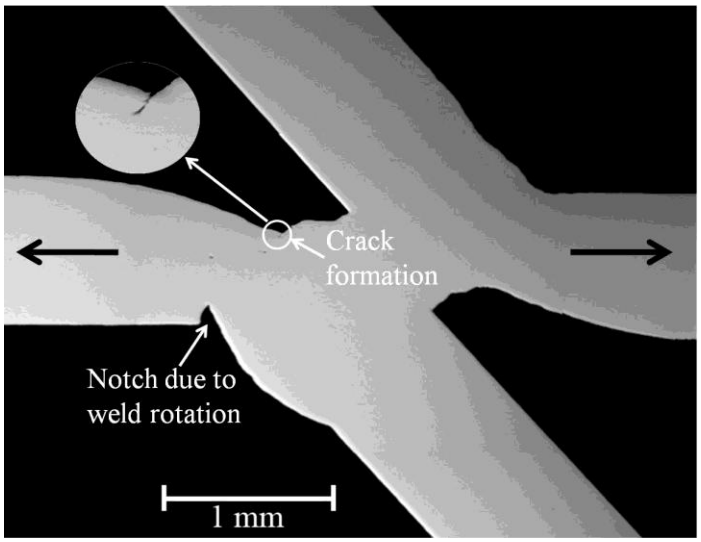

(a)

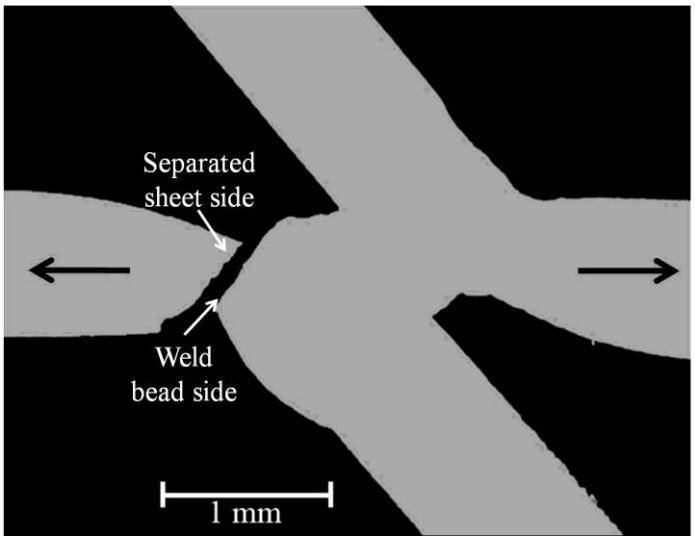

(b)

Figure 2.7. Optical micrographs of the cross sections of the weld for (a) a nearly failed and (b) a failed weld.

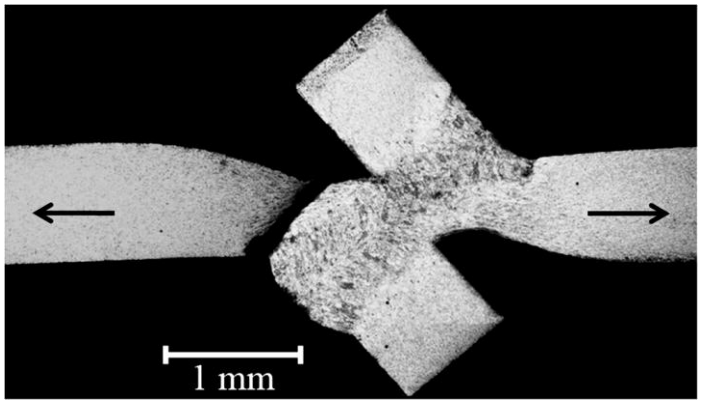

(a)

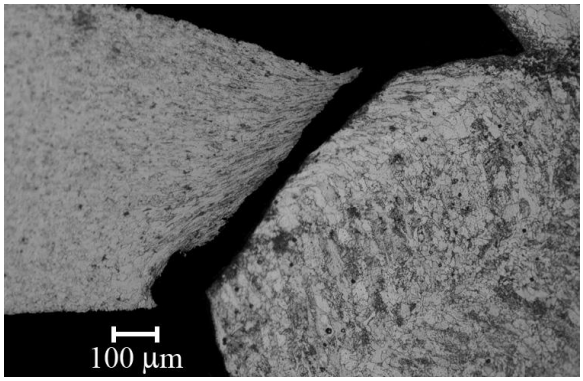

(b)

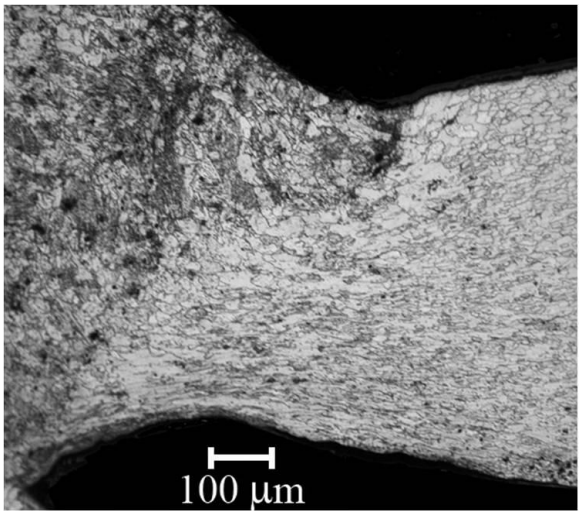

(c)

Figure 2.8. (a) An optical micrograph of the etched cross section of a failed weld, and close-up views of (b) the lower left sheet near the failure surface and (c) the upper right sheet near the pre-existing crack tip (3% Nital solution used as the etchant).

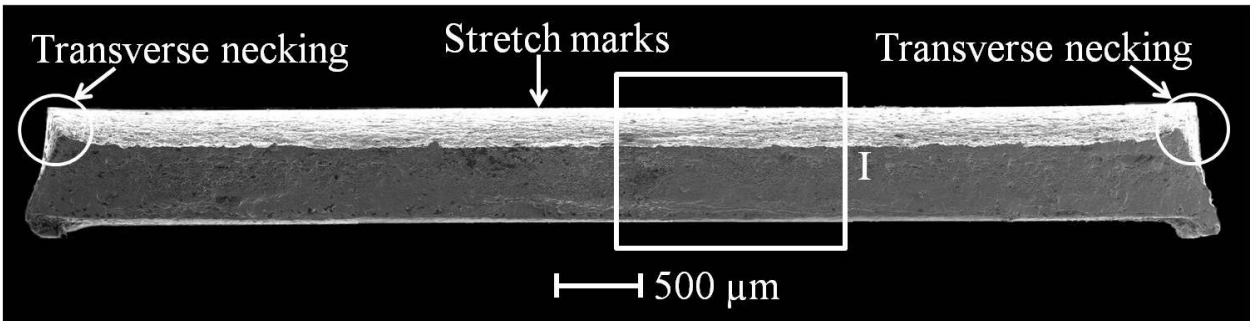

(a)

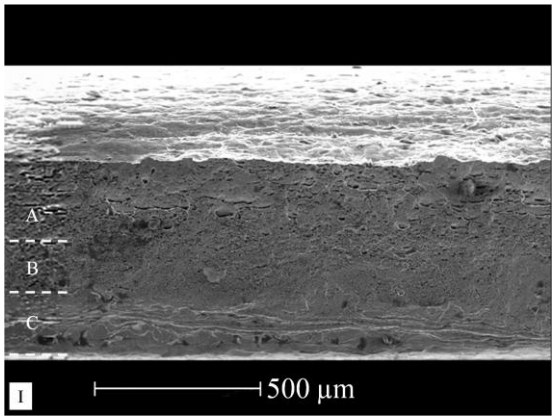

(b)

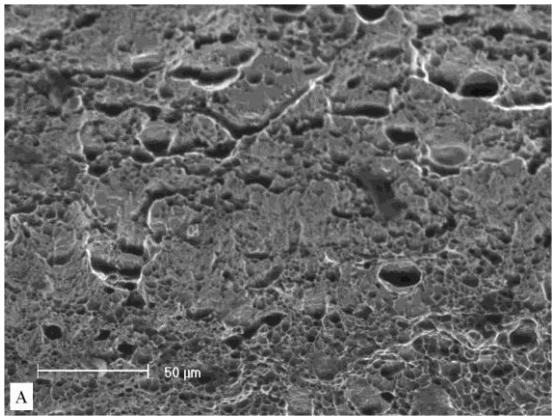

(c)

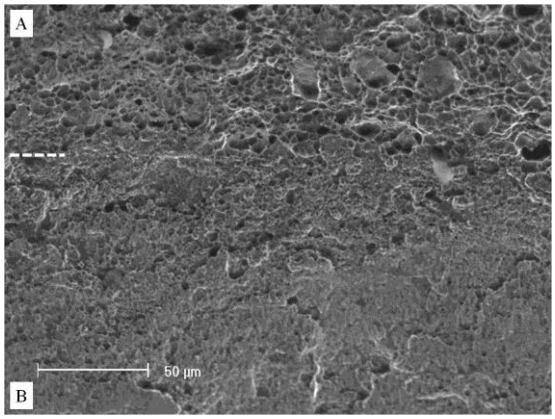

(d)

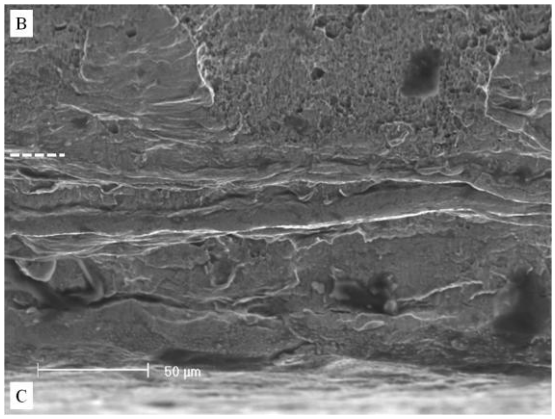

(e)

Figure 2.9. (a) A scanning electron micrograph of the failure surface on the separated sheet side, (b) a close-up view of region I in (a), and close-up views of portions of (c) region A, (d) the transition region between regions A and B, and (e) the transition region between regions B and C.

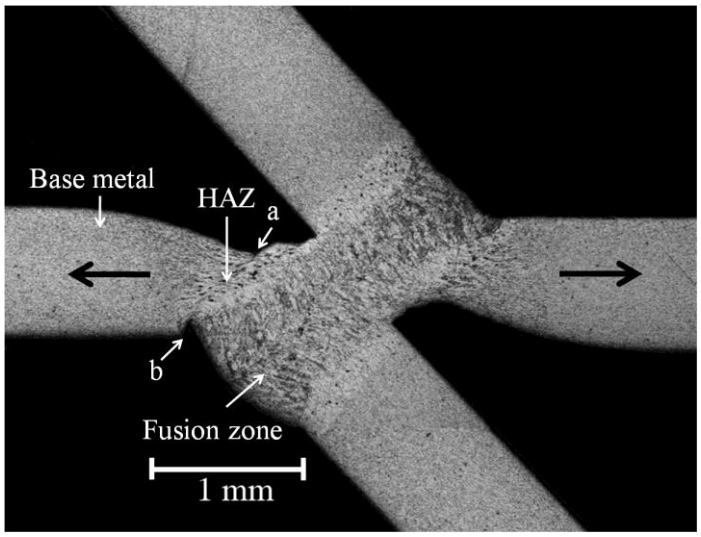

(a)

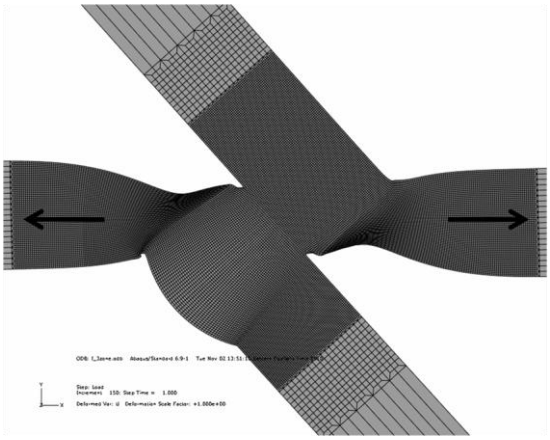

(b)

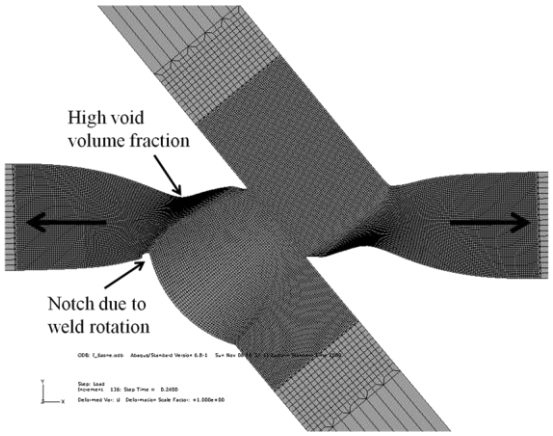

(c)

Figure 2.10. (a) An optical micrograph of the etched cross section of a weld in a lap-shear specimen at the applied displacement of 1.95 mm prior to the final failure, and the deformed mesh near a weld in a lap-shear specimen at the applied displacement of 2.4 mm from the finite element analysis based on (b) the 3-zone model and (c) the 6-zone model.

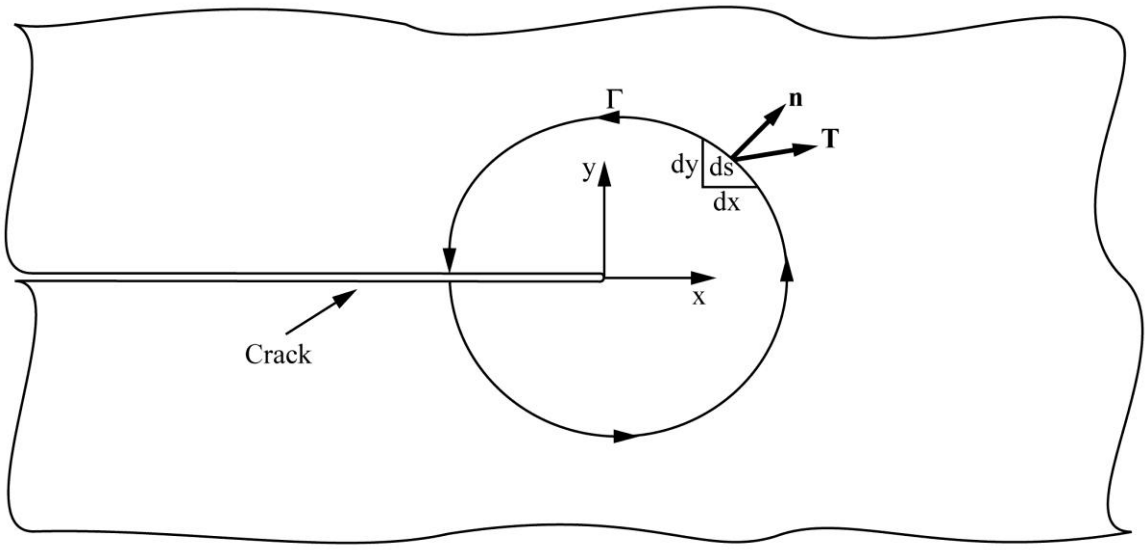

(a)

Figure 2.11. A schematic of a crack and an arbitrary contour Γ surrounding the crack tip.

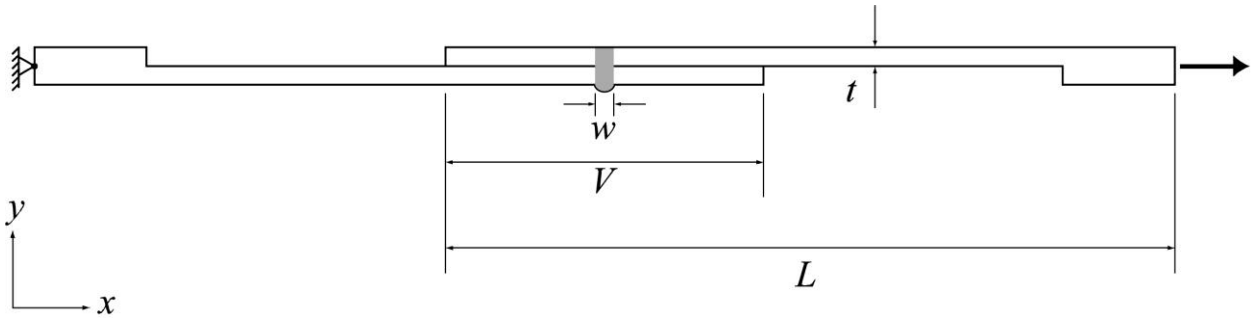
t
w
V
y
x
L

(a)

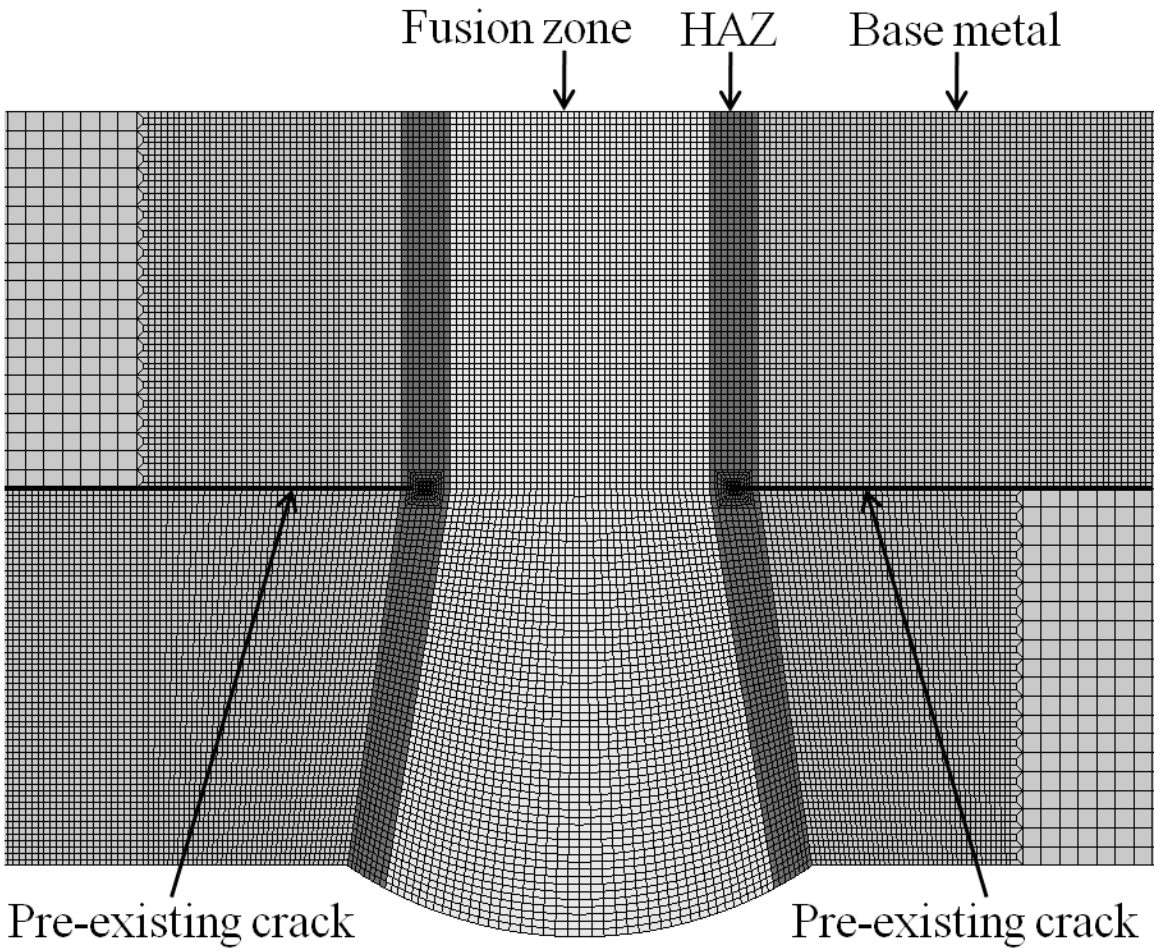
Fusion zone
HAZ
Base metal
Pre-existing crack
Pre-existing crack

(b)

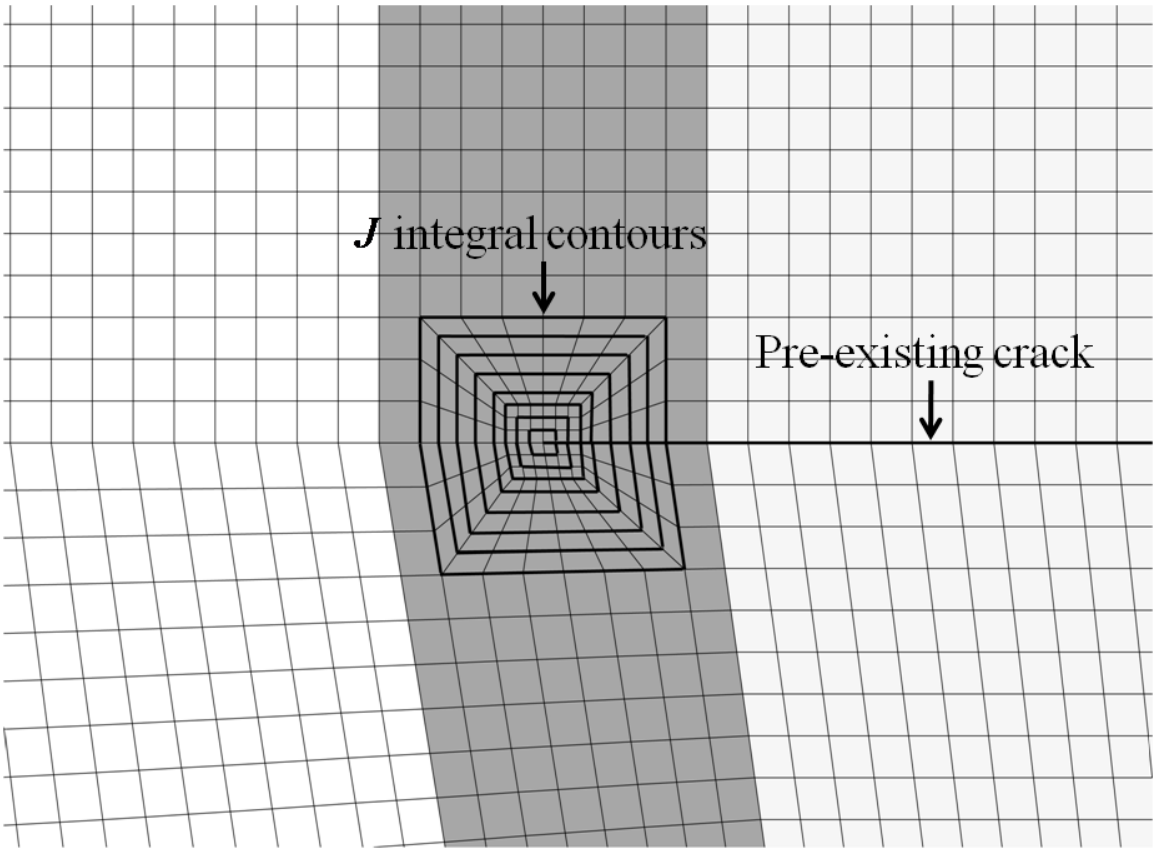

(c)

Figure 2.12. (a) A schematic of a two-dimensional finite element model of a lap-shear specimen and the boundary conditions, (b) the finite element mesh near the weld, and (c) a close-up view of the finite element mesh near the right pre-existing crack tip.

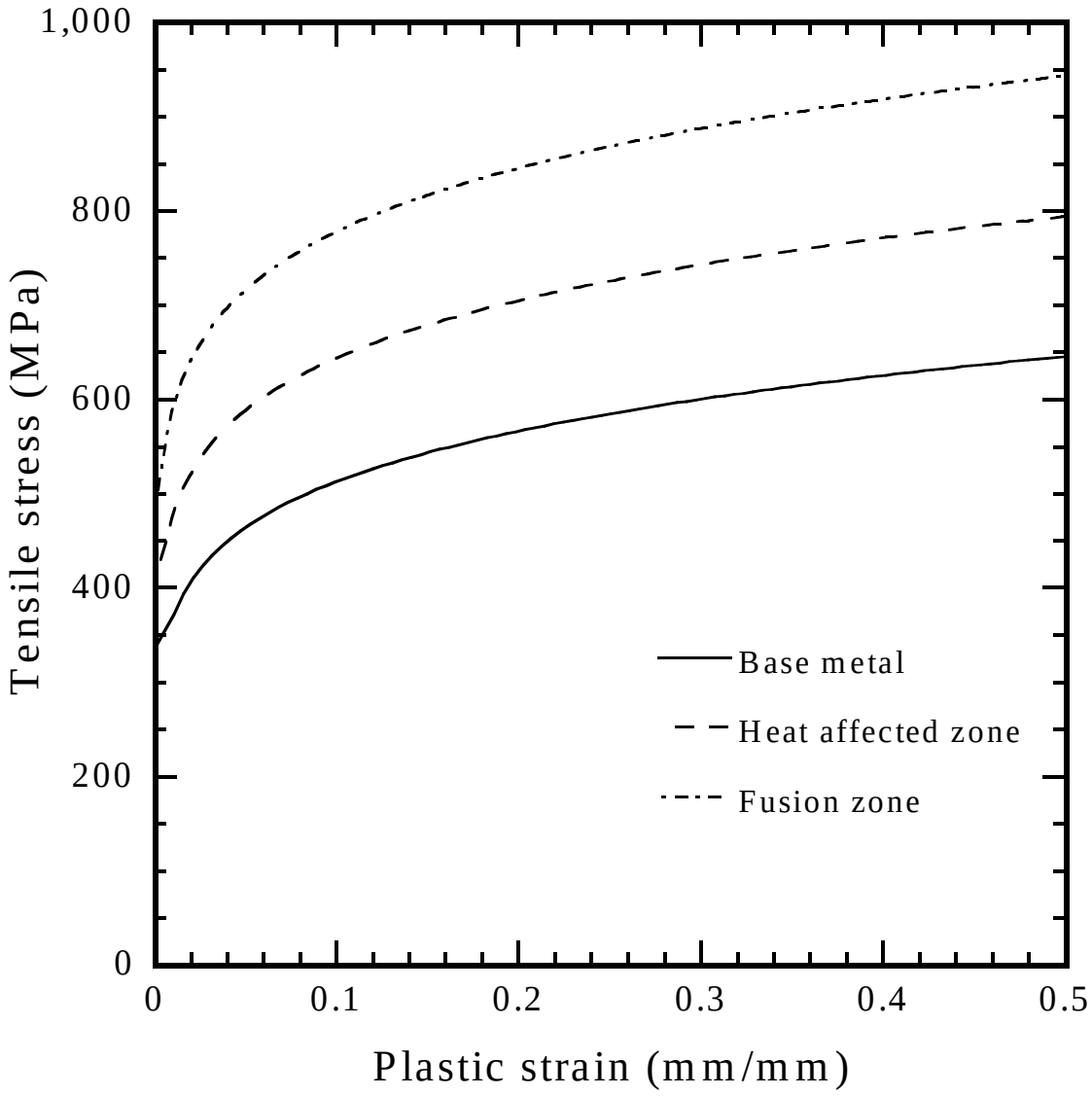

Figure 2.13. The tensile stresses as functions of the plastic strain for the base metal, heat affected and fusion zones used in the 3-zone finite element analysis.

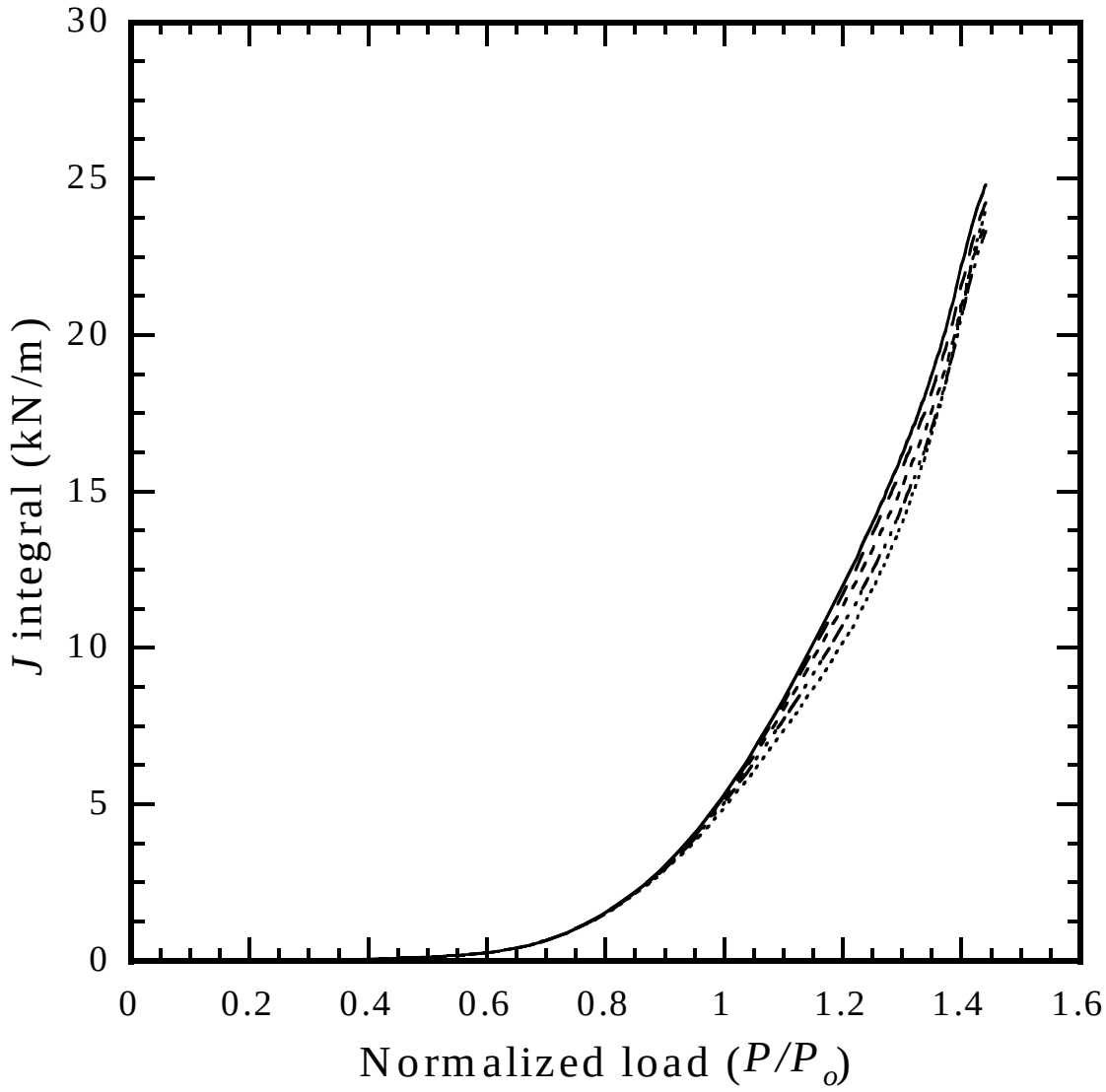

Figure 2.14. The J integral solutions for contours 4 to 8 for the right pre-existing crack tip as functions of the normalized load from the finite element analysis.

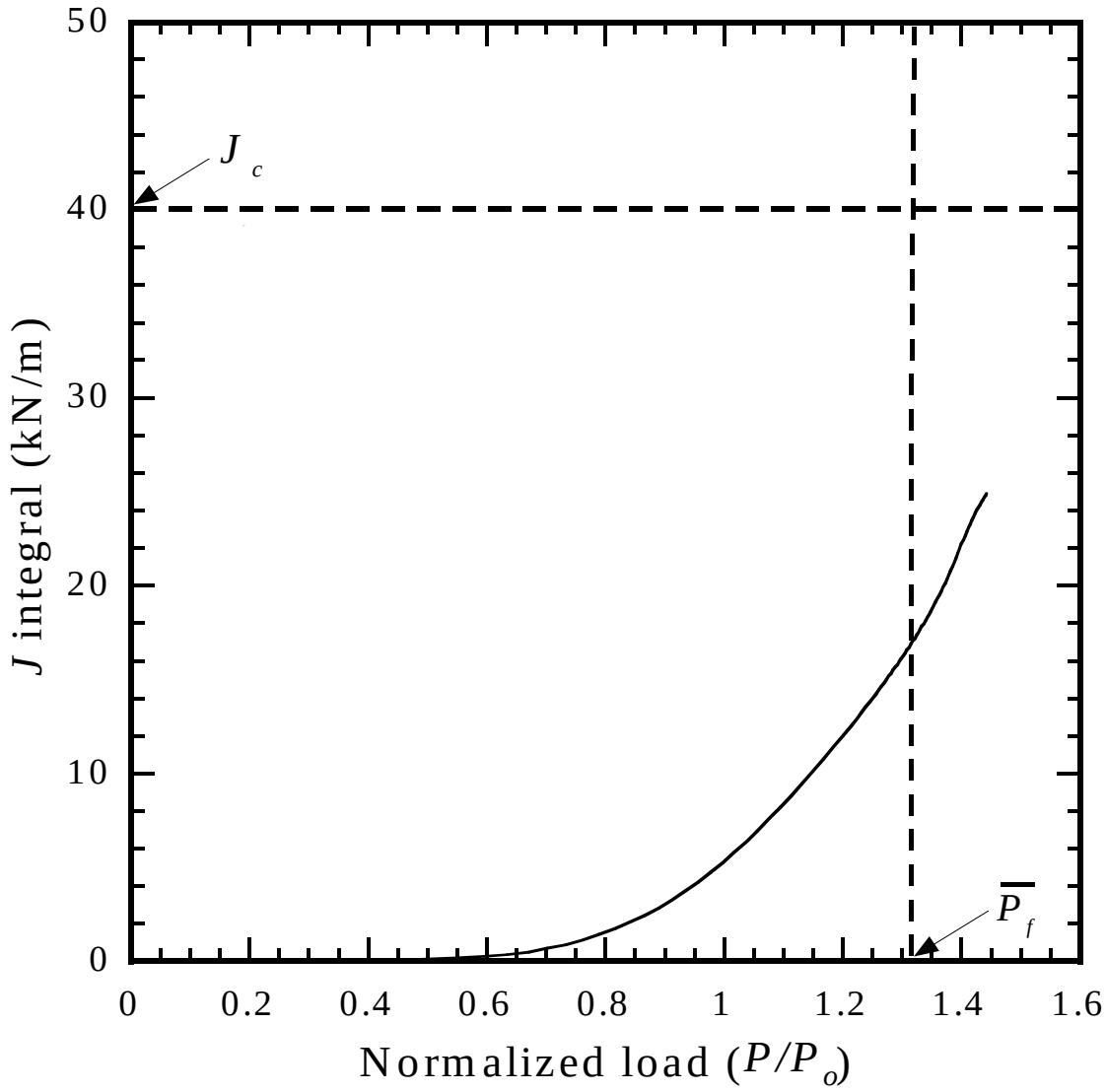

Figure 2.15. The J integral solution for contour 8 for the right pre-existing crack tip as a function of the normalized load from the finite element analysis.

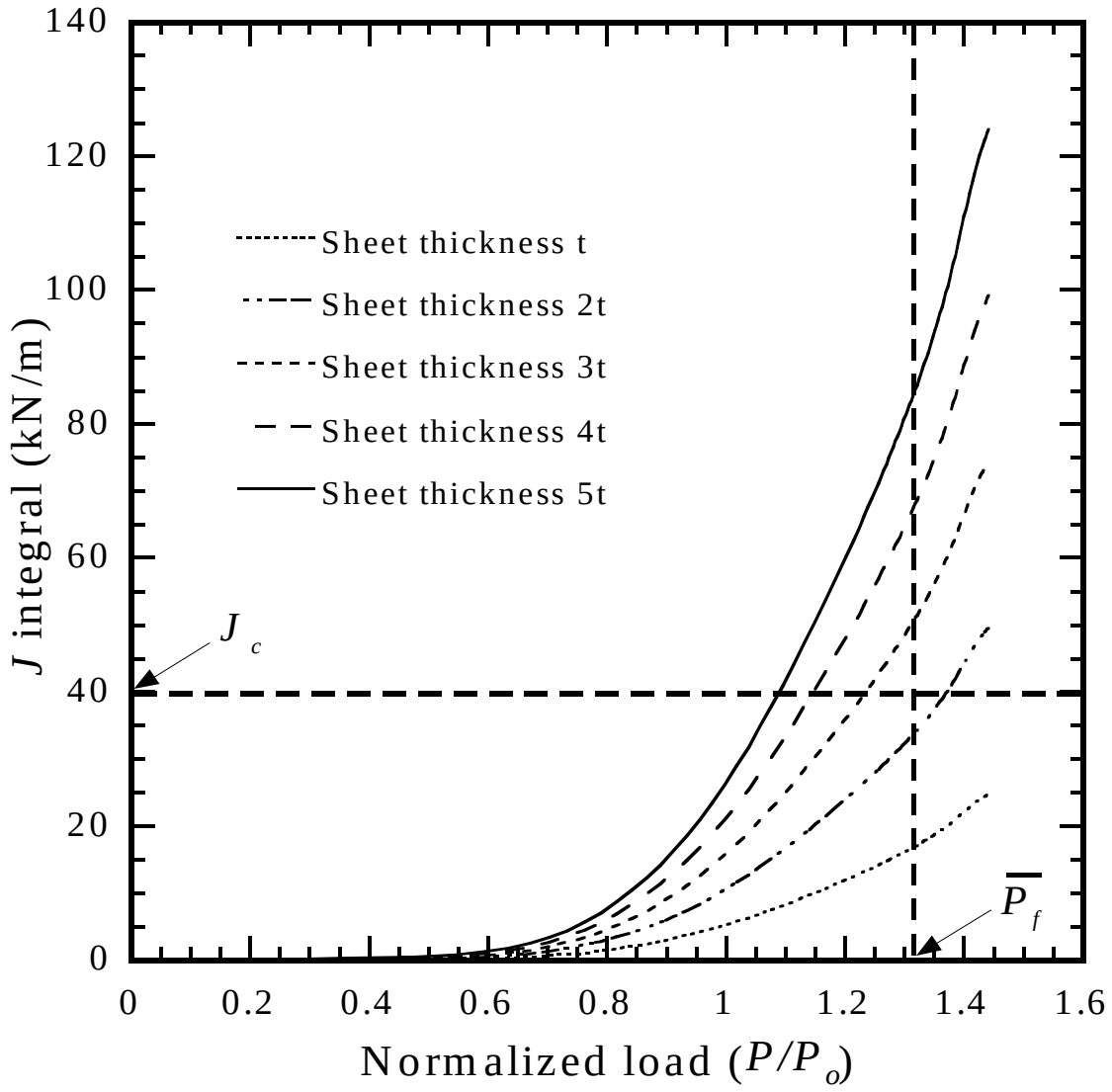

Figure 2.16. The J integral solutions for contour 8 for the right pre-existing crack tip as functions of the normalized load from the finite element analyses of the specimens with the sheet thicknesses of t, $2t$, $3t$, $4t$ and $5t$.

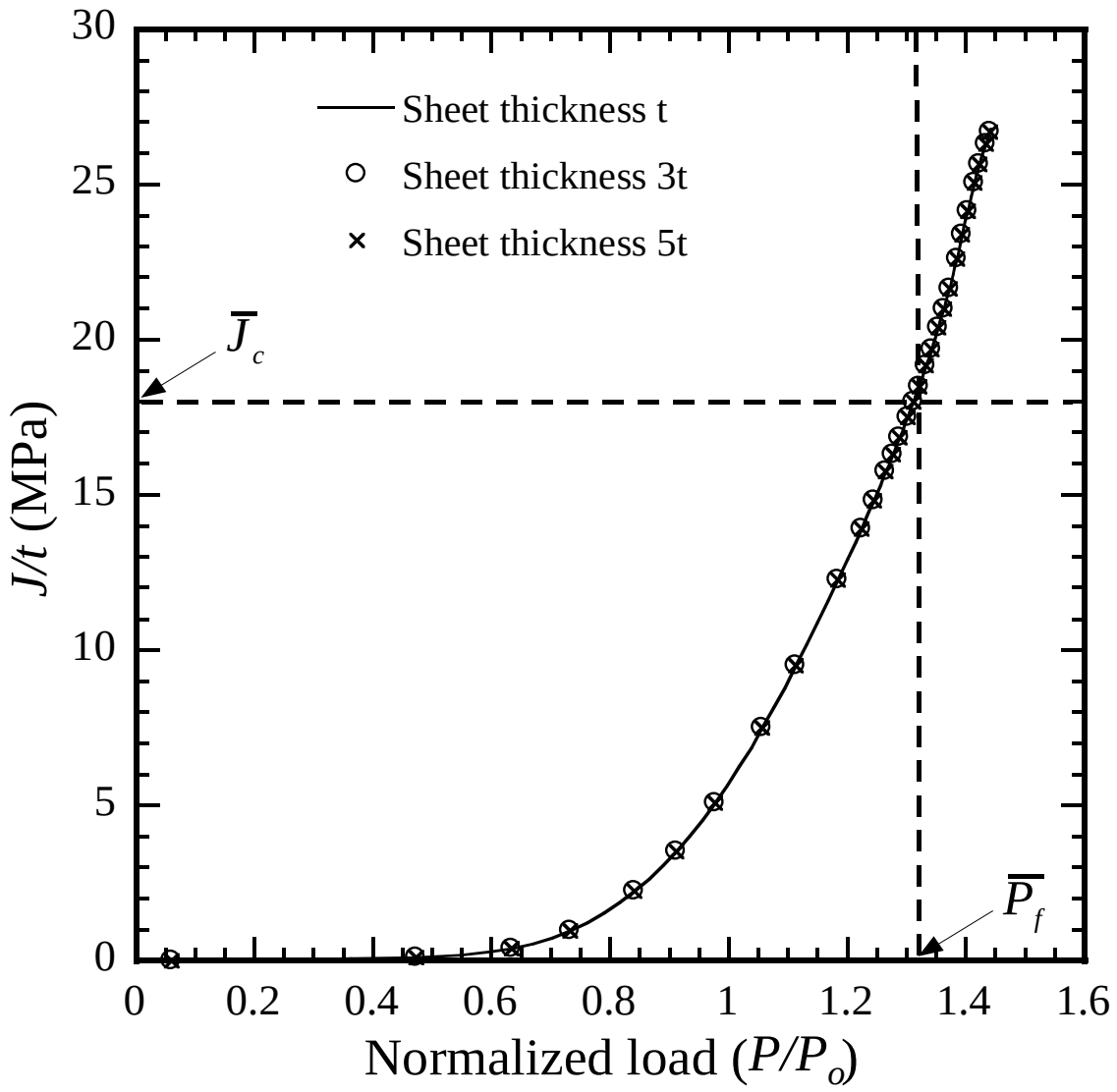

Figure 2.17. The values of the normalized $\bar{J}(=J/t)$ for contour 8 for the right pre-existing crack tips as functions of the normalized load from the finite element analyses of the specimens with the sheet thicknesses of t, $3t$ and $5t$.

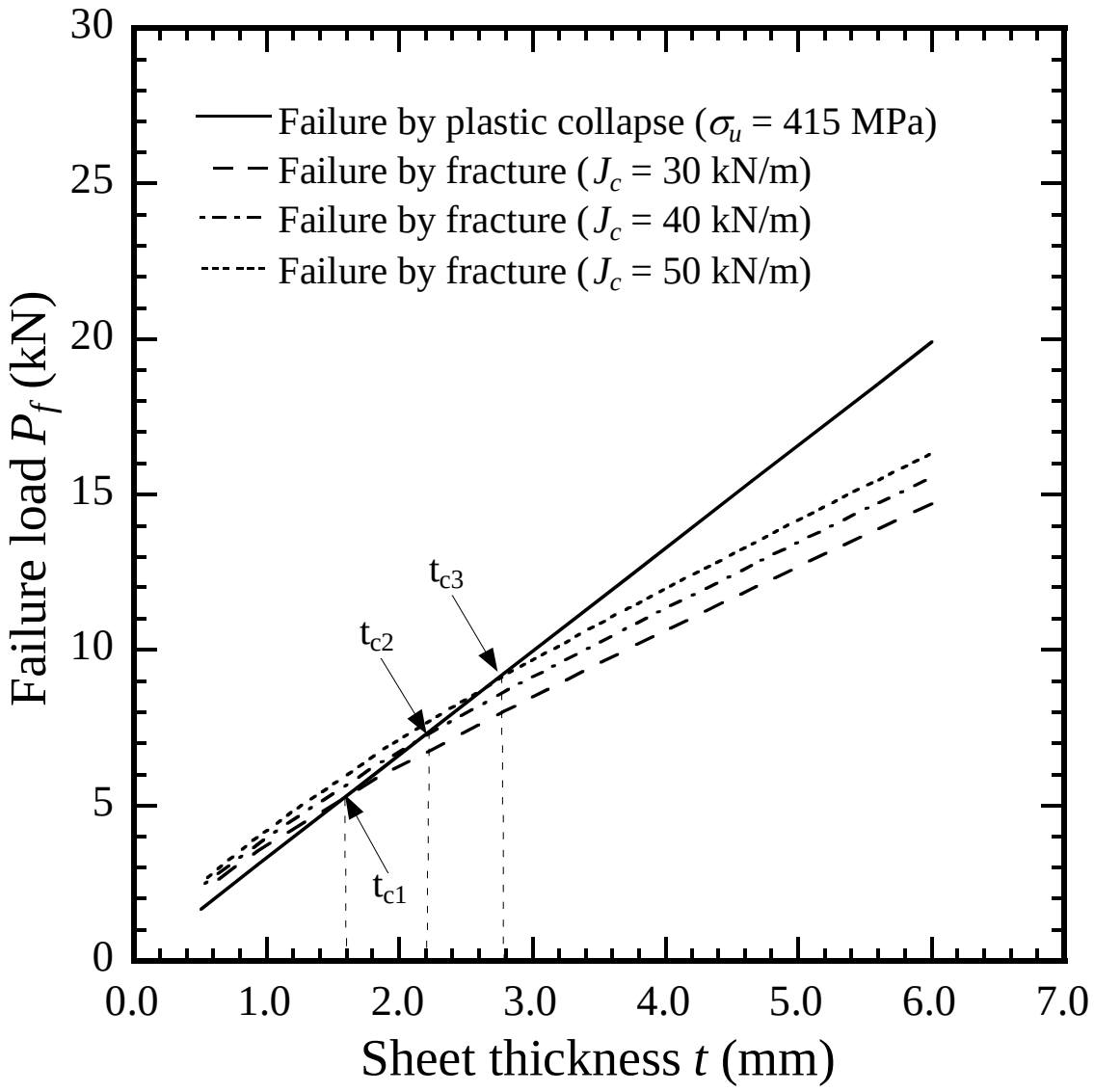

Figure 2.18. The values of the failure load P_f as functions of the sheet thickness t for different values of J_c.

References

[1] Hsu C, Albright CE. Fatigue analysis of laser welded lap joints. Engineering Fracture Mechanics 1991; 39: 575-580.

[2] Wang PC, Ewing KM. A comparison of fatigue strengths: Laser beam vs. resistance spot welds. Welding Journal 1991; 70: 43-47.

[3] Flavenot JF, Deville JP, Diboine A, Cantello M, Gobbi SL. Fatigue resistance of laser welded lap joints of steel sheets. Welding World 1993; 31: 12-15.

[4] Wang PC, Ewing KM. Effect of process parameters on the fatigue strength of laser beam welds. Journal of Laser Applications 1994; 6: 14-22.

[5] Terasaki T, Sobue T, Kitamura T. Study of fatigue strength of laser welded lap joint. Quarterly Journal of the Japan Welding Society 2001; 19: 507-512.

[6] Kaitanov A Yu, Ozersky AD, Zabelin AM, Kislov VS. Static and fatigue strengths of laser welded overlap joints with controlled penetration. Procedings of SPIE 2002; 4644: 116-126.

[7] Cho SK, Yang YS, Son KJ, Kim JY. Fatigue strength in laser welding of the lap joint. Finite Element Analysis and Design 2004; 40: 1059-1070.

[8] Sripichai K, Asim K, Pan J. Stress intensity factor solutions for estimation of fatigue lives of laser welds in lap-shear specimens. Submitted for publication in Engineering Fracture Mechanics 2010.

[9] Asim K, Sripichai K, Pan J. Fatigue behavior of laser welds in lap-shear specimens of high strength low alloy steel sheets. Submitted for publication in International Journal of Fatigue 2011.

[10] Ono M, Kabasawa M, Omura M. Static and fatigue strength of laser-welded lap joints in thin steel sheet. Welding International 1997; 11: 462-467.

[11] Chien WY, Friedman PA, Pan J. Failure prediction of aluminum laser-welded blanks. International Journal of Damage Mechanics 2003; 12: 193-223.

[12] Taban E, Deleu E, Dhooge A, Kaluc E. Laser welding of modified 12% Cr stainless steel: Strength, fatigue, toughness, microstructure and corrosion properties. Materials and Design 2009; 30: 1193-1200.

[13] Casavola C, Pappalettere C, Tattoli F. Experimental and numerical study of static and fatigue properties of titanium alloy welded joints. Mechanics of Materials 2009; 41: 231-243.

[14] Lee J, Asim K, Pan J. Modeling of failure mode of laser welds in lap-shear specimens of HSLA steel sheets. Engineering Fracture Mechanics 2011; 78: 374-396.

[15] Anand D, Chen DL, Bhole SD, Anderychuk P, Bourdeau G. Fatigue behavior of tailor (laser)-welded blanks for automotive applications. Materials Science and Engineering 2006; A 420: 199-207.

[16] Sripichai K, Asim K, Jo WH, Pan J, Li M. Fatigue behavior of laser welds in lap-shear specimens of high strength low alloy (HSLA) steels. SAE Technical Paper No. 2009-01-0028. Society of Automotive Engineers, Warrendale, PA: 2009.

[17] Mei L, Chen G, Jin X, Zhang Y, Wu Q. Research on laser welding of high strength galvanized automobile steel sheets. Optics Lasers Engineering 2009; 47: 1117-1124.

[18] Radaj D, Zhaoyun Z, Möhrmann W. Local stress parameters at the weld spot of various specimens. Engineering Fracture Mechanics 1990; 37: 933-951.

[19] Wang PC. Fracture mechanics parameter for the fatigue resistance of laser welds. International Journal of Fatigue 1995; 17: 25-34.

[20] Rice JR. A path independent integral and the approximate analysis of strain concentration by notches and cracks. Journal of Applied Mechanics 1968; 35: 379-386.

[21] ABAQUS v6.7 User Manual (2007). Providence, RI: SIMULIA.

[22] Wang Y, Pan J. Development of a multiaxial fatigue theory by considering constraint effects on small mixed mode cracks. International Journal of Solids and Structures 1999; 36: 4543-4562.

CHAPTER III

FATIGUE BEHAVIOR OF LASER WELDS IN LAP-SHEAR SPECIMENS OF HIGH STRENGTH LOW ALLOY STEEL SHEETS

3.1. Introduction

Laser welding offers many advantages over the conventional welding methods. These advantages include relatively low distortions of the weld, narrow heat affected zone, relatively high welding speed and high penetration. Over the past two decades, extensive research efforts have been spent on studying the fatigue behavior of laser welds for different materials and joint configurations. Lap joints have been commonly used to assess the strength and fatigue behavior of laser welds under shear dominant loading conditions. The geometry of a lap joint provides pre-existing cracks or notches at the edges of the weld bead. Therefore, the fatigue cracks were usually observed to be initiated from these stress concentration sites. Hsu and Albright [1] combined a static stress analysis and Neuber's rule to predict the fatigue lives of laser welded lap joints. Wang and Ewing [2] compared the fatigue strengths of laser welds and resistance spot welds in lap-shear specimens of steel sheets on the basis of equal weld volume. They reported that the fatigue failure in laser welds is dominated by crack propagation in the heat affected zone. Flavenot et al. [3] performed an experimental study to examine the influence of laser beam type, weld bead geometry, gap between the sheets and the input energy on the fatigue behavior of laser welded lap joints. Wang [4] correlated the experimental fatigue lives of laser welds in lap-shear specimens with the values of the J

integral obtained from finite element analyses. The results were also used to assess the influence of parameters such as the weld geometry, sheet thickness, bead width, metal fit-up and bead length. Ono et al. [5] investigated the static and fatigue strengths of laser welded lap joints of thin steel sheets and correlated the fatigue lives of laser welded lap joints with the maximum stress intensity factor ranges.

Terasaki et al. [6] examined the fatigue lives of laser welded lap joints and correlated the experimental results by the stress intensity factor solutions. Zhang [7] proposed structural stress solutions based on the outer surface strains of laser welded lap joints. Kaitanov et al. [8] conducted experiments to determine the static and fatigue strengths of laser welded lap joints of steel sheets with different weld widths and penetration depths. They found that the weld width affects the fatigue strength of laser welds. Cho et al. [9] examined the fatigue strength of laser welded lap joints with the consideration of residual stresses obtained from thermo-mechanical finite element analyses. Sripichai et al. [10] recently investigated the fatigue behavior of laser welds in lap-shear specimens of high strength low alloy steel sheets based on the closed-form and computational stress intensity factor solutions.

In this study, the fatigue behavior of laser welds in lap-shear specimens of non-galvanized SAE J2340 300Y HSLA steel sheets is investigated based on experimental observations and two fatigue life estimation models. Optical micrographs of the welds before and after failure under quasi-static and cyclic loading conditions are examined to investigate the microstructure and failure mechanisms of the welds. Scanning electron micrographs of the failure surfaces are also used to explain the failure modes of laser welds in lap-shear specimens under quasi-static and cyclic loading conditions. Finite

element analyses of the laser welded lap-shear specimens with consideration of the weld bead protrusion were carried out to obtain the global and local stress intensity factor solutions for the main cracks and kinked cracks, respectively. The stress intensity factor solutions are used to explain the kinked fatigue crack growth patterns under high-cycle loading conditions. A kinked fatigue crack growth model based on the global and local stress intensity factor solutions for finite kinked cracks obtained from the finite element analyses and a structural stress model based on the closed-form structural stress solutions of the beam bending theory are adopted to estimate the fatigue lives of the laser welds. Finally, the estimated fatigue lives based on the kinked fatigue crack growth model and the structural stress model are compared with the experimental results.

3.2. Experiment

HSLA steel sheets with a thickness of 0.93 mm were used in this investigation. The mechanical properties obtained from the tensile tests of the HSLA steel sheets are already listed in Table 2.2. The sheets were welded using CO_2 laser with an output power of 6KW. The laser beam was held stationary while the sheets were moved at a speed of 8 m/min in the welding direction. Helium was used as the shielding gas with a discharge rate of 20 ℓ/min. The laser beam parameters are listed in Table 3.1. The welded sheets were then sheared into 27 mm wide strips with a length of 275 mm. These sheet strips were machined into specimens with a dog-bone shaped profile using a CNC milling machine according to the guidelines provided in the ANSI/AWS B4.0:2007 standard for mechanical testing of welds and the ASTM E466-07 standard for conducting force controlled constant amplitude axial fatigue tests of metallic materials. After

machining, the specimen edges were manually smoothed by using 1200 grit coarse polishing papers. This was done to remove any notches or irregularities along the edges which may produce stress concentration sites. Figures 3.1(a) and 3.1(b), again, show the top and bottom views of a laser welded lap-shear specimen, respectively.

The geometry of the specimen was chosen to avoid failure due to the necking of the sheets far from the weld zone and to allow an investigation of the failure mechanism in the vicinity of the laser weld. Specimens with similar shapes were used for the study of laser welded joints, for example, see, Anand et al. [11] and Sripichai et al. [10]. Figure 3.2, again, shows a schematic of a lap-shear specimen. As shown in the figure, the specimen has a width W, sheet thickness t, and length L for the upper and lower sheets. The specimen has a width b and a length c for the central portion of the specimen, an overlap length V, and a width w for the weld zone, which is indicated as the shaded region in the figure. Two doublers were used to align the applied load to avoid the initial realignment of the specimen under lap-shear loading conditions. The doublers have a length s and a width W. The detailed dimensions of the lap-shear specimen are the same as listed in Table 2.1. The loading direction is indicated by two bold arrows on the left and right sides of the specimen in the schematic. Same types of arrows are used to indicate the loading directions in the subsequent figures.

Figure 3.3(a) shows an optical micrograph of the etched cross section of a laser weld in lap-shear specimen perpendicular to the welding direction before testing. Based on their distinct grain structures, three separate regions can be identified from the micrograph, namely, the base metal with equiaxed fine grains, the heat affected zone (HAZ) with fine and coarse grains, and the fusion zone with columnar grains. The width

of the fusion zone, as seen from the micrograph in Figure 3.3(a), is about 0.80 mm along the middle surface of the weld between the two pre-existing cracks. The width of the HAZ, as shown in the micrograph in Figure 3.3(a), is about 0.05 to 0.17 mm on both sides of the fusion zone from the top to the bottom of the weld. The two pre-existing cracks which are formed by joining the two steel sheets have been identified as N1 and N2 in Figure 3.3(a). Figure 3.3(b) shows a close-up view of the base metal with a fine grain microstructure. Figures 3.3(c) and 3.3(d) show close-up views of the left and right pre-existing crack tips, respectively. The tips of these cracks are located in the zone with both fine and coarse grains. These crack tips disappear in the fusion zone along the middle surface of the weld. The micrograph in Figure 3.3(a) also shows that the weld is free of porosities and other welding defects such as cracks and voids.

3.2.1. Quasi-static test of lap-shear specimen

Lap-shear specimens were first tested under quasi-static loading conditions by using an automated MTS testing machine equipped with a load cell and a built-in position sensor to track the movement of the cross-head. The cross-head speed was maintained constant at 1 mm/min during these tests. The load and displacement histories were simultaneously recorded during each test. The average failure or maximum load, defined as the average of the maximum loads of the load-displacement curves obtained from the quasi-static tests of five lap-shear specimens, is about 3.1 kN. This failure load was used as the reference load to determine the applied load ranges in the fatigue tests. The average maximum displacement obtained from these tests was about 2.16 mm. The

average failure load and displacement were used as the reference values to set the machine loading limits for the fatigue tests.

The tested specimens were sectioned perpendicular to the welding direction and prepared for micrographic analyses. A detailed study of the failure mechanism of HSLA lap-shear specimens under quasi-static loading conditions based on the micrographs and finite element analyses was reported in [12, 13]. In the present study, the micrographs of the cross sections of failed specimens under quasi-static loading conditions are presented for comparison of the failure mechanisms of the lap-shear specimens under quasi-static and cyclic loading conditions.

3.2.2. Fatigue test of lap-shear specimen

Lap-shear specimens were tested under cyclic loading conditions by using an Instron servo-hydraulic fatigue testing machine with the load ratio $R = 0.2$. A sinusoidal loading profile was chosen and its frequency was set at 10 Hz during the tests. The test was considered to be completed at the final separation of the welded sheets. A few tests were interrupted before the final separation to study the fatigue crack growth patterns. Life cycles to failure were recorded for different applied load ranges. A plot of the load range versus the fatigue life in a log-log scale is shown in Figure 3.4. The fatigue tests were terminated when specimens were subjected to one million loading cycles without separation and recorded as a run-off. Note that two specimens tested at the load ranges of 0.69 kN and 0.70 kN were marked as run-off although the threshold of one million life cycles was not reached. These two tests were interrupted at 1.86×10^5 and 2.6×10^5 cycles, respectively, to study the fatigue crack growth patterns under these load ranges.

However, no fatigue crack was observed in the micrographs of the cross-sections of the two specimens at these life cycles and load ranges. It is expected that the specimens would have crossed the threshold of one million life cycles under these load ranges and hence marked as run-off. The specimens failed under cyclic loading conditions were sectioned perpendicular to the weld direction using a low speed diamond wheel saw and prepared for micrographic analyses. Etching of the cross-sections was carried out using a 5% Nital solution. The failure surfaces of the failed specimens were also examined under a scanning electron microscope. These scanning electron micrographs provided additional information about the failure mode and crack propagation in lap-shear specimens under different load ranges. The optical micrographs of the cross sections and the scanning electron micrographs of the failure surfaces are presented in the following section.

3.3. Failure modes of laser welds under quasi-static and cyclic loading conditions

Experiments were conducted for laser welds in lap-shear specimens under quasi-static and cyclic loading conditions. The experimental observations indicate that the laser welds failed through the lower left sheets under quasi-static loading conditions and under cyclic loading conditions with the fatigue lives less than 10^4 cycles (low-cycle loading conditions). The laser welds failed through the upper right sheets under cyclic loading conditions with the fatigue lives from about 10^4 cycles to about 6×10^4 cycles (high-cycle loading conditions with high load ranges) and above 6×10^4 cycles (high-cycle loading conditions with low load ranges). The amount of plastic deformation in the load carrying sheets under high-cycle loading conditions with low load ranges is considerably less than

that observed under high-cycle loading conditions with high load ranges. The results of the present study show that laser welds failed in the base metal under quasi-static loading conditions and in the HAZ under cyclic loading conditions. The failure mode of laser welds in lap-shear specimens depends on the applied load ranges, and the failure location can change from the lower left sheet under low-cycle loading conditions to the upper right sheet under high-cycle loading conditions. Note that the definitions of low-cycle and high cycle fatigue loading conditions in this study are only provided for convenient presentation. In order to explain the change of the failure mode, a discussion of the micrographs of partially failed and failed laser welds under different load ranges is first presented in the following.

3.3.1. Failure mode under quasi-static (QS) loading conditions

Figures 3.5(a) and 3.5(b) show optical micrographs of the etched cross sections of a partially failed weld and a failed weld in lap-shear specimens under quasi-static loading conditions, respectively. The upper right and lower left sheets were the two load carrying sheets in these tests. The loading direction is schematically shown by the bold arrows in Figures 3.5(a) and 3.5(b). The dominant failure mode of the lap-shear specimens under quasi-static loading conditions is the necking/shear of the lower left sheet. The ductile failure was initiated in the base metal near the boundary of the base metal and HAZ as shown in Figure 3.5(a). The lower left sheet was then separated from the weld as shown in Figure 3.5(b). Figure 3.6(a) shows a scanning electron micrograph of the failure surface of the lower left sheet of a failed specimen under quasi-static loading conditions. The white vertical arrow in the micrograph indicates the crack propagation direction from

the inner surface toward the outer surface of the lower left sheet. Note that white vertical arrows in all the scanning electron micrographs indicate the crack propagation direction. Three distinct regions A, B and C can be identified and are marked on the failure surface in the figure. Region A of the failure surface in Figure 3.6(a) shows a fracture surface with large and small dimples. A close-up view of a portion of region A of the failure surface is shown in Figure 3.6(b). This region of the failure surface corresponds to a ductile fracture of void nucleation, growth and coalescence. Region B of the failure surface in Figure 3.6(a) shows a fracture surface with small elongated dimples. Region B of the failure surface corresponds to a shear dominant failure mode. A close-up view of a portion of the transition region between regions A and B is shown in Figure 3.6(c). Region C of the failure surface in Figure 3.6(a) shows a flat and cleavage fracture surface. The flat and cleavage fracture surface corresponds to the final failure of the sheet that took place in this region. A close-up view of a portion of this region is shown in Figure 3.6(d).

The results of the finite element analyses [12] show that the failure in lap-shear specimens under quasi-static loading conditions occurs in the lower left sheet due to the inhomogeneous material properties of the weld area and the geometry of the weld bead protrusion. The failure of the laser welds in lap-shear specimens is due to the large plastic strains in the material elements of the base metal located near the boundary of the base metal and HAZ and, finally, the necking/shear of the sheet. The weld bead protrusion imposes an additional geometric constraint to the lower left sheet and therefore, the plastic strains and the void volume fractions are larger for the material elements in the base metal near the boundary of the base metal and HAZ on the inner

surface of the lower left sheet, compared with those of the upper right sheet. Therefore, the welds failed through the lower left sheets. In summary, the laser welds mainly fail from the necking/shear of the lower left sheet and the failure is initiated at a distance from the pre-existing crack tips under quasi-static loading conditions. For a total of eight quasi-static tests, all the failures were observed to occur through the lower left sheets near the weld bead protrusion.

3.3.2. Failure mode under low-cycle (LC) loading conditions

Figures 3.7(a) and 3.7(b) show optical micrographs of the etched cross sections of a partially failed weld at the fatigue life of 6.47×10^3 cycles and a failed weld at the fatigue life of 8.6×10^3 cycles under a load range of 1.99 kN, respectively. The upper right and lower left sheets were the two load carrying sheets in these tests. The loading direction is schematically shown by the bold arrows in Figures 3.7(a) and 3.7(b). The lap-shear specimen with the partially failed weld was subjected to the same load range as the lap-shear specimen with the failed weld. However, the test for the lap-shear specimen with the partially failed weld was terminated at about 75% of the fatigue life of the lap-shear specimen with the failed weld under the same load range to examine the fatigue crack growth pattern before the final failure. The same notation will be followed for the other figures presented later. Figure 3.7(a) shows two kinked fatigue cracks emanating from the pre-existing crack tips. The length of the kinked fatigue crack in the upper right sheet appears to be longer than that of the kinked fatigue crack in the lower left sheet. Figure 3.7(b) shows the necking of the failed lower left sheet and a large weld rotation.

These features are quite similar to those shown in Figure 3.5(b) for the failed weld under quasi-static loading conditions.

Figure 3.8(a) shows a scanning electron micrograph of the failure surface of the lower left sheet of a failed specimen at the fatigue life of 5.44×10^3 cycles under a load range of 2.11 kN. The white vertical arrow in the micrograph indicates the crack propagation direction from the inner surface toward the outer surface of the lower left sheet. Three distinct regions A, B and C are identified and marked on the failure surface in the figure. Region A of the failure surface in Figure 3.8(a) is mainly characterized by large and small dimples. A close-up view of a portion of region A of the failure surface is shown in Figure 3.8(b). The micrograph indicates that the fatigue failure mechanism is still void nucleation, growth and coalescence as those under quasi-static loading conditions. Region B of the failure surface in Figure 3.8(a) exhibits a fracture surface with small elongated dimples. A close-up view of a portion of region B of the failure surface is shown in Figure 3.8(c). This portion of the failure surface indicates a shear dominant failure mode before the final failure of the sheet. Region C of the failure surface in Figure 3.8(a) shows a flat fracture surface. A close-up view of a portion of this region is shown in Figure 3.8(d). The flat fracture surface corresponds to the final failure of the sheet.

As shown in Figure 3.7(b), the dominant failure mode for the specimens under low-cycle loading conditions appears to be the through-thickness crack propagation and necking of the lower left sheet. This type of failure mode corresponds to the applied load ranges greater than 1.90 kN and the fatigue lives less than 10^4 cycles as indicated in Figure 3.4. In summary, the laser welds mainly fail from the through-thickness crack

propagation and necking of the lower left sheet under low-cycle loading conditions. The failure is most likely initiated from the pre-existing crack tips, in contrast to that under quasi-static loading conditions. A total of three specimens were tested to a complete separation failure under these load ranges and they all exhibited the same failure mode.

3.3.3. Failure mode under high-cycle loading conditions with high load ranges (HCHL)

Figures 3.9(a) and 3.9(b) show optical micrographs of the etched cross sections of a partially failed weld at the fatigue life of 1.02×10^4 cycles and a failed weld at the fatigue life of 1.45×10^4 cycles under a load range of 1.65 kN, respectively. The loading direction is schematically shown by the bold arrows in Figures 3.9(a) and 9(b). In Figure 3.9(a), two kinked fatigue cracks appear to emanate from the pre-existing crack tips and propagate into the upper right and lower left sheets. However, the length of the kinked fatigue crack in the upper right sheet is longer than that of the kinked fatigue crack in the lower left sheet. It will be shown later that the presence of the round weld bead protrusion on the outer surface of the lower left sheet lowers the global and local stress intensity factor solutions of the main crack and the kinked crack, respectively, corresponding to the lower left sheet as compared to those corresponding to the upper right sheet. This in turn provides a more favorable condition for the kinked fatigue crack propagation in the upper right sheet as compared to that for the lower left sheet. Figure 3.9(b) shows the etched cross section of a failed weld after the separation of the upper right sheet from the weld. This failure mode is different from that observed under low-cycle loading conditions as discussed earlier. Note that the fatigue crack propagated into the upper sheet thickness in the HAZ to about the middle of the sheet thickness and then

propagated into the fusion zone close to the boundary of the HAZ due to the fast fracture of the final stage of the specimen failure.

In Figure 3.9(b), the necking/shear can also be observed for the lower left sheet due to large plastic deformation. The kinked fatigue crack in the lower left sheet did not propagate through the lower left sheet. Another round notch can also be observed on the outer surface of the lower left sheet near the weld bead protrusion due to the weld rotation under lap-shear loading conditions. This weld rotation caused the relatively rigid weld bead protrusion to compress the material near the outer surface of the lower left sheet and created a notch as shown in Figure 3.9(b). However, the presence of this notch near the weld bead protrusion does not result in the final failure and separation of the lower left sheet.

Figure 3.10(a) shows a scanning electron micrograph of the failure surface of the upper right sheet of a failed specimen at the fatigue life of 1.08×10^4 cycles under a load range of 1.64 kN. The white vertical arrow in the micrograph indicates the crack propagation direction from the inner surface toward the outer surface of the upper right sheet. Three distinct regions A, B and C can be identified and are marked on the failure surface in the figure. Region A of the failure surface is mainly characterized by large and small dimples. A close-up view of a portion of region A of the failure surface is shown in Figure 3.10(b). As shown in Figure 3.10(b), the failure in this region is due to void nucleation, growth and coalescence. Region B of the failure surface in Figure 3.10(a) shows small elongated dimples which indicate a shear dominant failure mode. Region C shows a flat cleavage fracture surface. The flat fracture surface indicates the final failure of the sheet. A close-up view of a portion of the transition region between region B and

region C is shown in Figure 3.10(c). Small elongated dimples are visible in the lower part of Figure 3.10(c) and flat fracture surface is shown on the upper part of Figure 3.10(c).

The dominant failure mode for the specimens under high-cycle loading conditions with high load ranges appears to be the through-thickness crack propagation in the upper right sheet. This type of failure mode corresponds to the applied load ranges between 1.10 kN and 1.90 kN and the fatigue lives between 1.0×10^4 cycles and 6.0×10^4 cycles as indicated in Figure 3.4. In summary, the laser welds mainly fail due to the kinked fatigue crack emanating from the right pre-existing crack tip and propagating through the upper right sheet thickness under high-cycle loading conditions with high load ranges. A total of sixteen specimens were tested to a complete separation failure under these load ranges and they all exhibited the same failure mode.

3.3.4. Failure mode under high-cycle loading conditions with low load ranges (HCLL)

Figures 3.11(a) and 3.11(b) show optical micrographs of the etched cross sections of a partially failed weld at the fatigue life of 1.09×10^5 cycles and a failed weld at the fatigue life of 1.65×10^5 cycles under a load range of 0.82 kN. The loading direction is schematically shown by the bold arrows in Figures 3.11(a) and 3.11(b). It should be mentioned that although it was intended to stop the test of the specimen with the partially failed weld shown in Figure 3.11(a) at 75% of the fatigue life of the specimen with a failed weld shown in Figure 3.11(b), it appears from the micrograph for the partially failed specimen shown in Figure 3.11(a) that the specimen was close to a complete failure at the time that the test was interrupted. However, the micrograph shown in

Figure 3.11(a) is still helpful to explain the fatigue crack growth pattern. In Figure 3.11(a), two kinked fatigue cracks emanated from the pre-existing crack tips and propagated into the upper right and lower left sheets. However, the length of the kinked fatigue crack in the upper right sheet is much larger than that of the kinked fatigue crack in the lower left sheet. The right kinked fatigue crack has almost propagated through the thickness of the upper right sheet whereas the left kinked fatigue crack in the lower left sheet has been blunted into a notch. As mentioned earlier, the partially failed weld as shown in Figure 3.11(a) appears to be close to the final failure. The failure mode seems to be similar to that under high-cycle loading conditions with high load ranges. However, no visible necking is observed for the upper right and lower left sheets under this load range.

The more favorable path for the kinked fatigue crack propagation appears to be through the upper right sheet under these load ranges for the same reason as mentioned in the previous section. Figure 3.11(b) shows that the kinked fatigue crack has propagated through the thickness of the upper right sheet. However, at a distance close to the outer surface of the upper right sheet, the kinked fatigue crack seems to propagate in the fusion zone close to the boundary of the HAZ. This is similar to the behavior of the kinked fatigue crack propagation under high-cycle loading conditions with high load ranges. Figure 3.12(a) shows a scanning electron micrograph of the failure surface of the upper right sheet of a failed specimen at the fatigue life of 1.65×10^5 cycles under a load range of 0.82 kN. The white vertical arrow in the micrograph indicates the crack propagation direction from the inner surface toward the outer surface of the upper right sheet. Three distinct regions A, B and C can also be identified and are marked in the failure surface in

the figure. Region A of the failure surface is mainly characterized by large and small dimples, tearing ridges and inconspicuous striations. Two close-up views of portions of region A of the failure surface in Figure 3.12(a) are shown in Figures 3.12(b) and 3.12(c). This region corresponds to the kinked fatigue crack propagation and spans about 85% of the sheet thickness. Region B of the failure surface is mainly characterized by small elongated dimples that indicate a shear fracture mode. A close-up view of a portion of the transition region between regions A and B is shown in Figure 3.12(d). Region C of the failure surface is characterized by a flat fracture surface that indicates that the final failure took place in this region due to the loss of load carrying capability of the sheet. The span of region C is quite small for this case. A close-up view of a portion of the transition region between regions B and C is shown in Figure 3.12(e).

The dominant failure mode for the specimens under high-cycle loading conditions with low load ranges appears to be the through-thickness crack propagation in the upper right sheet. This type of failure mode corresponds to the applied load ranges less than about 1.0 kN and the fatigue lives more than 6.0×10^4 cycles as indicated in Figure 3.4. In summary, the laser welds mainly fail due to the kinked fatigue crack emanating from the right pre-existing crack tip and propagating through the upper right sheet thickness with very limited plastic deformation under high-cycle loading conditions with low load ranges. A total of six specimens were tested to complete sheet separation failure under these load ranges and they all exhibited the same failure mode. For load ranges less than 0.81 kN, the laser welds of the given HSLA steel sheets appear to exceed one million life cycles to failure.

3.4. Global and local stress intensity factor solutions

Here, the stress intensity factor solutions of the pre-existing cracks and the kinked fatigue cracks are developed in order to explain the change of the failure from the lower left sheets to the upper right sheets when the applied load range decreases. Also, the stress intensity factor solutions are used to correlate with the fatigue lives of the experiments. Sripichai et al. [14] developed closed-form global stress intensity factor solutions for idealized laser welds (without weld bead protrusion) in lap-shear specimens based on the beam bending theory, Westergaaard function and finite element analyses. For the laser welds in lap-shear specimens with the ratio of weld width to sheet thickness, w/t, of 0.86 in this investigation, the approximate global stress intensity factor solutions in [14] are

$$K_{\mathrm{I}} = \frac{\sqrt{3}}{2}\frac{F}{b\sqrt{t}}\frac{w}{2t} \tag{1}$$

$$K_{\mathrm{II}} = \frac{F}{b\sqrt{t}} \tag{2}$$

Figure 3.13 shows a schematic of a main crack and a kinked crack with the kink length a and the kink angle α. Here, K_{I} and K_{II} represent the global stress intensity factors for the main crack, and k_{I} and k_{II} represent the local stress intensity factors for the kinked crack. Note that the arrows in the figure represent the positive values of K_{I}, K_{II}, k_{I} and k_{II} solutions. For kinked cracks, when the kink length approaches to 0, the k_{I} and k_{II} solutions can be expressed as functions of the kink angle α and the global K_{I} and K_{II} for the main crack. The local stress intensity factor solutions for kinked cracks with vanishing crack length are given as [15, 16]

$$(k_{\mathrm{I}})_0 = \frac{1}{4}\left(3\cos\frac{\alpha}{2} + \cos\frac{3\alpha}{2}\right)K_{\mathrm{I}} - \frac{3}{4}\left(\sin\frac{\alpha}{2} + \sin\frac{3\alpha}{2}\right)K_{\mathrm{II}} \quad (3)$$

$$(k_{\mathrm{II}})_0 = \frac{1}{4}\left(\sin\frac{\alpha}{2} + \sin\frac{3\alpha}{2}\right)K_{\mathrm{I}} + \frac{1}{4}\left(\cos\frac{\alpha}{2} + 3\cos\frac{3\alpha}{2}\right)K_{\mathrm{II}} \quad (4)$$

The local stress intensity factor solutions for kinked cracks with finite crack lengths for laser welds in lap-shear specimens can be expressed as functions of the normalized kink length a/t as in [14] as

$$k_{\mathrm{I}}(a) = f_{\mathrm{I}} \cdot (k_{\mathrm{I}})_0 \quad (5)$$

$$k_{\mathrm{II}}(a) = f_{\mathrm{II}} \cdot (k_{\mathrm{I}})_0 \quad (6)$$

where f_{I} and f_{II} are geometric functions which depend on the geometric parameters of the laser welded lap-shear specimens such as the weld width w and the sheet thickness t. The local stress intensity factor solutions for idealized laser welds in lap-shear specimens were obtained and presented in the normalized form in [14] for $w/t = 1$ and 2.

The fatigue lives were estimated based on Equations (1) and (2) and the local stress intensity factor solutions in Equations (5) and (6) for $w/t = 1$. The fatigue life estimations are in good agreement with the experimental results. However, the stress intensity factor solutions for idealized laser welds in lap-shear specimens in [14] cannot be used to explain the change of the fatigue crack growth pattern and the failure mode observed in the experiments as discussed earlier. Finite element analyses are therefore adopted to investigate the effects of the weld geometry on the stress intensity factor solutions.

Figure 3.14(a) shows a schematic of a two-dimensional finite element model of a lap-shear specimen with the boundary and loading conditions. Here, the shaded region

represents the weld zone. The specimen has the sheet thickness t, the length L, the overlap length V, and the weld width w. Both the upper right and lower left sheets have the same thickness t. The $x-y$ coordinate system is shown in the figure. The left edge has a fixed displacement condition at the middle surface while the right edge has a concentrated force per unit width, F/b, applied at the middle surface in the $+x$ direction. Here, F denotes the applied force and b denotes the width of the central portion of the specimen with the reduced width.

The two-dimensional plane-strain finite element model has the weld width $w =$ 0.8 mm, sheet thickness $t = 0.93$ mm, length $L = 95$ mm, and overlap length $V = 30$ mm. The width b of the central portion of the specimen is taken as 8 mm to calculate the applied load per unit width for the finite element analyses. The ratio of weld width to sheet thickness, w/t, is 0.86. Figure 3.14(b) shows a close-up view of the finite element mesh near the weld. The weld bead protrusion is modeled based on the geometry of the weld in Figure 3.3(a). Second-order quarter point crack-tip elements (CPE8R) with collapsed nodes were used to model the $1/\sqrt{r}$ singularity near the crack tip. The weld metal and the base metal are assumed to be linear elastic with the Young's modulus $E =$ 206 GPa and the Poisson's ratio $\nu = 0.3$. Computations were performed using the commercial finite element software ABAQUS [17].

The normalized computational global stress intensity factor solutions for the two pre-existing crack tips for models with and without weld bead protrusions are listed in Table 3.2. Note that the computational stress intensity factor solutions have been normalized by the analytical K_{II} solution in Equation (2). The results of the finite element analysis for the idealized weld without the weld bead protrusion give the same

$\overline{K}_{\mathrm{I}}$ and $\overline{K}_{\mathrm{II}}$ solutions for the two pre-existing crack tips. The results of the finite element analysis for the weld with the weld bead protrusion show that the $\overline{K}_{\mathrm{I}}$ and $\overline{K}_{\mathrm{II}}$ solutions are higher for the right pre-existing crack tip as compared to those for the left pre-existing crack tip. This indicates that the presence of the weld bead protrusion increases the $\overline{K}_{\mathrm{I}}$ and $\overline{K}_{\mathrm{II}}$ solutions for the right pre-existing crack tip and decreases those for the left pre-existing crack tip. The results can be used to explain the favorable condition for kinked fatigue crack propagation in the upper right sheets under high cycle loading conditions.

As observed from the micrographs of partially failed specimens, kinked fatigue cracks are initiated from the pre-existing crack tips and propagate through the sheet thickness of the upper right sheet under high cycle loading conditions. From the micrographs of the failed specimens, the kinked crack angle was found to be very close to $90°$ for all the load ranges. Figure 3.15(a) again shows a schematic of a two-dimensional finite element model of a lap-shear specimen with two kinked cracks and the boundary and loading conditions. The boundary and loading conditions of the specimen are the same as those for the finite element model shown in Figure 3.14(a). In Figure 3.15(a), the thin solid lines indicate the two kinked cracks. The kink angle in this investigation is selected to be $90°$. Ten normalized kink lengths, namely, $a/t = 0.025$, 0.05, 0.075, 0.1, 0.2, 0.3, 0.4, 0.5, 0.6, and 0.7 are considered in this investigation. Figure 3.15(b) shows a close-up view of the finite element mesh near the right kinked crack tip for $a/t = 0.2$.

Figure 3.16 shows the values of $k_{\mathrm{I}}/(k_{\mathrm{I}})_0$ for the kinked cracks emanating from the right and left per-existing crack tips as functions of the normalized kink length a/t for $w/t = 0.86$ and $\alpha = 90°$. The results of Sripichai et al. [14] for an idealized weld with

$w/t = 1$ and $\alpha = 90°$ are also shown for comparison. Note that the solutions are normalized by $(k_I)_0$ in Equation (3) with kink angle $\alpha = 90°$ and the analytical global stress intensity factor $(K_I)_B$ and $(K_{II})_B$ solutions based on the beam bending theory in [14]. The solutions in [14] based on the beam bending theory are

$$(K_I)_B = \frac{\sqrt{3}}{2}\frac{F}{b\sqrt{t}} \tag{7}$$

$$(K_{II})_B = \frac{F}{b\sqrt{t}} \tag{8}$$

Figure 3.16 shows that the values of $k_I/(k_I)_0$ increase monotonically with the kink length. However, it is also seen that the values of $k_I/(k_I)_0$ are higher for the kinked crack emanating from the right pre-existing crack tip as compared to those for the kinked crack emanating from the left pre-existing crack tip. The values in [14] agree well with those of $k_I/(k_I)_0$ for the kinked crack emanating from the right pre-existing crack tip. This indicates that the effects of weld width and weld bead protrusion are not significant on the k_I solutions for the kinked crack emanating from the right pre-existing crack tip for the value of w/t close to 1. However, the difference between the values of the local stress intensity factor solutions for the right and left kinked cracks explains the propensity of the kinked fatigue crack propagation in the upper right sheet under high-cycle loading conditions.

Figure 3.17 shows the values of $k_{II}/(k_I)_0$ for the kinked cracks emanating from the right and left per-existing crack tips as functions of the normalized kink length a/t for $w/t = 0.86$ and $\alpha = 90°$. The results of Sripichai et al. [14] for an idealized weld with

$w/t = 1$ and $\alpha = 90°$ are also shown for comparison. Note that the local stress intensity factor k_{II} solutions are negative based on the definitions shown in Figure 3.13. Figure 3.17 shows that the absolute values of $k_{II}/(k_I)_0$ decrease monotonically with the kink length for the kinked crack emanating from the right pre-existing crack tip. The values in [14] agree well with those of $k_{II}/(k_I)_0$ for the kinked crack emanating from the right pre-existing crack tip. This again indicates that the effects of weld width and weld bead protrusion are not significant on the k_{II} solutions for the kinked crack emanating from the right pre-existing crack tip for the value of w/t close to 1. However, Figure 3.17 also shows that for the kinked crack emanating from the left pre-existing crack tip, the values of $k_{II}/(k_I)_0$ change sign from negative to positive at about the normalized kink length of $a/t = 0.4$, due to the effect of the weld bead protrusion. Figures 3.16 and 3.17 show that the kinked fatigue crack growth is under mixed mode I and II loading conditions with mode I being the dominant mode. Tables 3.3 and 3.4 list the normalized local stress intensity factor k_I and k_{II} solutions, respectively, for $w/t = 0.86$ and $\alpha = 90°$.

3.5. A structural stress model

The structural stress approach appears to be promising to estimate the fatigue lives of weld joints in thin sheets. Tran et al. [18, 19] recently used the closed-form analytical structural stress solutions for spot welds to estimate the fatigue lives of aluminum spot friction welds. The fatigue life estimations are in good agreement with the experimental results. In the present study, the structural stress solutions are based on the beam bending theory. The central portion of the lap-shear specimen with a reduced

width is modeled as two beams with connection. Figure 3.18(a) shows a schematic of a two-beam model under lap-shear loading conditions. The idealized weld is shown as the shaded region. Figure 3.18(b) shows a schematic of the two-beam model under an equivalent loading with the membrane force per unit width, F/b, and the bending moment per unit width, $Ft/2b$, applied at the middle surfaces of the upper and lower beams. Both the membrane force per unit width, F/b, and the bending moment per unit width, $Ft/2b$, contribute to the structural stress at the edge of the weld. The structural stress at the inner surface of the upper right sheet or the inner surface of the lower left sheet of the laser weld in a lap-shear specimen is

$$\sigma = \frac{4F}{bt} \tag{9}$$

Based on the structural stress ranges at the edge of the weld bead from Equation (9) and the experimental stress-life data of the HSLA steel, the fatigue lives of laser welds in lap-shear specimens can be estimated.

3.6. Fatigue life estimations

The local stress intensity factor k_{I} and k_{II} solutions as functions of the normalized kink length a/t can be obtained from the linear interpolation between the normalized local stress intensity factor k_{I} and k_{II} solutions obtained from the finite element analyses. The variations of the k_{I} and k_{II} solutions in the range of $0.7 < a/t < 1.0$ is assumed to be the same as those for $0.6 < a/t < 0.7$. The local and global stress intensity factor solutions obtained from the finite element analyses as expressed in Equations (5) and (6) and the experimentally observed kink angle of $90°$ are

used in a kinked fatigue crack growth model. The Paris law is adopted to describe the propagation of the kinked fatigue cracks emanating from the pre-existing crack tips of laser welds in lap-shear specimens. The Paris law is given as

$$\frac{da}{dN} = C\left(\Delta k_{\text{eq}}(a)\right)^m \tag{10}$$

where a is the kink length and N is the life or number of cycles. The material constants for ferrite-pearlite steels $C = 6.89\times10^{-9}\ \dfrac{\text{mm/cycle}}{\left(\text{MPa}\sqrt{\text{m}}\right)^{\text{m}}}$ and $m = 3$ [20] are used. Here, Δk_{eq} is the range of the equivalent stress intensity factor under mixed mode loading conditions. For the kinked fatigue crack growth model, the range of the equivalent stress intensity factor Δk_{eq} is given as

$$\Delta k_{\text{eq}}(a) = \sqrt{\Delta k_{\text{I}}(a)^2 + \gamma \Delta k_{\text{II}}(a)^2} \tag{11}$$

where γ is an empirical constant to account for the sensitivity of material to mode II loading conditions. The value of γ is taken as 1 here. The fatigue life N_f can be obtained numerically by integrating the Paris law in Equation (10) as

$$N_f = \frac{1}{C}\left[\int_0^{0.025t'}\left[\Delta k_{eq}(a)\right]^{-m} da + \int_{0.025t'}^{0.05t'}\left[\Delta k_{eq}(a)\right]^{-m} da + \ldots + \int_{0.70t'}^{t'}\left[\Delta k_{eq}(a)\right]^{-m} da\right] \tag{12}$$

here 0, 0.025, 0.05, 0.075, 0.10, 0.20,…, and 0.70 represent the values of the normalized kink length a/t where the computational local stress intensity factor solutions are available and t' is the crack growth distance $\left(= t/\sin\alpha\right)$. For $\alpha = 90°$, $t' = t$.

In this investigation, two kinked cracks of the same length emanating from both pre-existing crack tips are modeled in the finite element analyses to represent the kinked cracks in the laser weld as shown in the micrographs of partially failed specimens.

Usually, one kinked crack becomes dominant and results in the final failure of the specimen. Finite element analyses for a weld with single kinked crack of different kink lengths were also carried out. The results indicate that the effective local stress intensity factor ranges and then the fatigue lives are almost the same for the welds with single and two kinked cracks for a given normalized kinked crack length a/t. Note that the stress intensity factor solutions based on the model of two kinked cracks are also used to estimate the fatigue lives for kinked fatigue cracks emanating from the left pre-existing crack tips and propagating in the lower left sheets for low-cycle loading conditions.

Figure 3.19 shows the fatigue life estimations based on the kinked fatigue crack growth model in Equation (12) with the global and local stress intensity factor solutions from the finite element analyses, the fatigue life estimations based on the structural stress model in Equation (9) and the experimental results. The stress-life data for the SAE 300Y HSLA (with the yield strength of 315 MPa) used here were not available. Therefore, the stress-life data of SAE 950X (with the tensile yield strength of 350 MPa) provided by Dr. P. Friedman were used here in the structural stress model. It should be noted that the fatigue lives of laser welds based on the kinked fatigue crack growth model are plotted as thick and thin solid lines that correspond to the estimated fatigue lives under low-cycle and high-cycle loading conditions, respectively. The fatigue lives under low-cycle loading conditions were estimated based on the local stress intensity factor solutions for the kinked cracks emanating from the left pre-existing crack tips and propagating in the lower left sheets. The fatigue lives under high-cycle loading conditions were estimated based on the local stress intensity factor solutions for the kinked cracks emanating from the right pre-existing crack tips and propagating in the

upper right sheets. The fatigue life estimations based on the idealized laser weld model in Sripichai et al. [14] with two kinked fatigue cracks are also included in Figure 3.19 for comparison. The fatigue life estimations based on the kinked fatigue crack growth model in Equation (12) with the global and the local stress intensity factor solutions from finite element analyses are in good agreement with the experimental results. For the three fatigue tests with the load ranges less than 0.8 kN, the specimens did not fail. The values of the effective stress intensity factor range ΔK_{eff} obtained from the finite element analyses are less than 4 $\mathrm{MPa}\sqrt{\mathrm{m}}$ for the right pre-existing crack tips. The values of the ΔK_{th} for low alloy steels with $R = 0.2$ are about 5.8 $\mathrm{MPa}\sqrt{\mathrm{m}}$ [20]. It is possible that the values of ΔK_{eff} under mixed mode loading conditions are less than the threshold values of ΔK_{eff} for this HSLA steel. Therefore, fatigue cracks were not initiated under these load ranges. Therefore, a horizontal dash-dotted line is plotted in Figure 3.19 as the fatigue limit based on the concept of fracture mechanics. The fatigue life estimations based on the structural stress model are in agreement with the experimental results under higher load ranges and are higher than the experimental results under lower load ranges. However, it is interesting to note that the trend for the increase of fatigue life estimation at low load ranges based on the structural stress model is somewhat consistent with that of the experimental results with consideration of the fatigue limit based on the existence of a threshold value of ΔK_{eff} .

3.7. Discussion

Estimations of the plastic zones size based on the linear elastic fracture mechanics (LEFM) were also carried out for different kinked fatigue crack lengths under various load ranges. Plastic zone sizes were determined using $2\sigma_o'$ with σ_o' as the initial cyclic yield strength of the base metal. The initial cyclic yield strength for the HAZ should be higher due to the higher hardness. Therefore, the estimations of plastic zone sizes should be conservative. The estimations of the plastic zone sizes vary from 2% to 10% of the sheet thickness as the kinked fatigue crack propagates to about 20% of the sheet thickness for a load range of 0.60 kN to 1.60 kN. It is interesting to note that most of the fatigue life cycles are spent for the kinked fatigue crack length to reach about 20% of the sheet thickness. The plastic zone sizes become more than 33% of the sheet thickness as the kinked fatigue crack length reaches 40% of the sheet thickness for load ranges above 1.90 kN. This means that under these load ranges, the plastic zones extend about more than the half of the remaining ligament of the sheet. This can be used to explain the similarity of the failure modes under quasi-static loading conditions and low-cycle loading conditions under load ranges greater than 1.90 kN as discussed earlier. It is likely that the failure mechanisms similar to the ones observed under quasi-static loading conditions are dominant under low-cycle loading conditions and cause the failure of the lower left sheet by necking/shear instead of the failure through the upper right sheet by fatigue crack propagation.

Note that the structural stress solutions were used to estimate the stress intensity factor solutions at the critical locations of spot welds to correlate with the experimental results under cyclic loading conditions (Zhang [21, 22]). Note also that the effects of the

mean stress intensity factors on fatigue lives may not be significant at the load ratio R of 0.2 in this investigation. Therefore, the mean structural stress has not been considered in the structural stress model. Further investigation is needed to fully investigate the effects of the mean stress for the structural stress model. It is also noted that in this investigation, the residual stresses in the weld, HAZ and base metal are not considered for lack of any quantitative information on the residual stresses from the laser welding process. When the residual stress distributions are available, the stress intensity factor solutions due to the residual stresses can be considered for fatigue life estimations within the context of the linear elastic fracture mechanics as in Chien et al. [23].

3.8. Conclusions

In this paper, the fatigue behavior of laser welds in lap-shear specimens of non-galvanized SAE J2340 300Y high strength low alloy (HSLA) steel sheets is investigated based on experimental observations and two fatigue life estimation models. Optical micrographs of the laser welds before and after failure under quasi static and cyclic loading conditions are examined. The micrographs show that the failure modes of laser welds under quasi-static and cyclic loading conditions are different. Under quasi-static loading conditions, the weld failure appears to be initiated from the base metal near the boundary of the based metal and the heat affected zone at a distance to the pre-existing crack tip and the specimens fail due to the necking/shear of the lower left load carrying sheets. Under low-cycle loading conditions, the weld failure appears to be initiated from the pre-existing crack tips and the specimens finally fail from the ductile fracture through the lower left load carrying sheets. Under high-cycle loading conditions, the weld failure

appears to be initiated from the pre-existing crack tips and the specimens finally fail from the kinked fatigue crack propagating through the upper right load carrying sheets. Finite element analyses of the laser welded lap-shear specimens with consideration of the weld bead protrusion were carried out to obtain the global and local stress intensity factor solutions for the main cracks and kinked cracks, respectively. The stress intensity factor solutions can be used to explain the kinked fatigue crack growth patterns under high-cycle loading conditions. A kinked fatigue crack growth model based on the global and local stress intensity factor solutions for finite kinked cracks obtained from the finite element analyses and a structural stress model based on the closed-form structural stress solutions of the beam bending theory are adopted to estimate the fatigue lives of the laser welds. The fatigue life estimations based on the kinked fatigue crack growth model agree well with the experimental results of the welds whereas the fatigue life estimations based on the structural stress model agree with the experimental results under larger load ranges but are higher than the experimental results under smaller load ranges.

Acknowledgements

Partial support of this work by the National Science Foundation under Grant No. DMI-0456755 is greatly appreciated. The support of Dr. M. Li of TWB (Monroe, MI) to provide the laser welded specimens used in this investigation is also greatly appreciated. The support of Dr. P. Friedman of Ford is also acknowledged for providing the experimental stress-life data for SAE 950X HSLA steel.

Table 3.1. Laser beam parameters

Parameters	Values
Output power	6 kW
Laser output mode	TEM_{00}
Laser quality, M^2	3.3
Unfocused beam diameter	41 mm
Spot size diameter (theoretical)	0.27 mm
Focusing mirror focal length	250 mm
Shielding gas (Helium) discharge rate	20 ℓ/min
Welding speed	8 m/min

Table 3.2. The normalized computational global stress intensity factor $\overline{K}_{\mathrm{I}}$ and $\overline{K}_{\mathrm{II}}$ solutions for the right and left pre-existing crack tips.

		$\overline{K}_{\mathrm{I}}$	$\overline{K}_{\mathrm{II}}$
Model with weld bead protrusion	Right crack tip	0.327	1.088
	Left crack tip	0.321	1.016
Model without weld bead protrusion	-	0.361	1.057

Table 3.3 The normalized local stress intensity factor $k_I/(k_I)_0$ solutions for $w/t = 0.86$ and $\alpha = 90°$.

a/t	0.00	0.025	0.05	0.075	0.1	0.2	0.3	0.4	0.5	0.6	0.7
Right tip	0.929	1.493	1.707	1.883	2.062	2.791	3.671	4.885	6.727	9.820	15.762
Left tip	0.871	1.427	1.634	1.802	1.973	2.647	3.431	4.471	5.983	8.376	12.561

Table 3.4 The normalized local stress intensity factor $k_{II}/(k_I)_0$ solutions for $w/t = 0.86$ and $\alpha = 90°$.

a/t	0.00	0.025	0.05	0.075	0.1	0.2	0.3
Right tip	-0.366	-0.184	-0.166	-0.154	-0.145	-0.132	-0.123
Left tip	-0.345	-0.172	-0.151	-0.136	-0.124	-0.088	-0.039

Table 3.4 (continued).

a/t	0.4	0.5	0.6	0.7
Right tip	-0.105	-0.079	-0.049	-0.024
Left tip	0.053	0.217	0.515	1.120

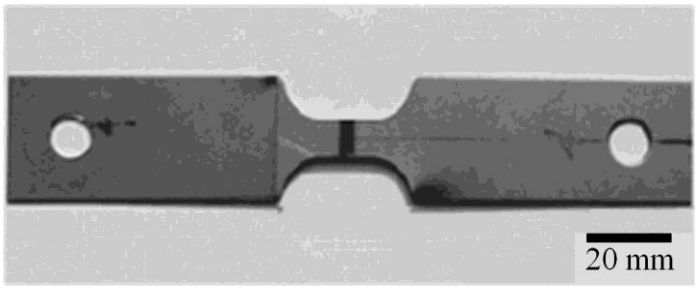

(a)

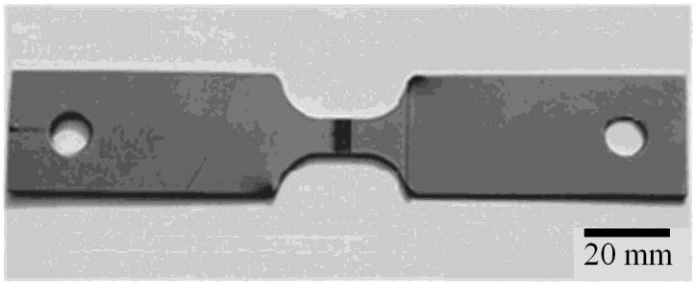

(b)

Figure 3.1. (a) A top view and (b) a bottom view of a laser welded lap-shear specimen.

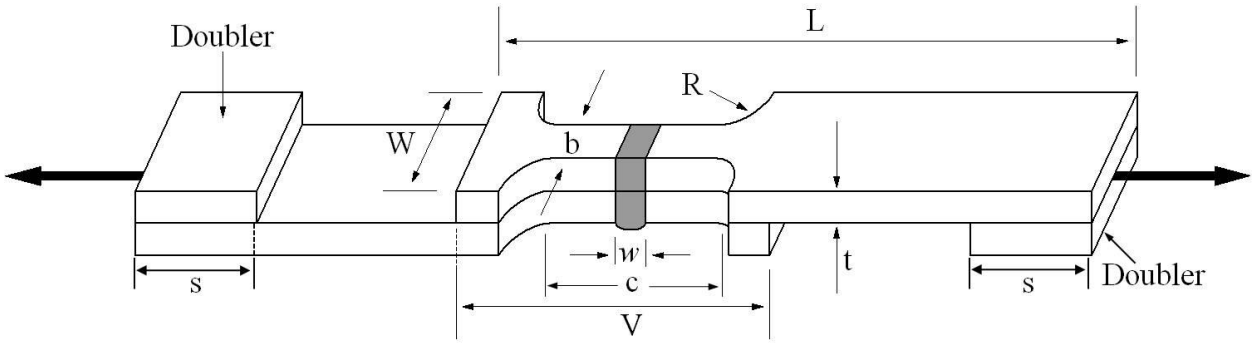

Figure 3.2. A schematic of a lap-shear specimen with the loading directions shown as the bold arrows.

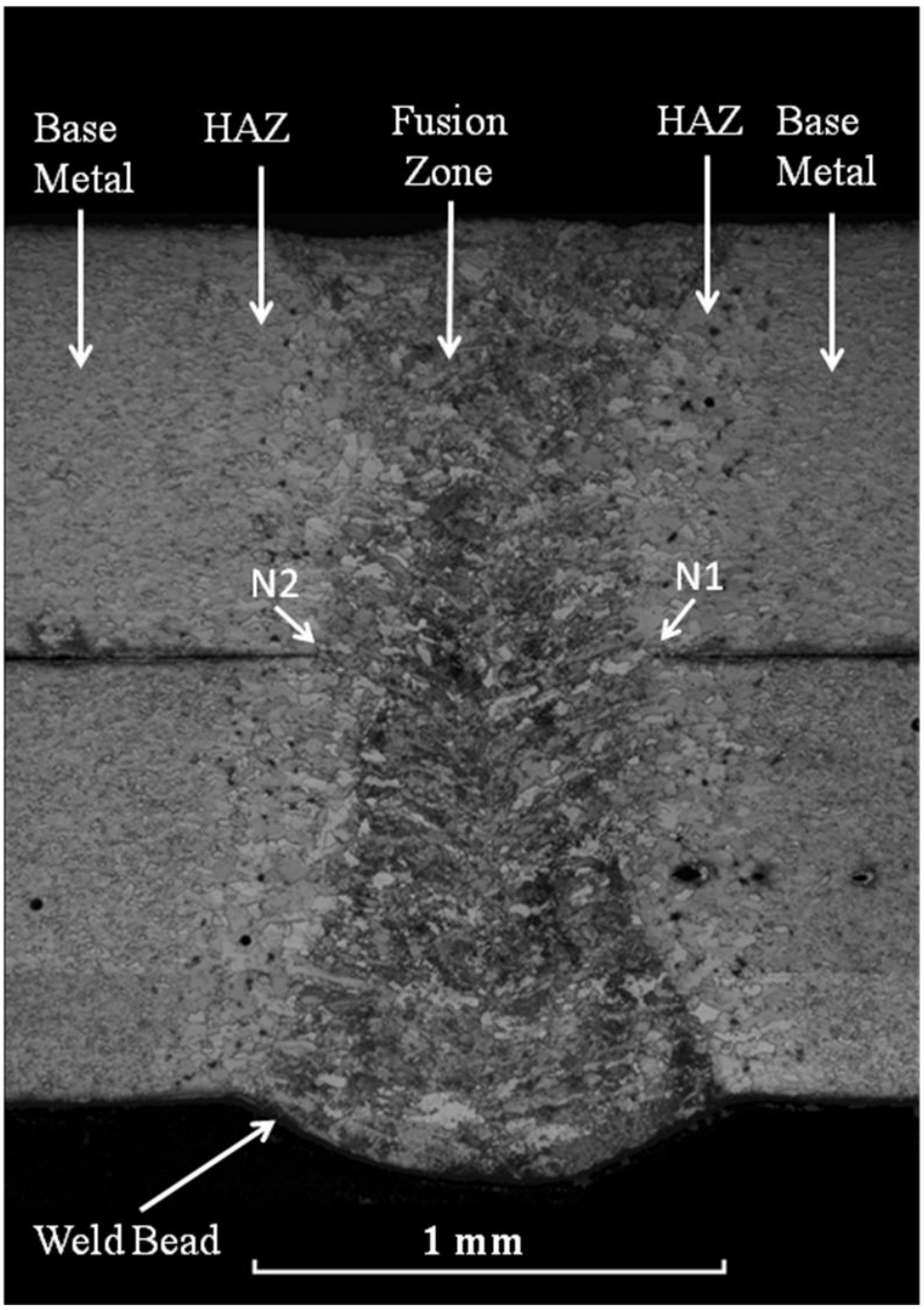

(a)

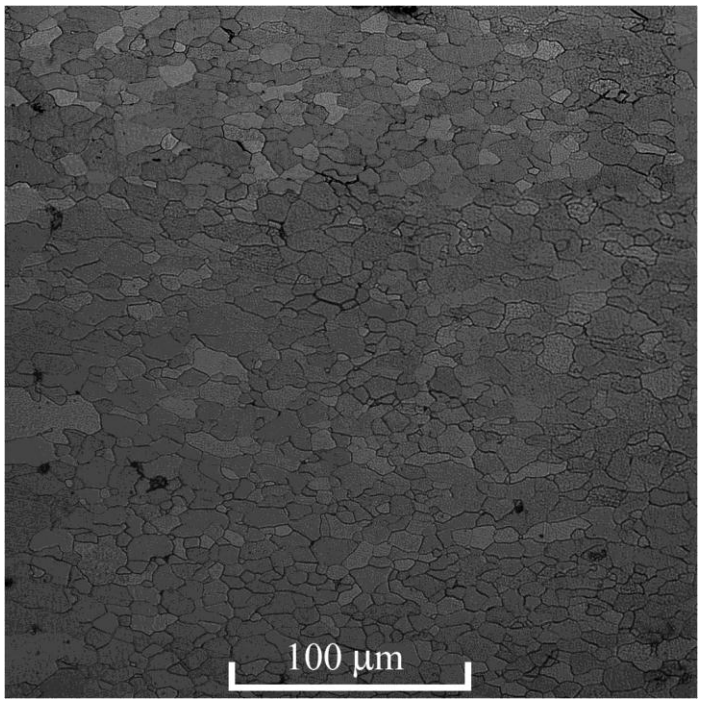

(b)

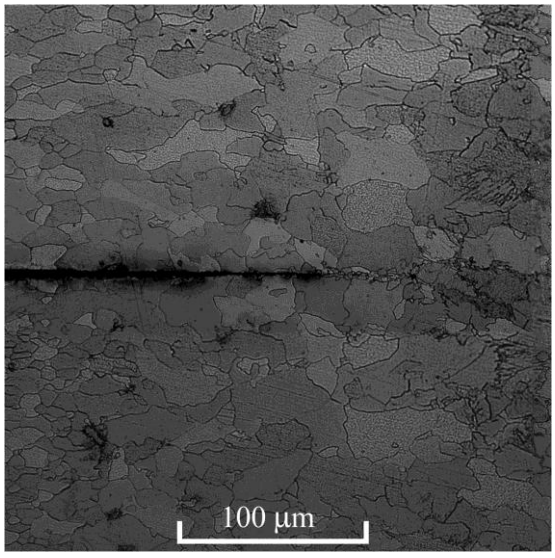

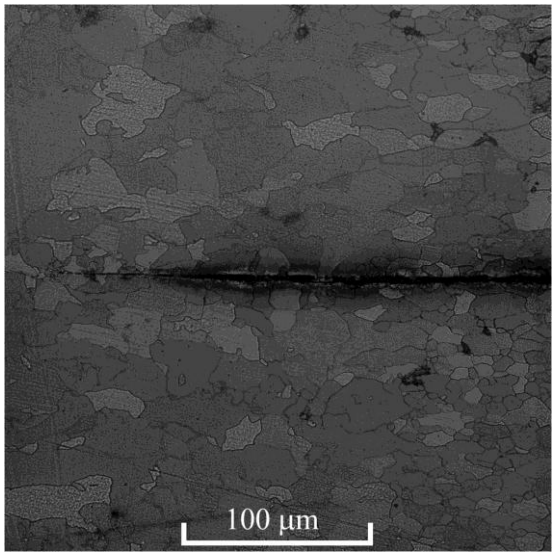

(c) (d)

Figure 3.3. (a) An optical micrograph of the etched cross section of a laser weld in lap-shear specimen perpendicular to the welding direction, and close-up views of (b) the base metal, (c) the left and (d) the right pre-existing crack tips.

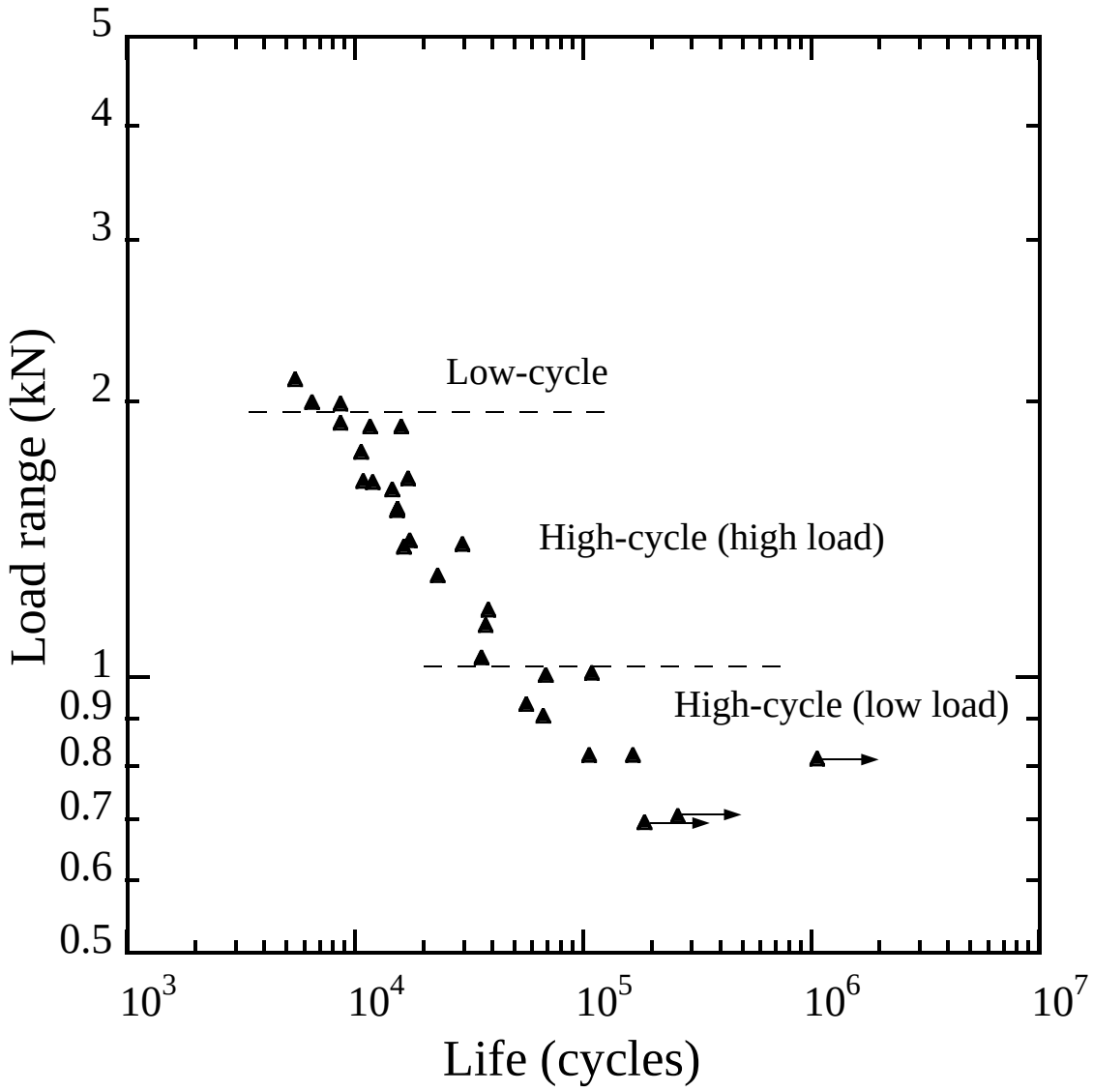

Figure 3.4. The experimental results of the fatigue tests of laser welds in lap-shear specimens under cyclic loading conditions.

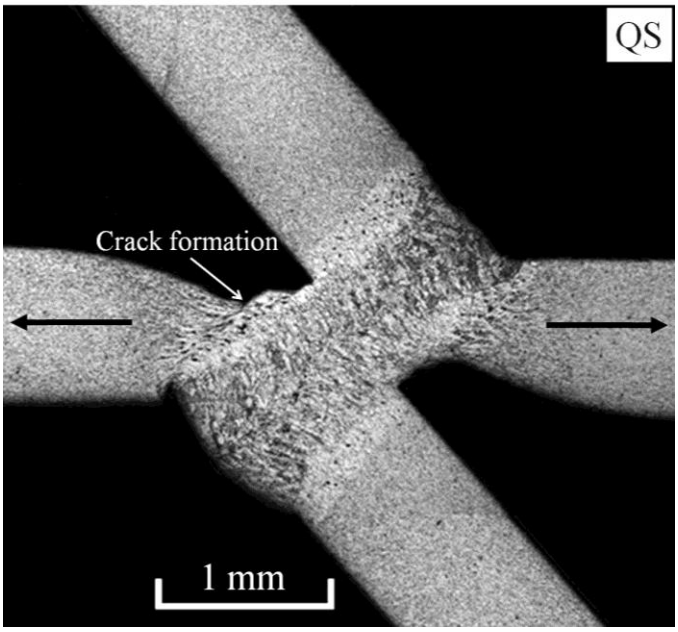

(a)

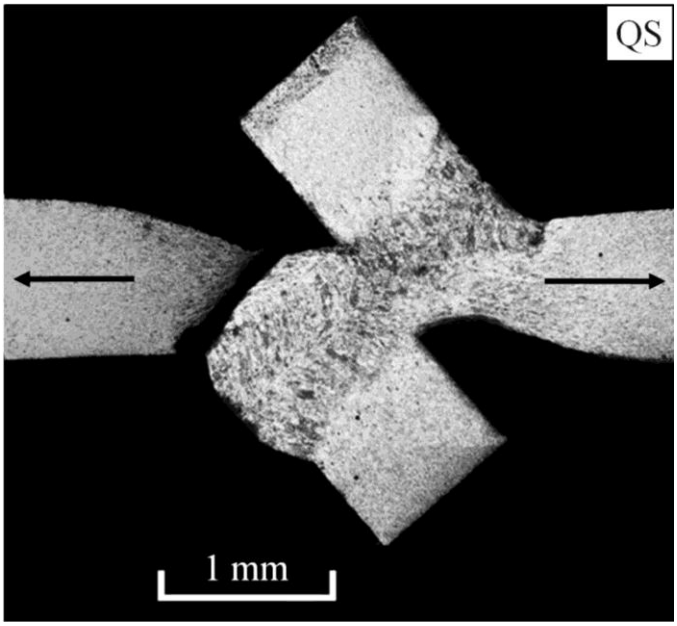

(b)

Figure 3.5. Optical micrographs of the etched cross sections of (a) a partially failed weld and (b) a failed weld under quasi-static (QS) loading conditions.

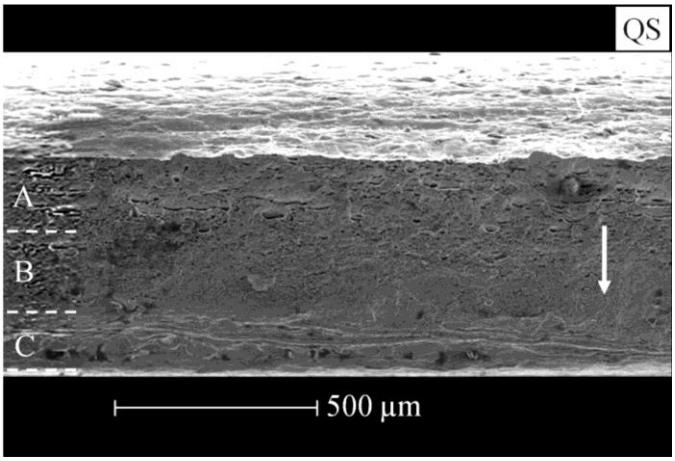

(a)

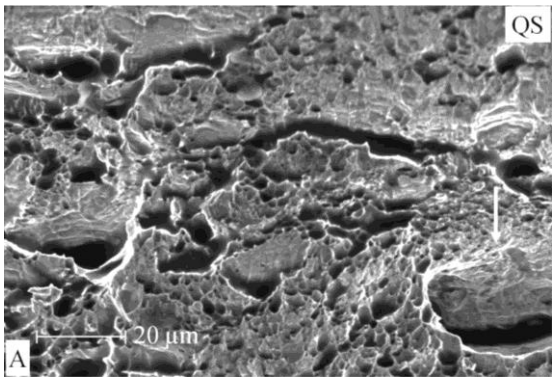

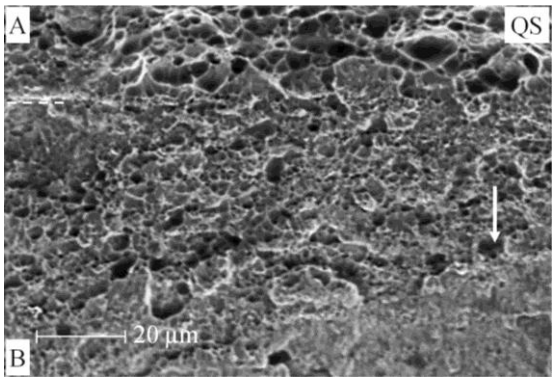

(b) (c)

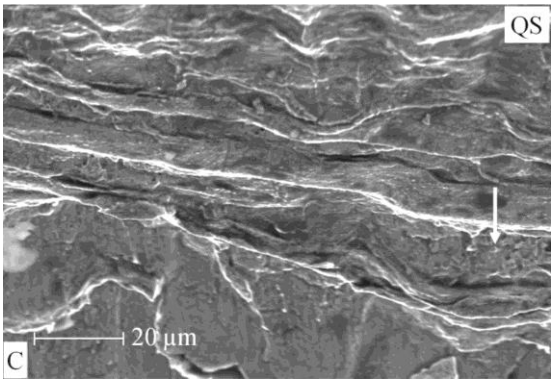

(d)

Figure 3.6. (a) A scanning electron micrograph of the failure surface of the lower left sheet of a failed specimen under quasi-static (QS) loading conditions, and close-up views of portions of (b) region A, (c) the transition region between regions A and B and (d) region C of the failure surface.

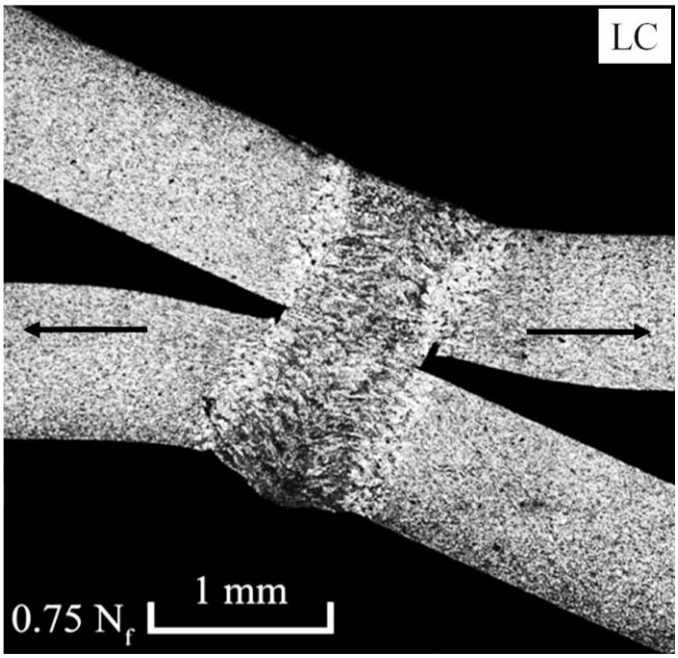

(a)

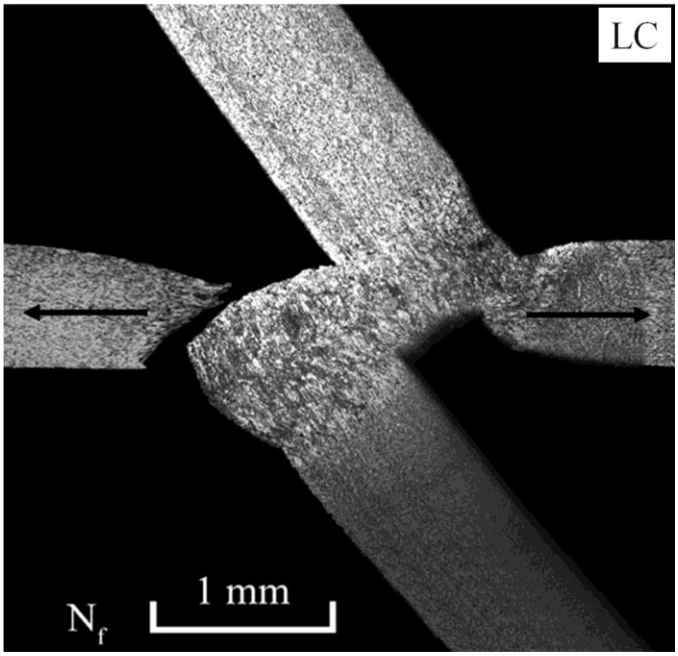

(b)

Figure 3.7. Optical micrographs of the etched cross sections of (a) a partially failed weld at the fatigue life of 6.47×10^3 cycles and (b) a failed weld at the fatigue life of 8.6×10^3 cycles under a load range of 1.99 kN (low-cycle (LC) loading conditions).

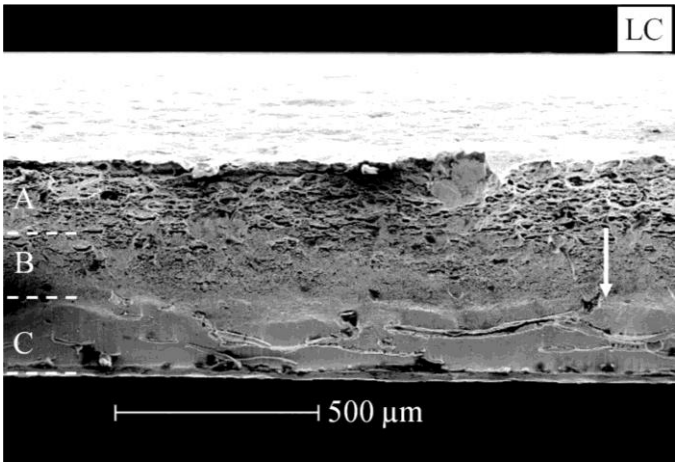

(a)

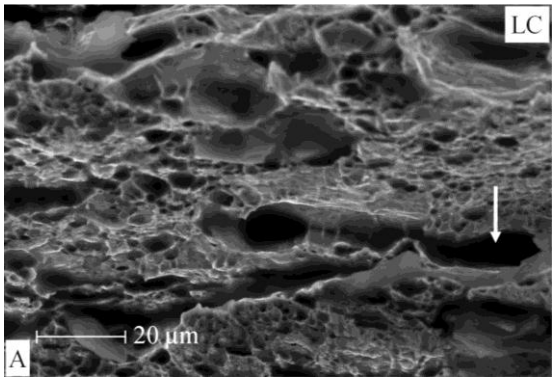

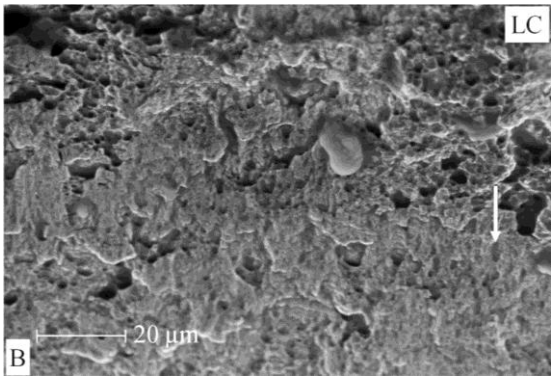

(b) (c)

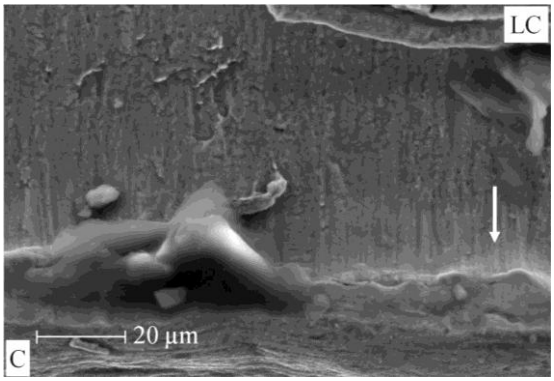

(d)

Figure 3.8. (a) A scanning electron micrograph of the failure surface of the lower left sheet of a failed specimen at the fatigue life of 5.44×10^{3} cycles under a load range of 2.11 kN (low-cycle (LC) loading conditions), and close-up views of portions of (b) region A, (c) region B and (d) region C of the failure surface.

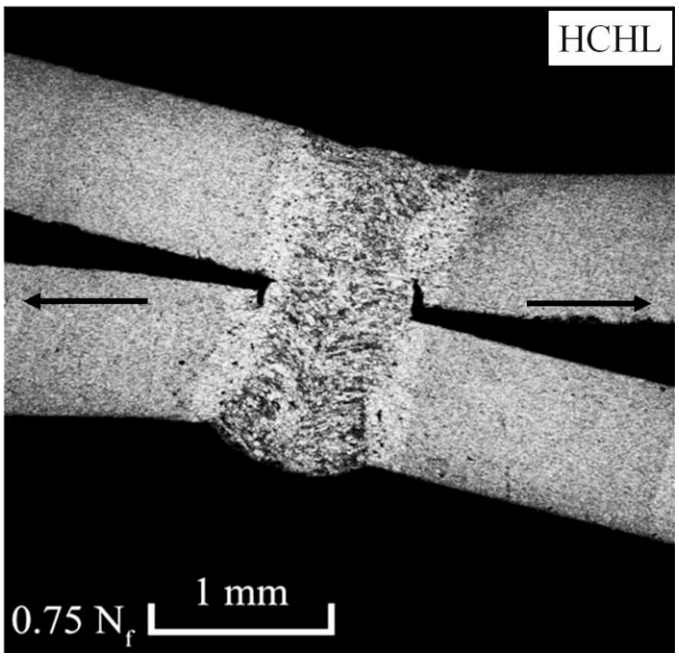

(a)

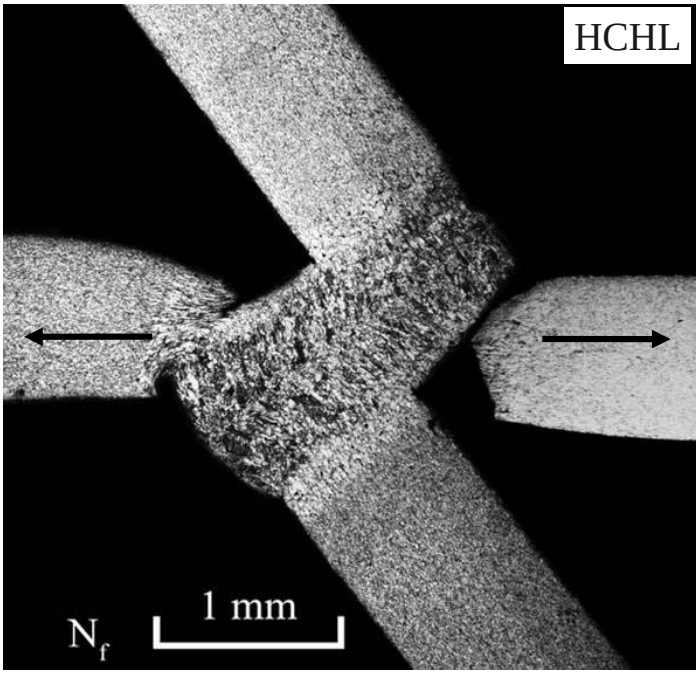

(b)

Figure 3.9. Optical micrographs of the etched cross sections of (a) a partially failed weld at the fatigue life of 1.02×10^4 cycles and (b) a failed weld at the fatigue life of 1.45×10^4 cycles under a load range of 1.64 kN (high-cycle loading conditions with a high load range (HCHL)).

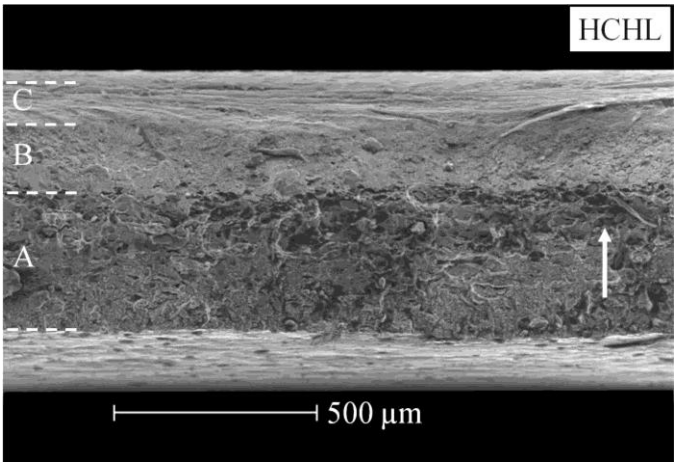

(a)

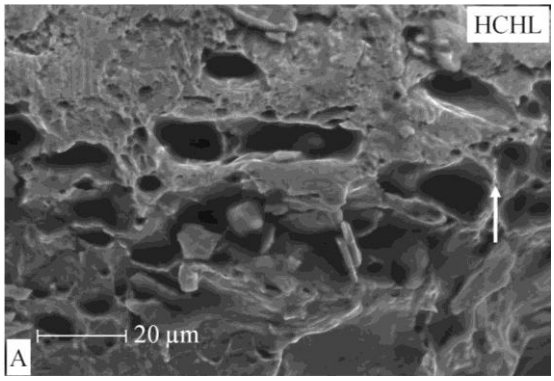

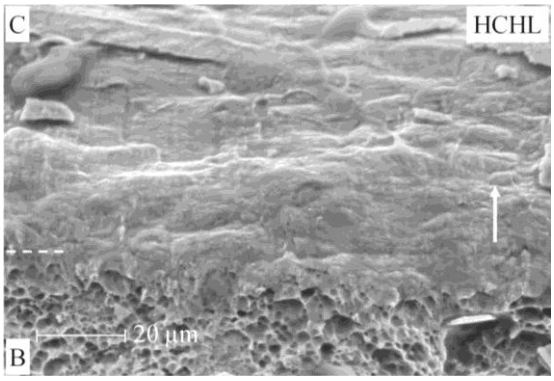

(b) (c)

Figure 3.10. (a) A scanning electron micrograph of the failure surface of the upper right sheet of a failed specimen at the fatigue life of 1.08×10^4 cycles under a load range of 1.64 kN (high-cycle loading conditions with a high load range (HCHL)), and close-up views of portions of (b) region A and (c) the transition region between regions B and C of the failure surface.

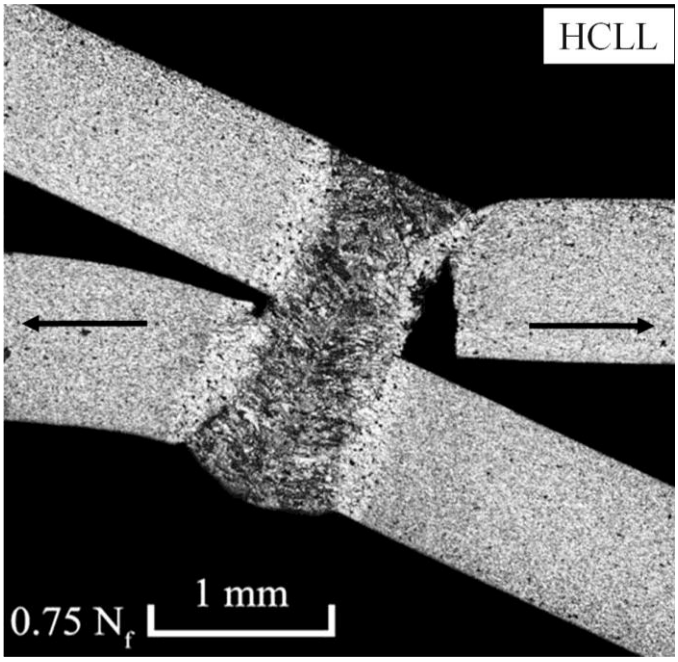

(a)

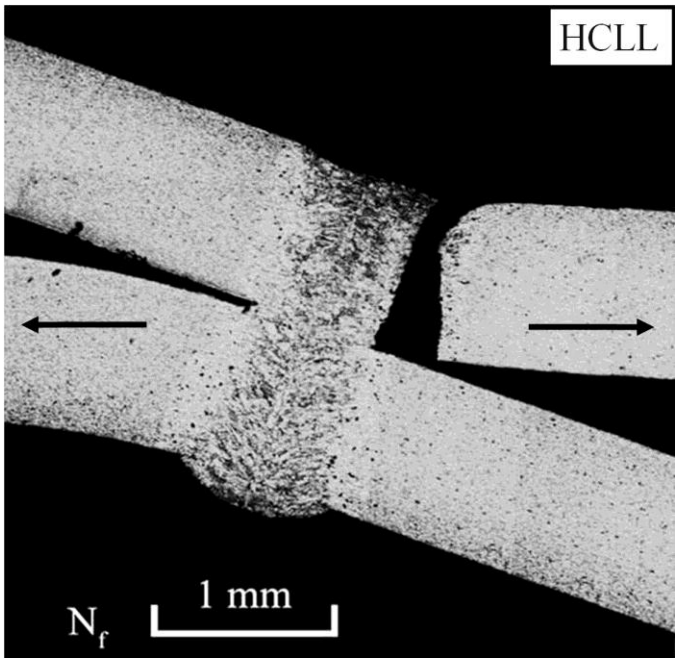

(b)

Figure 3.11 Optical micrographs of the etched cross sections of (a) a partially failed weld at the fatigue life of 1.09×10^5 cycles and (b) a failed weld at the fatigue life of 1.65×10^5 cycles under a load range of 0.82 kN (high-cycle loading conditions with a low load range (HCLL)).

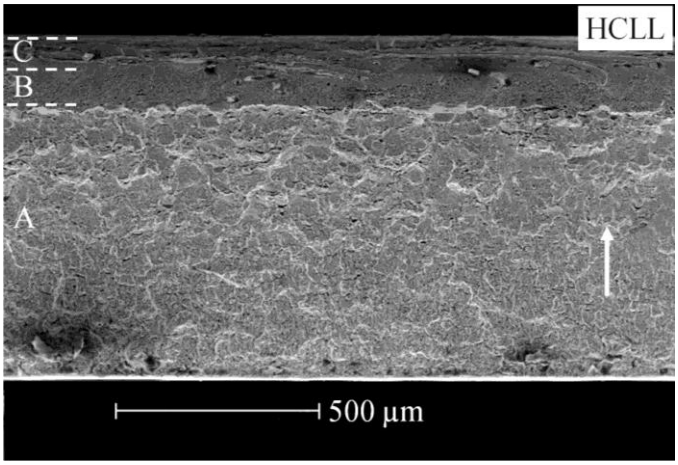

(a)

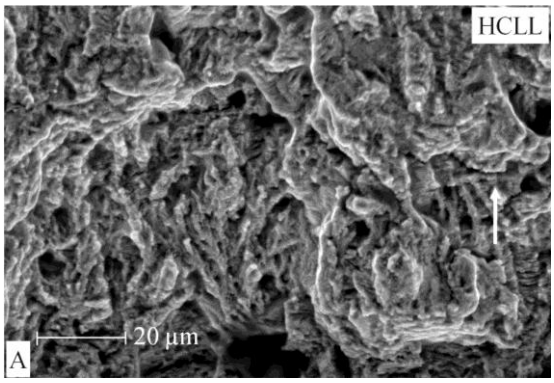

(b)

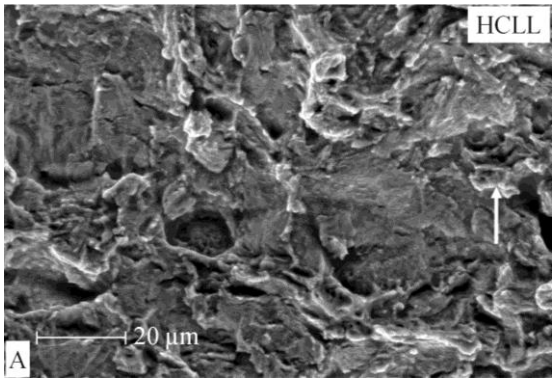

(c)

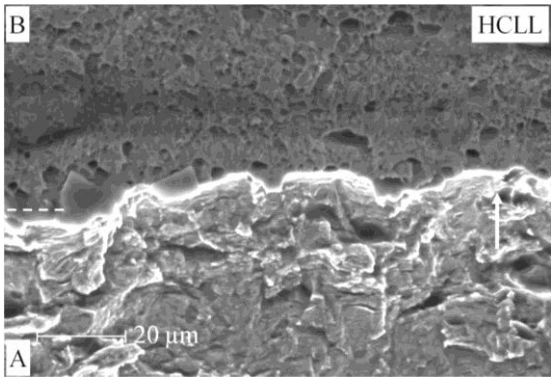

(d)

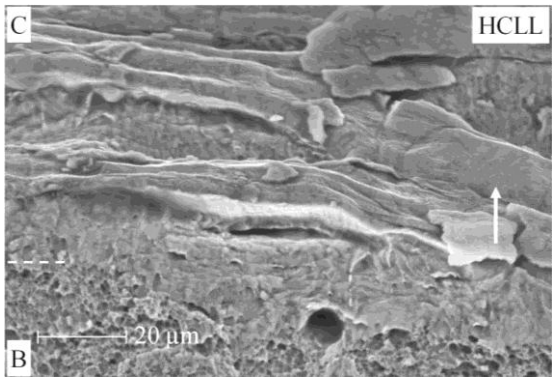

(e)

Figure 3.12. (a) A scanning electron micrograph of the failure surface of the upper right sheet of a failed specimen at the fatigue life of 1.65×10^5 cycles under a load range of 0.82 kN (high-cycle loading conditions with a low load range (HCLL)), close-up views of portions of (b) region A, (c) region A, (d) the transition region between regions A and B, and (e) the transition region between regions B and C of the failure surface.

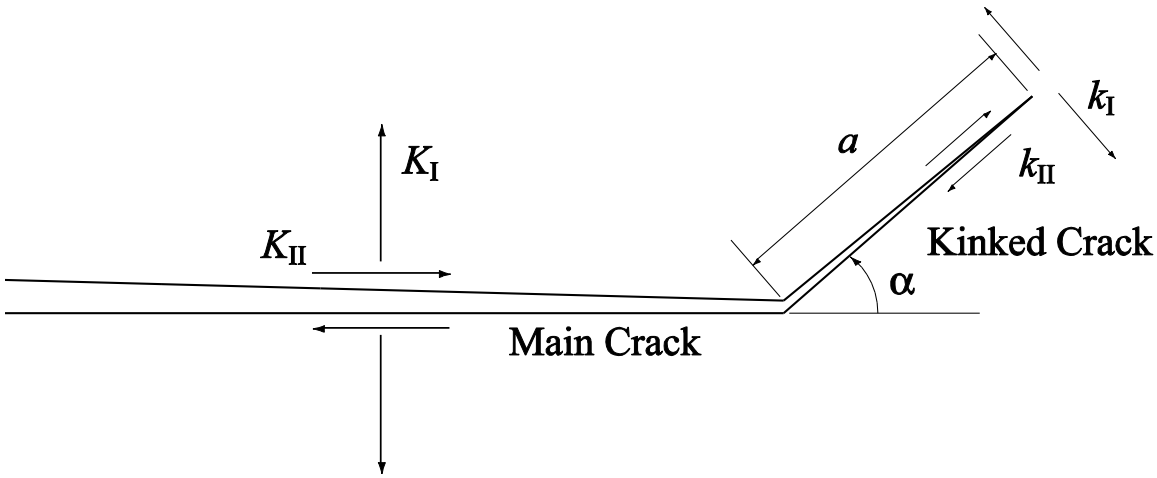

Figure 3.13. A schematic of a main crack and a kinked crack with the kink length a and the kink angle α.

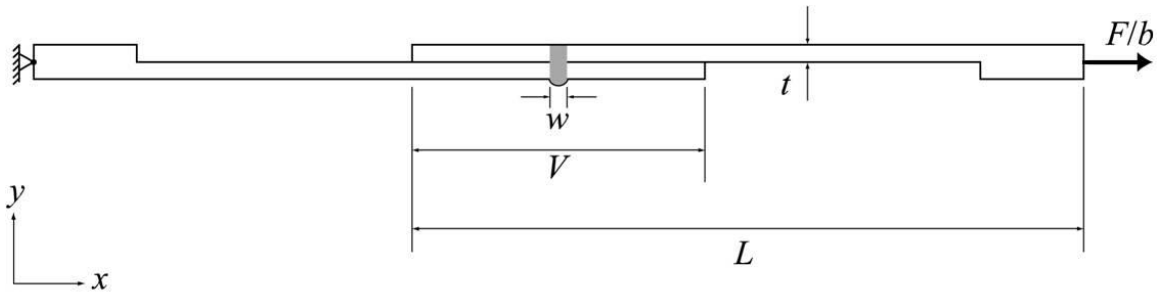

(a)

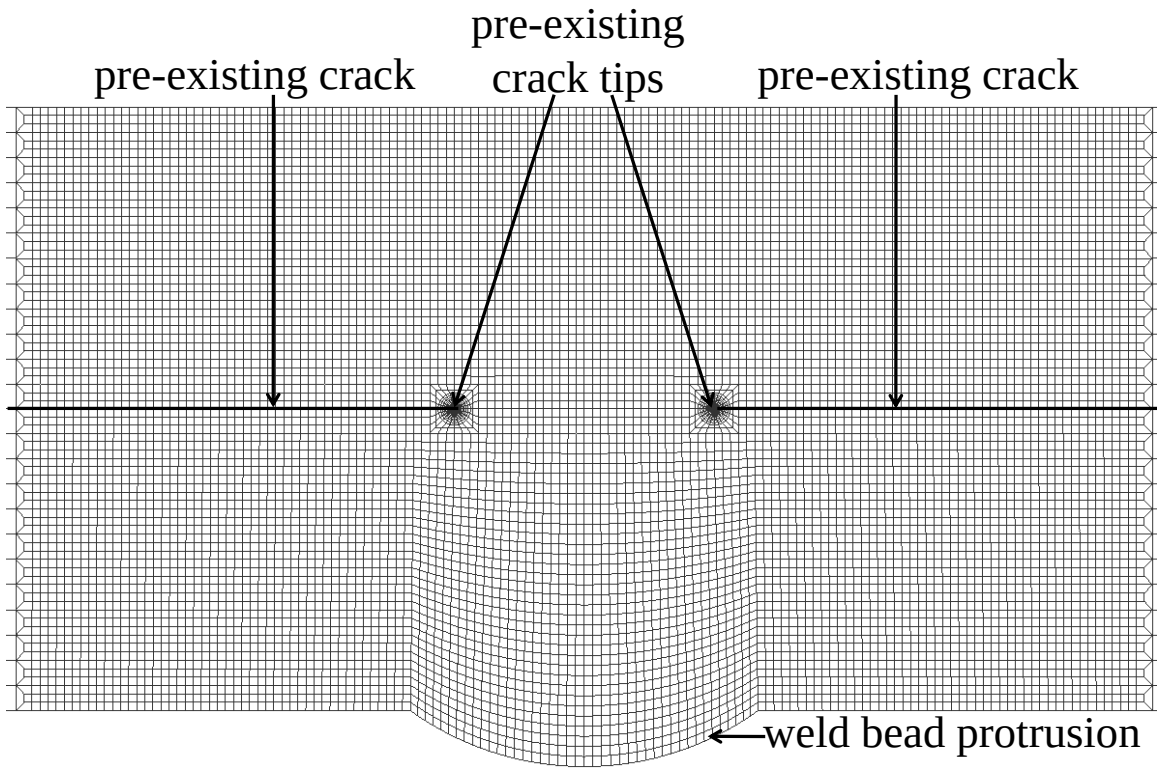

(b)

Figure 3.14. (a) A schematic of a two-dimensional finite element model of a lap-shear specimen with the boundary and loading conditions, and (b) a close-up view of the finite element mesh near the weld with $w/t = 0.86$.

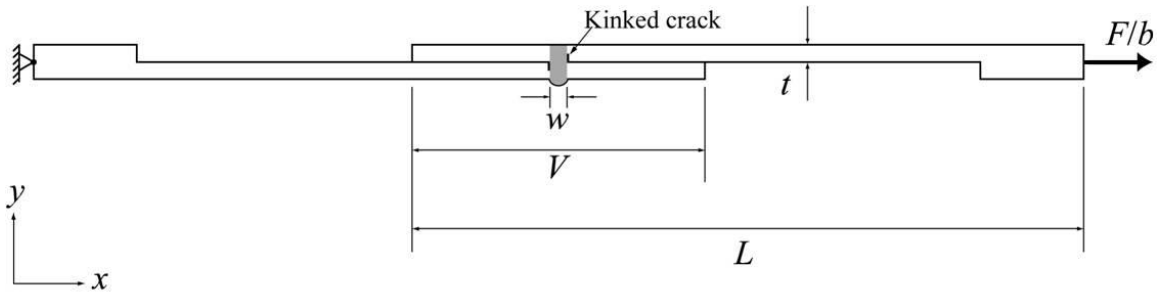

(a)

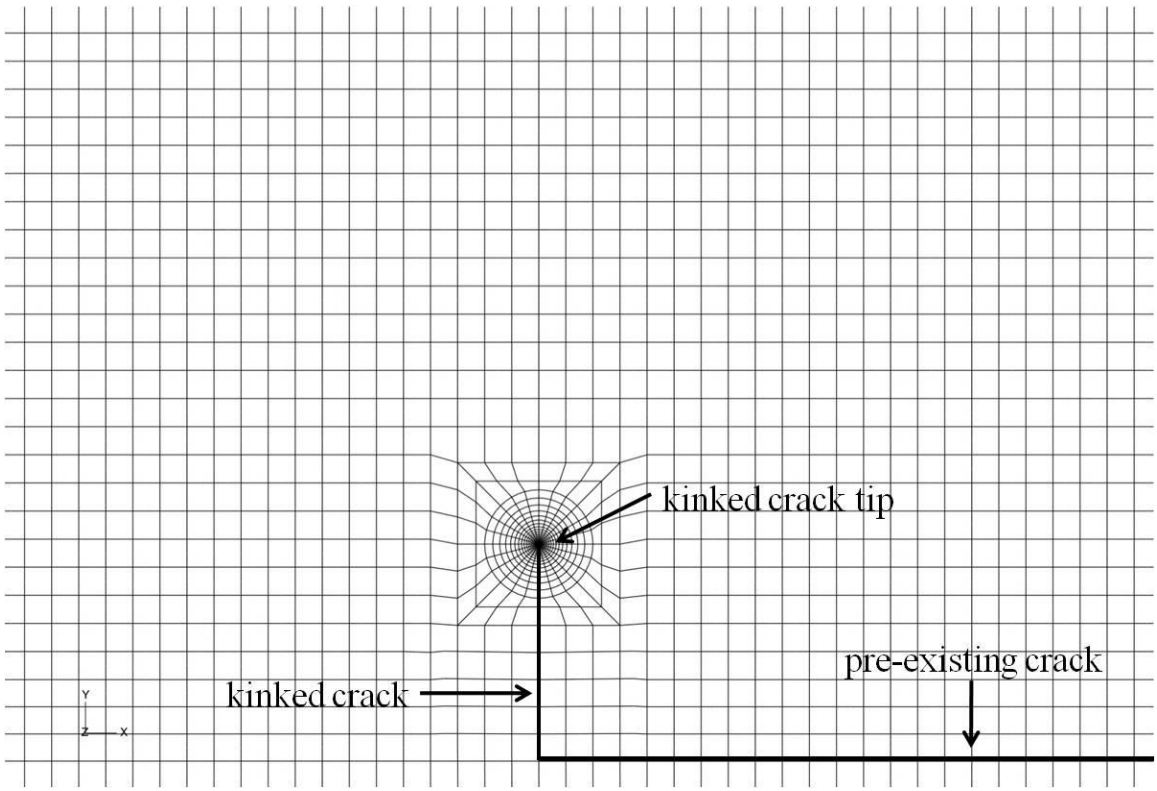

(b)

Figure 3.15. (a) A schematic of a two-dimensional finite element model of a lap-shear specimen with two kinked cracks and the boundary and loading conditions, and (b) a close-up view of the finite element mesh near the right kinked crack tip for $a/t = 0.2$.

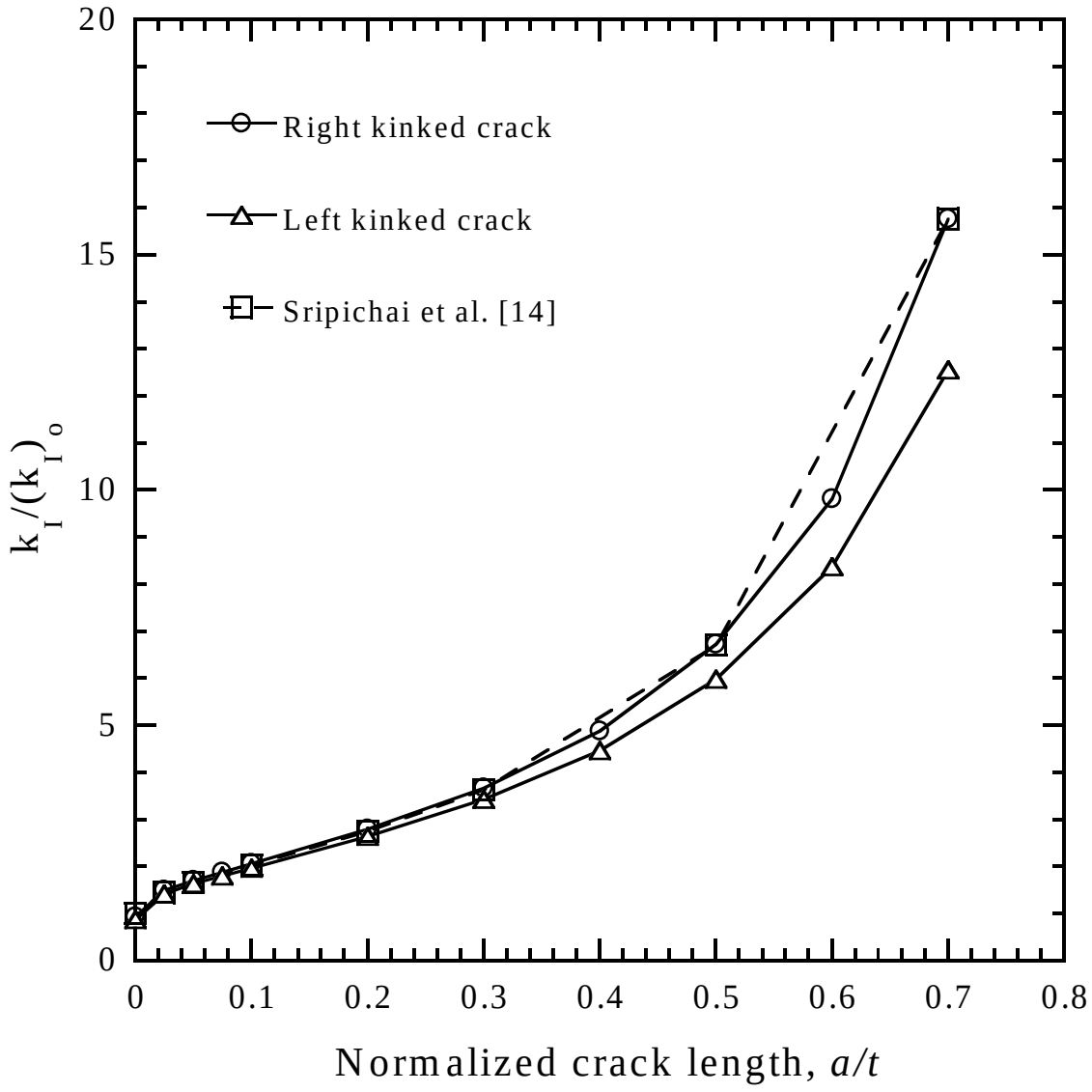

Figure 3.16. The values of $k_I/(k_I)_0$ for the kinked cracks emanating from the right and left per-existing crack tips as functions of the normalized kink length a/t for $w/t = 0.86$ and $\alpha = 90°$. The results of Sripichai et al. [14] for an idealized weld with $w/t = 1$ and $\alpha = 90°$ are also shown.

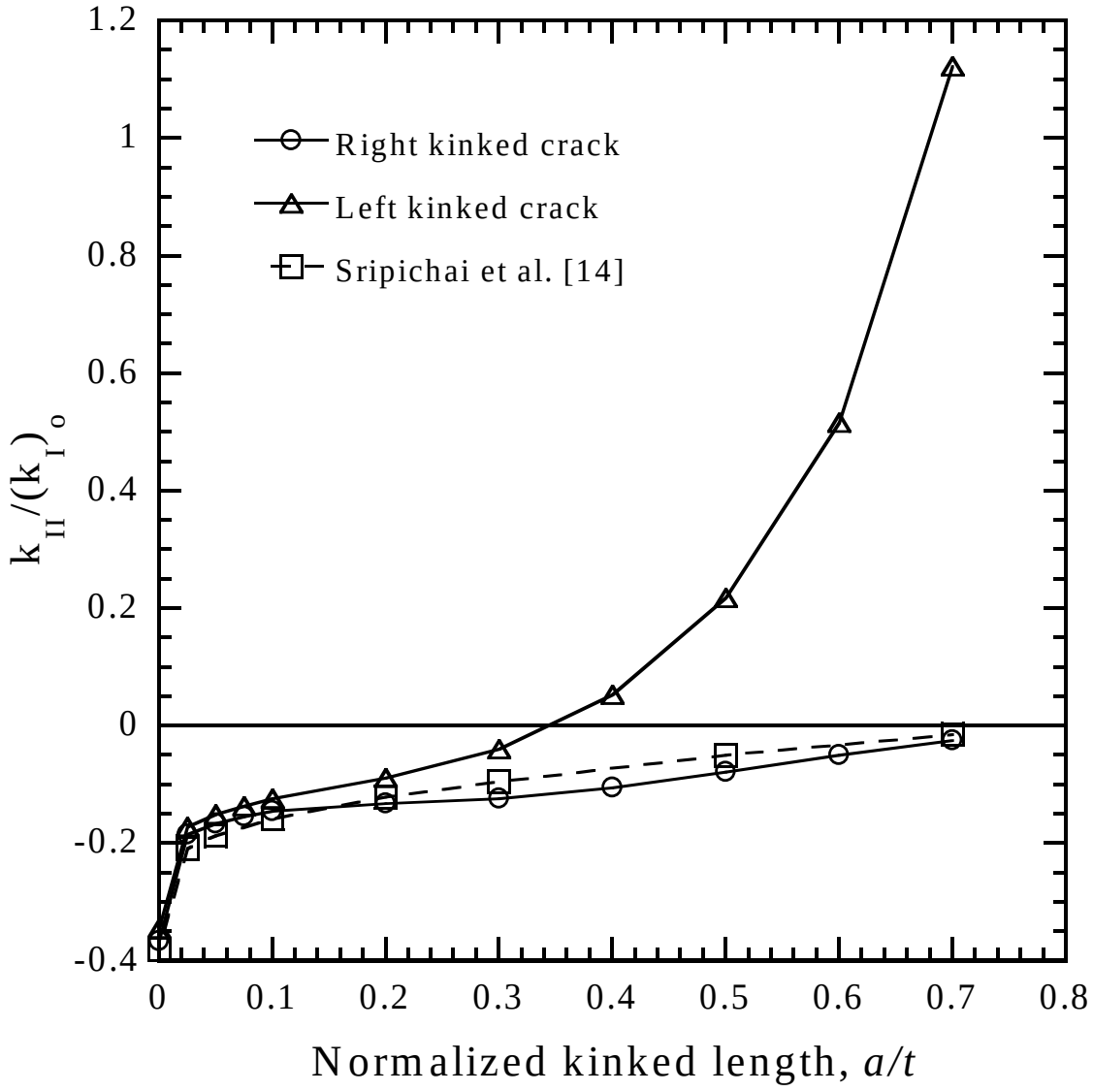

Figure 3.17. The values of $k_{II}/(k_I)_0$ for the kinked cracks emanating from the right and left per-existing crack tips as functions of the normalized kink length a/t for $w/t = 0.86$ and $\alpha = 90°$. The results of Sripichai et al. [14] for an idealized weld with $w/t = 1$ and $\alpha = 90°$ are also shown.

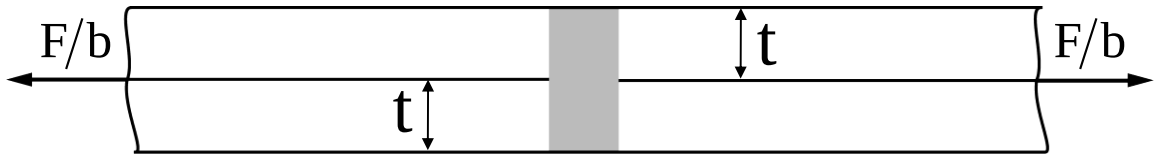

(a)

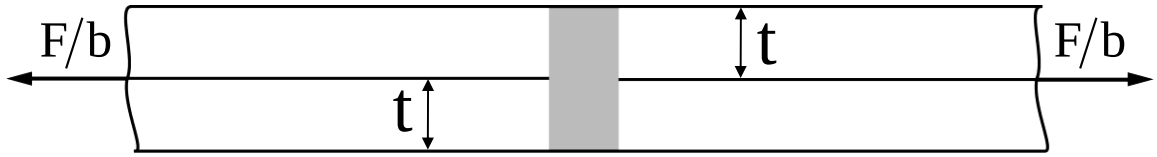

(b)

Figure 3.18. (a) A schematic of a two-beam model under lap-shear loading conditions. The idealized weld is shown as the shaded region and (b) a schematic of the two-beam model under an equivalent loading of (a).

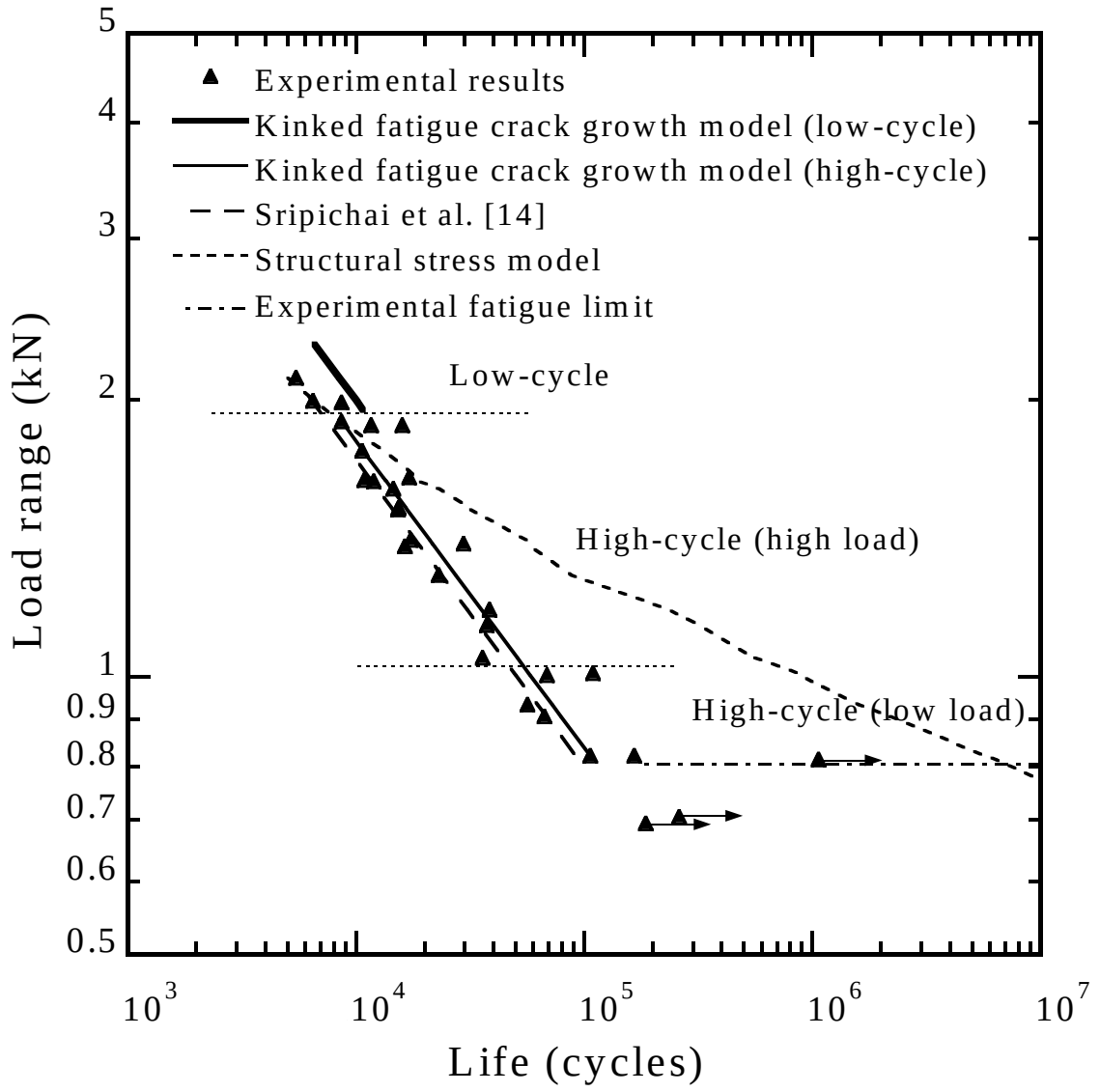

Figure 3.19. Experimental results and the fatigue life estimates based on the kinked fatigue crack growth models and structural stress model.

Reference

[1] Hsu C, Albright CE. Fatigue analysis of laser welded lap joints. Engineering Fracture Mechanics 1991; 39: 575-580.

[2] Wang PC, Ewing KM. A comparison of fatigue strengths: laser beam vs. resistance spot welds. Welding Journal 1991; 70: 43-47.

[3] Flavenot JF, Deville JP, Diboine A, Cantello M, Gobbi SL. Fatigue resistance of laser welded lap joints of steel sheets. Welding in the World 1993; 31: 12-15.

[4] Wang PC. Fracture mechanics parameter for the fatigue resistance of laser welds. International Journal of Fatigue 1995; 17: 25-34.

[5] Ono M, Kabasawa M, Omura M. Static and fatigue strength of laser-welded lap joints in thin steel sheet. Welding International 1997; 11: 462-467.

[6] Terasaki T, Sobue T, Kitamura T. Study of fatigue strength of laser welded lap joint. Quarterly Journal of Japan Welding Society 2001; 19: 507-512.

[7] Zhang S. Stress in laser welded lap joints determined by outer surface strains. Welding Journal 2002; 81: 14-18.

[8] Kaitanov AY, Ozersky AD, Zabelin AM, Kislov VS. Static and fatigue strengths of laser welded overlap joints with controlled penetration. Procedings of SPIE 2002; 4644: 116-126.

[9] Cho SK, Yang YS, Son KJ, Kim JY. Fatigue strength in laser welding of the lap joint. Finite Element Analysis and Design 2004; 40: 1059-1070.

[10] Sripichai K, Asim K, Jo WH, Pan J, Li M. Fatigue behavior of laser welds in lap-shear specimens of high strength low alloy (HSLA) steels. SAE Technical Paper No. 2009-01-0028, Society of Automotive Engineers, Warrendale PA: 2009.

[11] Anand D, Chen DL, Bhole SD, Anderychuk P, Bourdeau G. Fatigue behavior of tailor (laser)-welded blanks for automotive applications. Materials Science and Engineering 2006; A 420: 199-207.

[12] Lee J, Asim K, Pan J. Modeling of failure mode of laser welds in lap-shear specimens of HSLA steel sheets. Engineering Fracture Mechanics 2011; 78: 374-396.

[13] Asim K, Lee J, Pan J. Failure mode of laser welds in lap-shear specimens of high strength low alloy (HSLA) steel sheets. Submitted for publication in Fatigue and Fracture of Engineering Materials and Structures, 2011.

[14] Sripichai K, Asim K, Pan J. Stress intensity factor solutions for estimation of fatigue lives of laser welds in lap-shear specimens. Submitted for publication in Engineering Fracture Mechanics, 2010.

[15] Bilby BA, Cardew GE, Horward IC. Stress intensity factors at the tip of kinked and forked cracks. The fourth international conference on fracture, University of Waterloo, Ontario, June 19-24, 1977; Pergamon Press, NY, 1978; 3A: 197-200.

[16] Cotterell B, Rice JR. Slightly curved or kinked cracks. International Journal of Fracture 1980; 16: 155-169.

[17] ABAQUS v6.7 User Manual. Providence, RI: SIMULIA; 2007.

[18] Tran V-X, Pan J, Pan T. Fatigue behavior of aluminum 5754-O and 6111-T4 spot friction welds in lap-shear specimens. International Journal of Fatigue 2008; 30: 2175-2190.

[19] Tran V-X, Pan J, Pan T. Fatigue behavior of spot friction welds in lap-shear and cross-tension specimens of dissimilar aluminum sheets. International Journal of Fatigue 2010; 32: 1022-1041.

[20] Dowling NE. Mechanical Behavior of Materials, Second Edition, Prentice Hall, New Jersey, 1998.

[21] Zhang S. Stress intensities at spot welds. International Journal of Fracture 1997; 88: 167-185.

[22] Zhang S. Fracture mechanics solutions to spot welds. International Journal of Fracture 2001; 112: 247-274.

[23] Chien WY, Pan J, Close D, Ho S. Fatigue analysis of crankshaft sections under bending with consideration of residual stresses. International Journal of Fatigue 2005; 27: 1-19.

CHAPTER IV

EFFECT OF SHEET THICKNESS AND GAP BETWEEN THE SHEETS ON STRESS INTENSITY FACTOR SOLUTIONS FOR LASER WELDS IN LAP-SHEAR SPECIMENS

4.1. Introduction

Laser welding is used in the automotive industry due to its advantages such as relatively low distortion, narrow heat affected zone, relatively high welding speed, high penetration and flexibility. Over the past two decades, extensive research efforts have been spent on studying the fatigue behavior of laser welds for different materials and joint configurations. Lap joints are a common joint configuration. The geometry of a lap joint provides pre-existing cracks or notches at the edges of the weld bead. Therefore, the fatigue cracks were usually observed to initiate from these stress concentration sites. Hsu and Albright [1] conducted an experimental investigation to evaluate the effects of weld pattern and other factors such as the sheet thickness, gap between the sheets and the joint prebending on the fatigue strength of laser welded lap joints. They reported that the weld pattern can significantly affect the fatigue strength of the welds. Wang and Ewing [2] compared the fatigue strengths of laser welds and resistance spot welds in lap-shear specimens of steel sheets on the basis of equal weld volume. They reported that the fatigue failure in laser welds is dominated by crack propagation along the periphery of the weld bead in the heat affected zone. Flavenot et al. [3] performed an experimental study on the influence of laser beam type, weld bead geometry, gap between the sheets and the input energy on the fatigue behavior of laser welded lap joints. Wang [4]

investigated the fracture mechanics parameters for the fatigue resistance of laser welds in lap-shear specimens of steel sheets. The values of the J integrals were obtained from finite element analyses to correlate the fatigue lives of laser welds. These results were also used to assess the influences of parameters such as the weld geometry, sheet thickness, bead width, metal fit-up and bead length on fatigue lives. Kaitanov et al. [5] conducted experiments to determine the static and fatigue strengths of laser welded lap joints of steel sheets with different weld widths and penetration depths. They found that the weld width affects the fatigue strength of laser welds. Sripichai et al. [6] recently investigated the fatigue behavior of laser welds in lap-shear specimens of high strength low alloy steel sheets based on the closed-form and computational stress intensity factor solutions.

In this study, the effects of different sheet thicknesses and gaps on the stress intensity factor solutions of laser welds in lap-shear specimens are investigated. The analytical stress intensity factor solutions of Zhang [7] for welds with similar material and different sheet thicknesses in terms of the structural stresses are adopted to calculate the stress intensity factor solutions for laser welds in lap-shear specimens with different sheet thicknesses. The structural stresses for the stress intensity factor solutions are obtained from the beam bending theory for a two-strip model with connection under plane strain conditions. Two-dimensional finite element analyses were carried out to investigate the effects of the weld width and different thicknesses on the stress intensity factor solutions. The computational results are compared with the analytical stress intensity factor solutions. Approximate stress intensity factor solutions as a function of the normalized weld width are proposed for the right pre-existing crack tip of the load

carrying upper right thinner sheet with larger stress intensity factor solutions. Finite element analyses were also carried out to study the effects of gaps on the stress intensity factor solutions for cracks emanating from the pre-existing notch tips. Finally, a closed-form structural stress solution is developed for laser welded lap-shear specimens with a gap between the sheets. The closed-form structural stress model is also used to investigate the effect of the gap on the fatigue lives of the welds.

4.2. Stress intensity factor solutions for sheets with different thicknesses

4.2.1 Analytical stress intensity factor solutions for specimens with different sheet thicknesses

Figure 4.1 shows a schematic of a lap-shear specimen with sheets of equal thicknesses. The weld zone is shown as the shaded region. As shown in the figure, the specimen has a width W, sheet thickness t, and length L for the upper and lower sheets. The specimen has a width b and a length c for the central portion of the specimen, an overlap length V, and a width w for the weld zone, which is indicated as the shaded region in the figure. Two doublers were used to align the applied load to avoid the initial realignment of the specimen under lap-shear loading conditions. The doublers have a length s and a width W.

Figure 4.2(a) shows a schematic of the cross section near an idealized weld in a lap-shear specimen as a two-strip model of different thicknesses with connection under lap-shear loading conditions. The weld bead protrusion is not considered for the idealized weld. The two strips have thicknesses t_u and t_l for the upper and lower sheets,

respectively, with $t_l > t_u$. For the two-strip model shown in Figure 4.2(a), F/b represents the force per unit width of the central portion with a reduced width. The forces per unit width, F/b, are applied along the interfacial surface of the two strips. In Figure 4.2(b), the forces per unit width, F/b, become the membrane forces per unit width, F/b, and the bending moments per unit width, $Ft_u/2b$ and $Ft_l/2b$, applied at the middle surface of the upper and lower strips, respectively. Both membranes forces and bending moments shown in Figure 4.2(b) are statically equivalent to the shear forces of the two strips shown in Figure 4.2(a). Figure 4.3(a) shows the left half of the two-strip model near the crack tip with the distributions of the normal stresses through the thicknesses. In Figure 4.3(a), the normal stresses σ_{ui}, σ_{uo}, σ_{li} and σ_{lo} represent the normal stresses at the inner (i) and outer (o) surfaces of the upper (u) and lower (l) left strips, respectively. The normal stresses σ_u^* and σ_l^* represent the normal stresses at the upper and lower surfaces of the right strip, respectively. Zhang [7] obtained the closed form stress intensity factor K_I and K_{II} solutions for spot welds joining sheets of different materials and thicknesses using the analytical solutions of Suo and Hutchinson [8]. The K_I and K_{II} solutions in terms of σ_{ui}, σ_{uo}, σ_{li} and σ_{lo} for spot welds joining two sheets of different thicknesses are [7]

$$K_I = \frac{\sqrt{t_u}}{2\sqrt{2(1+\delta)(1+3\delta+3\delta^2)(1+\tan^2\omega)}}\left\{\left[\frac{1+3\delta+6\delta^2}{\sqrt{3}(1+\delta)}\tan\omega-1\right]\sigma_{ui}\right.$$
$$\left.-\left[\frac{1+3\delta}{\sqrt{3}(1+\delta)}\tan\omega+1\right]\sigma_{uo}+\left[\frac{\delta(1-3\delta)}{\sqrt{3}(1+\delta)}\tan\omega+2+\delta\right]\sigma_{li}-\delta\left[\frac{1+3\delta}{\sqrt{3}(1+\delta)}\tan\omega+1\right]\sigma_{lo}\right\} \quad (1)$$

$$K_{II} = \frac{\sqrt{t_u}}{2\sqrt{2(1+\delta)(1+3\delta+3\delta^2)(1+\tan^2\omega)}}\left\{\left[\frac{1+3\delta+6\delta^2}{\sqrt{3}(1+\delta)}+\tan\omega\right]\sigma_{ui}\right.$$
$$\left.-\left[\frac{1+3\delta}{\sqrt{3}(1+\delta)}-\tan\omega\right]\sigma_{uo}+\left[\frac{\delta(1-3\delta)}{\sqrt{3}(1+\delta)}-(2+\delta)\tan\omega\right]\sigma_{li}-\delta\left[\frac{1+3\delta}{\sqrt{3}(1+\delta)}-\tan\omega\right]\sigma_{lo}\right\} \quad (2)$$

where the ratio of the sheet thicknesses, δ, is defined as $\delta = t_u / t_l$, and the values of the angular quantity ω are listed in Suo and Hutchinson [8] for different values of δ. It is noted that the stress intensity factor solutions in Equations (1) and (2) are expressed in terms of the structural stresses σ_{ui}, σ_{uo}, σ_{li} and σ_{lo} as shown in Figure 4.3(a). The structural stresses required to determine the stress intensity factor solutions in Equations (1) and (2) for the two-strip model shown in Figure 4.2(b) are obtained from the beam bending theory. Figure 4.3(b) shows a schematic of the two-strip model with the linearly distributed structural stresses. The structural stresses σ_{ui}^A, σ_{uo}^A, σ_{li}^A and σ_{lo}^A represent the normal stresses for the region behind crack tip A at the inner (i) and outer (o) surfaces of the upper (u) and lower (l) right strips, respectively. The structural stresses $\sigma_{ui}^B, \sigma_{uo}^B$, σ_{li}^B and σ_{lo}^B represent the normal stresses for the region behind crack tip B at the inner (i) and outer (o) surfaces of the upper (u) and lower (l) left strips, respectively.

Based on the beam bending theory and the two-strip model in Figure 4.3(b), the normal stresses for the region behind crack tip A in Figure 4.3(b) are given as

$$\sigma_{ui}^A = 4F/bt_u \quad (3a)$$

$$\sigma_{uo}^A = -2F/bt_u \quad (3b)$$

$$\sigma_{li}^A = \sigma_{lo}^A = 0 \quad (3c)$$

Similarly, the normal stresses for the region behind crack tip B in Figure 4.3(b) are given as

$$\sigma_{ui}^{B} = \sigma_{uo}^{B} = 0 \tag{4a}$$

$$\sigma_{li}^{B} = 4F/bt_{l} \tag{4b}$$

$$\sigma_{lo}^{B} = -2F/bt_{l} \tag{4c}$$

The stress intensity factor K_I and K_{II} solutions for crack tip A can now be obtained from Equations (1) and (2) using the normal stresses in Equations (3a), (3b) and (3c)

$$K_I^A = \overline{K}_I^A \frac{F}{b\sqrt{t_u}} \tag{5}$$

$$K_{II}^A = \overline{K}_{II}^A \frac{F}{b\sqrt{t_u}} \tag{6}$$

where the normalized stress intensity factor $\overline{K}_I^A$ and $\overline{K}_{II}^A$ solutions are

$$\overline{K}_I^A = \frac{1}{2\sqrt{2(1+\delta)(1+3\delta+3\delta^2)(1+\tan^2\omega)}} \left\{ 4\left[\frac{1+3\delta+6\delta^2}{\sqrt{3}(1+\delta)} \tan\omega - 1 \right] + 2\left[\frac{1+3\delta}{\sqrt{3}(1+\delta)} \tan\omega + 1 \right] \right\} \tag{7}$$

$$\overline{K}_{II}^A = \frac{1}{2\sqrt{2(1+\delta)(1+3\delta+3\delta^2)(1+\tan^2\omega)}} \left\{ 4\left[\frac{1+3\delta+6\delta^2}{\sqrt{3}(1+\delta)} + \tan\omega \right] + 2\left[\frac{1+3\delta}{\sqrt{3}(1+\delta)} - \tan\omega \right] \right\} \tag{8}$$

In the same manner, the stress intensity factor K_I and K_{II} solutions for crack tip B can be obtained from Equations (1) and (2) using the normal stresses in Equations (4a), (4b) and (4c) as

$$K_I^B = \overline{K}_I^B \frac{F}{b\sqrt{t_u}} \tag{9}$$

$$K_{II}^B = \overline{K}_{II}^B \frac{F}{b\sqrt{t_u}} \tag{10}$$

where the normalized stress intensity factor $\overline{K}_I^B$ and $\overline{K}_{II}^B$ solutions are

$$\overline{K}_I^B = \frac{1}{2\sqrt{2(1+\delta)(1+3\delta+3\delta^2)(1+\tan^2\omega)}}\left\{4\delta\left[\frac{\delta(1-3\delta)}{\sqrt{3}(1+\delta)}\tan\omega + 2 + \delta\right] + 2\delta^2\left[\frac{1+3\delta}{\sqrt{3}(1+\delta)}\tan\omega + 1\right]\right\} \tag{11}$$

$$\overline{K}_{II}^B = \frac{1}{2\sqrt{2(1+\delta)(1+3\delta+3\delta^2)(1+\tan^2\omega)}}\left\{4\delta\left[\frac{\delta(1-3\delta)}{\sqrt{3}(1+\delta)} - (2+\delta)\tan\omega\right] + 2\delta^2\left[\frac{1+3\delta}{\sqrt{3}(1+\delta)} - \tan\omega\right]\right\} \tag{12}$$

The normalized stress intensity factors K_{I} and K_{II} solutions for the two crack tips can be obtained from Equations (5) – (12) in terms of the ratio of the sheet thicknesses, δ, for sheets of different thicknesses. Equations (5) – (12) were derived based on the assumption that the weld width w is large compared to the thicknesses of the upper and lower sheets. This assumption will be examined later by the results of the finite element analyses. When the weld width w becomes small compared to the thickness t_u, the stress intensity factor solutions should approach to the K_{I} and K_{II} solutions for two semi-infinite solids with connection under shear loading conditions based on the Westergaard stress function in Tada et al. [9]. The stress intensity factors $K_{\mathrm{II,TPI}}$ and $K_{\mathrm{I,TPI}}$ based on the Westergaard stress function are [9]

$$K_{\mathrm{II,\,TPI}} = \frac{\sqrt{2}F}{b\sqrt{\pi w}} \tag{13}$$

and

$$K_{\mathrm{I,\,TPI}} = 0 \tag{14}$$

An approximate K_{I} solution is also proposed by Sripichai et al. [10] as a linear function of w/t for $0 \le w/t < 2$ for laser welds in lap-shear specimens with sheets of equal thicknesses as

$$K_{\mathrm{I}} = \frac{\sqrt{3}}{2}\frac{F}{b\sqrt{t}}\frac{w}{2t} \tag{15}$$

4.2.2 Computational stress intensity factor solutions for specimens with different sheet thicknesses

Finite element analyses were carried out in order to obtain the global stress intensity factor solutions as functions of the weld width and to determine the ranges of the weld width where the analytical solutions in Equations (5) – (12) are applicable. Figure 4.4(a) shows a schematic of a two-dimensional finite element model of a lap-shear specimen where the shaded region represents the idealized weld zone. The specimen has the sheet thickness t_u and t_l for the upper and lower sheets, respectively, the length L, the overlap length V, and the weld width w. The $x-y$ coordinate system is shown in the figure. The left edge has a fixed displacement condition along the interfacial surface while the right edge has a concentrated force per unit width, F/b, applied along the interfacial surface in the $+x$ direction. Here, F denotes the applied force and b denotes the width of the central portion of the specimen with the reduced width.

The two-dimensional plane-strain finite element model has the sheet thickness $t_u = 0.93$ mm and $t_l = 1.86$ mm for the upper right and lower left sheets, respectively, length $L = 95$ mm, and overlap length $V = 30$ mm. The width b of the central portion of the specimen is taken as 8 mm to calculate the applied load per unit width for the finite element analyses. The ratio of the sheet thicknesses δ is fixed at 0.5 and the weld width *w* is varied in the finite element analyses to investigate the effect of the weld width on the stress intensity factor solutions. Figure 4.4(b) shows a close-up view of the finite element mesh near the pre-existing crack tips for $w/t_u = 4$. Although the laser welds in lap-shear specimens have weld bead protrusions [11], the weld, in the present study, is modeled as an idealized weld without weld bead protrusion in the finite element analyses to validate the analytical stress intensity factor solutions in Equations (5) – (12). Second-order quarter point crack-tip elements (CPE8R) with collapsed nodes were used to model the $1/\sqrt{r}$ singularity near the crack tip. The weld metal and the base metal are assumed to be linear elastic material with Young's modulus of $E = 206$ GPa and the Poisson's ratio $\nu = 0.3$. Computations were performed using the commercial finite element software ABAQUS [12].

Figure 4.5(a) shows the normalized analytical K_{I} and K_{II} solutions in Equations (7) and (8) for the right pre-existing crack tip based on the structural stress of the two-beam model. The normalized computational K_{I} and K_{II} solutions and the normalized $K_{\mathrm{II,TPI}}$ solution in Equation (13) are also shown in Figure 4.5(a). All the solutions in Figure 4.5(a) are normalized by $F/b\sqrt{t_u}$. Figure 4.5(a) shows that when the normalized weld width w/t_u increases, the normalized computational K_{I} and K_{II} solutions

approach to the analytical solutions in Equations (7) and (8). As the normalized weld width w/t_u decreases, the normalized computational K_{I} and K_{II} solutions approach to the analytical solutions based on the Westergaard stress function in Equations (13) and (14). After a normalized weld width $w/t_u = 3$, the analytical solutions in Equations (7) and (8) and the computational solutions are almost equal.

For small weld widths, the stress singularity due to the crack tip may cause the stress distribution in the middle portion of the connection of the two beams in Figures 4.2(a) and 4.2(b) to deviate from the stress distribution derived from the beam bending theory and thus the energy released rate is different from that based on the beam bending theory. Therefore, the computational K_{I} and K_{II} solutions are different from the analytical K_{I} and K_{II} solutions based on Equations (5) and (6). For a large weld widths, the effect of the crack tip singularity is only limited to the small regions near the crack tips in the connection region of the two beams and thus the stress distribution in the middle portion agrees with that derived from the beam bending theory far away from the tips.

The computational results shown in Figure 4.5(a) indicate that the analytical stress intensity factor solutions in Equations (7) and (8) based on the beam bending theory seem to be able to characterize reasonably well the global stress intensity factors of laser welded lap-shear specimens for $w/t_u \geq 3$. From the computational results in Figure 4.5(a), the K_{II} solutions can be estimated by Equation (13) for $0 \leq w/t_u < w_t/t_u$ and by Equation (6) for $w/t_u > w_t/t_u$. Here, w_t/t_u can be determined by Equations (13) and (6)

as about 0.5. From Figure 4.5(a), an approximate K_{I} solution is also proposed as a linear function of w/t for $0 \le w/t < 2$ as

$$K_I^A = \overline{K}_I^A \frac{F}{b\sqrt{t_u}} \frac{w}{2t_u} \tag{16}$$

where, $\overline{K}_I^A$ is obtained from Equation (7) for a particular value of δ. For $w/t_u \ge 2$, the K_{I} solutions can be estimated by Equation (5). In summary, the K_{I} and K_{II} solutions can be determined by Equations (5), (6), (13) and (16) for a wide range of w/t_u for the right pre-existing crack tip for sheets with different thicknesses.

Figure 4.5(b) shows the normalized analytical K_{I} and K_{II} solutions in Equations (11) and (12) for the left pre-existing crack tip based on the structural stress of the two-beam model. A trend similar to that in Figure 4.5(a) is also observed in Figure 4.5(b). Figure 4.5(b) shows that when the normalized weld width w/t_u increases, the normalized computational K_{I} and K_{II} solutions approach to the analytical solutions in Equations (11) and (12). When the normalized weld width w/t_u is larger than 2, the analytical and computational $\overline{K}_{\mathrm{II}}$ solutions are very close. However, the computational $\overline{K}_{\mathrm{I}}$ solutions appear to approach the analytical $\overline{K}_{\mathrm{I}}$ solutions when the normalized weld width w/t_u is larger than 5. It should be noted that the thickness of the lower sheet is twice that of the upper sheet in the finite element analyses. As the stress intensity factor solutions for the right pre-existing crack tip are higher than those for the left pre-existing crack tip, the stress intensity factor solutions for the right pre-existing crack tip are more important from the viewpoint of engineering applications. Therefore, it is not attempted here to

propose approximate stress intensity factor solutions for the left pre-existing crack tip to cover a wide range of w/t_u as is done for the right pre-existing crack tip.

Figures 4.6(a) and 4.6(b) show the normalized analytical stress intensity factor K_{I} and K_{II} solutions , respectively, based on Equations (7), (8), (11) and (12) for the right and left pre-existing crack tips as a function of the ratio of the sheet thicknesses δ. It is noted that $\overline{K}_{\mathrm{I}}$ and $\overline{K}_{\mathrm{II}}$ solutions are larger for the right pre-existing crack tip as compared to the $\overline{K}_{\mathrm{I}}$ and $\overline{K}_{\mathrm{II}}$ solutions for the left pre-existing crack tip. The two pre-existing crack tips have the same stress intensity factor solutions as the thicknesses of the two sheets become equal. Note that the thickness of the lower sheet affects the stress intensity factor solutions for both pre-existing crack tips. The $\overline{K}_{\mathrm{I}}$ solutions for the two crack tips increase as the thickness ratio δ increases to 1. However, $\overline{K}_{\mathrm{II}}$ solutions of the right crack tip decrease while the $\overline{K}_{\mathrm{II}}$ solutions of the left crack tip increase as the thickness ratio δ increases to 1.

4.3. Effect of gap on fatigue behavior of laser welds

4.3.1 Experimental observations

A gap between the laser welded sheets may be left intentionally to provide an escape route for the vapors produced during the welding process. The gap can also be produced inadvertently from a lack of good metal fit-up due to the improper clamping and positioning of the sheets during the welding process. Figure 4.7 shows an optical micrograph of the etched cross section of a weld with a gap in a specimen that was

partially tested under quasi-static loading conditions. The gap between the welded sheets is marked on both sides of the weld in Figure 4.7. The gap between the sheets can cause the spread of the molten metal in the lateral direction between the two sheets and increase the width of the weld joint. The presence of the gap between the welded sheets can also influence the formation of the round weld bead protrusion. Examination of a limited number of cross sections of laser welded lap-shear specimens showed that if a gap exists between the two sheets, the round bead protrusion becomes shallow or even cause an underfill due to the molten metal being distributed into the gap as shown in Figure 4.7.

Wang and Ewing [13] reported increase in the static strength of 2.7 mm thick laser welded steel sheets with a gap between the sheets due to increase of the weld width. Under lap-shear loading conditions, the gap can create extra moment to the weld zone and may negate the increase in strength associated with the larger weld width. Further study may be required to fully understand the effect of the gap on the strength of laser welded lap joints. The effect of the gap on the fatigue strength of laser welded joints was investigated experimentally by Flavenott [3] and Wang and Ewing [13]. They reported that the presence of the gap between the welded sheets caused a reduction in the fatigue lives of the welds. As observed from the micrographs of partially failed specimens of laser welded high strength low alloy steel sheets [10, 14], fatigue cracks are initiated from the pre-existing crack tips and propagate through the sheet thickness of the upper right sheet under high cycle loading conditions. From the micrographs of the failed specimens, the crack propagation angle was found to be very close to $90°$ for all the load ranges.

4.3.2 Analytical local stress intensity factor solutions for kinked cracks

Figure 4.8 shows a schematic of a main crack and a kinked crack with the kink length a and the kink angle α. Here, K_{I} and K_{II} represent the global stress intensity factors for the main crack, and k_{I} and k_{II} represent the local stress intensity factors for the kinked crack. Note that the arrows in the figure represent the positive values of the global and local stress intensity factors K_{I}, K_{II}, k_{I} and k_{II}. For kinked cracks, when the kink length approaches to 0, the local stress intensity factors k_{I} and k_{II} can be expressed as functions of the kink angle α and the global K_{I} and K_{II} for the main crack. The local stress intensity factor solutions for kinked cracks with vanishing crack length are given as [15, 16]

$$\left(k_{\mathrm{I}}\right)_0 = \frac{1}{4}\left(3\cos\frac{\alpha}{2} + \cos\frac{3\alpha}{2}\right)K_{\mathrm{I}} - \frac{3}{4}\left(\sin\frac{\alpha}{2} + \sin\frac{3\alpha}{2}\right)K_{\mathrm{II}} \tag{17}$$

$$\left(k_{\mathrm{II}}\right)_0 = \frac{1}{4}\left(\sin\frac{\alpha}{2} + \sin\frac{3\alpha}{2}\right)K_{\mathrm{I}} + \frac{1}{4}\left(\cos\frac{\alpha}{2} + 3\cos\frac{3\alpha}{2}\right)K_{\mathrm{II}} \tag{18}$$

where $\left(k_{\mathrm{I}}\right)_0$ and $\left(k_{\mathrm{II}}\right)_0$ represent the local k_{I} and k_{II} solutions for the kink length a approaching to 0. As shown in Figure 4.7, the crack tips become notch tips with the presence of the gap. When the crack becomes a rectangular notch, the singularity for the stresses and strains near the notch tips changes. No analytical solutions as in Equation (17) and (18) for cracks emanating from the notch tips are available. Therefore, finite element analyses were used to obtain the local stress intensity factor solutions for the cracks emanating from the notch tips.

4.3.3 Stress intensity factor solutions for cracks from notch tips

Finite element analyses were carried out to obtain the stress intensity factor solutions for cracks emanating from the notch tips of the weld with gap in lap-shear specimens. Five normalized gaps g/t of 0, 0.05, 0.1, 0.2 and 0.3 are considered in this investigation to study the effect of the gap on the stress intensity factor solutions for the cracks. Figure 4.9(a) shows a schematic of a two-dimensional finite element model of a lap-shear specimen with a weld gap and the boundary conditions. Based on the experimental observations of the micrographs of welds with gaps, the gap is modeled as a rectangular notch in the finite element analyses. The thin solid lines in the schematic show the cracks emanating from the pre-existing notch tips and propagating in the upper right and lower left sheets. The shaded region in the figure represents the weld zone. The specimen has the sheet thickness t for both the upper right and lower left sheets, the length L, the overlap length V, the weld width w, and the gap g. The $x-y$ coordinate system is shown in the figure. The left edge has a fixed displacement condition along the interfacial surface of the lower sheet and the doubler while the right edge has a concentrated force per unit width, F/b, applied along the interfacial surface of the upper sheet and the doubler in the $+x$ direction. Here, F denotes the applied force and b denotes the width of the central portion of the specimen with the reduced width.

The two-dimensional plane-strain finite element model has the weld width $w = 1$ mm, sheet thickness $t = 1$ mm for both the upper and lower sheets, respectively, length $L = 95$ mm, and overlap length $V = 30$ mm. The width b of the central portion of the specimen is taken as 8 mm to calculate the applied load per unit width for the finite element analyses. Figure 4.9(b) shows a close-up view of the finite element mesh near

the weld. The weld was modeled as an idealized weld without weld bead protrusion or underfill. In this investigation, two cracks of the same length emanating from both pre-existing notches are modeled in the finite element analyses to represent the cracks in the laser weld as shown in the micrographs of partially failed specimens. Usually, one crack becomes dominant and results in the final failure of the specimen. Finite element analyses for a weld with single crack of different crack lengths were also carried out. The results indicate that the effective stress intensity factor ranges are almost the same for the welds with single and two cracks for a given normalized crack length, a/t. Second-order quarter point crack-tip elements (CPE8R) with collapsed nodes were used to model the $1/\sqrt{r}$ singularity near the crack tip. The weld metal and the base metal are assumed to be linear elastic material with Young's modulus of $E = 206$ GPa and the Poisson's ratio $\nu = 0.3$. Ten normalized crack lengths a/t of 0.025, 0.05, 0.075, 0.1, 0.2, 0.3, 0.4, 0.5, 0.6 and 0.7 are considered in the finite element analyses. Computations were performed using the commercial finite element software ABAQUS [12].

Figure 4.10(a) shows the values of $k_I/(k_1)_0$ as functions of the normalized crack length a/t for $\alpha = 90°$ and different values of the normalized gap g/t. Note that the solutions are normalized by $(k_1)_0$ in Equation (17) with kink angle $\alpha = 90°$ and the analytical global stress intensity factor $(K_I)_B$ and $(K_{II})_B$ solutions based on the beam bending theory in Sripichai et al. [10]. The solutions of Sripichai et al. [10] based on the beam bending theory are

$$(K_I)_B = \frac{\sqrt{3}}{2}\frac{F}{b\sqrt{t}} \tag{19}$$

$$(K_{II})_B = \frac{F}{b\sqrt{t}} \tag{20}$$

Figure 4.10(a) shows that the values of $k_I/(k_I)_0$ increase monotonically with the kink length. However, as the gap increases, the stress intensity factor solutions increase for a given a/t. The average differences between the stress intensity factor $k_I/(k_I)_0$ solutions for cracks with gap and without gap range from about 3.3% to 21.5% as the normalized gap g/t increases from 0.05 to 0.3. Figure 4.10(b) shows the values of $|k_{II}|/(k_I)_0$ as functions of the normalized crack length a/t for $\alpha = 90°$ and different values of the normalized gap g/t. Note that the local stress intensity factor k_{II} solutions are negative based on the definitions shown in Figure 4.8. Figure 4.10(b) shows that the absolute values of $|k_{II}|/(k_I)_0$ decrease monotonically with the crack length and appear to approach to 0 for a very large crack length. However, the values of $|k_{II}|/(k_I)_0$ are higher for larger gaps. The average differences between the stress intensity factor $|k_{II}|/(k_I)_0$ solutions for cracks with gap and without gap range from about 15% to 80% as the normalized gap g/t increases from 0.05 to 0.3. The higher effective stress intensity factor ranges due to the gap can significantly reduce the fatigue lives of the welds with gap as compared to those for welds without gap. Figures 4.10(a) and 4.10(b) show that the crack growth is under mixed mode I and II loading conditions. However, the cracks are under dominant mode I loading conditions.

4.4. A structural stress model for welds with gap and fatigue life estimations

Figure 4.11(a) shows a schematic of a laser weld with a gap in a lap-shear specimen under the applied load per unit width F/b, marked as the bold arrows. Here, F denotes the applied force and b denotes the width of the central portion of the specimen with the reduced width. The upper and lower sheets have the same thickness t. The weld width w, the sheet length L, the overlap length V, and the gap g are shown in the schematic. The resultant force per unit width F/b is applied to the inner surfaces of the right edge of the upper sheet and the left edge of the lower sheet. Due to the presence of the gap between the upper right and lower left sheets, the specimen becomes a two-force member when mounted in the lap-shear testing fixture without the constraint of the bending moment at the specimen ends. The action line of the applied resultant force per unit width F/b is therefore realigned as shown in Figure 4.11(a). Figure 4.11(b) shows a schematic of the applied loading condition near the right edge surface of the specimen. The angle of inclination of the force per unit width, F/b, with respect to the horizontal axis is represented as θ. As shown in Figure 4.11(b), the inclined resultant force F/b is resolved into the horizontal and vertical components F_1/b and F_2/b, respectively.

Figure 4.11(c) shows the resultant forces F_1/b and F_2/b and the resultant moment M_1 acting on the cross section of the upper right sheet at the weld edge. As shown in the figure, the horizontal force per unit width F_1/b is shifted from the inner surface of the upper right sheet to the middle surface. Since the value of g is small compared to $2L-V$, θ can be determined from Figure 4.11(a) as

$$\theta = \frac{g}{(2L - V)} \tag{21}$$

Also, the two force components per unit width, F_1/b, and F_2/b, can be approximated as F/b and $(F/b)\,\theta$, respectively.

The moment per unit width, M_1, at the weld edge can be written as

$$M_1 = \frac{Ft}{2b} + \frac{F\theta}{b} L' \tag{22}$$

Here, L' is

$$L' = L - \frac{1}{2}(V + w) \tag{23}$$

Both the membrane force per unit width, F_1/b, and the bending moment per unit width, M_1, contribute to the structural stress at the edge of the weld. For small θ's and w's, the structural stress at the lower surface of the cross section near the weld of the upper right sheet can be written as

$$\sigma = \frac{F}{bt}\left(4 + 3\frac{g}{t}\right) \tag{24}$$

For a weld without gap, the above equation simplifies to

$$\sigma = \frac{4F}{bt} \tag{25}$$

Equation (24) indicates that the gap between the welded sheets increases the structural stress at the inner surface of the upper right or lower left sheet near the edge of the weld. The increased structural stress reduces the fatigue lives of the specimens with weld gap as compared to those for the specimens without weld gap.

The structural stress approach appears to be promising to estimate the fatigue lives of weld joints in thin sheets. Tran et al. [17, 18] recently used the closed-form

analytical structural stress solutions for spot welds to estimate the fatigue lives of aluminum spot friction welds. Sripichai et al. [10] and Asim et al. [14] also used the closed-form analytical structural stress solutions to estimate the fatigue lives of laser welds in HSLA steels. In the present study, the structural stress model is based on the structural stress solutions derived from the beam bending theory. Equation (24) for the structural stress ranges at the edge of the weld bead can be used with the experimental stress-life fatigue data of the HSLA steel to estimate the fatigue lives of laser welds in lap-shear specimens. Note that the weld zone is assumed to be perfectly bonded to the base metal. The varying mechanical behavior of the material in the weld zone is also not considered in the above expression. Figure 4.12 shows the fatigue live estimates based on the structural stress model of Equation (24) for different values of the normalized gap g/t based on the stress-life fatigue data of SAE 950X steel. Reduction in the fatigue lives can be observed as the gap between the two sheets increases from 5% to 20% of the sheet thickness.

4.5. Conclusions

In this study, the effects of different thickness and gaps on the stress intensity factor solutions of laser welds in lap-shear specimens are investigated. An analytical approach based on the structural stress of the beam bending theory is used to obtain the stress intensity factor solutions for laser welds in lap-shear specimens with different sheet thicknesses. Two-dimensional finite element analyses were also carried out to obtain the stress intensity factor solutions for the welds as functions of the normalized weld width. The results of the finite element analyses are compared with the analytical stress intensity

factor solutions. The stress intensity factor solutions are higher for the right pre-existing crack tip of the load carrying upper right thinner sheet as compared to those for the left pre-existing crack tip of the load carrying lower left thicker sheet. Approximate stress intensity factor solutions as functions of the normalized weld width are also proposed for the right pre-existing crack tip of the load carrying upper right thinner sheet. Finite element analyses were also carried out to study the effects of gaps on the local stress intensity factor solutions for cracks emanating from the tips of the pre-existing notches. The results indicate that the stress intensity factor solutions for the cracks increase as the gap increases. Finally, a closed-form structural stress solution with consideration of the gap in a lap-shear specimen is developed. The closed-form structural stress solution is used to investigate the effect of gap on the fatigue lives of the welds. The results indicate that the fatigue life decreases as the gap increases.

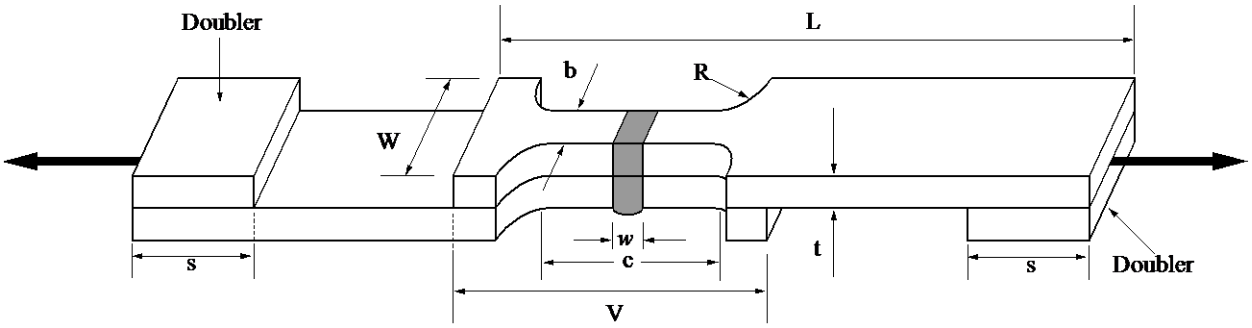

Figure 4.1. A schematic of a lap-shear specimen with sheets of equal thicknesses. The loading directions are shown as the bold arrows.

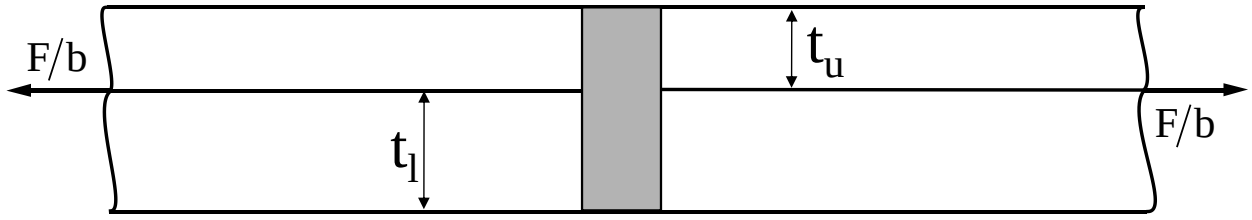

(a)

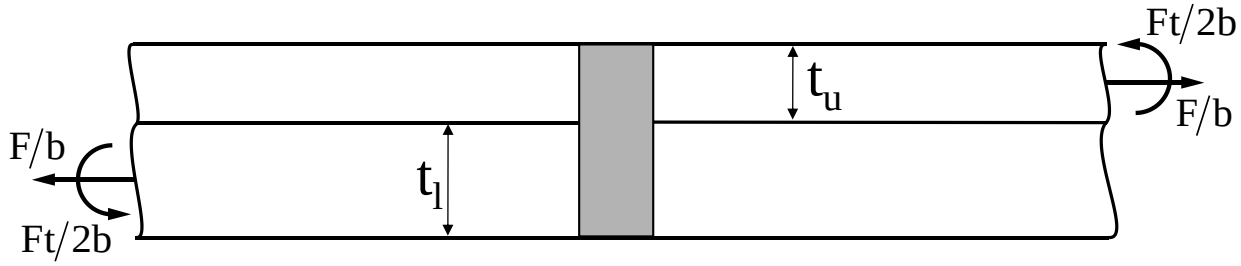

(b)

Figure 4.2. (a) A schematic of the cross section near an idealized weld as a two-strip model under lap-shear loading conditions with the weld shown as the shaded region and (b) a schematic of the two-strip model under an equivalent loading of (a).

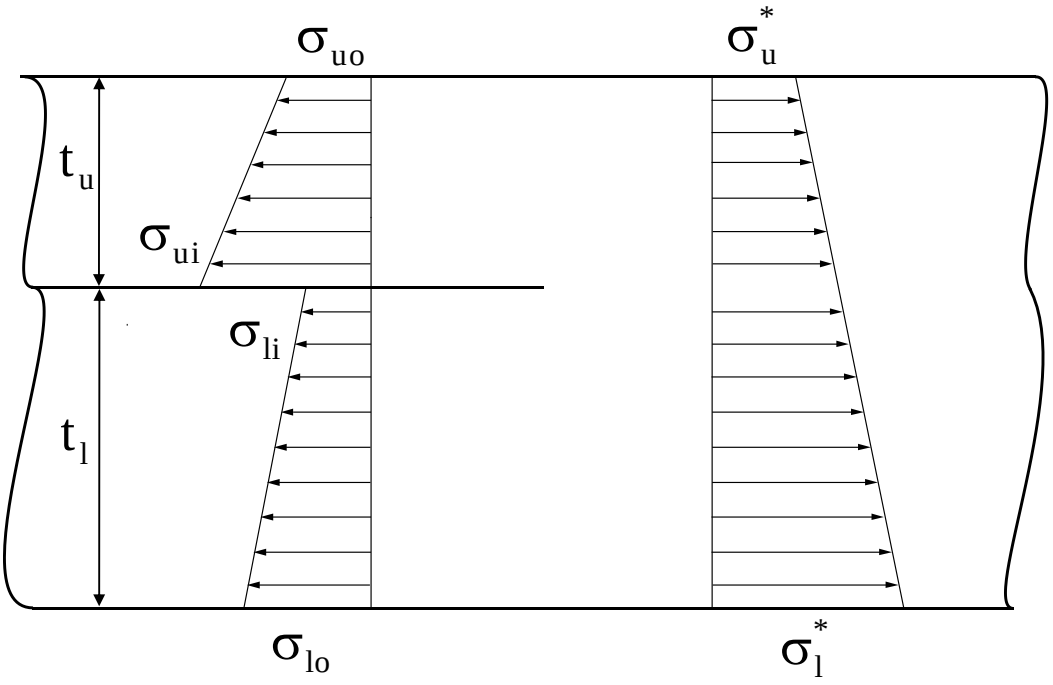

(a)

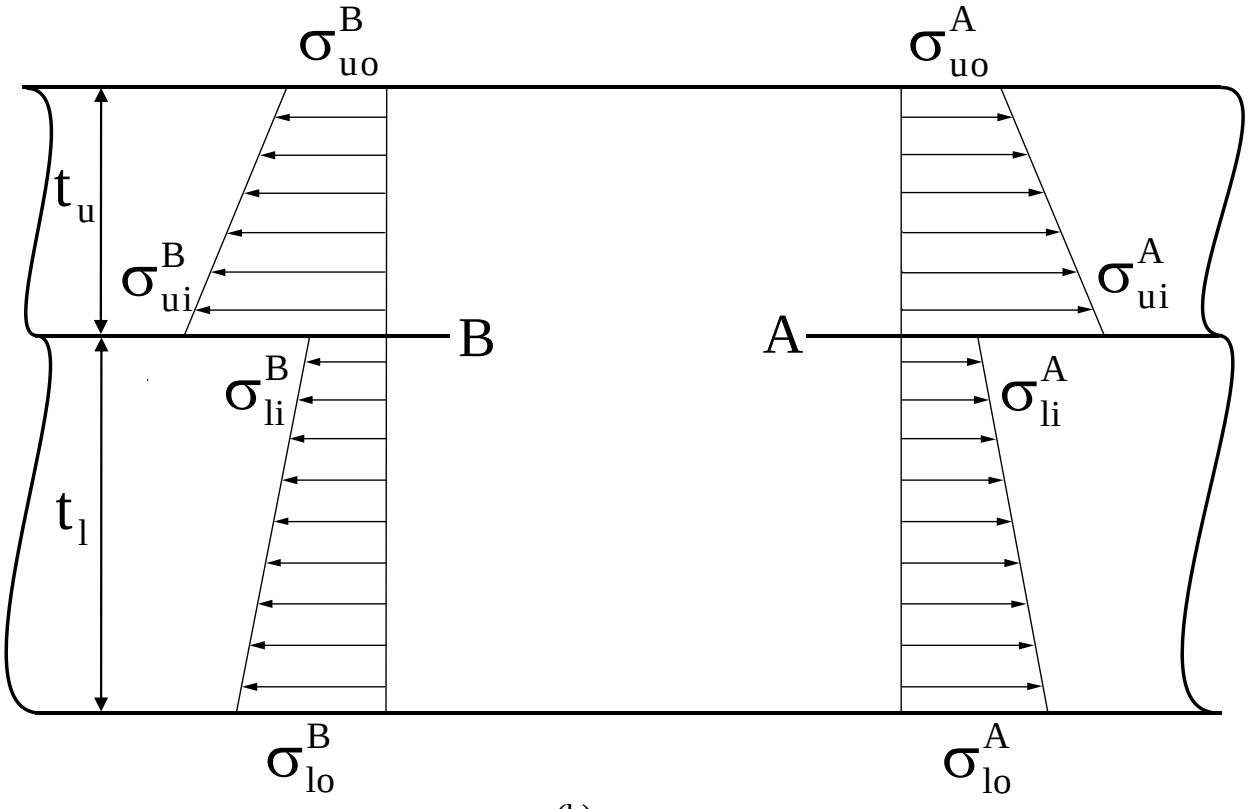

(b)

Figure 4.3. Schematics of (a) the left part of the two-strip model and (b) the two-strip model of different thicknesses with connection.

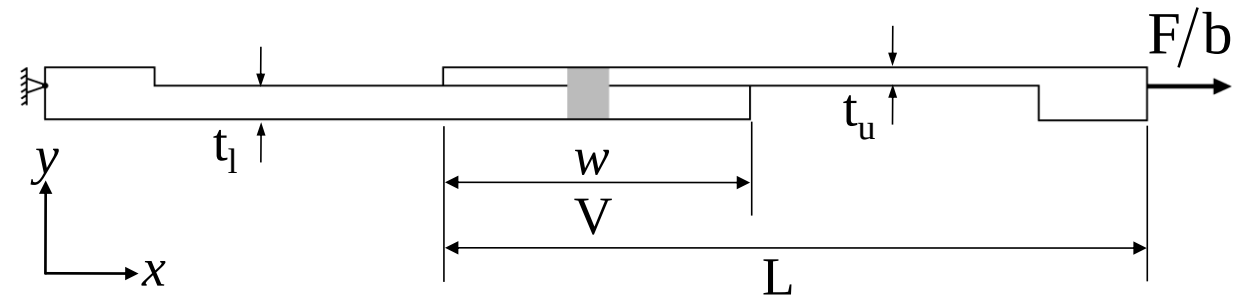

(a)

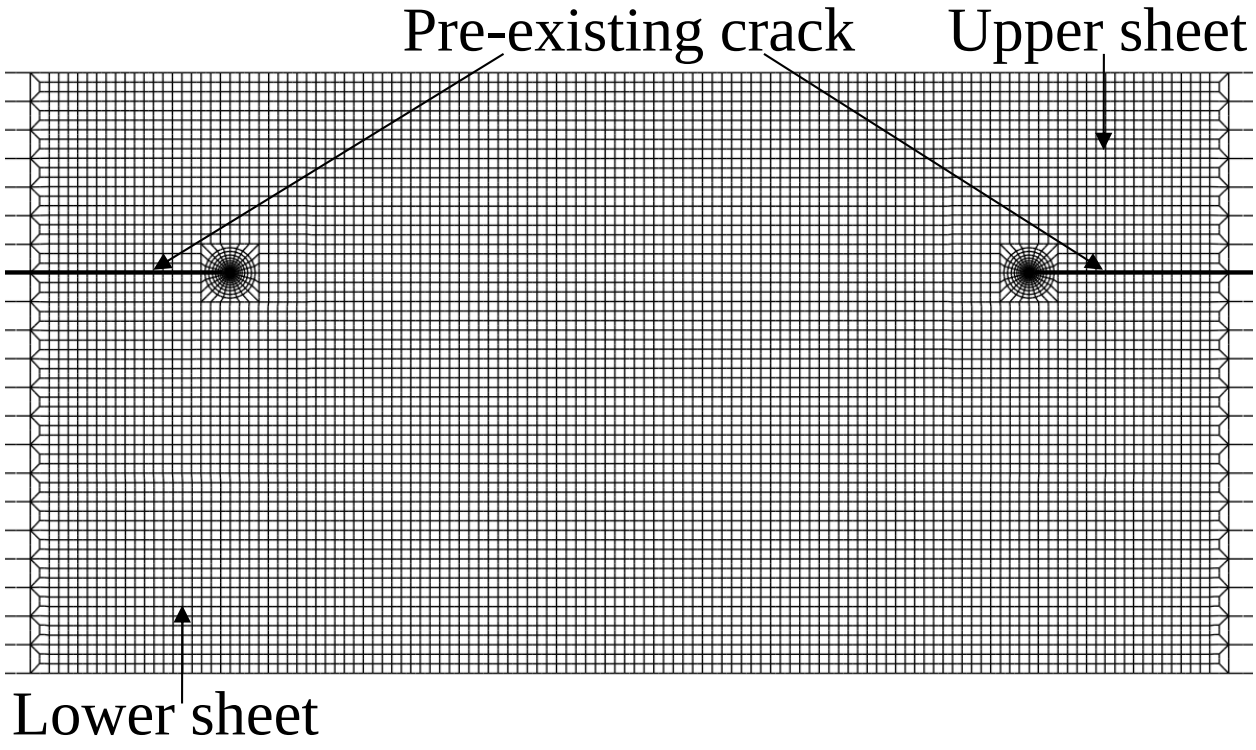

(b)

Figure 4.4. (a) A schematic of a two-dimensional finite element model of a lap-shear specimen and the boundary and loading conditions, and (b) a close-up view of the finite element mesh near the pre-existing crack tips for $w/t_u = 4$.

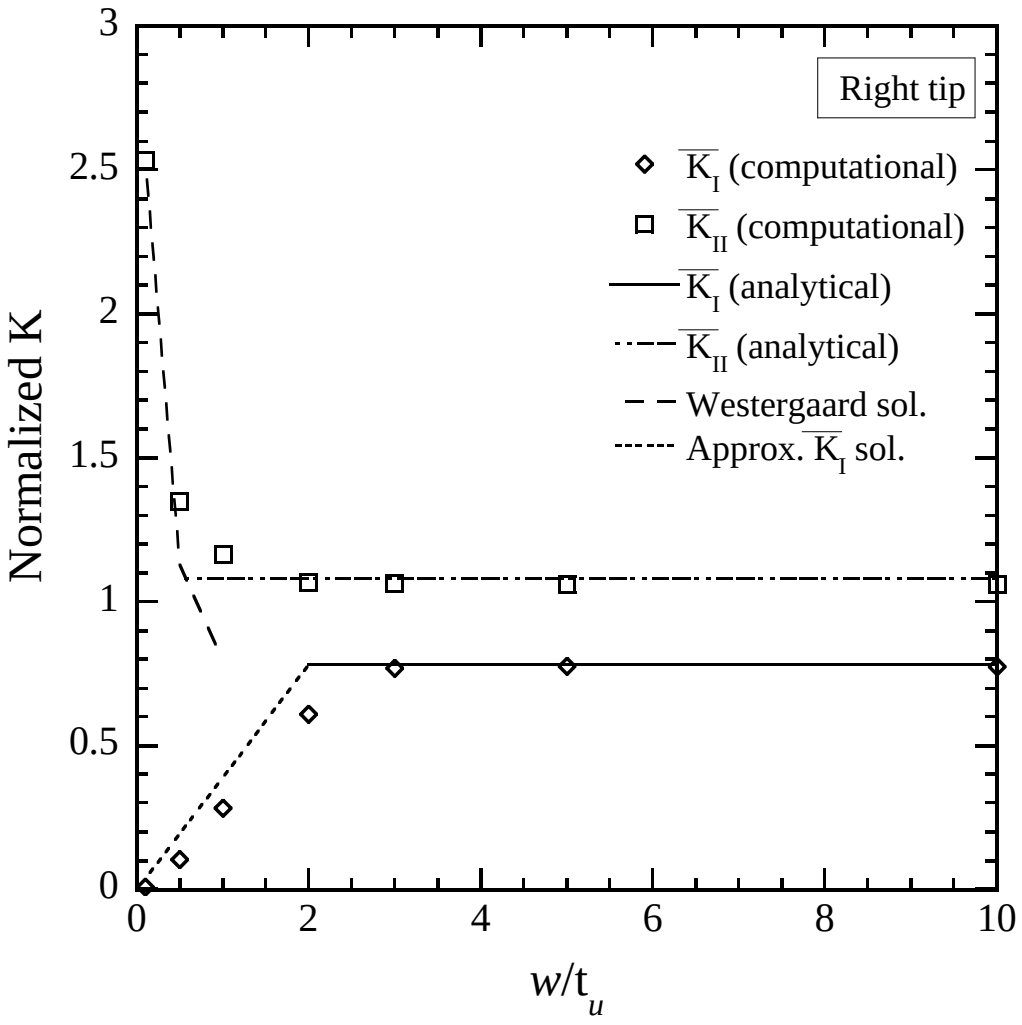
Right tip
$\overline{K_I}$ (computational)
$\overline{K_{II}}$ (computational)
$\overline{K_I}$ (analytical)
$\overline{K_{II}}$ (analytical)
Westergaard sol.
Approx. $\overline{K_I}$ sol.
Normalized K
w/t_u
0
0.5
1
1.5
2
2.5
3
0
2
4
6
8
10

(a)

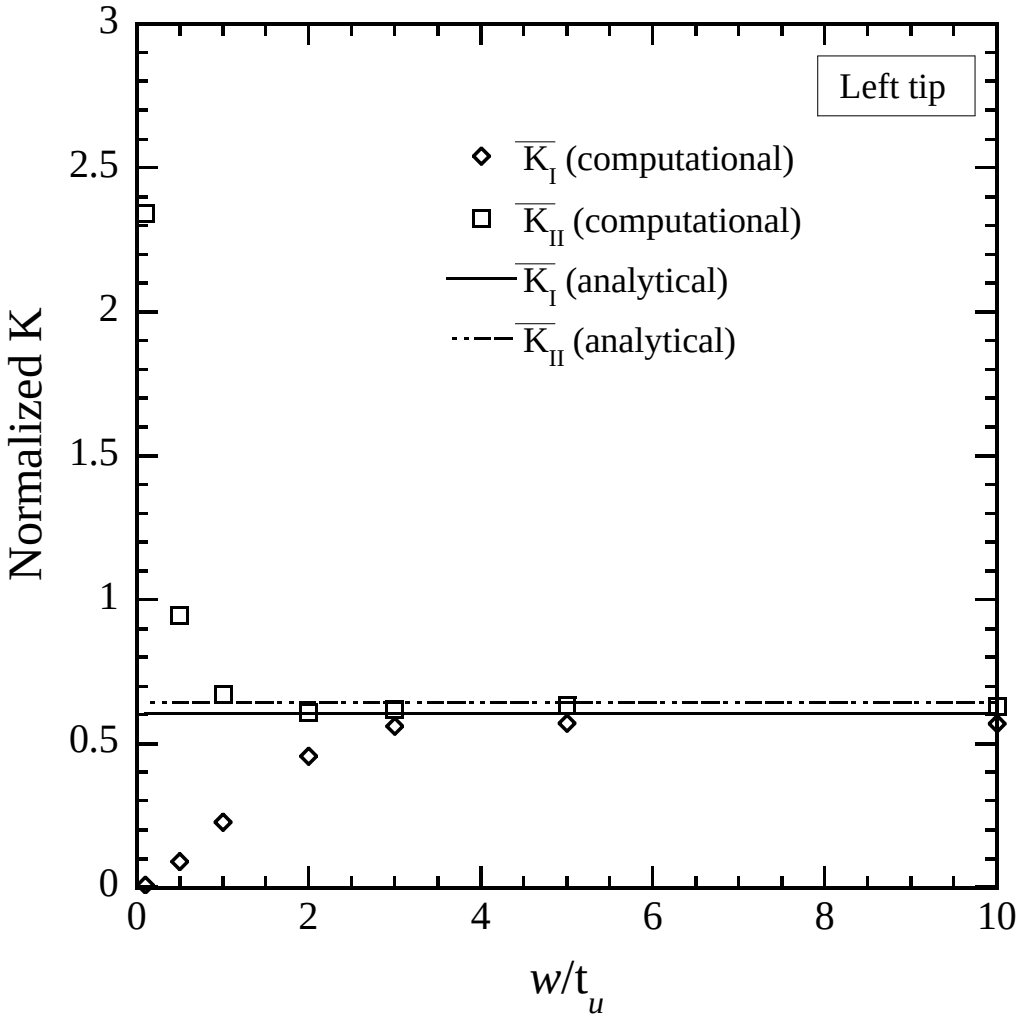

(b)

Figure 4.5. The analytical and computational normalized K_I and K_{II} solutions for (a) the right crack and (b) the left crack as functions of w/t_u for $\delta = 0.5$.

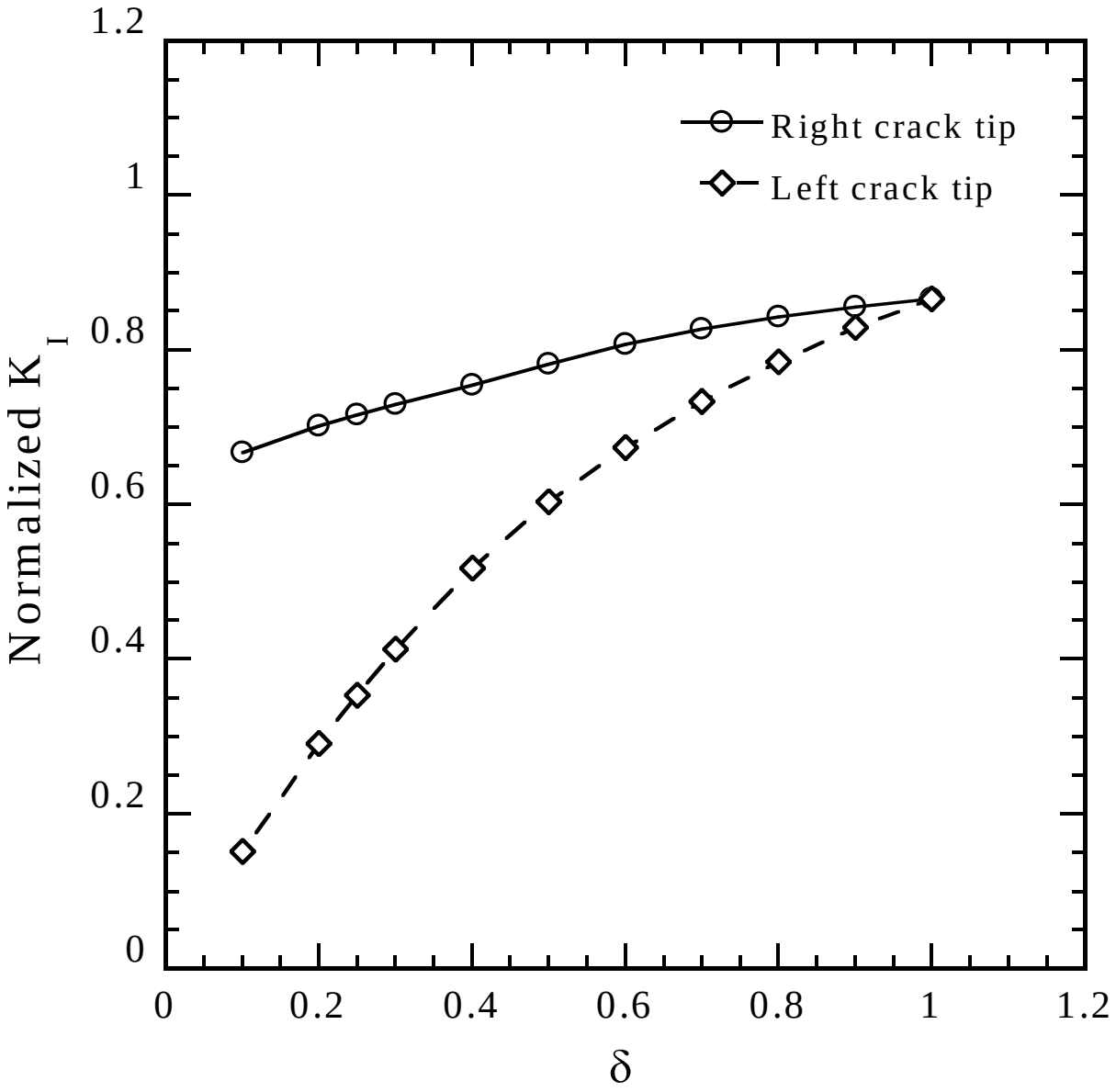
Right crack tip
Left crack tip
Normalized K_I
δ
0
0.2
0.4
0.6
0.8
1
1.2

(a)

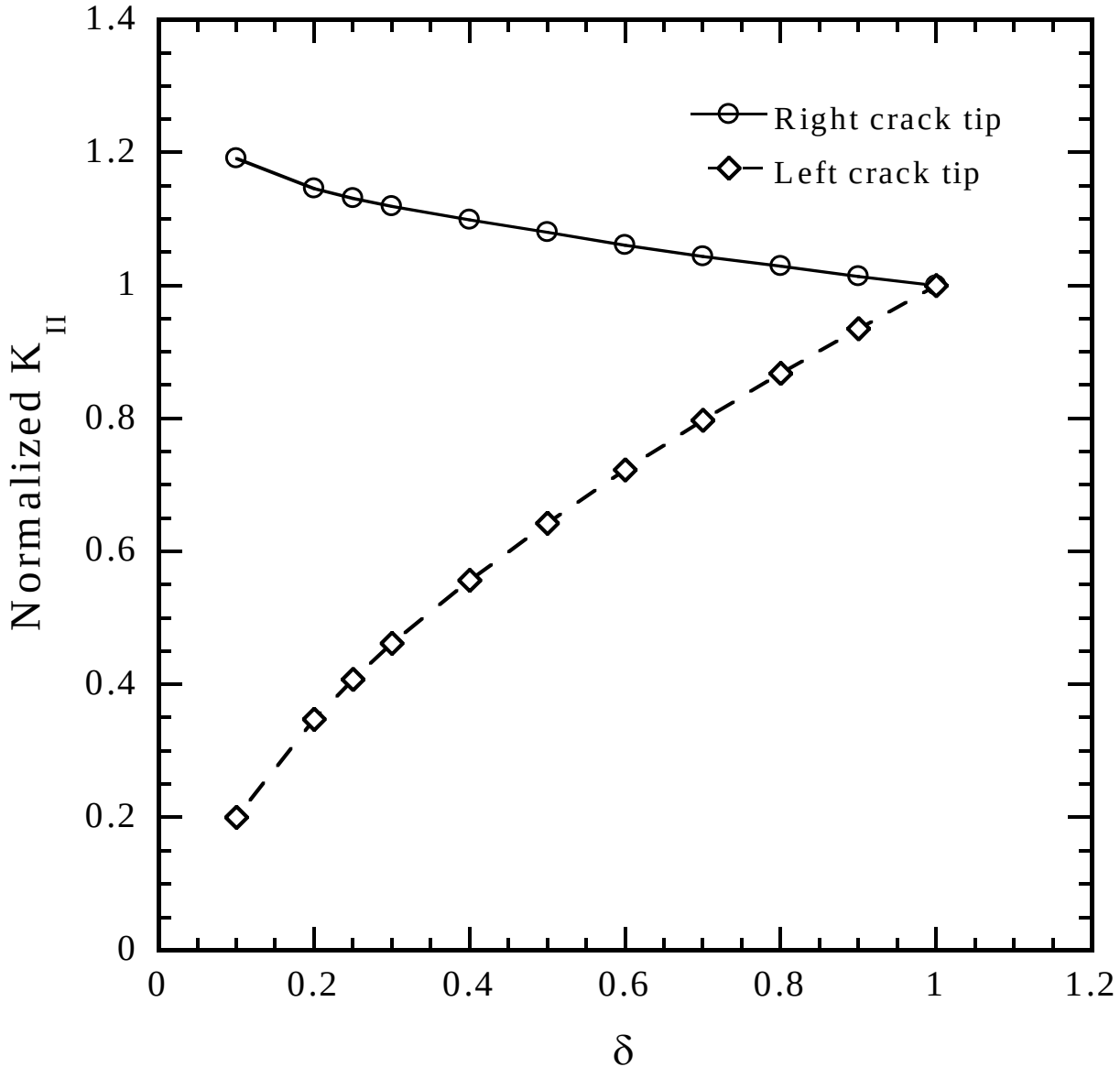

(b)

Figure 4.6. (a) The normalized K_I and (b) the normalized K_{II} solutions for the right and left pre-existing crack tips based on the analytical model of strips with different thicknesses.

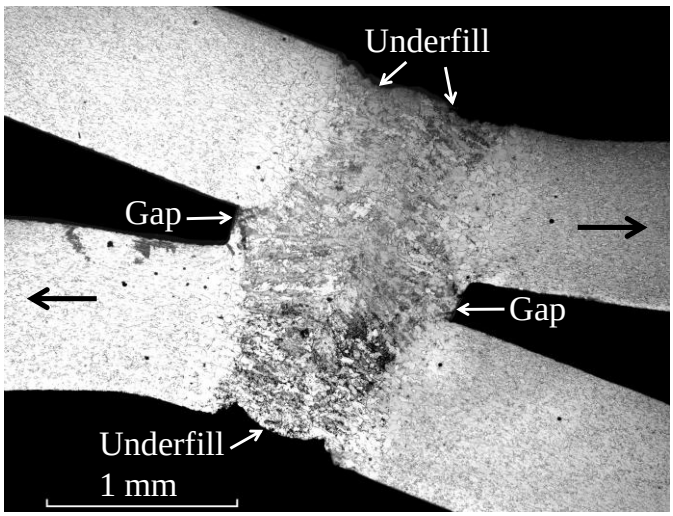

Figure 4.7. An optical micrograph of the etched cross section of a weld with a gap in a specimen that was partially tested under quasi-static loading conditions.

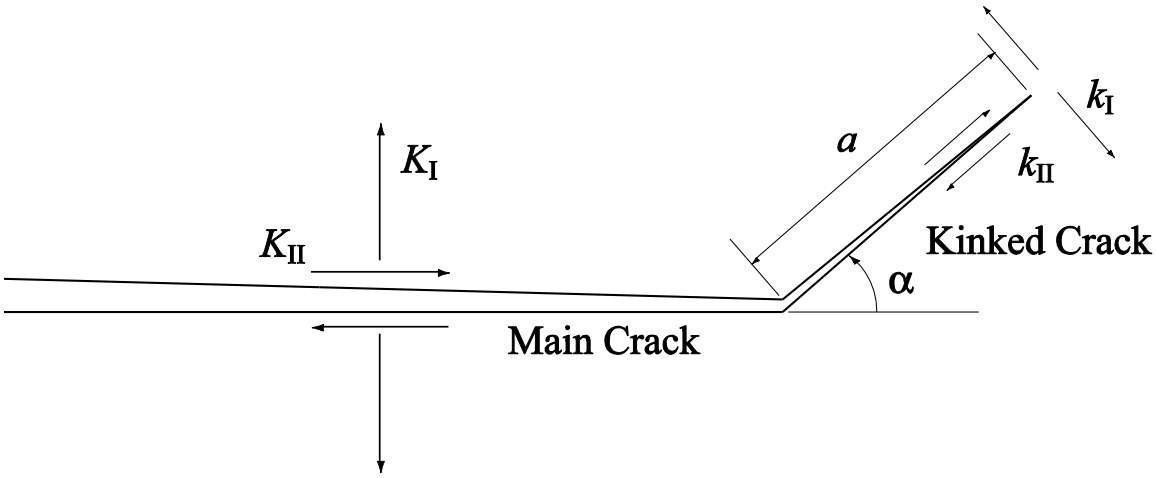

Figure 4.8. A schematic of a main crack and a kinked crack with the kink length a and the kink angle α.

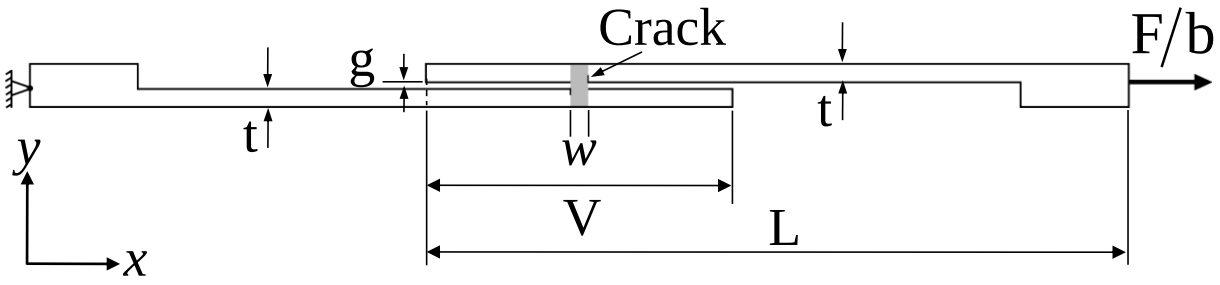

(a)

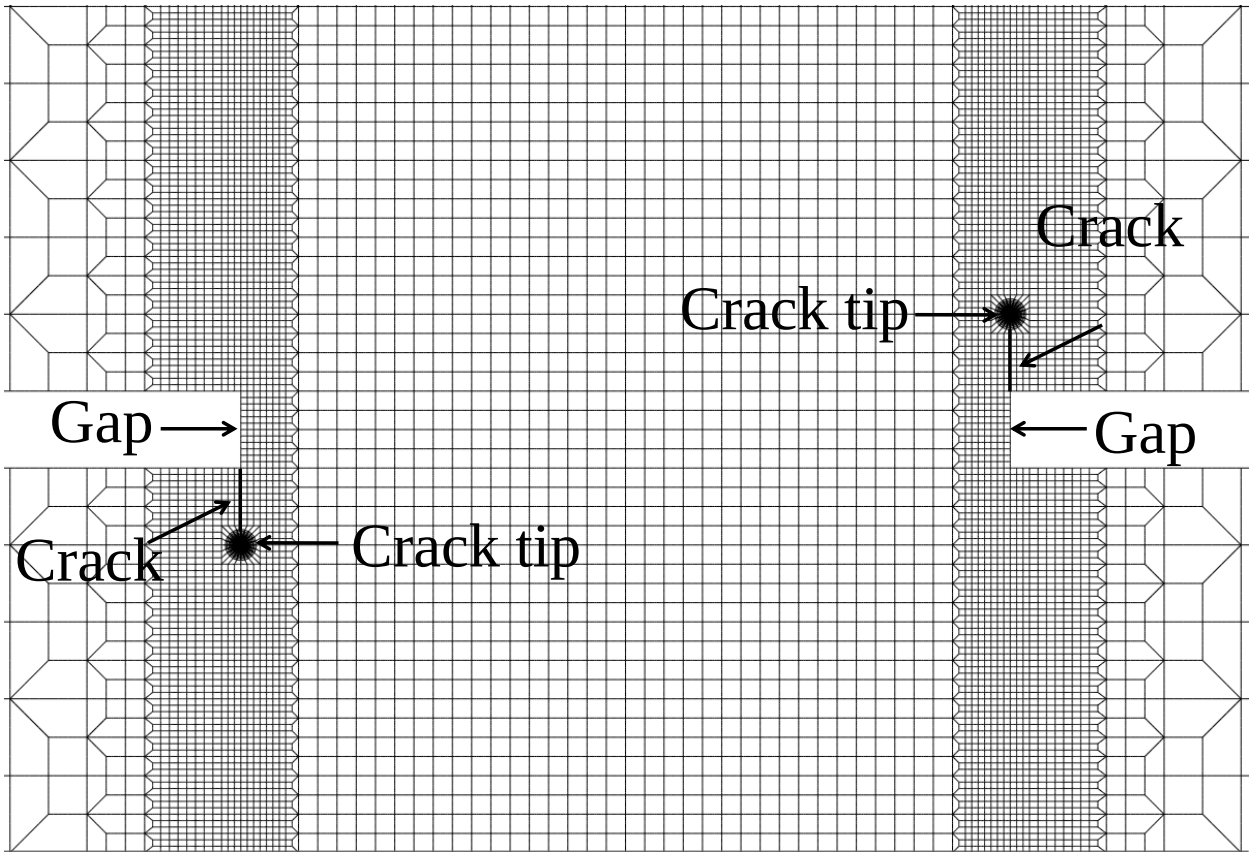

(b)

Figure 4.9. (a) A schematic of a two-dimensional finite element model of a lap-shear specimen with gap and two cracks. The boundary and loading conditions are also shown in the schematic. (b) A close-up view of the finite element mesh near the weld for the normalized gap $g/t = 0.1$ and the normalized crack length $a/t = 0.1$.

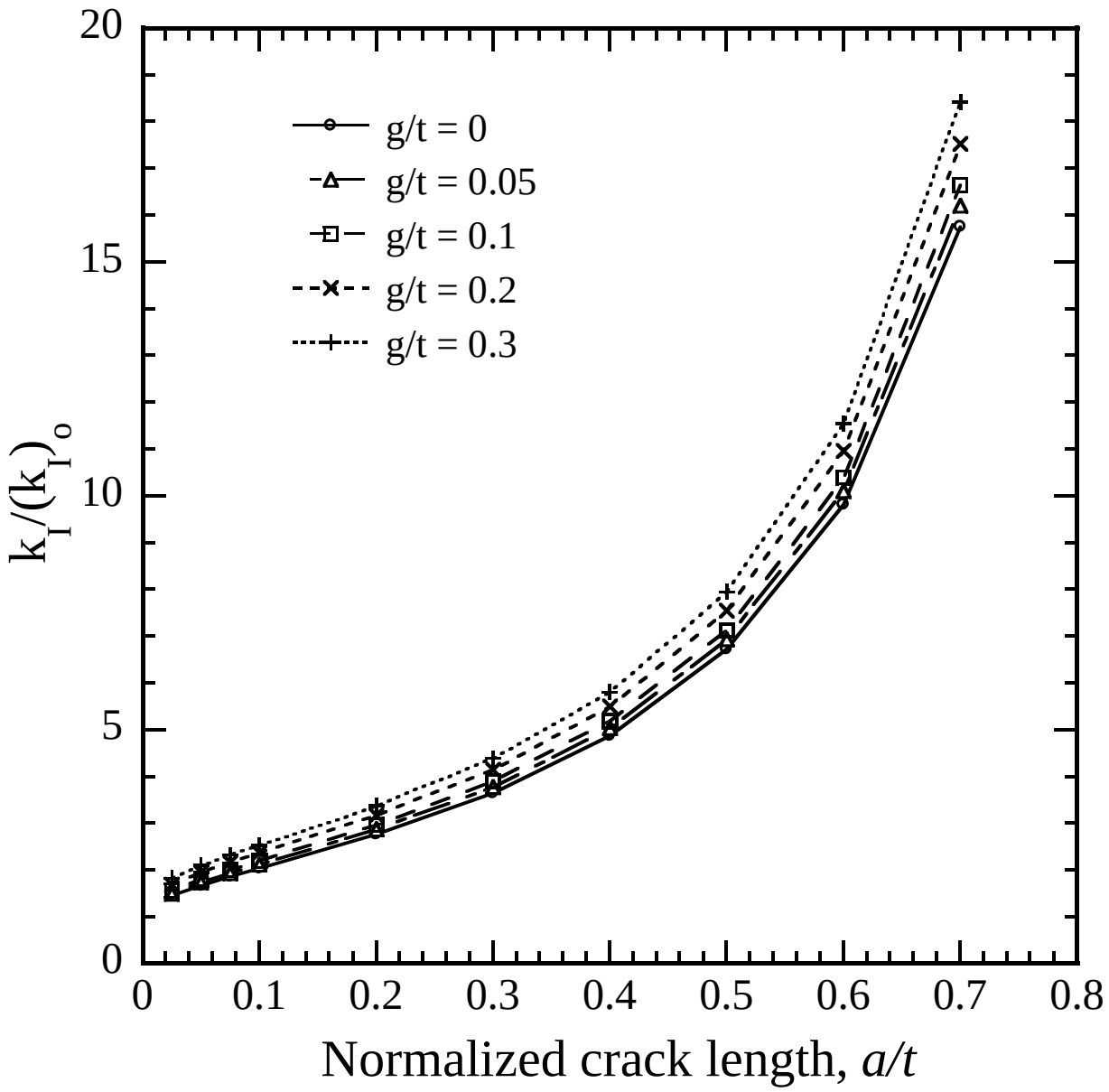
20
15
10
5
0
0
0.1
0.2
0.3
0.4
0.5
0.6
0.7
0.8
g/t = 0
g/t = 0.05
g/t = 0.1
g/t = 0.2
g/t = 0.3
$k_I/(k_I)_o$
Normalized crack length, *a/t*

(a)

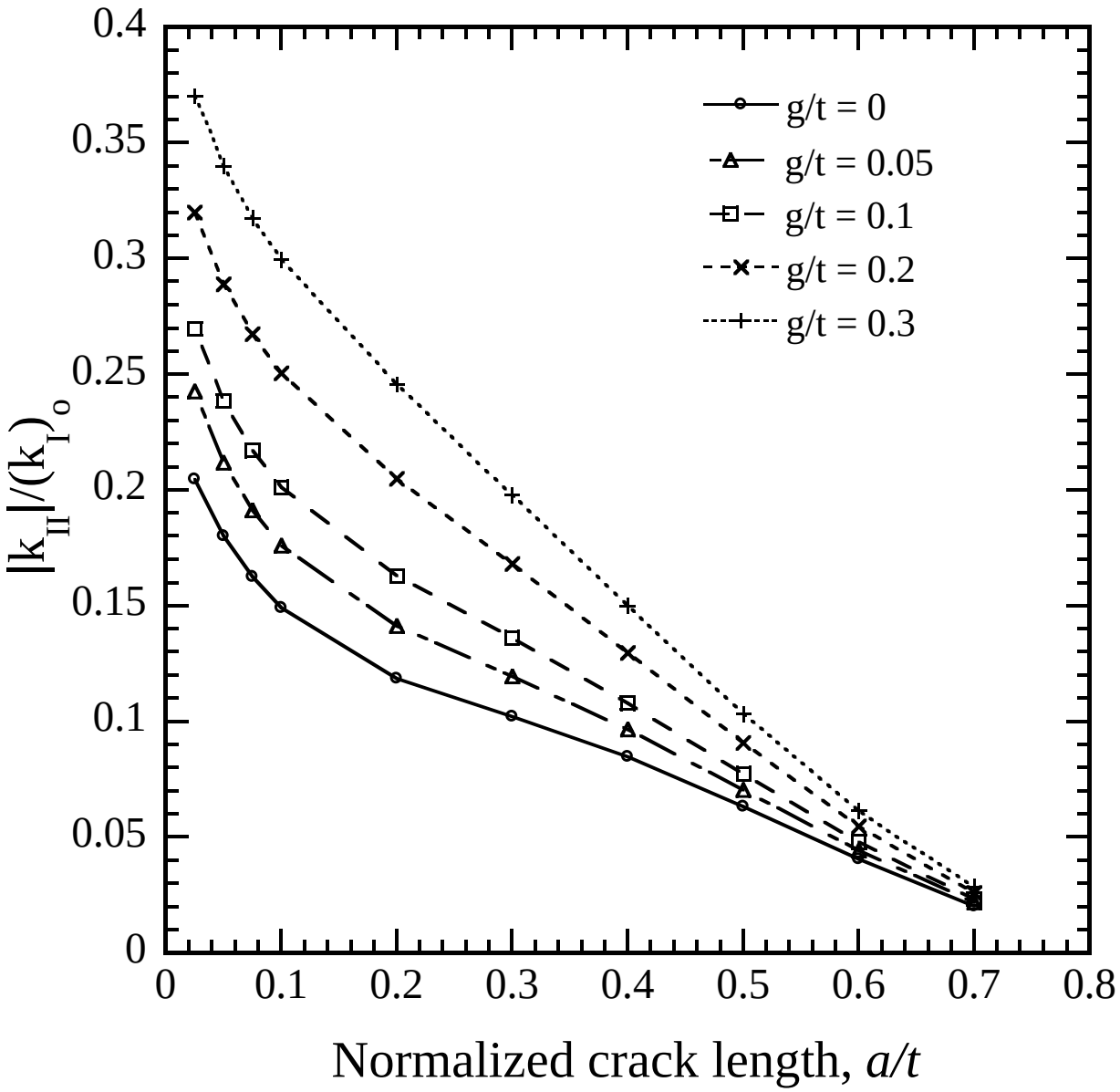

(b)

Figure 4.10. (a) The value of $k_I/(k_I)_0$ and (b) the value of $|k_{II}|/(k_I)_0$ as functions of the normalized crack length a/t for $\alpha = 90°$ and different values of the normalized gap g/t.

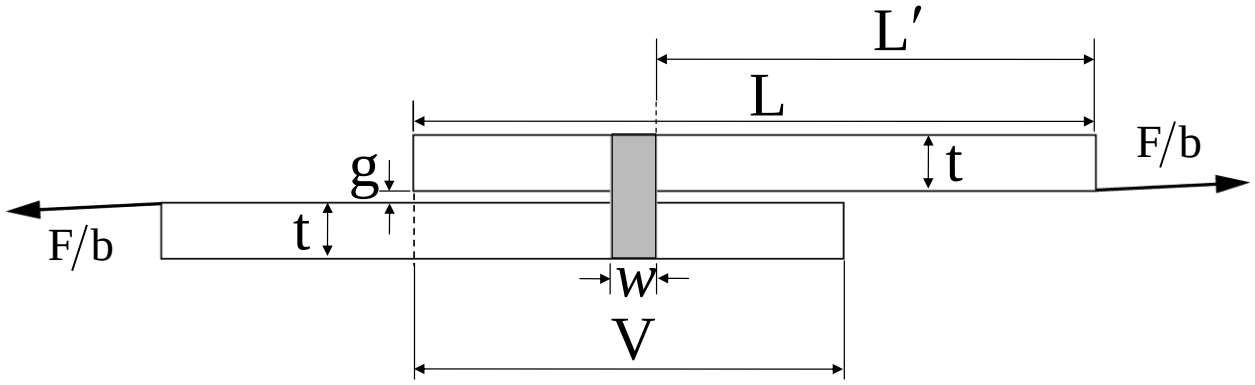

(a)

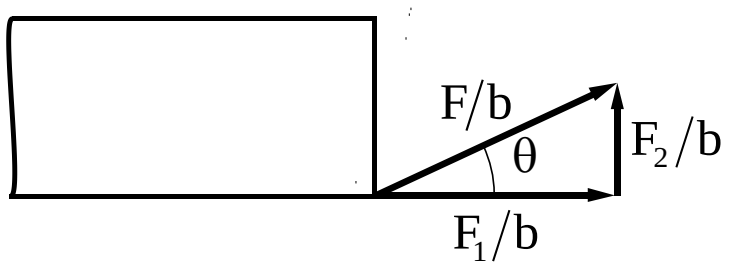

(b)

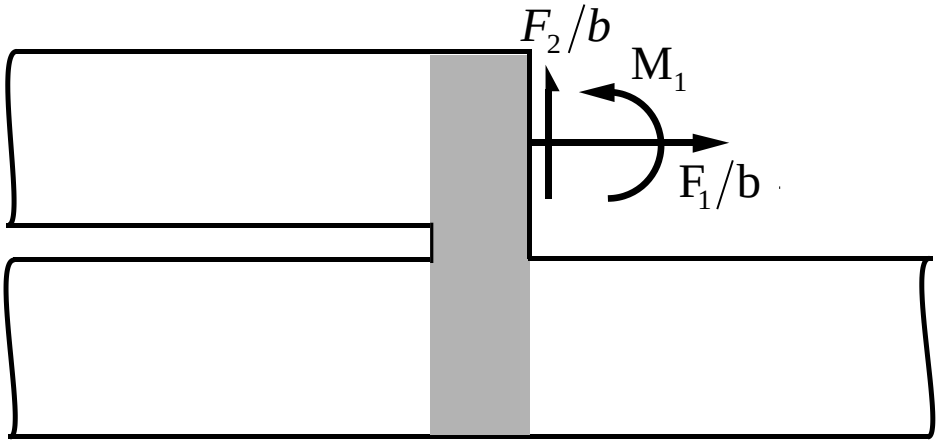

(c)

Figure 4.11. (a) A schematic of a lap-shear specimen with gap under the applied load per unit width F/b marked as the bold arrow, (b) a schematic of the applied loading condition near the right edge surface of the specimen and (c) the resultant forces F_1/b and F_2/b and the resultant moment M_1 acting on the cross section of the upper right sheet at the weld.

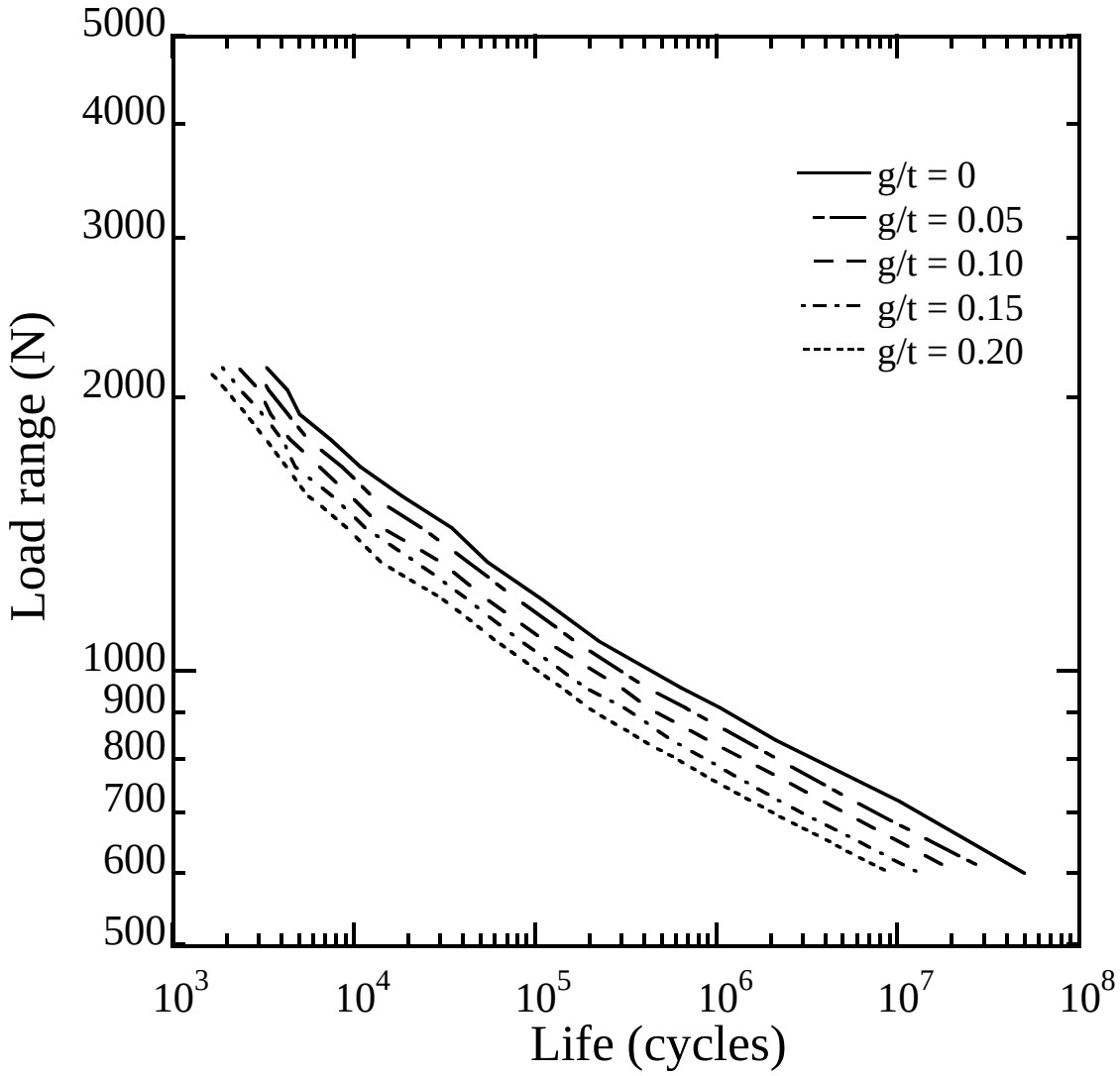

Figure 4.12. Fatigue life estimates based on the structural stress model for different values of the normalized gap g/t.

Reference

[1] Hsu C, Albright, CE, Lund RO. Fatigue strength of laser-welded lap joints. Journal of Laser Applications 1990; 2: 26-32.

[2] Wang PC, Ewing KM. A comparison of fatigue strengths: laser beam vs. resistance spot welds. Welding Journal 1991; 70: 43-47.

[3] Flavenot J-F, Deville J-P, Diboine A, Cantello M, Gobbi S-L. Fatigue resistance of laser welded lap joints of steel sheets. Welding in the World 1993; 31: 12-15.

[4] Wang PC. Fracture mechanics parameters for the fatigue resistance of laser welds. International Journal of Fatigue 1995; 17: 25-34.

[5] Kaitanov A Yu, Ozersky AD, Zabelin AM, Kislov VS. Static and fatigue strengths of laser welded overlap joints with controlled penetration. SPIE 2002; 4644: 116-126.

[6] Sripichai K, Asim K., Jo WH, Pan J, Li M. Fatigue behavior of laser welds in lap-shear specimens of high strength low alloy (HSLA) steels. SAE technical Paper No. 2009-01-0028, Society of Automotive Engineers, Warrendale PA: 2009.

[7] Zhang S. Stress intensities derived from stresses around a spot weld. International Journal of Fracture 1999; 99: 239-257.

[8] Suo Z, Hutchinson JW. Interface crack between two elastic layers. International Journal of Fracture 1990; 43: 1-18.

[9] Tada H, Paris PC, Irwin GR. The stress analysis of cracks handbook. Third Edition. New York, ASME Press; 2000.

[10] Sripichai K, Asim K, Pan J. Stress intensity factor solutions for estimation of fatigue lives of laser welds in lap-shear specimens. Submitted for publication in Engineering Fracture Mechnaics 2010.

[11] Lee J, Asim K, Pan J. Modeling of failure mode of laser welds in lap-shear specimens of HSLA steel sheets. Eng Fract Mech 2011; 78: 374-396.

[12] ABAQUS v6.7 User Manual. Providence, RI: SIMULIA; 2007.

[13] Wang PC, Ewing KM. Effects of process parameters on the fatigue strength of laser beam welds. Journal of Laser Applications 1994; 6: 14-22.

[14] Asim K, Sripichai K, Pan J. Fatigue behavior of laser welds in lap-shear specimens of high strength low alloy steel sheets. Submitted for publication in International Journal of Fracture, 2011.

[15] Bilby BA, Cardew GE, Horward IC. Stress intensity factors at the tip of kinked and forked cracks. The fourth international conference on fracture, University of

Waterloo, Ontario, June 19-24, 1977, Pergamon Press, New York, 1978; 3A: 197-200.

[16] Cotterell B, Rice JR. Slightly curved or kinked cracks. International Journal of Fracture 1980; 16: 155-169.

[17] Tran V-X, Pan J, Pan T. Fatigue behavior of aluminum 5754-O and 6111-T4 spot friction welds in lap-shear specimens. International Journal of Fatigue 2008; 30: 2175-2190.

[18] Tran, V.-X., Pan, J. and Pan, T. Fatigue behavior of spot friction welds in lap-shear and cross-tension specimens of dissimilar aluminum sheets. International Journal of Fatigue 2010; 32: 1022-1041.

CHAPTER V

MECHANICAL BEHAVIOR AND FAILURE MECHANISMS OF NB-CLAD STAINLESS STEEL SHEETS

5.1. Introduction

The growing interest in stainless steel for use as bipolar plates in Polymer electrolyte membrane (PEM) fuel cells [1, 2] has been further accelerated by the recent advances in the micro-forming technology of metals, for example, see [3-5]. Efforts are also being made to model micro-scale forming processes and to investigate the effects of size scaling [6-8]. Recently, Mahbunphacahi and Koc [9] used hydro-forming to develop micro-scale channels in thin stainless steel sheets for bipolar plate applications. However, the use of stainless steel sheets for bipolar plates has two main problems. The first is the development of corrosive products in a low pH environment of the fuel cell and the second is the formation of surface passivation film [10]. The corrosive products are harmful to the membrane electrode assembly (MEA) and can interrupt the action of electrode catalyst. The passive film also adversely affects the contact resistance of the bipolar plates. In order to overcome these issues, coated metal sheets are under investigation. Two types of coatings, carbon-based and metal-based, have been investigated for this purpose [11, 12]. Metal-based coatings include noble metals, metal nitrides and metal carbides [13-15] but a viable and inexpensive commercial product is yet to be developed.

Weil et al. [10] evaluated the electrochemical properties of Nb-clad stainless steel sheets for application as PEM bipolar plates. Their test results demonstrated good corrosion stability under accelerated corrosion conditions. The use of Nb-clad sheets is intended to reduce the material costs of metallic bipolar plates as compared to the other coating schemes, by incorporating the conductive and corrosion resistant Nb as a thin layer roll cladded to a more robust and inexpensive steel sheet. Hong and Weil [16] conducted an initial evaluation of the tensile and bend properties of Nb-clad stainless steel sheets. Their chemical analyses indicated that an iron–niobium compound is present at both the interfaces. The exact chemical composition of the intermetallic compound is yet to be determined. In the present study, experimental investigation of Nb-clad stainless steel sheets is further pursued to study the effects of annealing conditions on the ductility and formability of these sheets.

5.2. Clad assembly preparation

A 304L stainless steel sheet with an initial thickness of about 12 mm was cladded to a 1.3 mm thick Nb sheet by rolling with a 98% reduction in the total thickness. The final thicknesses were about 0.025 mm and 0.23 mm for Nb and stainless steel sheets, respectively. The rolled sheets were vacuum annealed to restore the original ductility. In the present study, specimens with different annealing conditions were studied. These specimens were annealed at $850\,^{\circ}C$, $950\,^{\circ}C$ and $1050\,^{\circ}C$ for either 15 minutes or 60 minutes. The nomenclature for the specimens in this paper is such that the first identification number indicates the annealing temperature and the second number stands for the annealing time. Therefore, 850/15 represents a specimen that has been annealed

at 850 °C for 15 minutes. The microstructure of the interfacial area was examined using the optical and scanning electron microscopy.

5.3. Experiments

5.3.1. Tensile test

These tests were conducted for Nb-clad stainless steel sheets according to ASTM standard E8-04 [17] for tension testing of metallic materials. Due to the limited supply of the sheet material, the tensile specimens were cut into subsize rectangular specimens with a gauge length of 25.4 mm. The dog bone profile was made using a CNC milling machine. The tests were carried out using an automated MTS tensile testing machine with a 10 kN load cell. An extensometer with a one inch gauge length was used to automatically record the extension in the uniform gauge section. The cross-head speed was maintained at 1 mm/min throughout the tests. Three specimens were tested for the as-rolled and each of the different annealed Nb-clad stainless steel sheets.

5.3.2. Bend and flattening test

Specimens were bent to 180° and flattened as described in the ASTM standard E290-97a [18] with the Nb layer on the outside of the bend. The bend was produced by the guided-bend test fixture using a plunger of radius of 5.5 mm. The 180° bent specimens were further flattened between two platens under a predefined maximum load (15 kN/m or 60 kN/m) or until a preselected separation between the bent legs was

reached. The bend and flattening tests were carried out using an automated MTS testing machine.

5.3.3. Nano-indentation

These tests were carried out using a Berkovich diamond tip which has three-sided pyramid geometry. The total downward displacement was limited to about 0.5 µm. Indentations were made in the outer Nb sheet, intermetallic layer and the stainless steel sheet. Three indents were made in each of the layers for the as-rolled and different annealed specimens.

5.4. Results and discussion

5.4.1. Microstructural analysis

Figure 5.1(a) shows an optical micrograph of the cross-sections of an as-rolled specimen. The interface between the two sheets seems to be free of voids and porosities. Figure 5.1(b) shows an optical micrograph of the cross-section of an annealed 1050/60 specimen. The figure shows that there is no interfacial porosity or voids after annealing the specimens at $1050\,^{\circ}C$ for 60 minutes. It also shows that an intermetallic layer of a few microns in thickness was formed in the annealed specimen between the Nb layer and the stainless steel sheet. The thickness of the intermetallic layer is dependent on the annealing temperature and time. The sizes of the intermetallic layer in the annealed 850/15 and 950/15 specimens are very small and high magnification scanning electron micrographs were used to identify the layers in these specimens as shown in Figures

5.2(a) and 5.2(b), respectively. It is observed from these figures that the intermetallic layer in the annealed 850/15 specimen is present as irregular and intermittent segments along the entire bond line instead of a nearly continuous layer as occurs in the annealed 950/15 specimen and shown in Figure 5.2(b).

The thicknesses of the intermetallic layer for different annealed conditions were measured manually from the scanning electron micrographs of the cross sections of the annealed specimens. The approximate values of these thicknesses are listed in Table 5.1. As per Fick's second law of diffusion, the diffusion length is proportional to the square root of the diffusion time. The measured thicknesses of the intermetallic layers for different annealed specimens as given in Table 5.1 shows that for a given annealing temperature, the thickness of the intermetallic layer is about twice for the specimen annealed at 60 minutes as compared to that for the specimen annealed at 15 minutes.

Chemical analysis by Hong and Weil [16] of similar specimens suggested the presence of a transition metal reaction phase. The EDAX analysis [16] indicated that the intermetallic compound observed in the Nb-clad stainless steel after annealing is likely to be the elusive η-phase compound. This compound was reported by Kripyakevitch et al. [19] in ferroniobium alloys annealed at $900\,°C$ in an inert argon environment. The transition metal η-phase is metastable which can be stabilized by very small amounts of phosphorus and sulfur [20]. The brittleness of intermetallic compounds and their low fracture strength is a known issue; moreover, these compounds also suffer from environmental embrittlement problems [21]. Their brittle nature has limited their utility and applications.

5.4.2. Tensile test

5.4.2.1. Mechanical properties

Tensile tests were conducted to evaluate the mechanical properties of the clad assembly. The engineering stress-strain curves for different annealed specimens are shown in Figure 5.3. By comparing the nominal stress-strain curve of the as-rolled specimen with those of the annealed specimens, it is clear that the annealed specimens exhibit a sharp drop in the yield strength along with an increased elongation before failure caused by the recrystallization of the stainless steel sheet. Some of the mechanical properties which were obtained from these tests are listed in Table 5.2 [22].

5.4.2.2. Canoeing phenomenon

Annealed specimens started to warp along the longitudinal axis after a tensile extension of about 5%, producing a shape like the bottom of a canoe [23]. The Nb layer was in the outside of the canoe while the stainless steel layer was in the inside. Figure 5.4 shows this effect in the annealed 850/60 and 1050/60 specimens. Figure 5.4 shows that the "canoeing" phenomenon was more pronounced in the specimens that were annealed at higher temperatures. To calculate the radius of curvature, the width and height of the tested specimen was measured in the middle of the gauge section. From these data points, the radius of curvature was calculated at the peak of the canoe-like profile. Figure 5.5 shows the average values of the radius of curvature after failure under uniaxial loading conditions for specimens with different annealing conditions. These average values for the radius of curvature are obtained from three tensile specimens for

each annealing condition. Figure 5.5 shows that the radius of curvature decreases as the annealing temperature and time increase. To study the change of the canoeing curvature as the uniaxial strain increases, six different annealed 1050/60 specimens were deformed to 5%, 10%, 15%, 20%, 30% and about 47% of uniaxial strains. Figure 5.6 shows the radius of curvature for the annealed 1050/60 specimen as a function of uniaxial strain. The radius of curvature decreases monotonically with the strain. However, it is noted that the curvature is almost the same after a strain of about 30%. This corresponds to the unaxial strain level at which Nb layer has delaminated from the stainless steel sheet.

The canoeing phenomenon can be explained by the differences in the crystal texture of the two layers in the clad assembly. Due to the mismatch of the plastic strain ratios for these two materials, unequal strains are developed in the transverse directions which are compensated by the canoe-like shape of the deformed sheets. The constant value of the curvature for the annealed 1050/60 specimens after Nb layer delamination also seems to support this argument, as the curvature does not change once the Nb layer seize to support the unaxial applied load. Similar warping behavior was reported by Choi et al. [24] while investigating the tensile deformation of stainless steel clad aluminum sheets.

5.4.2.3. Nb layer delamination

Another observation noticed from the tensile tests, was de-bonding of the Nb layer from the stainless steel sheet at strains above 27%. Figure 5.7 illustrates this type of delamination observed in an annealed 1050/60 specimen. It is likely that the less ductile intermetallic layer between Nb and stainless steel sheet developed cracks perpendicular

to the direction of tensile extension. These cracks are likely to promote the interfacial crack growth causing the peeling-off of the Nb layer from the stainless steel sheet. A detailed micrographic analysis of the cross sections is required for the specimens that have been deformed to different strain values to investigate this phenomenon in detail. The Nb layer did not delaminate in other annealed specimens which have thinner intermetallic layers due to the annealing conditions.

5.4.3. Bend and flattening test

Surface examination of the bent tip revealed no scratches or defects in any of the samples, which meant that they can survive this type of bend with the plunger of a given radius as shown in the schematic in Figure 5.8. The final bend angle was measured after the 180° test to determine the springback after elastic recovery. A comparison of the springback angles for different annealing conditions is shown in Figure 5.9. Annealing reduced the springback by about 50%, 58% and 65% in the annealed 850/15, 950/15 and 1050/15 sheets, respectively, as compared to that in the as-rolled specimen.

Figure 5.10 shows a schematic of a flattening test apparatus. A surface examination of the flattened tip showed signs of cracking in the as-rolled and annealed 1050/60 specimens. Rough surfaces were observed in the annealed 950/60 and 1050/15 specimens as shown in Figure 5.11. Other specimens produced no visible surface defects. The cross-sections of the flattened specimens were further examined under an optical microscope to investigate the failure mechanism in the clad sheets. Figure 5.12 presents micrographs of the as-rolled and annealed 1050/60 specimens after flattening by a load per width of 60 kN/m. The failure mechanism of the as-rolled flattened specimen

is different from that of the annealed specimen. Lack of ductility causes the failure of the protective Nb layer in the as-rolled specimen. However, for the annealed specimen the failure initiates at the brittle intermetallic layer and the layer breaks at almost evenly spaced intervals. The fracture of the intermetallic layer produces strain concentration sites which causes localized necking and subsequent failure of the Nb layer. Debonding of the Nb sheet is also shown in Figure 5.12(b) as the cracks propagate in the intermetallic layer. This type of failure mechanism was also observed by Matsumoto et al. [25] in Al-clad Mg-Li plates.

As the thickness of the intermetallic layer depends on the annealing temperature and time, the damage was more pronounced in the annealed 1050/60 specimens than in the annealed 1050/15 specimens. Other specimens showed relatively moderate defects while the annealed 850/15 and 950/15 specimens developed very small voids along the bond line between the outer Nb layer and the stainless steel sheet.

5.4.4. Nano-indentation

Nano-indentation tests were conducted to determine some information about the mechanical behavior of the individual layers in the clad assembly. Figure 5.13 shows the nano-indentation images in different layers of the annealed 1050/60 specimen. As it was difficult to position the nano-indenter tip on the intermetallic layer in specimens with very thin layers and because the effect of the surrounding material was dominant in the case of a thinner intermetallic layer, only the data obtained from the annealed 1050/60 specimen could be used to determine the mechanical properties such as the hardness and the elastic modulus of the intermetallic compound. The values of the hardness and elastic

modulus for the Nb layer, the interface region and the stainless steel layer are plotted and illustrated in Figures 5.14(a) and 5.14(b) respectively, for the as-rolled and annealed 1050/60 specimens. These values are the average of the data obtained from three indents for each layer. For the interface region of the as-rolled specimen, there is no intermetallic layer of a significant thickness. Therefore, the values of the hardness and elastic modulus of this region just relates to the average mechanical properties of the material near the interface. On the contrary, the values of the hardness and elastic modulus of the interface region for the annealed 1050/60 specimen represents the mechanical properties of the intermetallic layer.

The values of the elastic modulus obtained from these tests are very close to the typical values available in the literature. The average measured value of the elastic modulus for the stainless steel layer was 208 GPa which is in good agreement with a value of 200 GPa, that can be found from the Metals hand book [26]. Similarly, for the Nb layer the average measured value of the elastic modulus was 130 GPa as compared to a value of 105 GPa which is quoted in the Metals hand book [26]. It was also observed that the hardness of the Nb layer remained the same in the as-rolled and annealed specimens. However, the hardness decreased in the stainless steel layer after annealing due to the recrystallization of grains. It is likely that the Nb layer did not recrystallize after annealing at $1050\,^{\circ}C$. The effect of the intermetallic layer is visible from the values of the hardness and elastic modulus which are much higher than those of the interface region of the two constitutive layers as shown in Figures 5.14(a) and 5.14(b). A higher elastic modulus is in accord with the observation that the modulus of the intermetallic materials lie between those of the metals and the ceramics [21]. It should be noted that

no cracks are found at the indentation sites which indicate that the adhesion is strong between the two sheets although a brittle intermetallic compound is formed at the interface after annealing.

Figure 5.15(a) shows the load-displacement curves from the nano-indentations tests for the Nb layer of the as-rolled and annealed 950/60, 1050/15 and 1050/60 specimens. The figure shows that the annealing has a little effect on the load-displacement curves. The values of the maximum indentation depth h_m and the residual indentation depth h_r are very close for the as-rolled and different annealed specimens. This is in agreement with the similar hardness values of the Nb layer for the as-rolled and the annealed 1050/60 specimens in Figure 5.15(a).

Figure 5.15(b) shows the load-displacement curves from the nano-indentations tests for the stainless steel layer of the as-rolled and different annealed specimens. Unlike the Nb layer, the load-displacement curves from the nano-indentation tests for the stainless steel layer show some differences between the as-rolled and the annealed conditions. The values of the maximum depth h_m reduce with the annealing temperature. The h_m value from the load-displacement curve of the annealed 1050/60 is about half of that from the load-displacement curve of the as-rolled specimen. The residual depth h_r increases slightly with the annealing, indicating more plastic deformation corresponding to a more ductile material. This is also in agreement with the lower hardness value of the stainless steel layer for the annealed 1050/60 specimen as compared to that for the stainless steel layer in the as-rolled specimen as shown in Figure 5.16(b).

Table 5.3 lists the ratios of the maximum indentation depth to the residual indentation depth h_r/h_m for different layers of the as-rolled and the annealed 950/60,

1050/15 and 1050/60 specimens. The ratio h_r/h_m can be used to provide a qualitative assessment of the degree of ductility in the individual layers of the clad assembly. The stainless steel layer shows the highest h_r/h_m value after annealing. The annealing does not appear to affect the h_r/h_m values for the Nb layer and the value is almost constant at about 0.86. It should be noted that the h_r/h_m of the intermetallic layer is only listed for the 1050/60 specimen because it was difficult to get a reliable data for the thinner intermetallic layers in other specimens that were annealed at lower temperatures and for shorter time. The intermetallic layer shows the least value of h_r/h_m that indicates a lower ductile nature of the layer.

5.5. Conclusions

The mechanical behavior and failure mechanism of Nb-clad stainless steel sheets were investigated. A microstructural analysis of the roll-cladded specimens suggested a good metallurgical bond free of interfacial defects. The as-rolled specimens were annealed to increase their ductility. The annealing also reduced the amount of springback as compared to that of the as-rolled specimen. Annealing caused the development of a brittle intermetallic layer at the Nb and stainless steel interface. Tensile tests showed increased ductility in terms of lower yield strength and larger elongation before failure. A "canoeing" effect during tensile testing of the clad sheets increased with increasing annealing temperature. Nb layer delaminated from the stainless steel sheet in the annealed 1050/60 tensile specimens. Failure in the flattened annealed specimens is caused by localized necking of the Nb layer after brittle fracture of the intermetallic layer. Nano-indentation was used to evaluate the mechanical properties of the individual layers

in the Nb-clad stainless steel sheets. The hardness of the stainless steel layer decreased slightly after annealing, but no noticeable hardness change was observed in the Nb layer after annealing. The hardness and elastic modulus of the intermetallic layer were large as compared to those of the Nb and stainless steel sheets. The results of the present study will provide a better understanding of the mechanical behavior of clad metallic sheets and provide general criteria and guidelines for formability of Nb-clad stainless steel sheets. This knowledge can be used to model and study the channel forming process in the clad sheets for its application as bipolar plates in PEM fuel cells.

Table 5.1. Measured thicknesses of intermetallic layer for various annealed specimens.

Annealing Temperature (°C)	**Annealing Time (minutes)**	**Intermetallic Thickness (μm)**
850	15	Less than 0.5 *
950	15	0.8
1050	15	1.8
850	60	0.9
950	60	1.3
1050	60	4.2

* Not a continuous layer

Table 5.2. Mechanical properties of the Nb-clad stainless steel sheets from tensile tests.

Specimen	Youngs Modulus E (GPa)	Yield Strength (MPa)	Ultimate Strength UTS (MPa)	% Elongation	Strain Hardening Exponent n[2]	Strength Coefficient K[2] (MPa)
as-rolled	211	790	1028	4.9	-	-
850/15	216	201	577	44.4	0.38	1066
950/15	214	155	558	54.0	0.38	1159
1050/15	222	128	545	55.1	0.39	1108
850/60	215	192	556	55.6	0.38	1220
950/60	217	145	523	54.2	0.38	1090
1050/60[1]	220	105	469	48.1	0.36[3]	879[3]

[1] Nb layer delamination occurred above at a strain of about 27%.
[2] ASTM E646-07, 2007.
[3] Calculated up to a strain of about 25% due to the delamination of the Nb layer.

Table 5.3. The ratio of the maximum indentation depth to the residual indentation depth h_r/h_m of different layers for specimens annealed at different annealing conditions.

	Nb	**Intermetallic**	**Stainless steel**
as-rolled	0.86	-	0.83
950/60	0.86	-	0.89
1050/15	0.85	-	0.89
1050/60	0.85	0.66	0.91

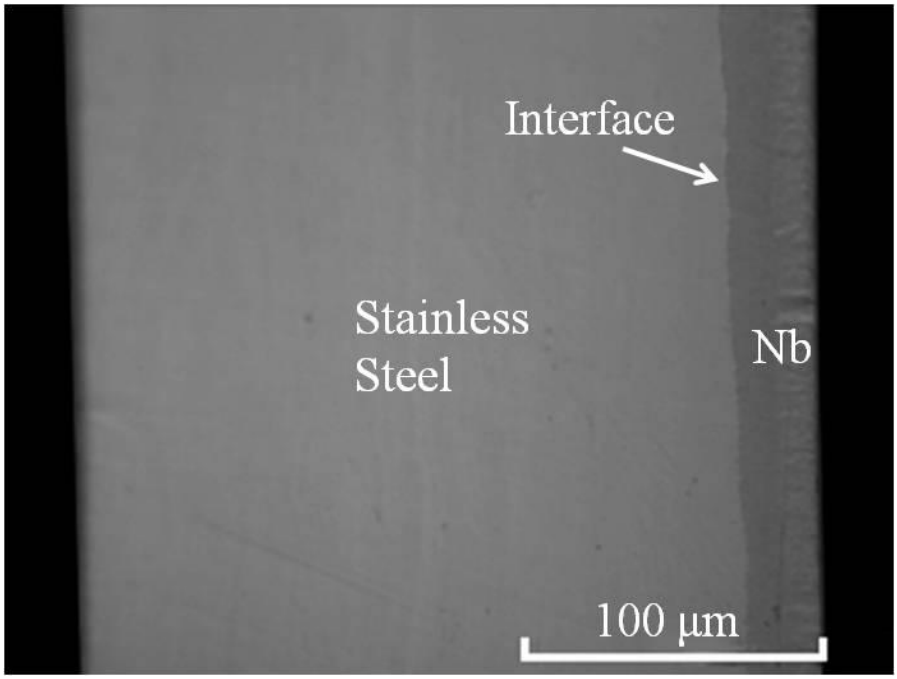

(a)

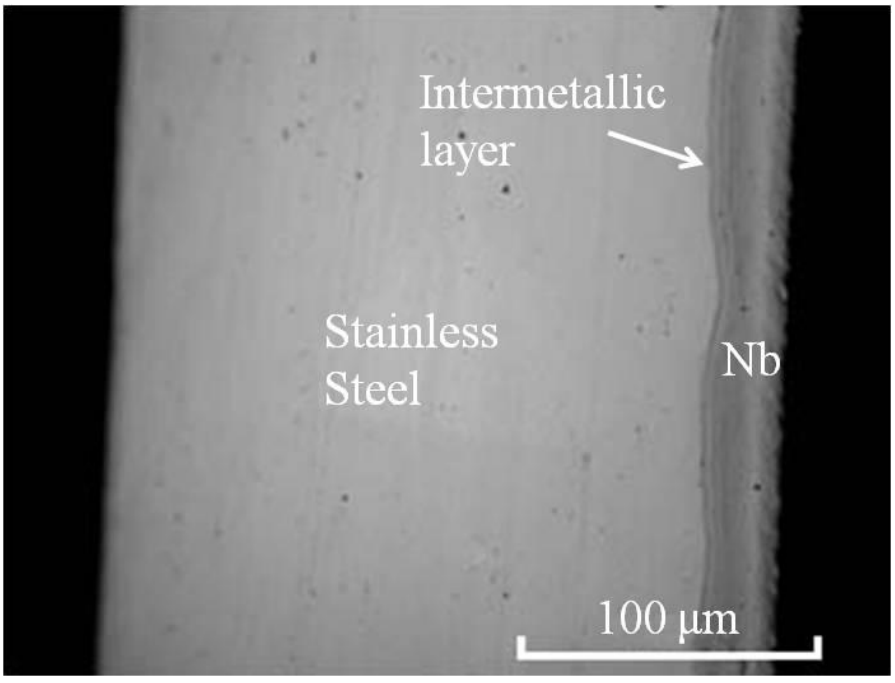

(b)

Figure 5.1. Optical micrographs of the cross-sections of (a) an as-rolled and (b) an annealed 1050/60 specimens.

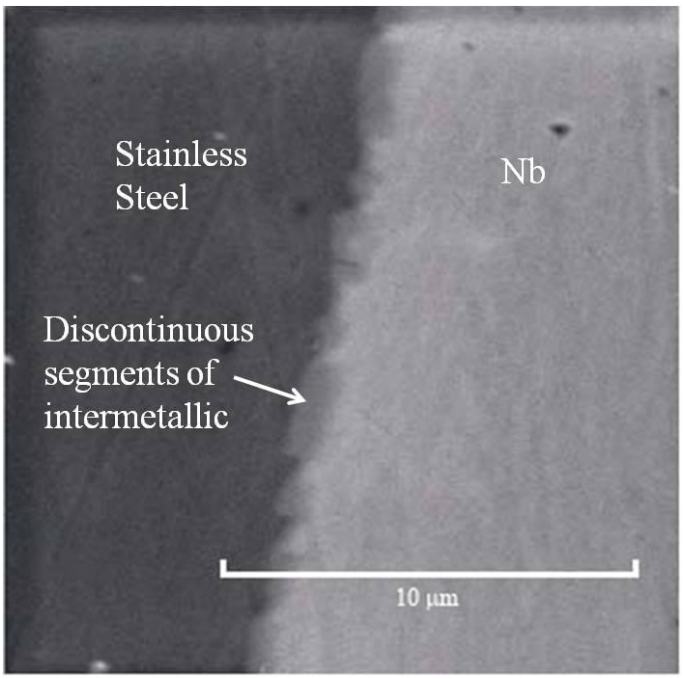

(a)

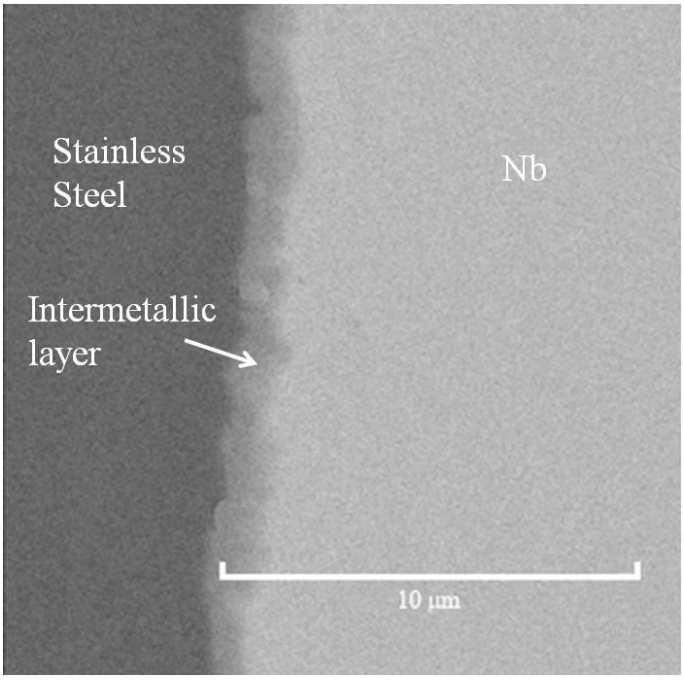

(b)

Figure 5.2. A scanning electron micrograph of the cross-section of the annealed (a) 850/15 and (b) 950/15 specimens.

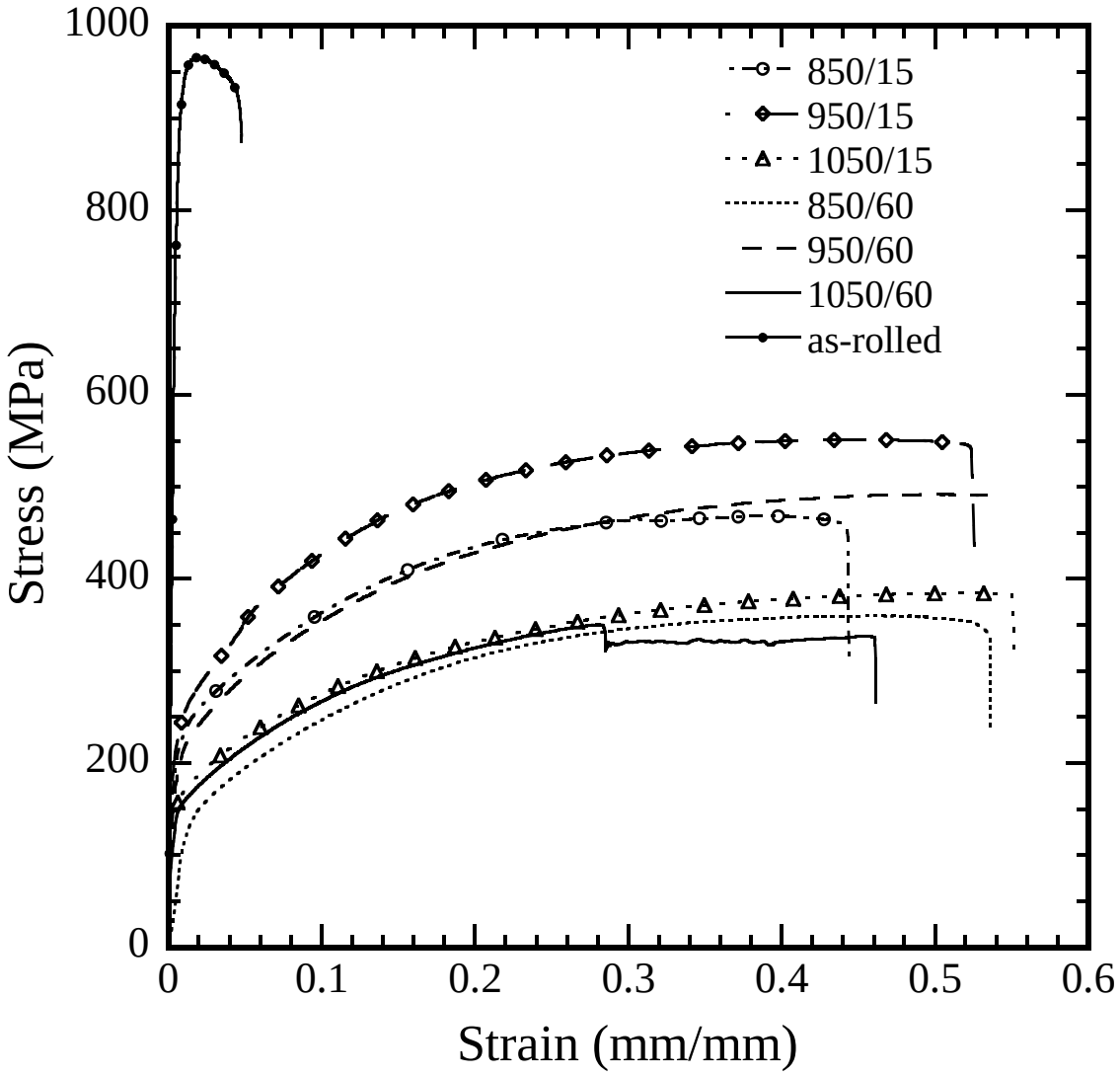

Figure 5.3. The engineering stress-strain curves for an as-rolled specimen and specimens with different annealing conditions.

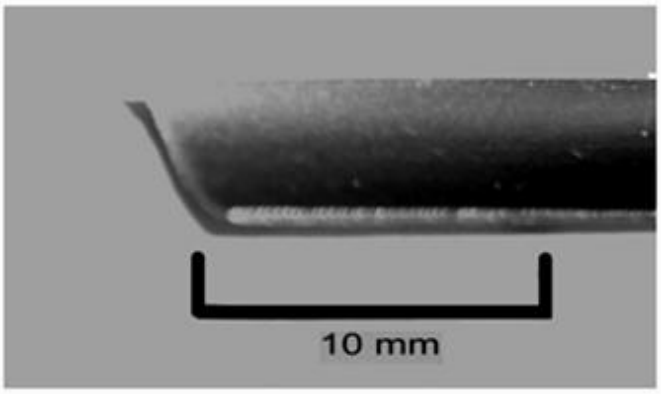

(a)

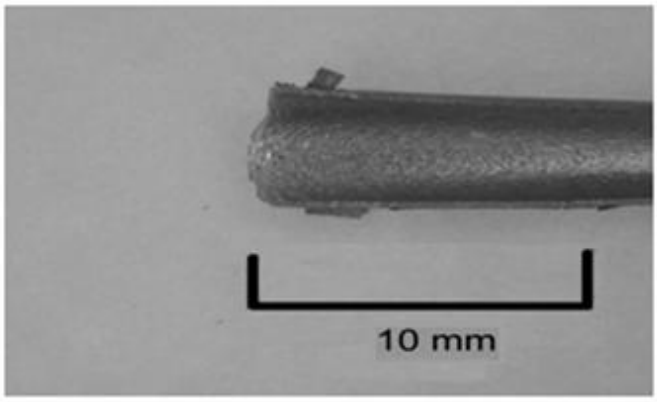

(b)

Figure 5.4. "Canoeing" effect in the annealed (a) 850/60 and (b) 1050/60 specimens.

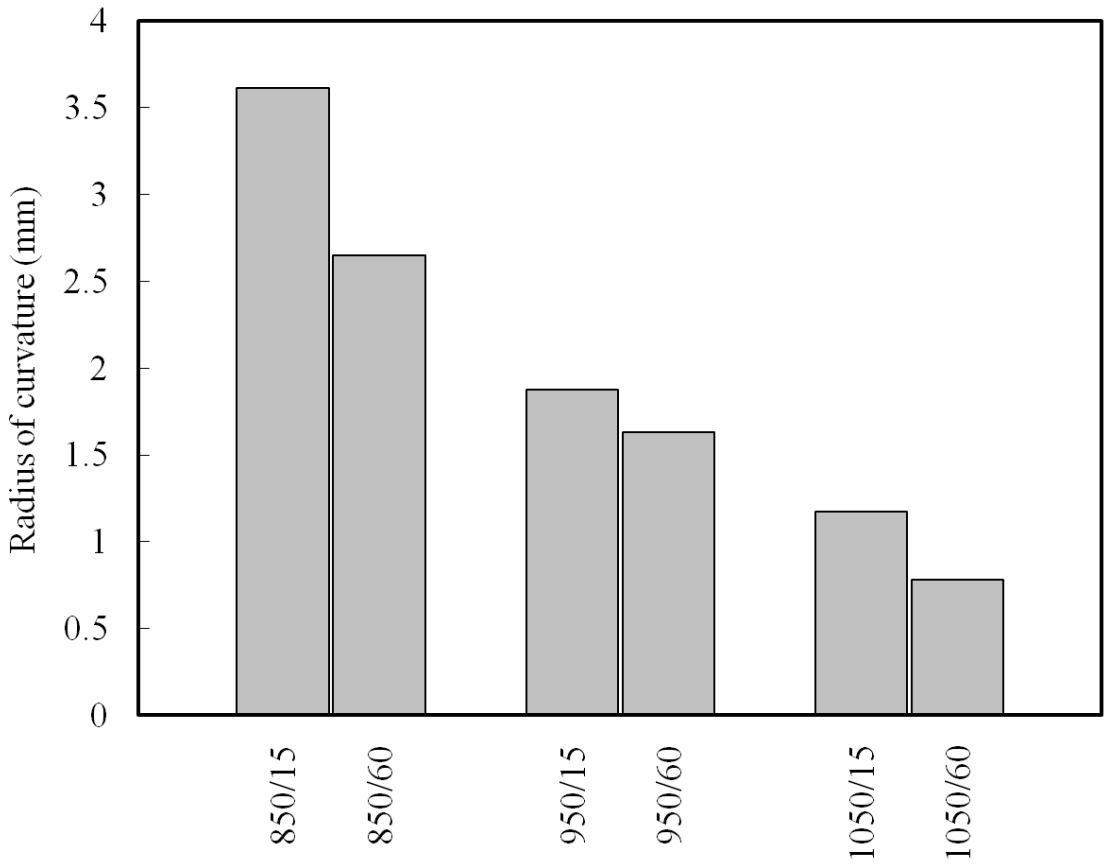

Figure 5.5. Radius of curvature after failure under uniaxial loading conditions for specimens with different annealing conditions.

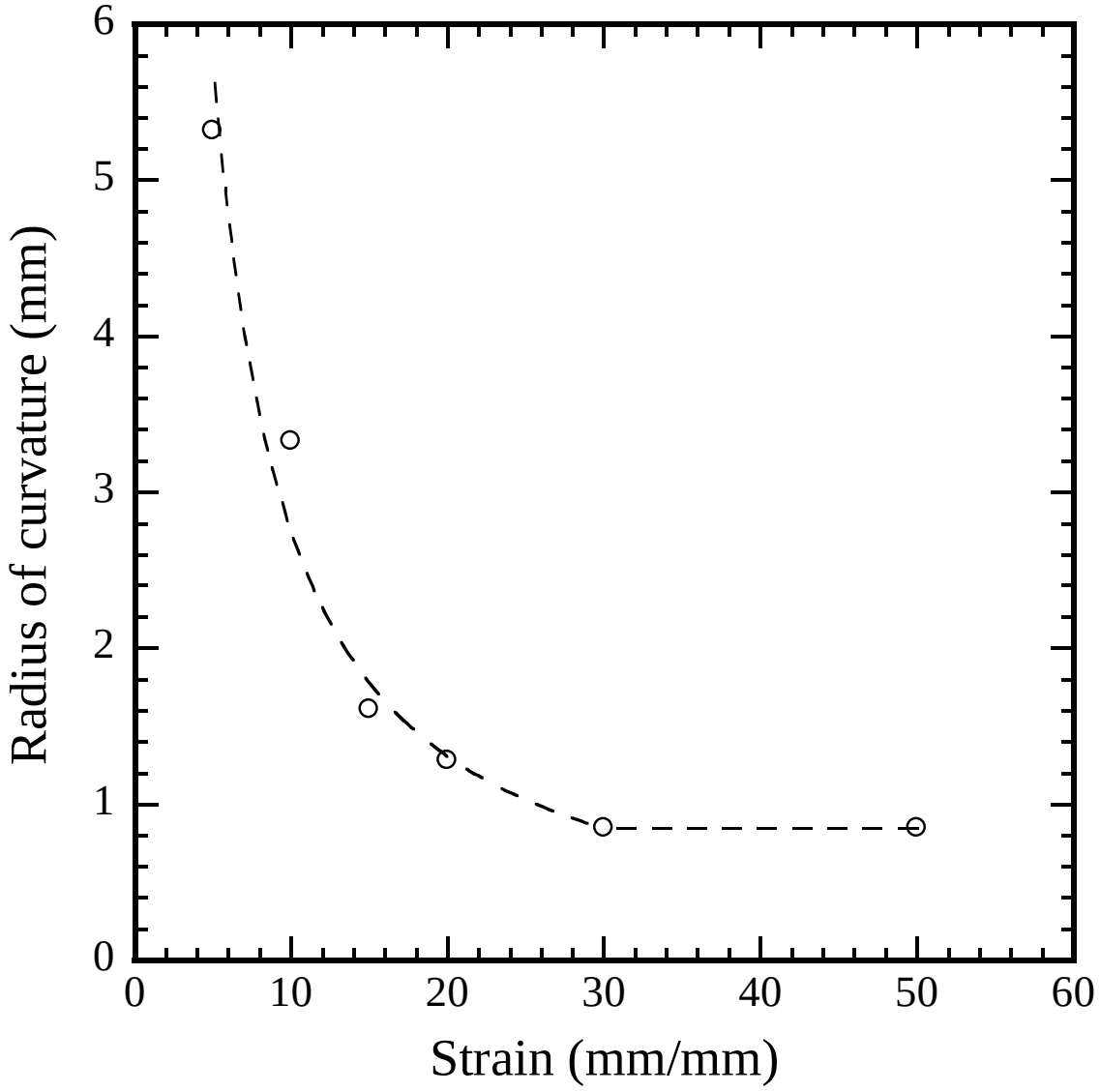

Figure 5.6. Radius of curvature for the annealed 1050/60 specimens as a function of uniaxial strain.

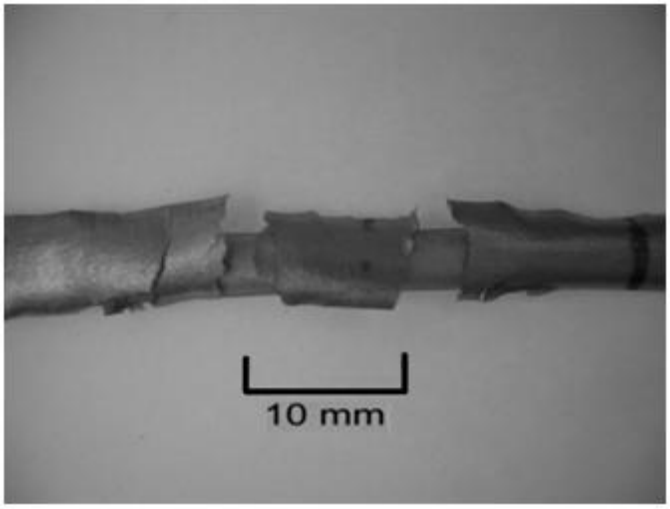

Figure 5.7. Delamination of the Nb layer form the stainless steel sheet in an annealed 1050/60 specimen after uniaxial strain of about 47%.

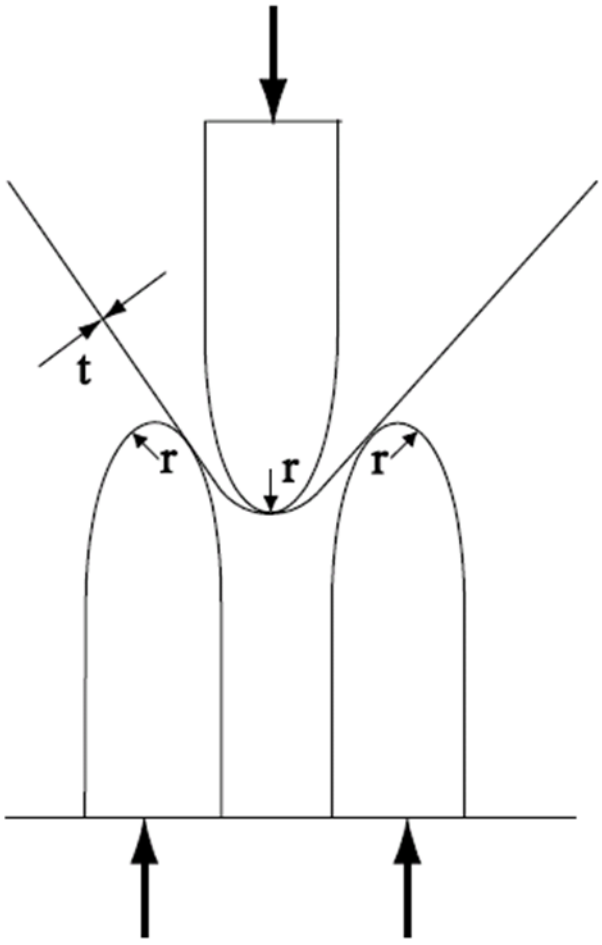

Figure 5.8. A schematic of a guided-bend test apparatus.

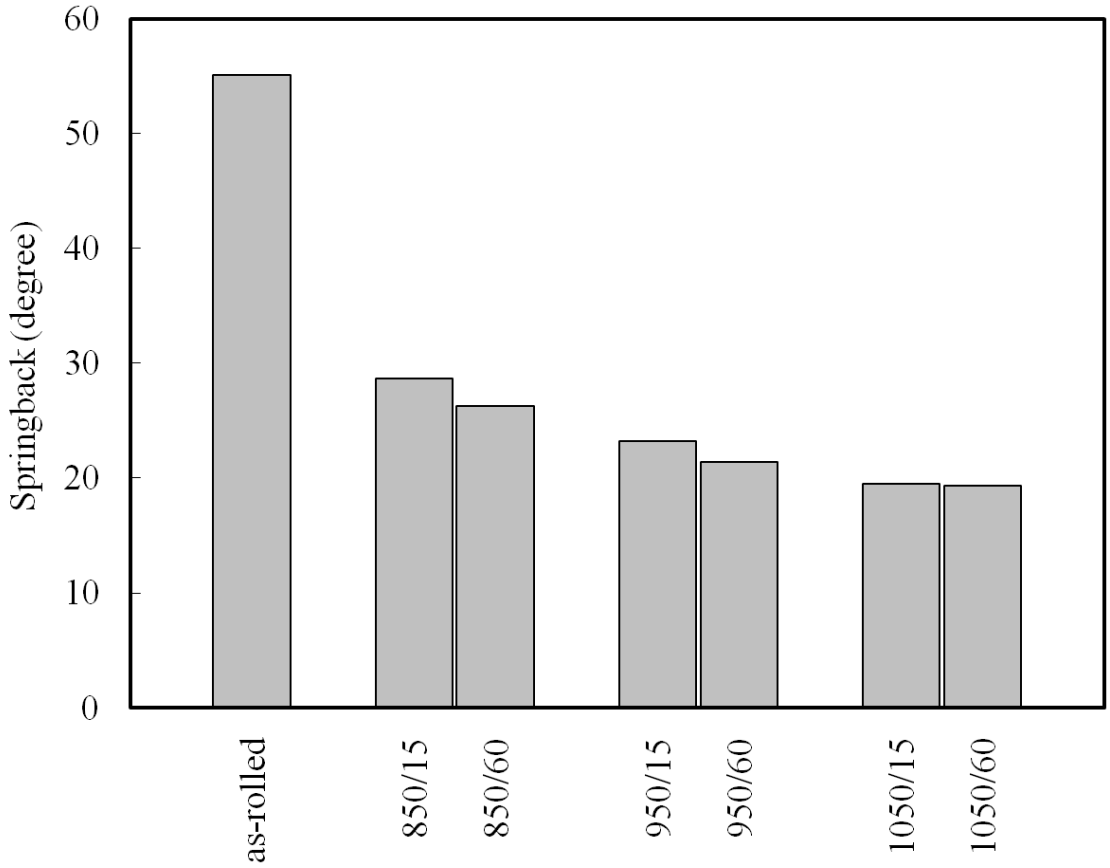

Figure 5.9. Springback angles for specimens with different annealing conditions.

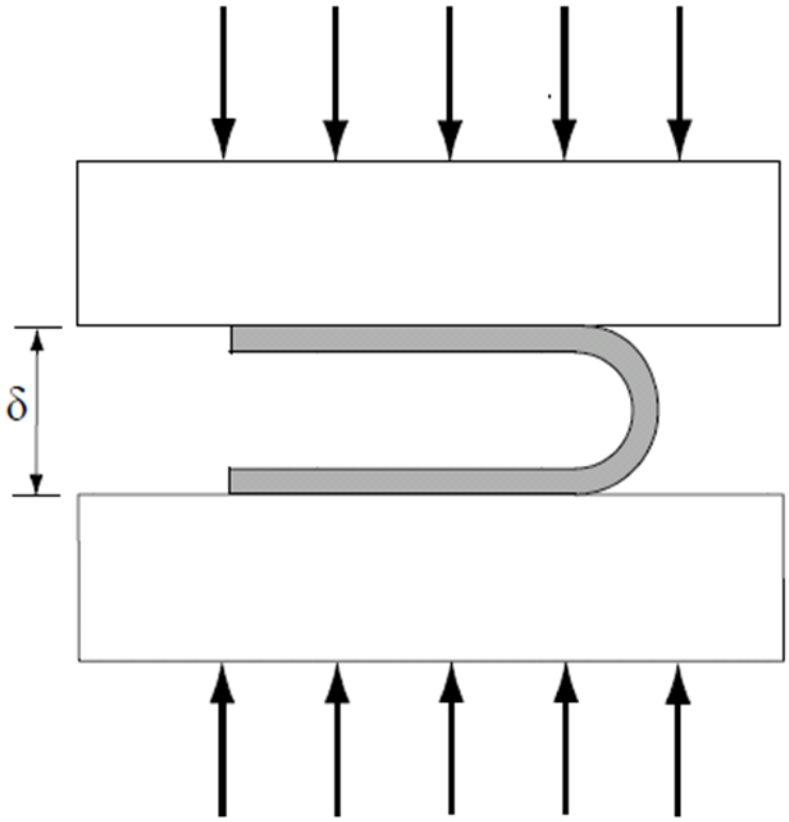

Figure 5.10. A schematic of a flattening test apparatus.

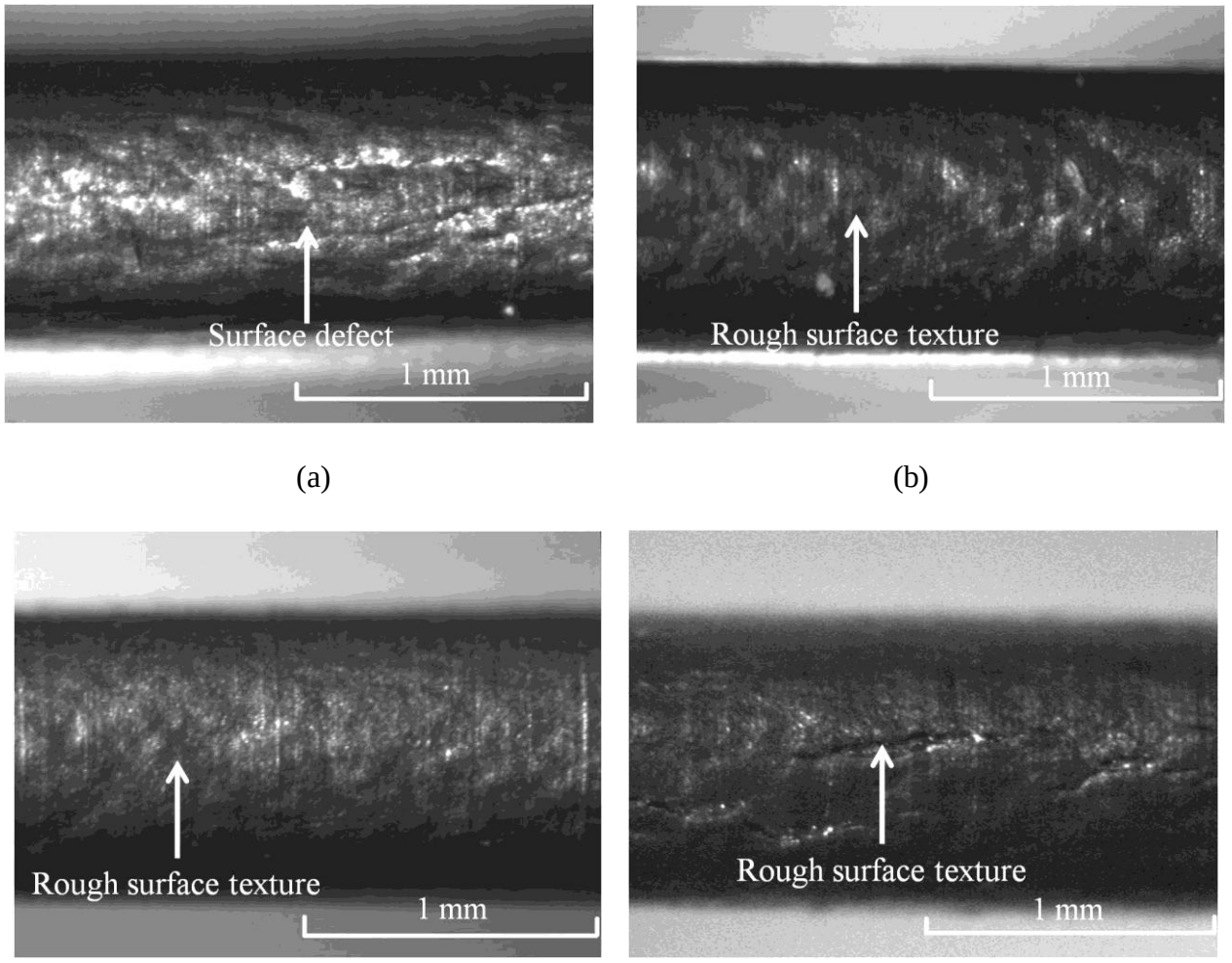

Figure 5.11. Surface examination of (a) an as-rolled specimen flattened by a load per width of 15 kN/m, annealed (b) 1050/15 (c) 950/60 and (d) 1050/60 specimens flattened by a load per width of 60 kN/m.

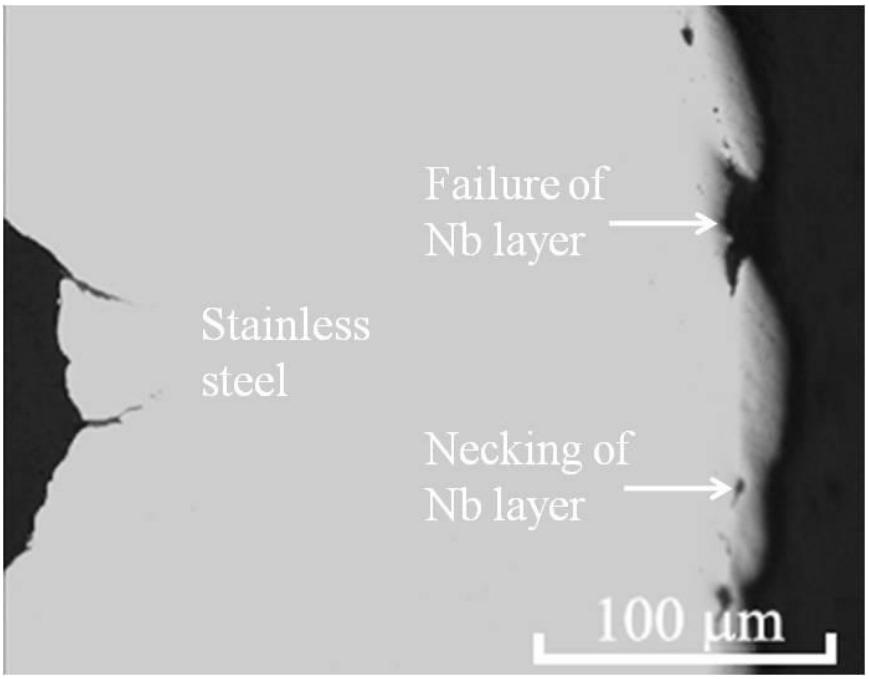

(a)

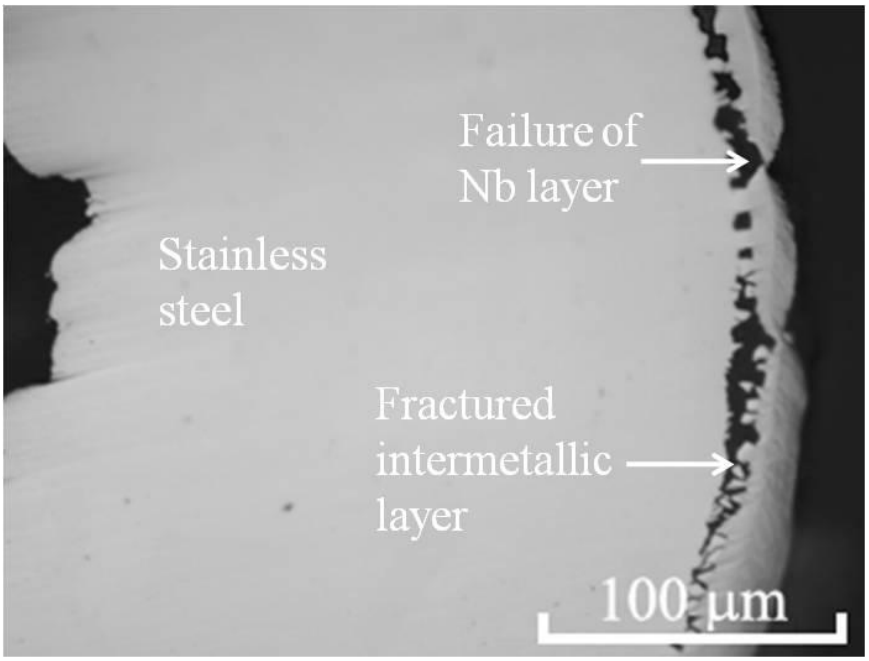

(b)

Figure 5.12. Optical micrographs of the cross sections of (a) an as-rolled and (b) an annealed 1050/60 specimen after flattening tests.

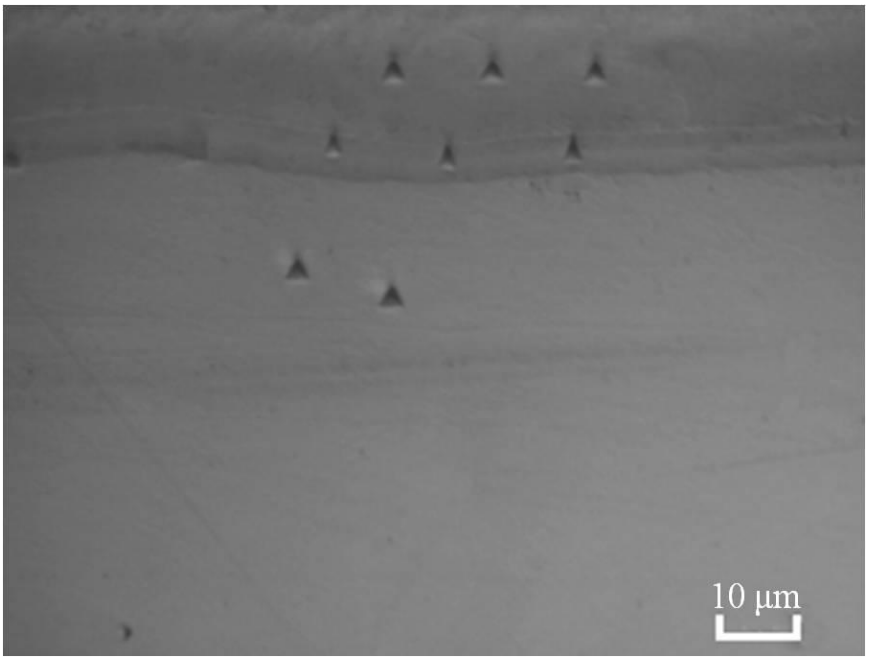

Figure 5.13. An optical micrograph of the cross section of an annealed 1050/60 specimen showing the nano-indents.

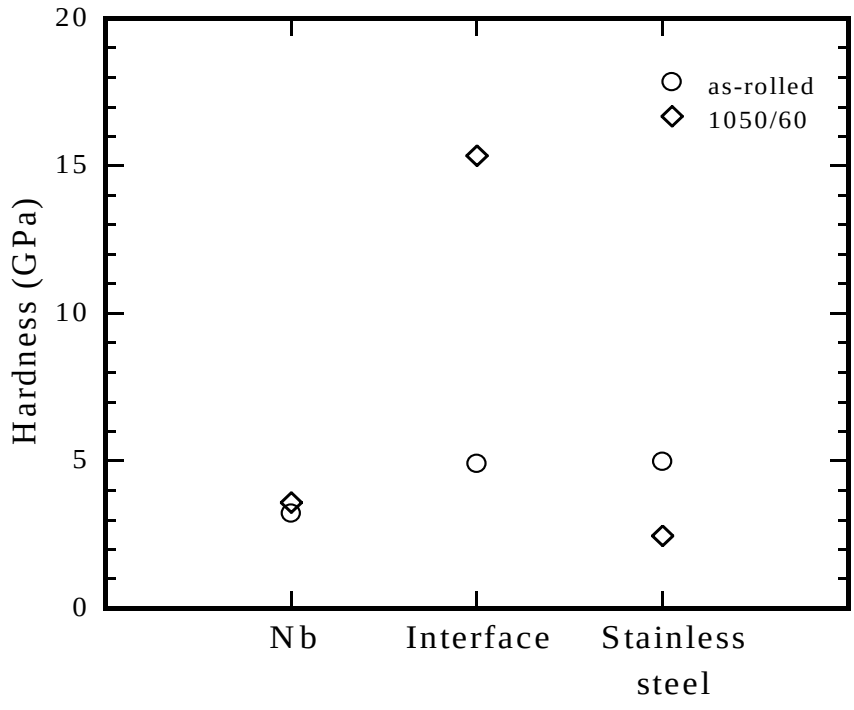

(a)

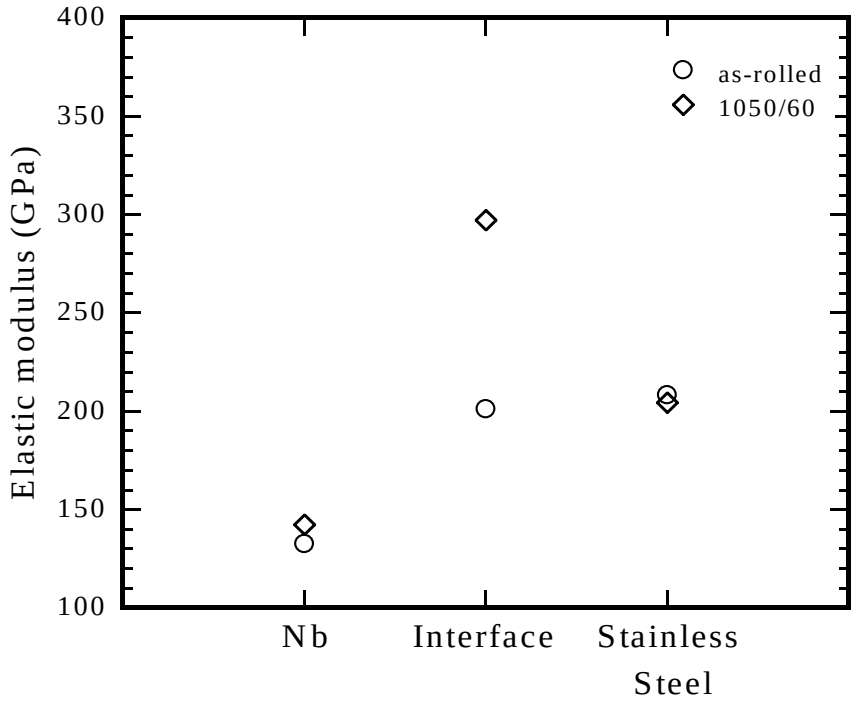

(b)

Figure 5.14. Plots of the values of (a) hardness and (b) elastic modulus of individual layers in an as-rolled and an annealed 1050/60 specimens.

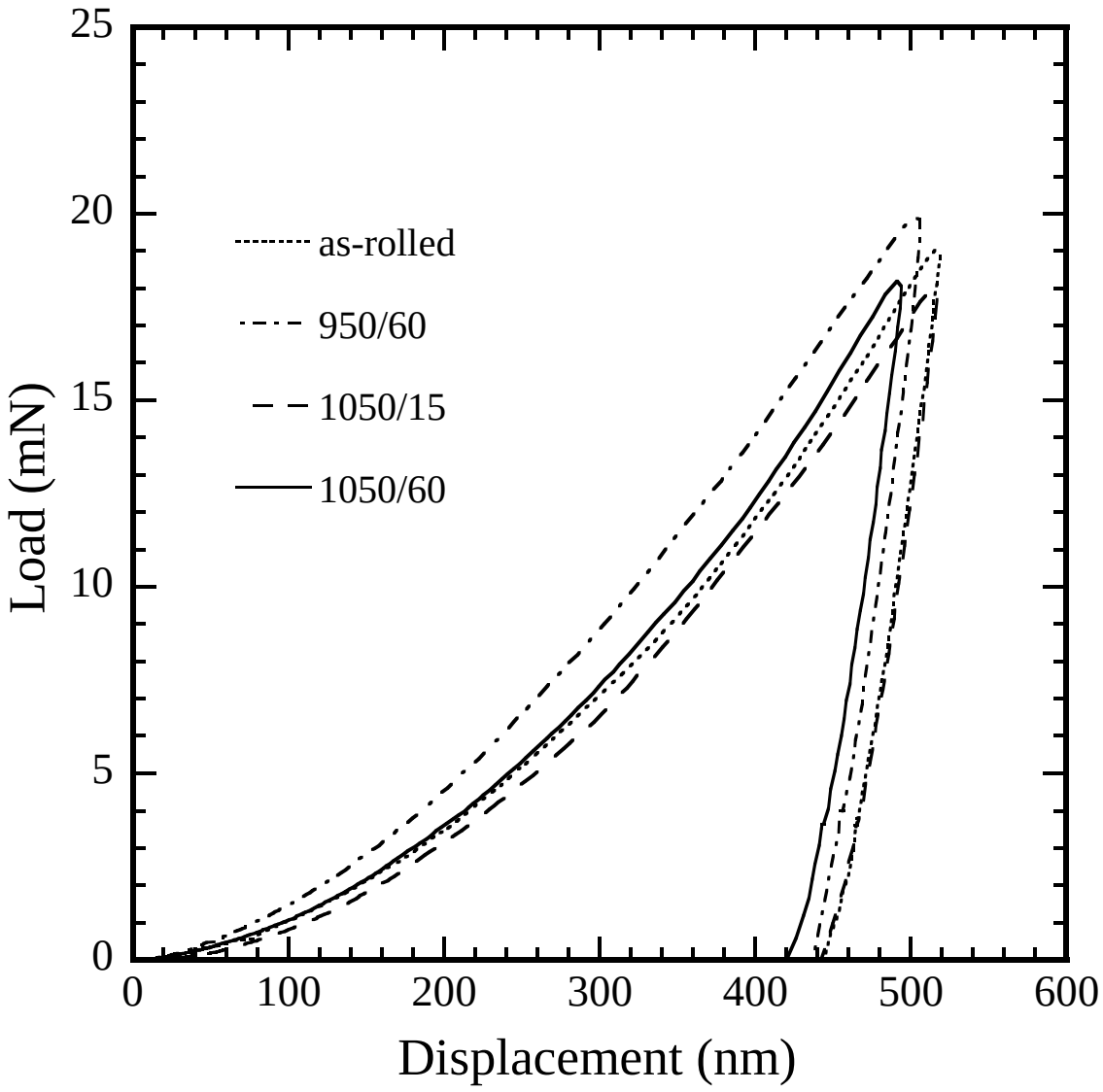
25
20
15
10
5
0
Load (mN)
as-rolled
950/60
1050/15
1050/60
0
100
200
300
400
500
600
Displacement (nm)

(a)

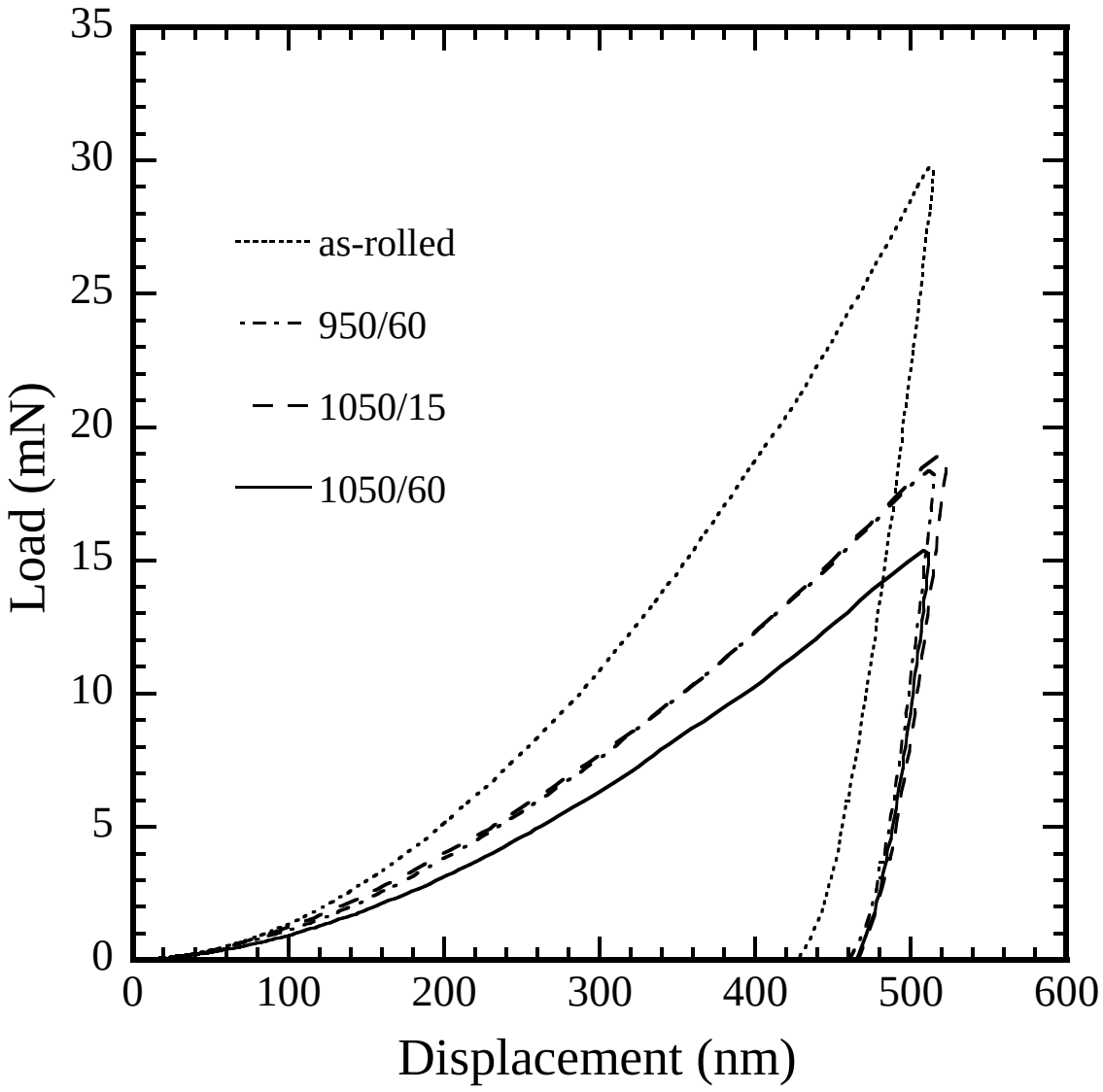

(b)

Figure 5.15. Load-displacement curves from the nano-indentations tests for (a) the Nb and (b) the stainless steel layers of the as-rolled and 950/60, 1050/15 and 1050/60 specimens.

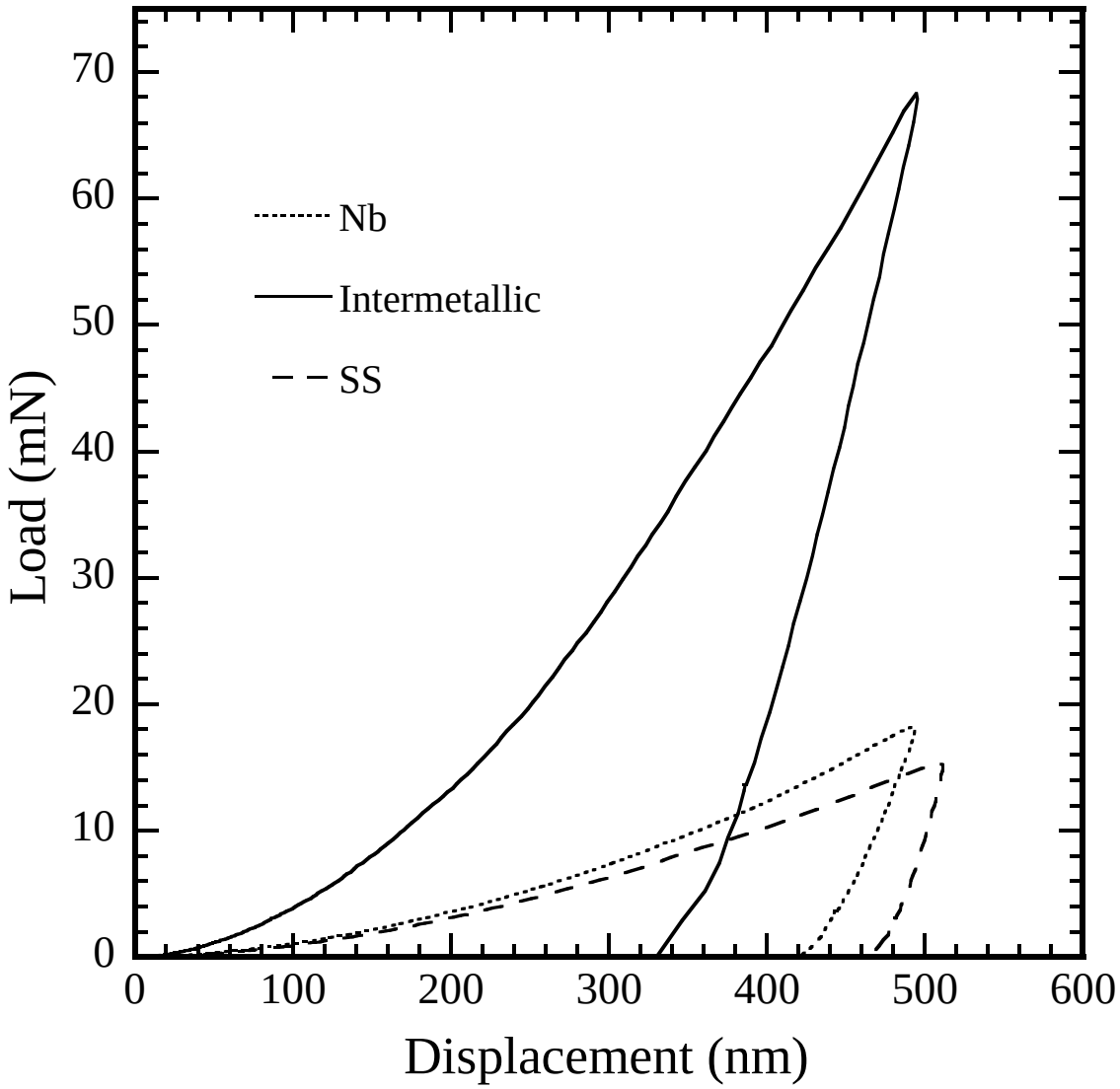

Figure 5.16. Load-displacement curves from the nano-indentation tests for different layers of an annealed 1050/60 specimen.

References

[1] Makkus RC, Janssen AHH, de Bruijn FA, Mallant RKAM. Stainless steel for cost-competitive bipolar plates in the SPFC. Journal of Power Supply 2000, 86: 274-282.

[2] Wang H, Sweikart MA, Turner JA. Stainless steel as bipolar plate material for polymer electrolyte membrane fuel cells. Journal of Power Sources 2003; 115: 243-251.

[3] Engel U, Eckstein R. Microforming-from basic research to its realization. Journal of Materials Processing Technology 2002; 125-126: 35-44.

[4] Cao J, N. Krishnan N. Recent advances in microforming: Science, technology and applications. Proceedings of Materials Science and Technology 2005; 225-234.

[5] Saotome Y, Yasuda K, Kaga H. Microdeep drawability of very thin sheet steels. Journal of Materials Processing Technology 2001; 113: 641-647.

[6] Lalli LA. Multiscale modeling for light metals alloy development. Current Opinion in Solid State and Material Science 1998; 3: 283-287.

[7] Horstemeyer MF, Baskes MI, Plimpton SJ. Computational nanoscale plasticity simulations using embedded atom potentials. Theoratical and Applied Fracture Mechincs 2001; 37: 49-98.

[8] Koc M, Kim GY, Ni J. Modeling of the size effects on the behavior of metals in microscale deformation processes. Transactions of the ASME 2007; 129: 470-476.

[9] Mahabunphachai S, Koc M. Fabrication of micro-channel arrays on thin metallic sheet using internal fluid pressure: Investigations on size effects and development of design guidelines. Journal of Power Sources 2008; 175: 363-371.

[10] Weil KS, Xia G, Z.G. Yang ZG, Kim JY. Development of niobium clad PEM fuel cell bipolar plate material. International Journal of Hydrogen Energy 2007; 32: 3724-3733.

[11] Borup RL, Vanderborgh NE. Design and testing criteria for bipolar plate materials for PEM fuel cell applications. Proceedings of Materials Research Society Symposium 1995; 393: 151-155.

[12] V. Mehta V, Cooper JS. Review and analysis of PEM fuel cell design and manufacturing. Journal of Power Sources 2003; 114: 32-53.

[13] Wind J, Späh R, Kaiser W, Böhm G. Metallic bipolar plates for PEM fuel cells. Journal of Power Sources 2002; 105: 256-260.

[14] Lee S-J, Huang C-J, Lai J-J, Chen Y-P. Corrosion-resistant component for PEM fuel cells. Journal of Power Sources 2004; 131: 162-168.

[15] Brady MP, Weisbrod K, Paulauskas I, Buchanan RI, More KL, Wang H, Wilson M, Garzon F, Walker LR. Preferential thermal nitridation to form pin-hole free Cr-nitrides to protect proton exchange membrane fuel cell metallic bipolar plates. Scripta Materialia 2004; 50: 1017-1022.

[16] Hong S-T, Weil KS. Niobium-clad 304L stainless steel PEMFC bipolar plate material: Tensile and bend properties. Journal of Power Sources 2007; 168: 408-417.

[17] ASTM E8-04: Standard test methods for tension testing of metallic materials. American Society of Testing and Materials, West Conshohocken, PA, USA 2004.

[18] ASTM E290-97: Standard test methods for bend testing of material for ductility. American Society of Testing and Materials, West Conshohocken, PA, USA 2004.

[19] Kripyakevitch PI, Gladyshevskii EI, Skolozdra RV, Sov. Physical Crystallography 1968; 12: 525.

[20] Schön CG, Tenorio JAS. The chemistry of the iron-niobium intermetallics. Intermetallics 1996; 4: 211-216.

[21] Russell AM. Ductility in Intermetallic Compounds. Advanced Engineering Materials 2003; 5: 629-639.

[22] ASTM E646-07: Standard test method for tensile strain-hardening exponents (*n* - values) of metallic sheet materials. American Society of Testing and Materials, West Conshohocken, PA, USA 2007.

[23] ASTM E517-00: standard test method for plastic strain ratio *r* for sheet metal. American Society of Testing and Materials, West Conshohocken, PA, USA 2006.

[24] Choi S-H, Kim K-H, Oh KH, Lee DN. Tensile deformation behavior of stainless steel clad aluminum bilayer sheet. Materials Science and Engineering 1997; A222: 158-165.

[25] H. Matsumoto H, S. Watanabe S, Handa S. Fabrication of pure Al/Mg-Li alloy clad plate and its mechanical properties. Journal of Materials Processing Technology 2005; 169: 9-15.

[26] Metals Handbook, Second Edition, Davis and Associates, ASM International Handbook Committee, 1998.

CHAPTER VI

FAILURE MECHANISMS OF POLYMER-GRAPHITE COATED STAINLESS STEEL SHEETS

6.1. Introduction

There is a growing interest in fuel cells as a power source due to their higher efficiency and environmental friendliness. Polymer electrolyte membrane (PEM) fuel cells are considered very attractive for automotive propulsion system. These cells have operating temperatures less than $100\,°C$ and a higher power density than other fuel cells. They also respond swiftly to varying loads and can sustain large load cycles. Efforts are underway to increase the reliability and performance of these cells while reducing their cost and size. Bipolar plates are an important part of PEM fuel cells. They contribute 80% to the total stack weight and account for 45% of the cost [1, 2]. Materials such as graphite, coated/non-coated metals and polymer composites have been used as bipolar plates. However, stainless steel is explored by many researchers for bipolar plate development due to its relatively high strength, high chemical stability, low gas permeability, wide range of alloy choice, and applicability to mass production and low cost [3].

Stainless steel sheets have been tested and stainless steel bipolar plates have been developed by different investigators [4-8]. These products have demonstrated a low corrosion rate and a stable output for thousands of operating hours. However, they produce corrosive products in a low pH environment of a fuel cell and the contact

resistance increases due to the formation of surface passivation film. Use of protective coating has been investigated by researchers to mitigate this problem [3, 9]. Noble metals, metal nitrides and metal carbides are some of the metal-based coatings. In the present study, an inexpensive polymer-graphite layer is considered as a protective coating. Note that polymer composites have been explored and used in fuel cell bipolar plates [10-13].

The main objectives of this research are to study the formability of polymer-graphite coated stainless steel sheets and investigate the failure mechanism of the protective polymer-graphite layer. In the present work, polymer-graphite coated 316L stainless steel sheets were selected to examine their mechanical behavior and suitability for use as bipolar plates. The 316L stainless steel sheets were obtained from ArcelorMittal. A conductive, chemical resistant EB-815 polymer-graphite coating from Acheson Colloids (Port Huron, MI) is chosen for this preliminary study. A set of standard tests were conducted to determine the ductility of the coated sheets. These tests include uniaxial tensile test, bend/flattening test and limited dome height test.

6.2. Coated assembly preparation

Stainless steel sheets having a thickness of 100 µm were coated with a commercially available EB-815 polymer-graphite coating at Acheson Colloids. The coating is composed of a thermoset binder with graphite flakes of thickness 1 µm and a size of 2 to 20 µm. The oxidation, corrosion, adhesion and electrical properties were investigated earlier to determine an optimal volume fraction of the graphite flakes to

ensure high electrical conductivity of the coating. The average thickness of polymer-graphite layer was maintained at about 20 µm.

Figures 6.1(a) and 6.1(b) show the scanning electron micrographs of the cross sections of EB-815 coating at a magnification of 1000x and 1500x, respectively. The EB-815 layer and the graphite particles are identified in the micrograph. Selective measured values for the thickness of EB-815 coating and the graphite particle sizes are shown in Figures 6.1(c) and 6.1(d), respectively, at a magnification of 1500x. The thickness of the EB-815 layer varies from about 15 µm to about 18 µm. Graphite particles of dimensions of 9 µm and 17 µm are shown in Figure 6.1(d). Some defects in the EB-815 layer are also shown in Figures 6.1(c) and 6.1(d).

Figures 6.2(a), 6.2(b) and 6.2(c) show the scanning electron micrographs of the surface of EB-815 coating at the center of the coated sheet at a magnification level of 100x, 250x and 500x, respectively. The rough surface texture is observed in the higher magnification micrograph. The graphite particles also appear as shiny features in the micrograph. Figures 6.3(a), 6.3(b) and 6.3(c) show the scanning electron micrographs of the surface of EB-815 coating at the edge of the coated sheet at a magnification level of 100x, 250x and 500x, respectively. A surface texture similar to those in Figures 6.2(a), 6.2(b) and 6.2(c) is observed in Figures 6.3(a), 6.3(b) and 6.3(c). It appears that the polymer coating is consistent across the surface of the stainless steel sheet with a uniform surface texture.

6.3. Experiments

6.3.1. Tensile test of polymer coated stainless steel sheets

Tensile tests were conducted for the polymer coated stainless steel sheets according to the ASTM standard E8-04 [14]. Test specimens had a gauge length of 25.4 mm. The tests were carried out with a constant crosshead speed of 1 mm/min. The engineering stress-strain curves are shown in Figure 6.4 for the base metal from the representative stainless steel and polymer-coated stainless steel sheets specimens. Test results indicated no noticeable effect of the polymer-graphite coating on tensile properties of stainless steel sheets.

Tensile tested specimens showed a deterioration of the surface quality as the unaxial strain increased. A comparison of the surface texture is presented in Figures 6.5(a) - 6.5(h) for specimens subjected to unaxial strains of 8% to 17%, respectively. Surface topology becomes rough with increased strain. At a strain of about 16%, the surface was visibly scratched and large cracks can be seen in the micrograph. Thus a strain limit of about 15% is appropriate for the uniaxial extension of the polymer coated stainless steel sheets to ensure integrity of the coated layer. At a strain level of 17%, the polymer-graphite layer started to visibily delaminate and flakes of the coating began to peel off from the base metal sheet.

The extent of surface roughness with the amount of tensile strain was quanitifed by measuring the surface profile of the tested specimens using a stylus profilometer. The values of the arithematic surface roughness R_a for several strains are plotted in Figure 6.6. The graph shows a continuous increase in the roughness value as the uniaxial strain

increases. The knowledge of surface roughness is important as the amount of contact resistance and the resistance due to reactant flow depend strongly on the surface quality of bipolar plates.

6.3.2. Tensile test of EB-815 polymer epoxy sheets

Tensile tests were also conducted for the EB-815 polymer epoxy sheets. A five inch square sheet of EB-815 without the graphite particles was prepared by spray applying over a plastic release liner rigidly held in a jig. Fourteen layers of EB-815 were applied to achieve a sheet of thickness of about 0.43 mm. A curing process of 20 minutes at $150\,^{\circ}C$ was carried out after application of each layer. The layered sheet was removed from the fixture and the plastic release film was detached. The EB-815 sheet was then placed between two Emralon 333 coated plates and cured for 15 minutes at $260\,^{\circ}C$. After cooling, the EB-815 sheet was removed from the steel plates. Tensile specimens with a 25.4 mm gauge length were prepared from this epoxy sheet using a water jet cutting machine. The tensile tests were conducted using an automated MTS testing machine with a 10 kN load cell. The cross-head speed was maintained constant at 0.015 mm/min during the tests. The uniaxial extension of the gauge section was measured using an extensometer with a one inch gauge length. It is noted that a total of four specimens were tested and the extensometer was used to record the displacement in the gauge section for three specimens. One of the specimens had surface defect and the extensometer was not used to record the guge section displacement measurements due to the fragility of the specimen, instead, the cross-head displacement was recorded to calculate the gauge section extension for this specimen. Figure 6.7 shows the

engineering stress-strain curves for EB-815 epoxy sheet from the four test specimens. The curves have almost the same initial slope, however, there is a variation in the uniaxial elongation. In general, the epoxy layer has a very limited uniaxial elongation. The average elastic modulus from these curves is about 15 GPa.

6.3.3. Semi-guided bend test

Semi-guided bend tests were conducted according to the ASTM standard E290-97a [15]. The setup for the test is schematically shown in Figure 6.8. Dimensions of the specimens were set at 40 mm by 20 mm. The tests were conducted until a bend angle of 180º was reached. Two sets of specimens were used in these tests. In the first set, specimens were bent with the bend axis along the longitudinal direction and in the second set of tests the bend axis was kept perpendicular to the longitudinal direction of the sheets. The test specimens were bent by different radii of 0.8, 1.0, 2.4 and 3.2 mm. These tests produced a plane strain bending condition. Visual surface inspection of the outer surface of the coating at the bend tip indicated that the outer polymer-graphite coating remained intact after the 180º bend as shown in Figures 6.9 and 6.10. Figures 6.9(a) to 6.9(d) show the optical micrographs of the outer surfaces of the coating in the bend tip after the 180º bend tests with a bend radius of 0.8 mm, 1.0 mm, 2.4 mm and 3.2 mm, respectively. The bend axis is along the longitudinal direction for these specimens. Figures 6.10(a) to 6.10(d) show the optical micrographs of the outer surfaces of the coating in the bend tip after the 180º bend tests with a bend radius of 0.8 mm, 1.0 mm, 2.4 mm and 3.2 mm, respectively. The bend axis is perpendicular to the longitudinal direction for the specimens shown in Figures 6.10(a) to 6.10(d). There are no visible

signs of the deterioration of the surface quality for the specimens after the 180º bend tests.

6.3.4. Flattening test

To study the failure mechanism and ductility of coated sheets and the behavior of individual layer, the specimens, which were bent to 180º during semi-guided bend tests, were flattened as shown schematically in Figure 5.10. The separation distance δ of the two bent legs of the sheet is marked in the figure. The flattening continued until a selected vertical separation distance was reached between the bent legs. The tests were carried out at a constant crosshead speed of 1 mm/min. Specimens which were bent to 180º were flattened under a controlled speed of 1mm/min such that the separation between the two legs of the flattened specimen was 0.5 mm. The flattened specimens were placed under an optical microscope to examine the outer bent surface for cracks, voids or surface roughness. Optical micrographs of the outer surfaces of the bend tip are shown in Figures 6.11(a) to 6.11(d) for sheets flattened after bending by a radius of 0.8 mm, 1.0 mm, 2.4 mm and 3.2 mm, respectively, with the bend axis along the longitudinal direction. Optical micrographs of the outer coated surfaces on the bend tip after flattening test with a bend radius of 0.8 mm, 1.0 mm, 2.4 mm and 3.2 mm are shown in Figures 6.12(a) to 6.12(d), respectively, with the bend axis perpendicular to the longitudinal direction. Visible failure of the polymer-graphite layer can be found on the bend tips as shown in the figures. There are visible surface cracks on all the specimens. However, the surface damage seems to be smaller for a higher initial bend angle.

6.3.5. Micrographic examination of the cross sections of the bent and flattened specimens

Optical micrographs of the cross sections of the flattened specimens were examined to study the failure mechanism of the polymer-graphite layer. Figures 6.13(a) and 6.13(b) show the micrographs of the cross sections of stainless steel sheets with two-sided coating. These specimens were flattened until a flattening separation distance of 0.6 mm was attained between the bent legs of the specimens. The bend radii for these specimens were 0.8 mm and 1.0 mm, respectively. The corresponding strain values are estimated to be 8% and 10%, respectively. The coatings did not suffer any visible damage but appear to develop a rougher surface.

The bendability of the polymer-graphite-coated stainless steel sheets was further explored with one-sided polymer-graphite coating and a separation distance of 0.5 mm with the pre-bend radii of 0.8 mm, 1.0 mm, 2.4 mm and 3.2 mm. This flattening step produced a strain of approximately 18% in the outer layer. The micrographs of the cross sections of the flattened sheets are shown in Figure 6.14. It is observed from comparing Figures 6.14(a) and 6.14(d) that a tighter bend radius causes a more severe failure of the polymer-graphite coating. Similar observations were obtained from the micrographs of the specimens that were bent and flattened with the bend axis transverse to the longitudinal direction as shown in Figures 6.15(a) to 6.15(b). The micrographs of the cross sections are in agreement with the surface micrographs and show an increased damage to the coating for tight bend radius.

6.3.6. Ball punch deformation test

The ball punch deformation test is used to evaluate the formability of the polymer coated stainless steel sheet. Figure 6.16 shows a schematic of the test apparatus. 45 mm by 45 mm square blanks of the specimens were clamped between two metallic dies. The polymer coated side of the specimen was held on the outer side away from the spherical penetrator contact side. The hold-down force was provided by tightening six bolts along the circumference of the punch bore. The torque on the bolts was adjusted by a hit and trial procedure to achieve the necessary hold-down force to prevent any material draw-in during the test. A torque of about 130 N-m was applied to each bolt to prevent any noticeable material draw-in. A metallic ball of diameter of 11 mm was used as the spherical penetrator. An automated MTS testing machine was used to push the spherical penetrator down onto the test specimen through the punch bore of diameter of 12.7 mm. The penetrator downward speed was maintained constant at 1 mm/min during the tests. The penetrator downward displacement was recorded through the built-in motion sensor in the MTS testing machine. Lubricant was not applied on the surface of the spherical punch. The tests were conducted for different penetrator displacements. The tests generally followed the guidelines of ASTM standard E643-84 [16].

Figures 6.17(a) to 6.17(d) show the optical micrographs of the outer coated surfaces of the specimens after the ball punch tests with a penetrator displacement of 3.5 mm, 3.6 mm, 4.0 mm and 4.85 mm, respectively. The outer coating seems to be intact after a punch depth of 3.5 mm. However, the coating shows a rough texture and some delamination after the punch depth of 3.6 mm. The stainless steel sheet fractured after the punch depth of 4.85 mm. It should be noted that although the surface coating does not show extensive delamination from the stainless steel sheet after a punch depth of

about 3.6 mm, the coating has a blistered appearance that is likely to be poorly bonded to the underlying substrate.

6.4. Discussion

Polymer-graphite coating did not significantly affect the tensile properties of the stainless steel base metal due to dominance of the mechanical properties of the stainless steel substrate. The coating surface started to deteriorate and developed a blistered texture as the uniaxial stretching continued and finally delaminated from the metal layer at a tensile strain of about 17%. Surface profile measurements indicated a progressive increase in the R_a value. A rougher surface can increase the contact resistance and also affect the flow of reactants thorough the channel therefore, it is important to control the surface quality of the coated sheets during any forming process. The failure mechanism in tensile tests can be explained on the basis of the interaction of interfacial and transverse cracks. It is likely that interface cracks are developed between the coating and the stainless steel substrate during the baking and curing process. The presence of graphite particles initiates transverse cracks which can coalescence with the interfacial cracks as the specimen is extended in uniaxial direction. This will cause the polymer-graphite flakes to separate and peel off from the metal surface.

The polymer-graphite coating also experienced failure during flattening tests. The severity of delamination is dependent upon the pre-bend radius. It is apparent that a larger bend radius produced less delamination. The direction of the bend axis did not affect the amount of damage in the polymer-graphite layer. This set of experiments suggests that a multistage forming process can be used to form the channels of stainless steel bipolar

plates with polymer-graphite coating. The experimental results also suggest that, based on the mechanics of bending, a thinner stainless steel sheet with a thinner polymer-graphite coating can withstand the strains produced during the flattening test with a separation distance of 0.5 mm. The polymer coating can survive a punch depth of about 3.5 mm and starts to develop a rough surface texture and shows signs of delamination from the stainless steel substrate beyond 3.5 mm of ball punch displacement.

6.5. Conclusions

The mechanical behavior of polymer-graphite coated stainless steel sheets has been explored and issues related to the surface quality and delamination of the coating has been identified. The failure mechanism of the polymer-graphite coating is also proposed. During tensile tests, the surface roughness of the coating changes and finally delamination occurs at a strain of about 17%. The delamination is likely to have caused by the propagation and coalescence of interfacial and transverse cracks. Bend tests and flattening tests of bent specimens were carried out to study the behavior of polymer-graphite protective layer under plane strain bending conditions. An important result derived from these tests is that the polymer-graphite coating can survive large strains if multi-step forming process is carried out. Use of thinner sheets can also reduce the amount of strain developed in the polymer-graphite layer. Ball punch deformation tests were also carried out to assess the behavior of the coating under dominant biaxial stretching conditions. The results of these tests will assist to better understand the channel forming process in polymer-graphite coated stainless steel sheets.

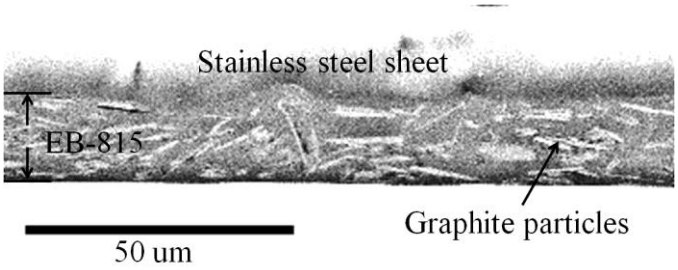

(a)

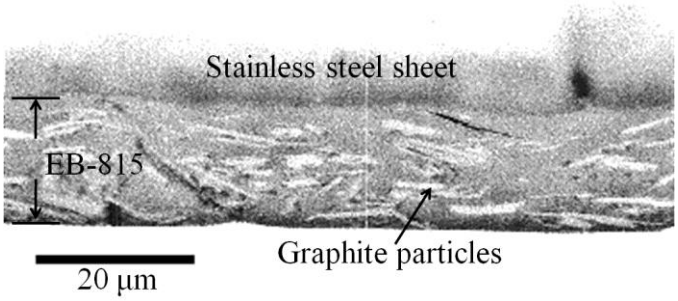

(b)

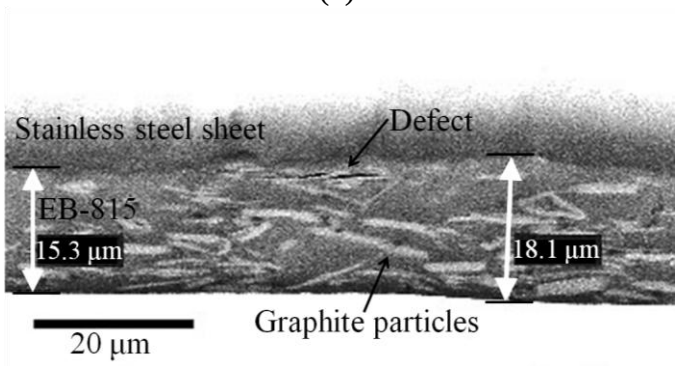

(c)

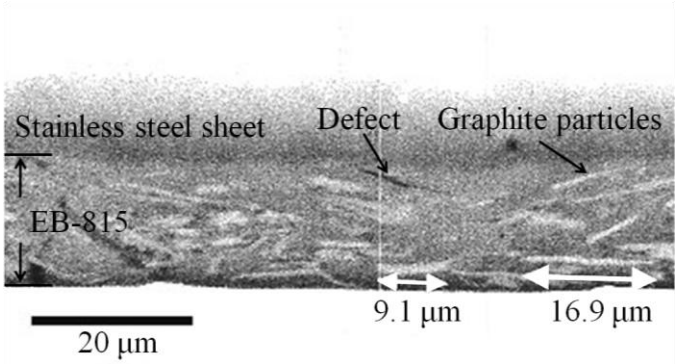

(d)

Figure 6.1. Scanning electron micrographs of the cross sections of EB-815 coating at a magnification of (a) 1000x and (b) 1500x. Selective measured values of the (c) EB-815 coating thickness and (d) graphite particle sizes at a magnification of 1500x.

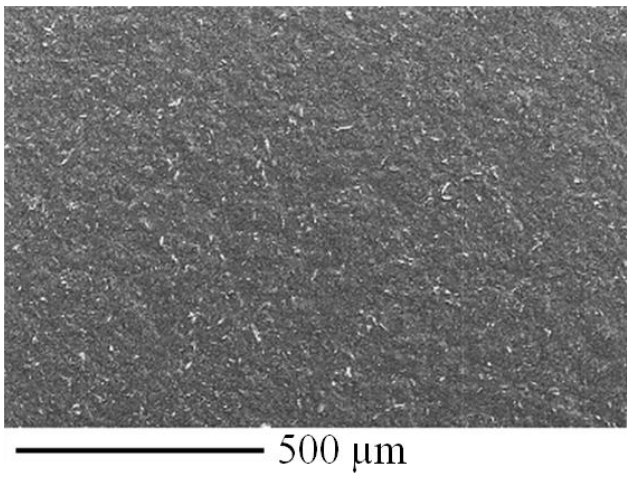

(a)

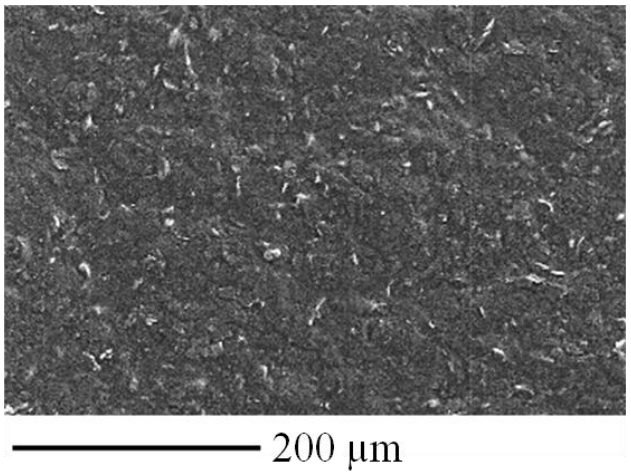

(b)

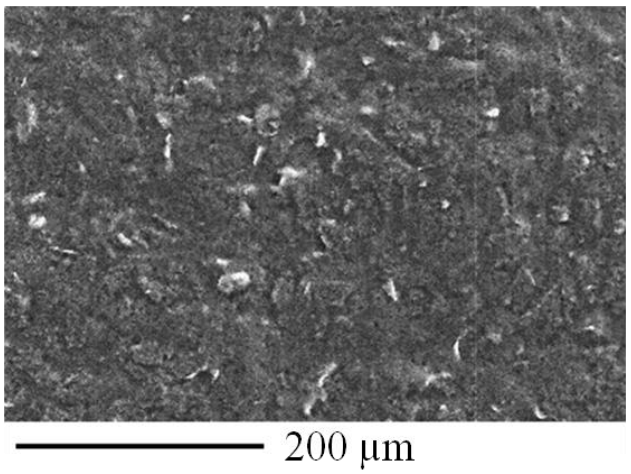

(c)

Figure 6.2. Scanning electron micrographs of the surface of EB-815 coating at the center of the coated sheet at a magnification level of (a) 100x, (b) 250x and (c) 500x.

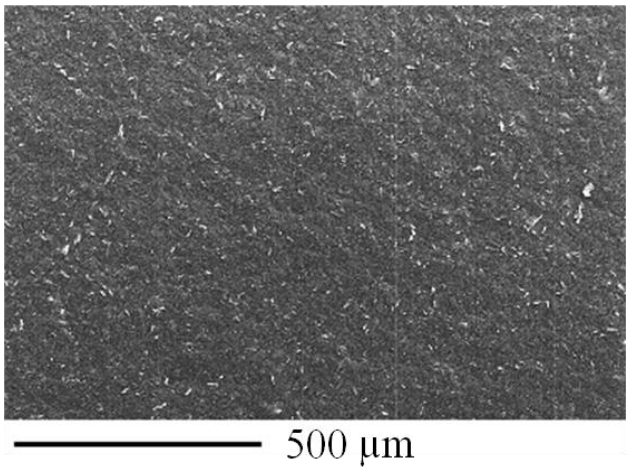

(a)

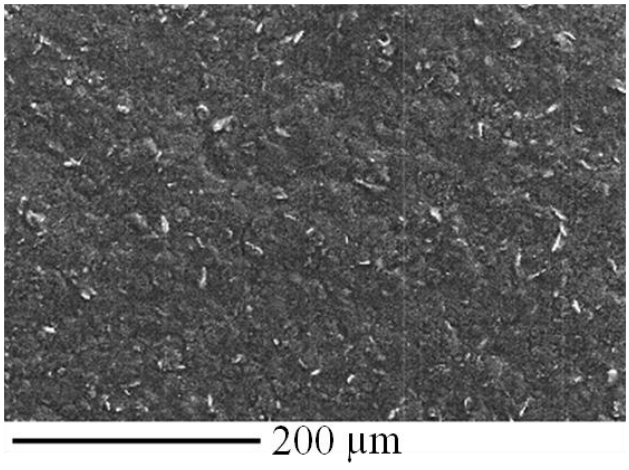

(b)

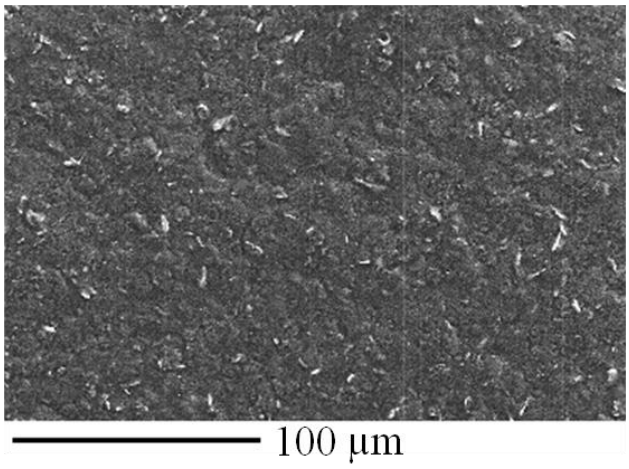

(c)

Figure 6.3. Scanning electron micrographs of the surface of EB-815 coating at the edge of the coated sheet at a magnification level of (a) 100x, (b) 250x and (c) 500x.

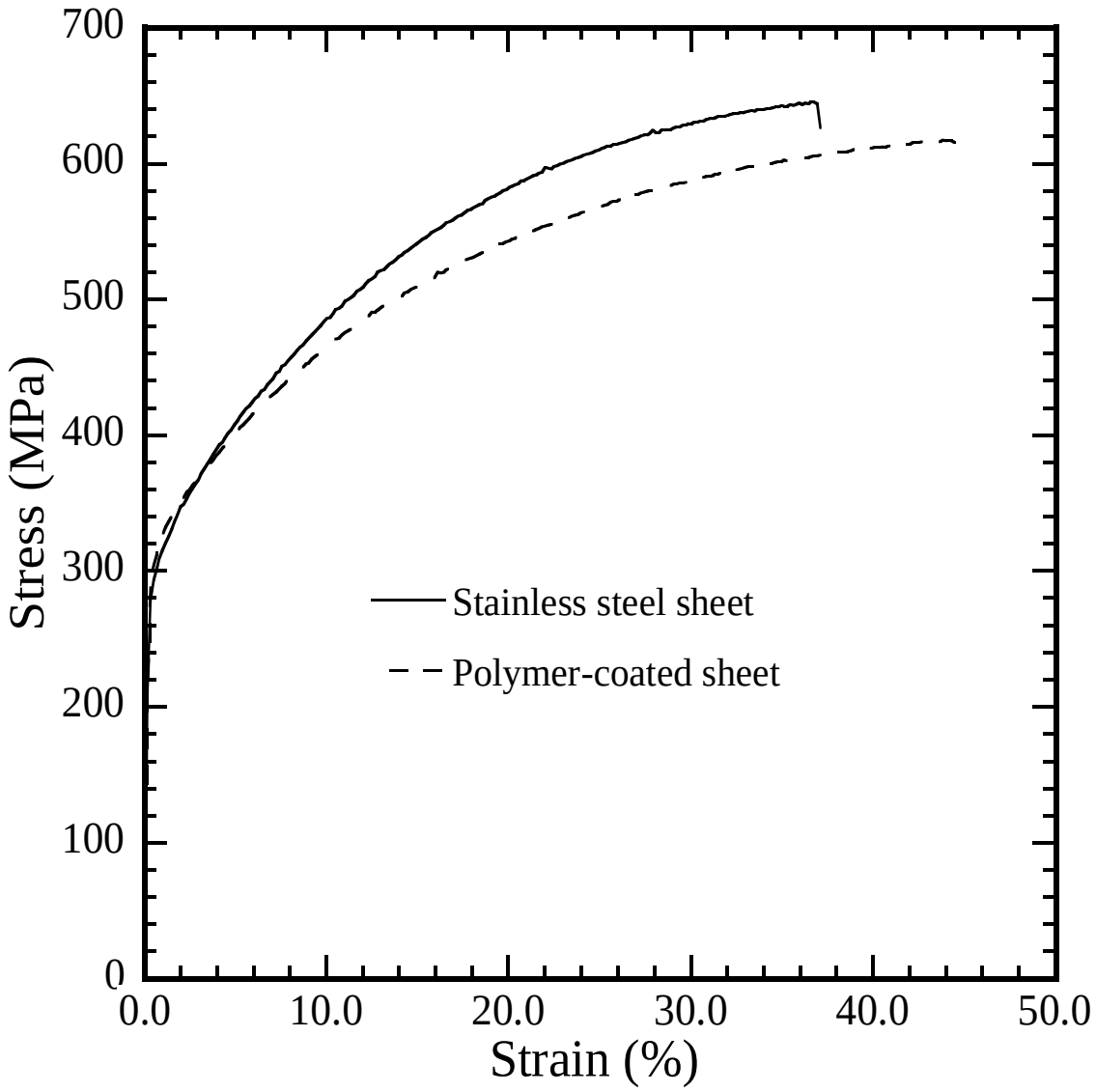

Figure 6.4. The engineering stress-strain curves for representative stainless steel and polymer-coated stainless steel sheets.

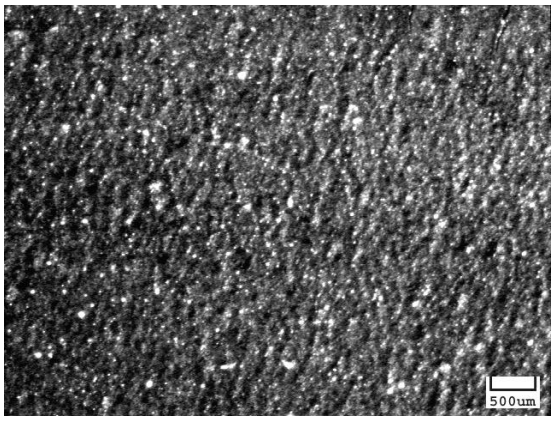

(a)

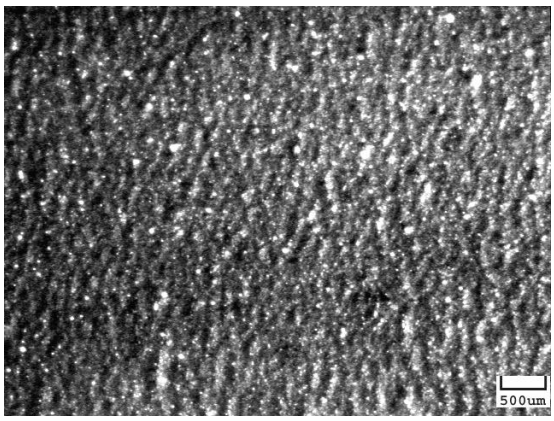

(b)

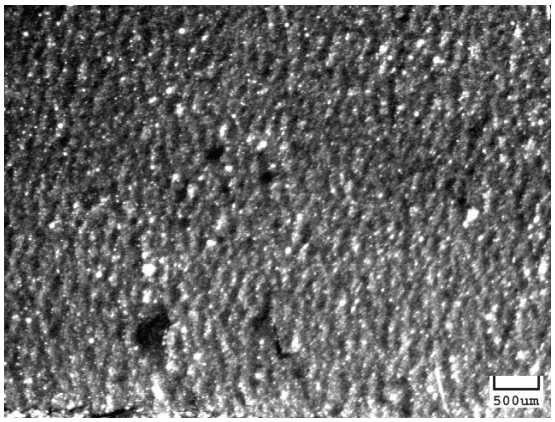

(c)

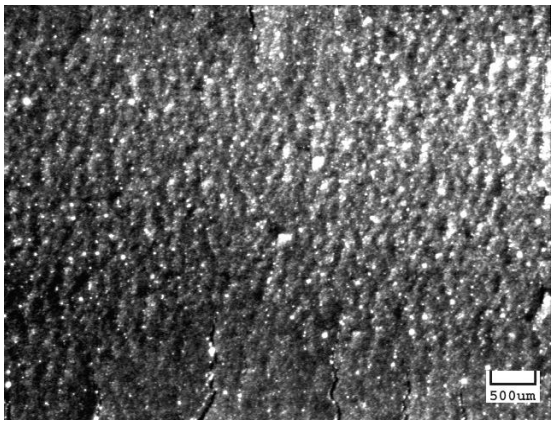

(d)

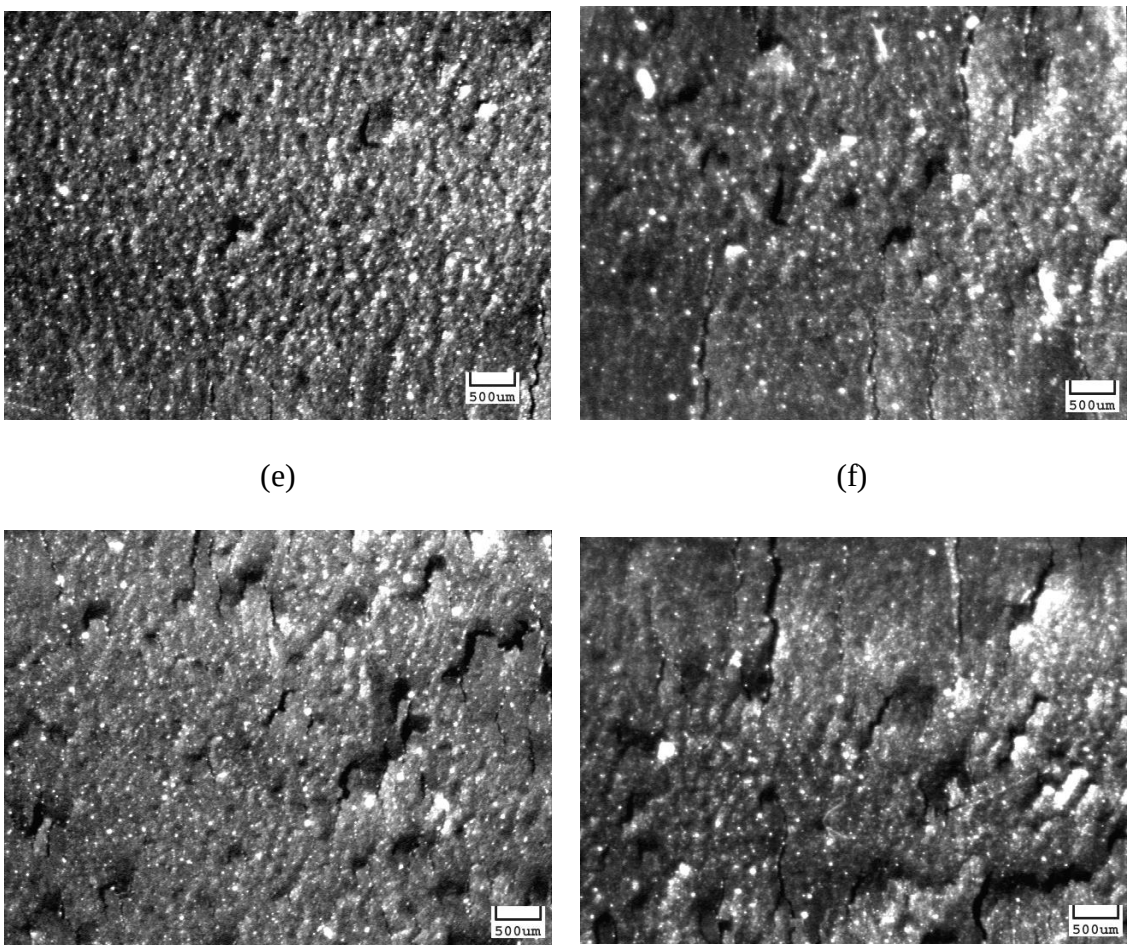

(e) (f)

(g) (h)

Figure 6.5. Optical micrographs of the surface texture for tensile specimens subjected to a uniaxial strain of (a) 8%, (b) 10% , (c) 11%, (d) 12%, (e) 13.5%, (f) 14.5%, (g) 16% and (h) 17%.

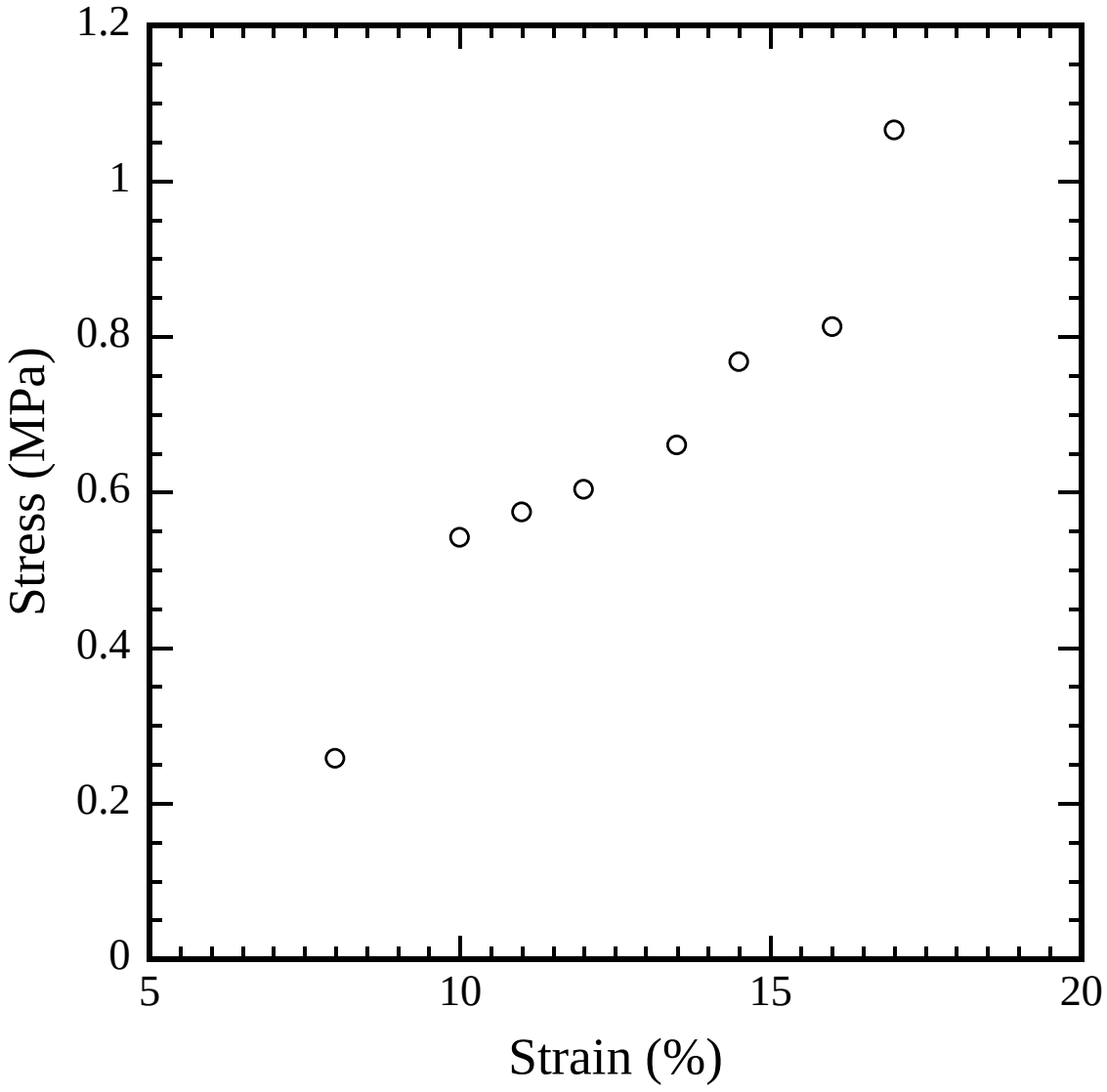

Figure 6.6. Plot of R_a values as a function of uniaxial strain.

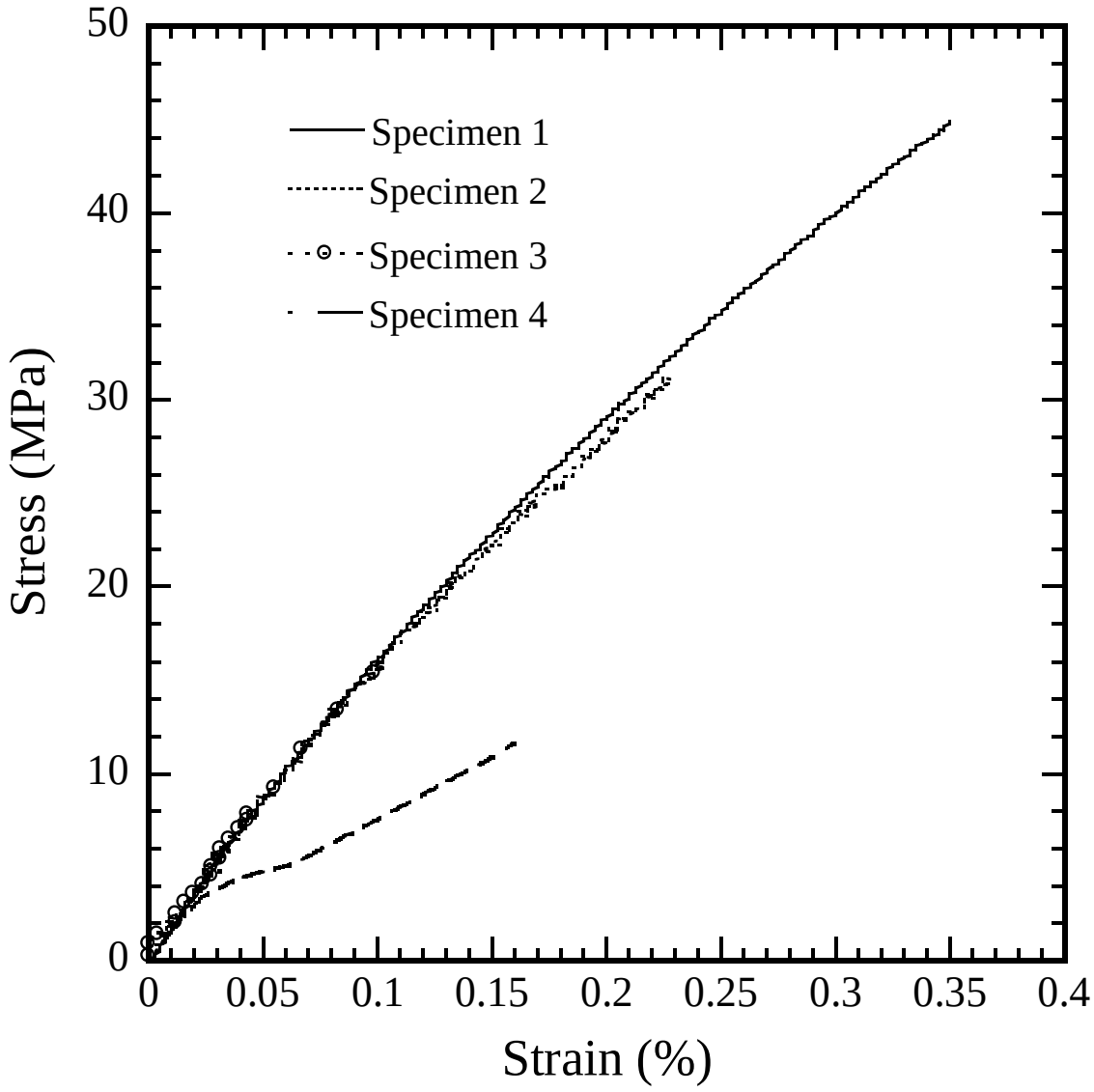

Figure 6.7. The engineering stress-strain curves EB-815 epoxy sheets from four test specimens.

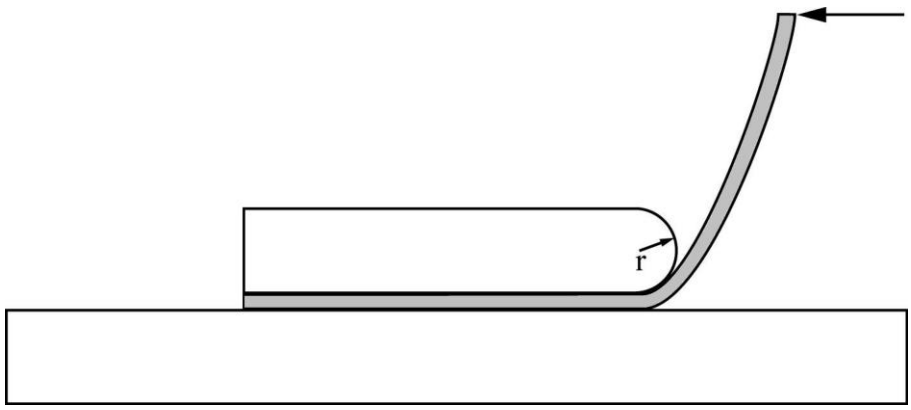

Figure 6.8. A schematic of the semi-guided bend test apparatus.

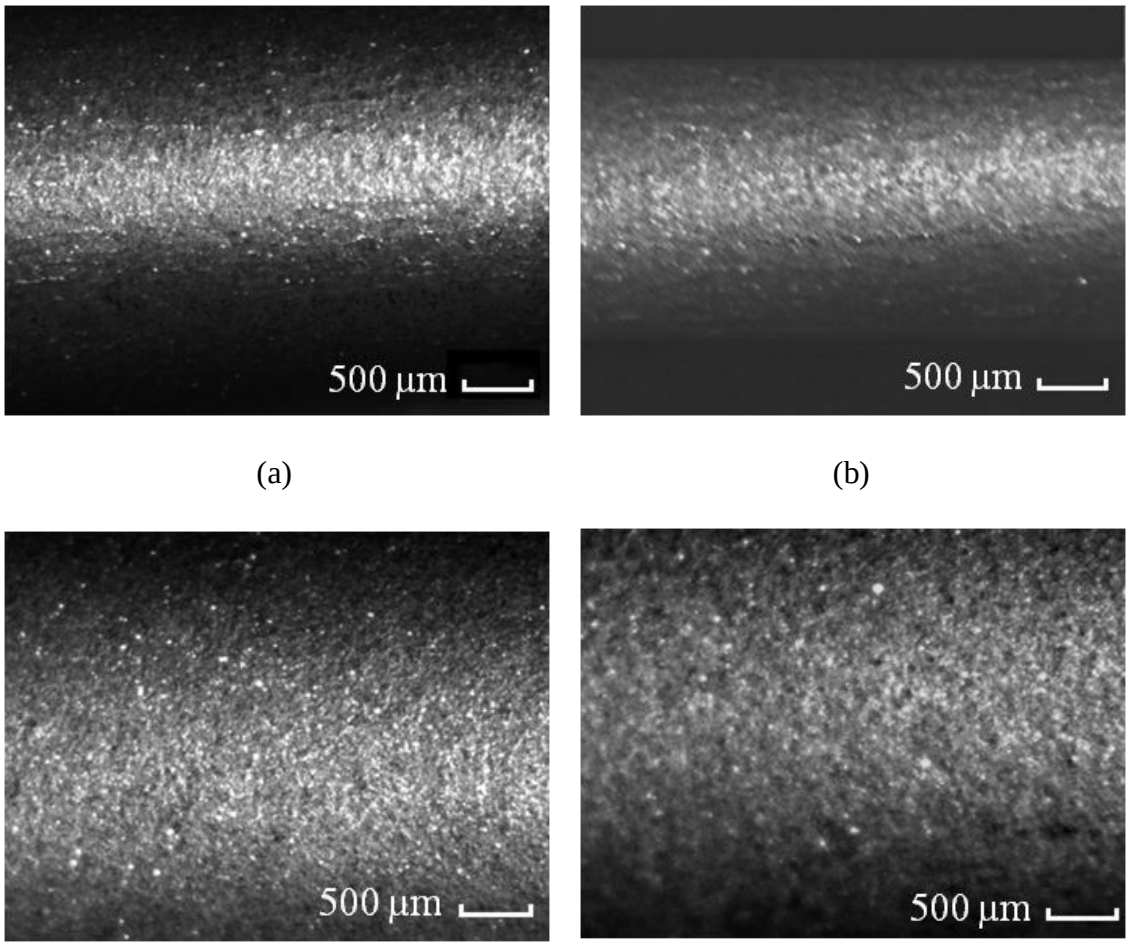

Figure 6.9. Optical micrographs of the outer surfaces of the coating in the bend tip after the 180^{o} bend tests with a bend radius of (a) 0.8 mm, (b) 1.0 mm, (c) 2.4 mm and (d) 3.2 mm. The bend axis is along the longitudinal direction.

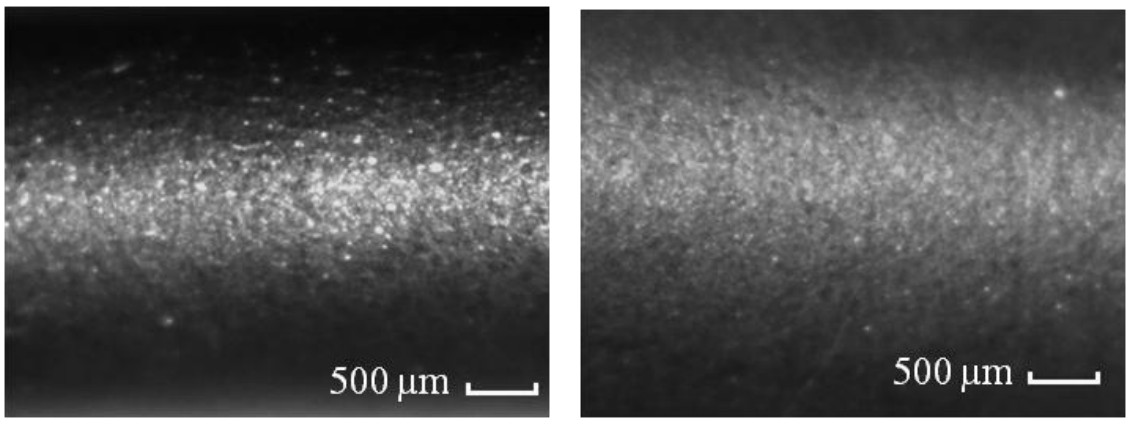

(a) (b)

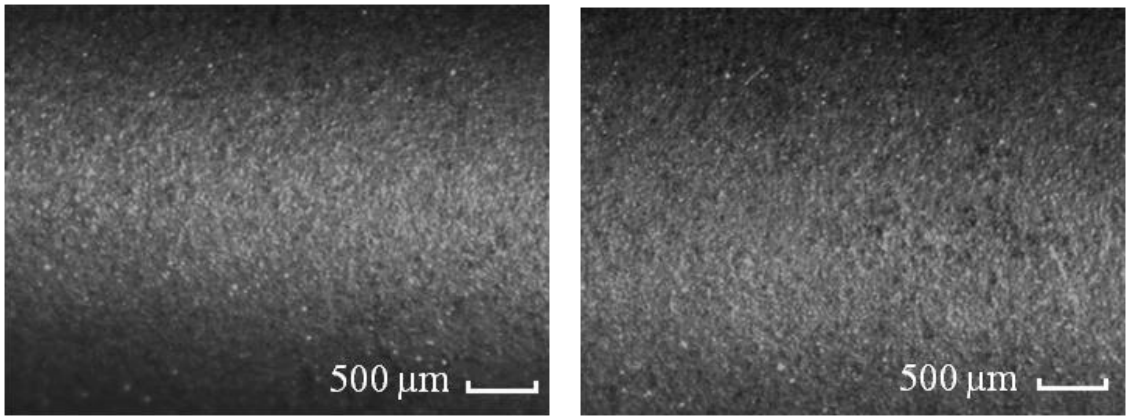

(c) (d)

Figure 6.10. Optical micrographs of the outer surfaces of the coating in the bend tip after the 180^{o} bend tests with a bend radius of (a) 0.8 mm, (b) 1.0 mm, (c) 2.4 mm and (d) 3.2 mm. The bend axis is perpendicular to the longitudinal direction.

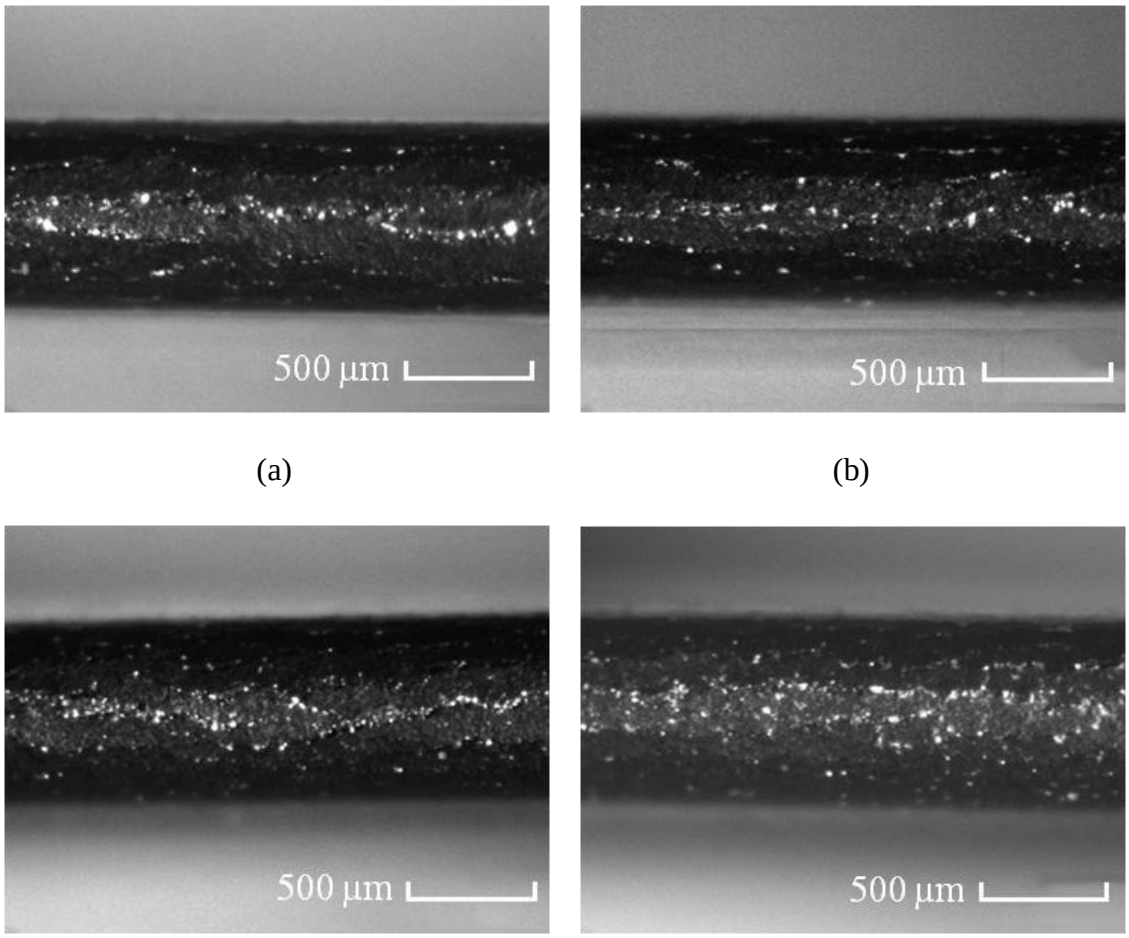

Figure 6.11. Optical micrographs of the outer coated surfaces on the bend tip after flattening test with a bend radius of (a) 0.8 mm, (b) 1.0 mm, (c) 2.4 mm and (d) 3.2 mm. The bend axis is along the longitudinal direction.

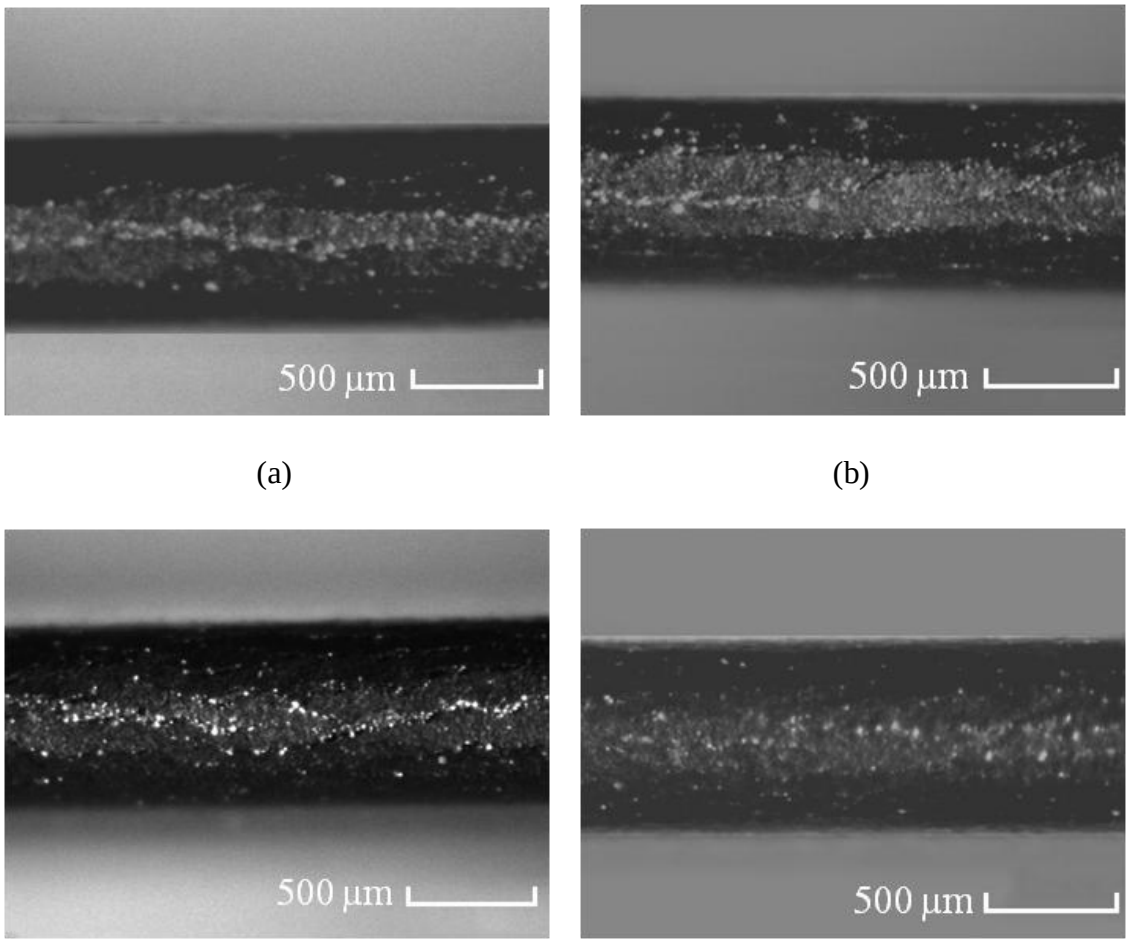

Figure 6.12. Optical micrographs of the outer coated surfaces on the bend tip after flattening test with a bend radius of (a) 0.8 mm, (b) 1.0 mm, (c) 2.4 mm and (d) 3.2 mm. The bend axis is perpendicular to the longitudinal direction.

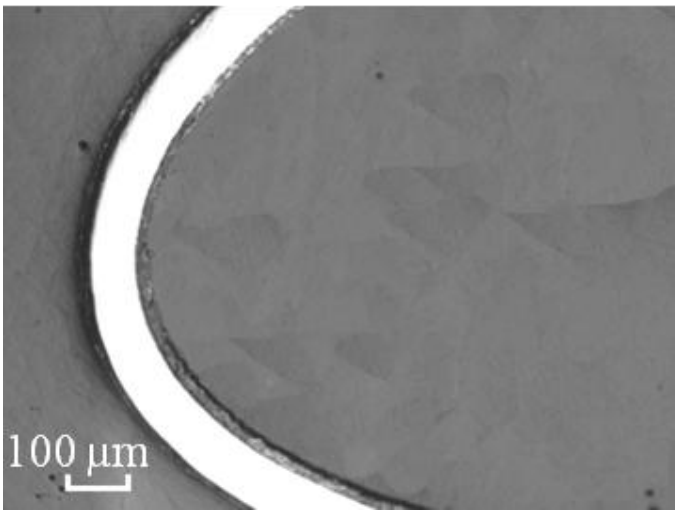

(a)

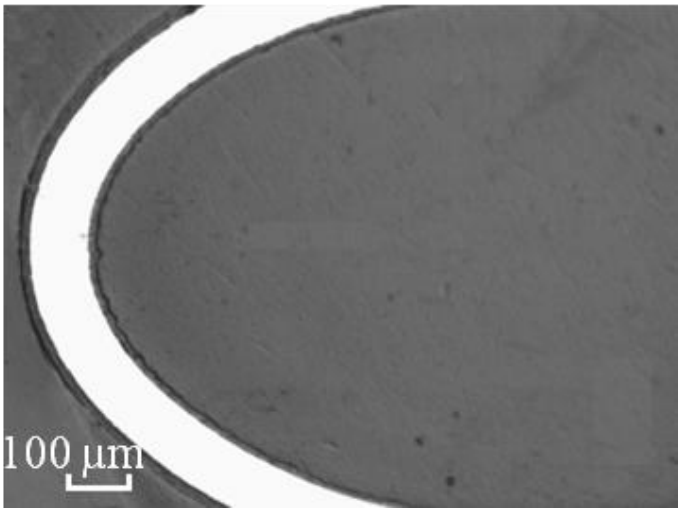

(b)

Figure 6.13. Optical micrographs of the cross sections of two-sided coated stainless steel sheets flattened to a separation distance of 0.6 mm. The bend radius is (a) 0.8 mm and (b) 1.0 mm.

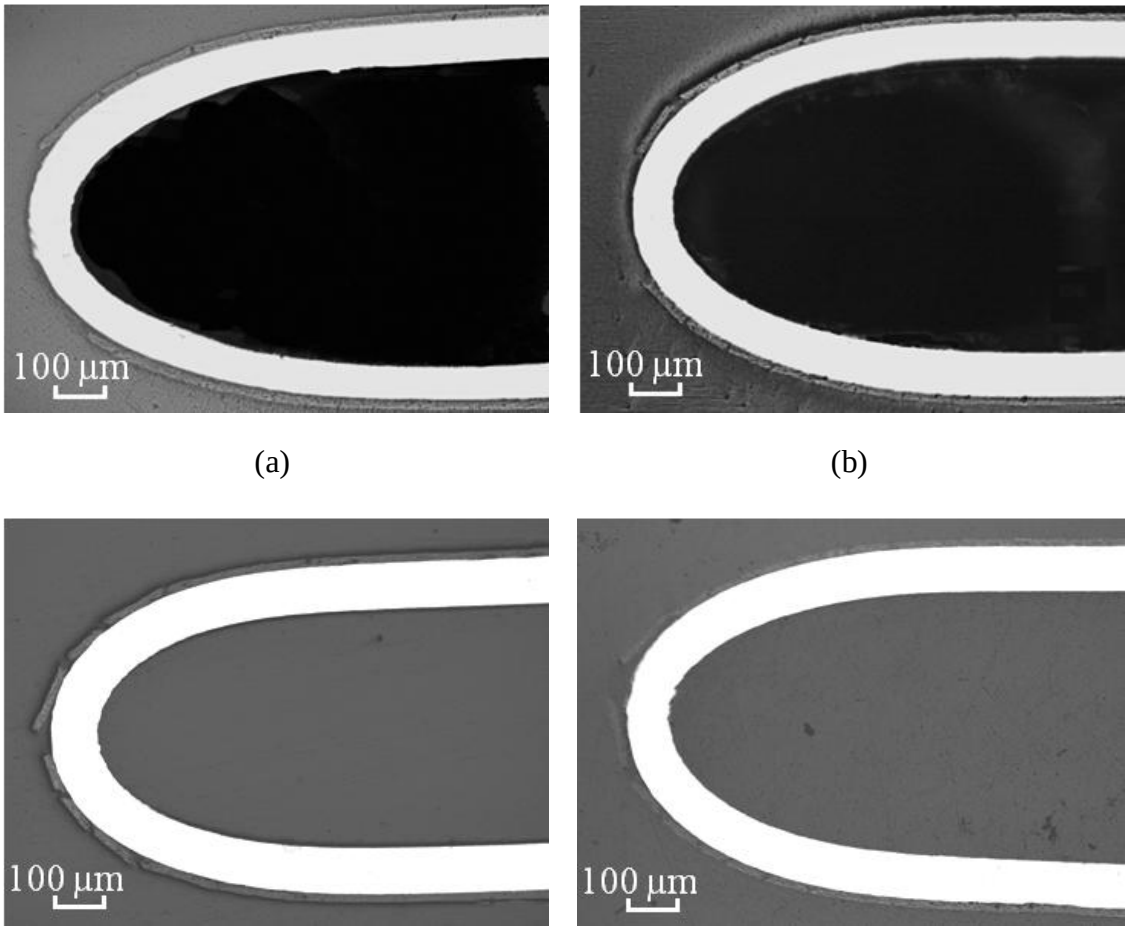

Figure 6.14. Optical micrographs of the cross sections of the one-sided coated stainless steel sheets, flattened to a separation distance of 0.5 mm with a bend radius of (a) 0.8 mm, (b) 1.0 mm, (c) 2.4 mm and (d) 3.2 mm. The bend axis is along the longitudinal direction.

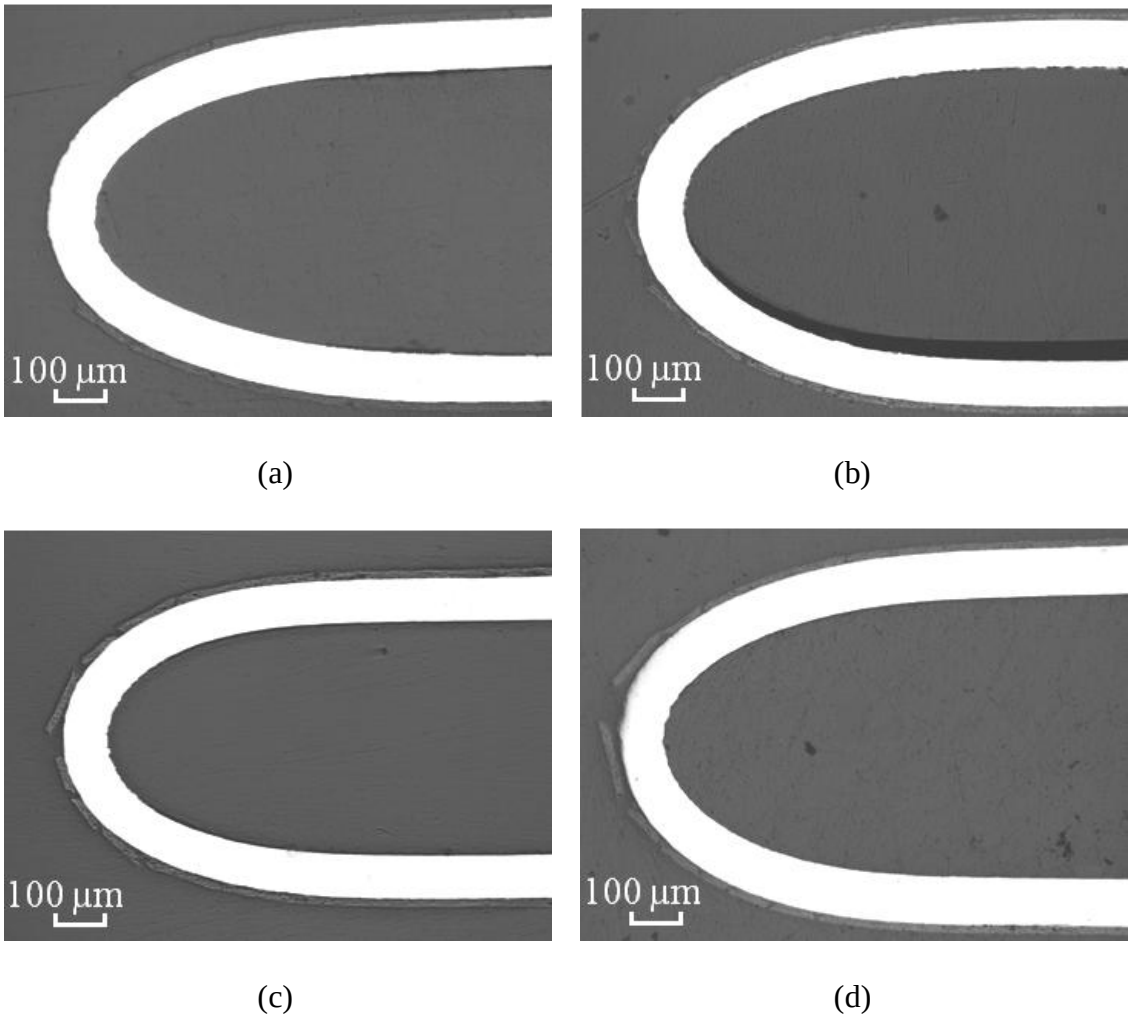

Figure 6.15. Optical micrographs of the cross sections of the one-sided coated stainless steel sheets, flattened to a separation distance of 0.5 mm with a bend radius of (a) 0.8 mm, (b) 1.0 mm, (c) 2.4 mm, and (d) 3.2 mm. The bend axis is perpendicular to the longitudinal direction.

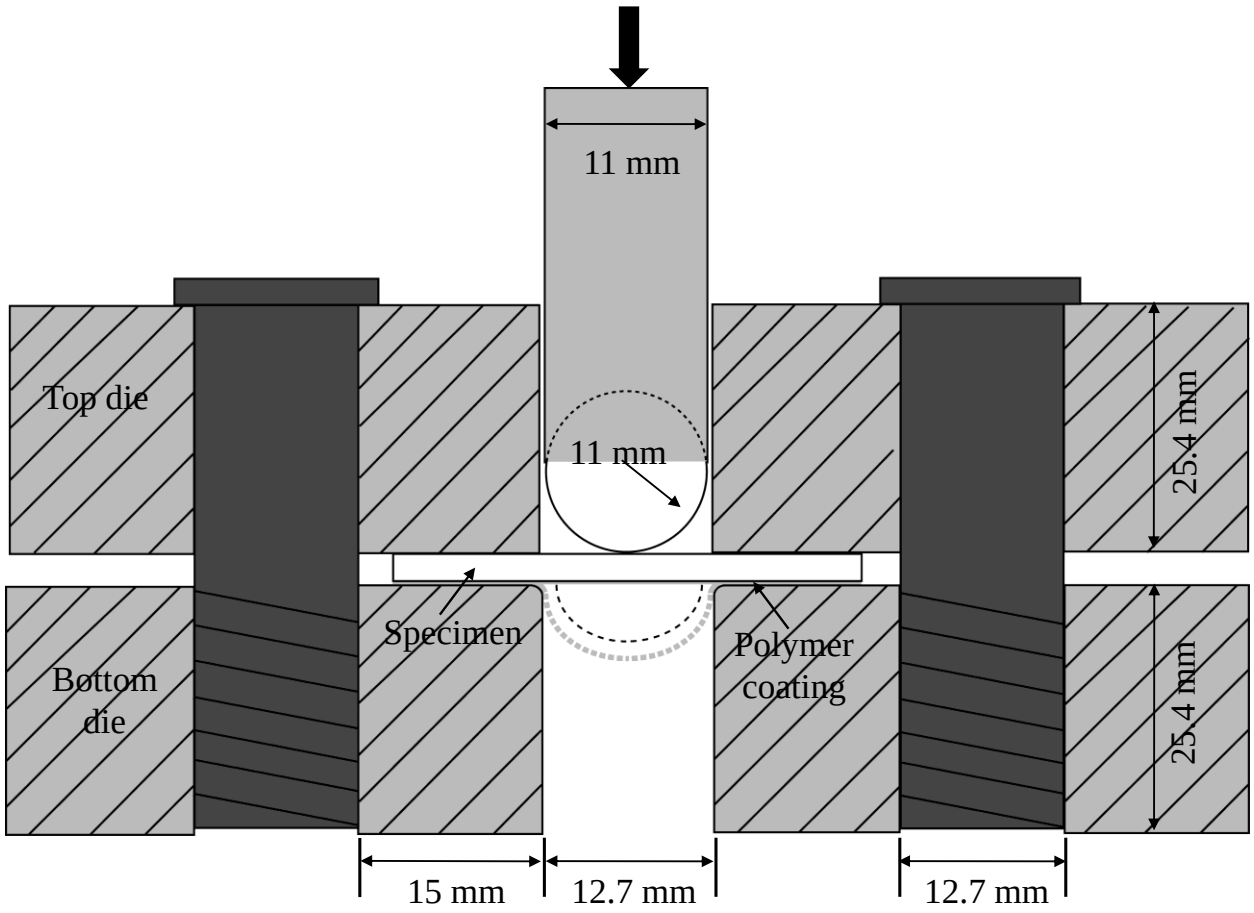

Figure 6.16. A schematic of the ball punch deformation test apparatus.

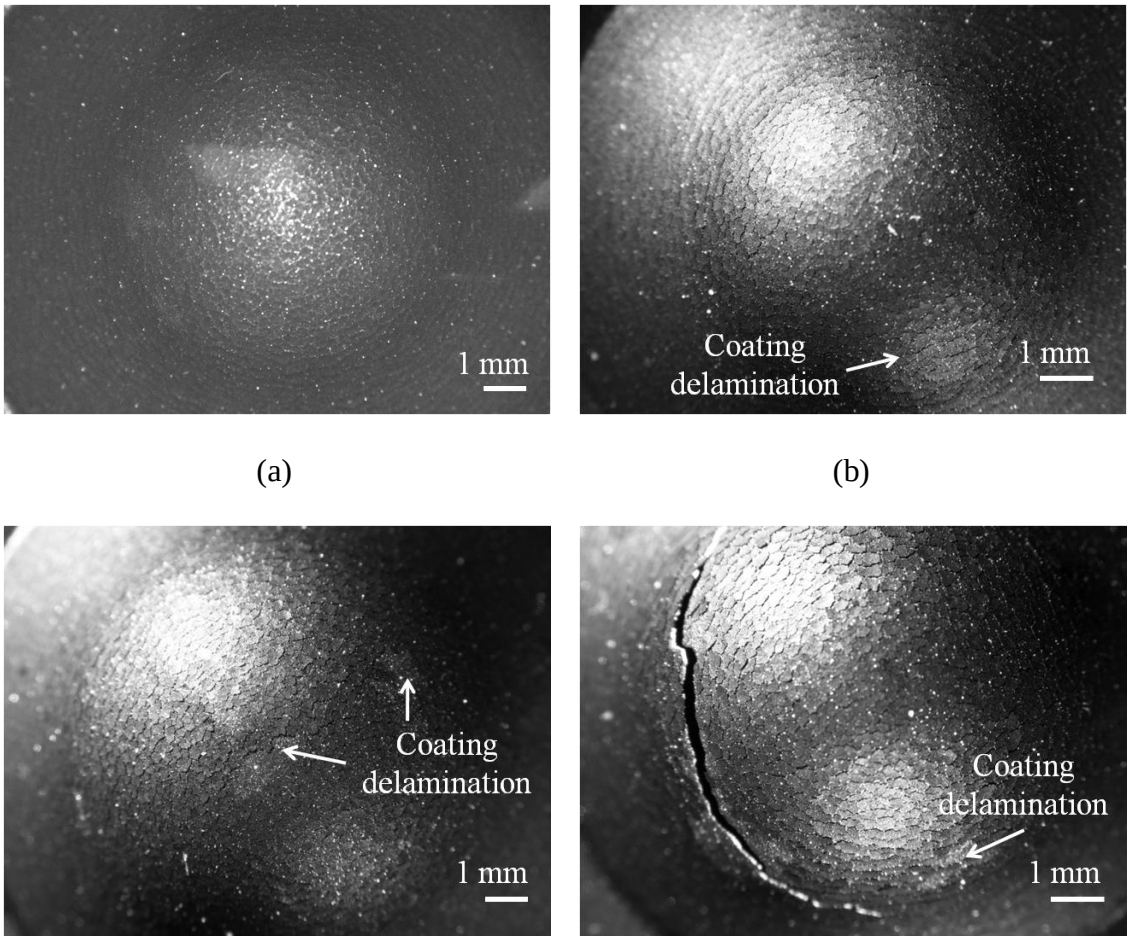

Figure 6.17. Optical micrographs of the outer coated surfaces of the specimens after ball punch deformation tests with a penetrator displacement of (a) 3.5 mm, (b) 3.6 mm, (c) 4.0 mm and (d) 4.85 mm.

References

[1] Li X, Sabir I. Review of bipolar plates in PEM fuel cells: Flow-field designs. International Journal of Hydrogen Energy 2005; 359-371.

[2] Hermann A, Chaudhuri T, Spagnol P. Bipolar plates for PEM fuel cells: A review. International Journal of Hydrogen Energy 2005; 1297-1302.

[3] Borup RL, Vanderborgh NE. Design and testing criteria for bipolar plate materials for PEM fuel cell applications. Materials Research Society Symposium - Proceedings 1995; 393: 151-155.

[4] Makkus RC, Janssen AHH, de Bruijn FA, Mallant RKAM. Stainless steel for cost competitive bipolar plates in the PEMFCs. Fuel cell Bulletin 2000; 17: 5-9

[5] Davies DP, Adcock PL, Turpin M, Rowen SJ. Stainless steel as a bipolar plate material for solid polymer-graphite fuel cells. Journal of Power Sources 2000; 86: 237-242.

[6] Davies DP, Adcock PL, Turpin M, Rowen SJ. Bipolar plate materials for solid polymer-graphite fuel cells. Journal of Applied Electrochemistry 2000; 30: 101-105.

[7] Wang H, Sweikart MA and Turner JA. Stainless steel as bipolar plate material for polymer-graphite electrolyte membrane fuel cells. Journal of Power Sources 2003; 115: 243-251.

[8] Wang H, Turner JA. Ferritic stainless steels as bipolar plate material for polymer-graphite electrolyte membrane fuel cells. Journal of Power Sources 2004; 128: 193-200.

[9] Mehta V, Cooper JS. Review and analysis of PEM fuel cell design and manufacturing. Journal of Power Sources 2003; 114: 32-53.

[10] Middelman E, Kout W, Vogelaar B, Lenssen J, Waal Ede. Bipolar plates for PEM fuel cells. Journal of Power Sources 2003; 118: 44-46.

[11] Cho EA, Jeon US, Ha H Y, Hong SA, Oh IH. Characteristics of composite bipolar plates for polymer electrolyte membrane fuel cells. Journal of Power Sources 2004, 125: 178-182.

[12] Heinzel A, Mahlendorf F, Niemzig O, Kreuz C. Injection moulded low cost bipolar plates for PEM fuel cells. Journal of Power Sources 2004; 131: 35-40.

[13] Kuan HC, Ma CCM, Chen KH, Chen SM. Preparation, electrical, mechanical and thermal properties of composite bipolar plate for a fuel cell. Journal of Power Sources 2004; 134: 7-17.

[14] ASTM E8-04: Standard test methods for tension testing of metallic materials. American Society of Testing and Materials, West Conshohocken, PA, USA 2004.

[15] ASTM E290-97: Standard test methods for bend testing of material for ductility. American Society of Testing and Materials, West Conshohocken, PA, USA 2004.

[16] ASTM E643-84: Standard test methods for ball punch deformation of metallic sheet material. American Society of Testing and Materials, West Conshohocken, PA, USA 2000.

CHAPTER VII

CONCLUSIONS

In Chapter II, the failure mode of laser welds in lap-shear specimens of non-galvanized SAE J2340 300Y high strength low alloy (HSLA) steel sheets under quasi-static loading conditions is examined based on the experimental observations and finite element analyses. Laser welded lap-shear specimens with reduced cross sections were made to avoid the failure not directly related to the welds. Optical micrographs of the cross sections near the welds in the specimens before and after tests are examined to understand the microstructure of the weld and the failure mode of the welds. Micro-hardness tests were also conducted to provide an assessment of the mechanical properties in the base metal, heat affected and fusion zones. The micrographs indicate that the weld failure appears to be initiated from the base metal near the boundary of the base metal and the heat affected zone at a distance to the pre-existing crack tip, and the specimens fail due to the necking/shear of the lower left load carrying sheets. Finite element analyses based on non-homogenous multi-zone material models were conducted to model the ductile/necking shear failure and to obtain the J integral solutions for the pre-existing cracks. The results of the finite element analyses are used to explain the ductile fracture initiation sites and the necking/shear of the lower left load carrying sheets. The J integral solutions obtained from the finite element analyses based on the 3-zone finite element model indicate that the J integral for the pre-existing cracks are low compared

to the fracture toughness at the failure loads of the experiments and the specimens should fail in a plastic collapse mode of necking/shear. The effects of the sheet thickness on the failure mode were then investigated for laser welds with a fixed ratio of the weld width to the thickness. For the given non-homogenous material model, the J integral solutions appear to be scaled by the thickness as those for a homogeneous material model. With consideration of the plastic collapse failure mode and fracture initiation failure mode, a critical thickness can be obtained for the transition of the plastic collapse failure mode of necking/shear to the fracture initiation failure mode. Finally, the failure load is expressed as a function of the sheet thickness based on the two failure modes for engineering design purposes. The results demonstrate that the failure criteria of welds based on the plastic collapse failure mode should be used cautiously for welds of thicker sheets due to possible lower failure loads due to the fracture initiation from the pre-existing crack tips.

In Chapter III, the fatigue behavior of laser welds in lap-shear specimens of non-galvanized SAE J2340 300Y high strength low alloy (HSLA) steel sheets is investigated based on experimental observations and two fatigue life estimation models. Optical micrographs of the laser welds before and after failure under quasi static and cyclic loading conditions are examined. The micrographs show that the failure modes of laser welds under quasi-static and cyclic loading conditions are different. Under quasi-static loading conditions, the weld failure appears to be initiated from the base metal near the boundary of the based metal and the heat affected zone at a distance to the pre-existing crack tip and the specimens fail due to the necking/shear of the lower left load carrying sheets. Under low-cycle loading conditions, the weld failure appears to be initiated from the pre-existing crack tips and the specimens finally fail from the ductile fracture through

the lower left load carrying sheets. Under high-cycle loading conditions, the weld failure appears to be initiated from the pre-existing crack tips and the specimens finally fail from the kinked fatigue crack propagating through the upper right load carrying sheets. Finite element analyses of the laser welded lap-shear specimens with consideration of the weld bead protrusion were carried out to obtain the global and local stress intensity factor solutions for the main cracks and kinked cracks. The stress intensity factor solutions can be used to explain the kinked fatigue crack growth patterns under high-cycle loading conditions. A kinked fatigue crack growth model based on the global and local stress intensity factor solutions for finite kinked cracks obtained from the finite element analyses and a structural stress model based on the closed-form structural stress solutions of the beam bending theory are adopted to estimate the fatigue lives of the laser welds. The fatigue life estimations based on the kinked fatigue crack growth model agree reasonably well with the experimental results of the welds whereas the fatigue life estimations based on the structural stress model agree with the experimental results for larger load ranges but are higher than the experimental results for smaller load ranges.

In Chapter IV, the effects of different thickness and gaps on the stress intensity factor solutions of laser welds in lap-shear specimens are investigated. An analytical approach based on the structural stress of the beam bending theory is used to obtain the stress intensity factor solutions for laser welds in lap-shear specimens with different sheet thicknesses. Two-dimensional finite element analyses were also carried out to obtain the stress intensity factor solutions for the welds as functions of the normalized weld width. The results of the finite element analyses are compared with the analytical stress intensity factor solutions. The stress intensity factor solutions are higher for the right pre-existing

crack tip of the load carrying upper right thinner sheet as compared to those for the left pre-existing crack tip of the load carrying lower left thicker sheet. Approximate stress intensity factor solutions as functions of the normalized weld width are also proposed for the right pre-existing crack tip of the load carrying upper right thinner sheet. Finite element analyses were also carried out to study the effects of gaps on the stress intensity factor solutions for cracks emanating from the tips of the pre-existing notches. The results indicate that the stress intensity factor solutions for the cracks increase as the gap increases. Finally, a closed-form structural stress solution with consideration of the gap in a lap-shear specimen is developed. The closed-form structural stress solution is used to investigate the effect of gap on the fatigue lives of the welds. The results indicate that the fatigue life decreases as the gap increases.

In Chapter V, the mechanical behavior and failure mechanism of Nb-clad stainless steel sheets were investigated. A microstructural analysis of the roll-cladded specimens suggested a good metallurgical bond free of interfacial defects. The as-rolled specimens were annealed to increase their ductility. The annealing also reduced the amount of springback as compared to that of the as-rolled specimen. Annealing caused the development of a brittle intermetallic layer at the Nb and stainless steel interface. Tensile tests showed increased ductility in terms of lower yield strength and larger elongation before failure. A "canoeing" effect during tensile testing of the clad sheets increased with increasing annealing temperature. Nb layer delaminated from the stainless steel sheet in the annealed 1050/60 tensile specimens. Failure in the flattened annealed specimens is caused by localized necking of the Nb layer after brittle fracture of the intermetallic layer. Nano-indentation was used to evaluate the mechanical properties of

the individual layers in the Nb-clad stainless steel sheets. The hardness of the stainless steel layer decreased slightly after annealing, but no noticeable hardness change was observed in the Nb layer after annealing. The hardness and elastic modulus of the intermetallic layer were very large as compared to those of the Nb and stainless steel sheets. The results of the present study will provide a better understanding of the mechanical behavior of clad metallic sheets and provide general criteria and guidelines for formability of Nb-clad stainless steel sheets. This knowledge can be used to model and study the channel forming process in the clad sheets for its application as bipolar plates in PEM fuel cells.

In Chapter VI, the mechanical behavior of polymer-graphite coated stainless steel sheets has been explored and issues related to surface quality and delamination of the coating has been identified. The failure mechanism of the polymer-graphite coating is also proposed. During tensile tests, the surface roughness of the coating changes and finally delamination occurs at a strain of 17%. The delamination is likely to have caused by the propagation and coalescence of interfacial and transverse cracks. Bend tests and flattening tests of bent specimens were carried out to study the behavior of polymer-graphite protective layer under plane strain bending conditions. Ball punch deformation tests were also carried out to assess the behavior of the coating under dominant biaxial stretching conditions. An important result derived from these tests is that the polymer-graphite coating can survive large strains if multistep forming process is carried out. Use of thinner sheets can also reduce the amount of strain developed in the polymer-graphite layer. The results of these tests will assist to better understand the channel forming process in polymer-graphite coated stainless steel sheets.